Search for supersymmetry in opposite-charge, same-flavor dilepton events recorded with the CMS detector at $\sqrt{s} = 13\,\text{TeV}$ in 2016 data

Von der Fakultät für Mathematik, Informatik und Naturwissenschaften der RWTH Aachen University zur Erlangung des akademischen Grades eines Doktors der Naturwissenschaften genehmigte Dissertation

vorgelegt von

Christian Schomakers, M. Sc.

aus Münster

Berichter:

Univ.-Prof. Dr. rer. nat. Lutz Feld

Univ.-Prof. Dr. rer. nat. Thomas Hebbeker

Termin der mündlichen Prüfung 06.04.2018

Zusammenfassung

In dieser Arbeit wird eine Suche nach neuer Physik in Ereignissen mit einem entgegengesetzt geladenem Elektron- oder Muonpaar, Jets und fehlendem Transversaleimpuls vorgestellt. Zu diesem Zweck werden Daten aus Proton-Proton Kollisionen genutzt, die im Jahr 2016 bei einer Schwerpunktsenergie von 13 TeV mit dem CMS Detektor am LHC aufgenommen wurden. Der Datensatz entspricht einer integrierten Luminosität von $35{,}9\,\mathrm{fb}^{-1}$. In supersymmetrischen Modellen kann die gesuchte Signatur aus dem Kaskadenzerfall schwerer Teilchen in das leichteste supersymmetrische Teilchen, in diesem Fall das leichteste Neutralino, resultieren, welches als stabil angenommen wird und das Experiment unbeobachtet verlässt. Leptonpaare des gleichen Flavors und mit entgegengesetzter Ladung können aus dem Zerfall eines schweren Neutralinos in ein leichteres stammen. In diesem Fall wird ein oberes Limit in der Verteilung der invarianten Masse des Dileptonsystems $m_{\ell\ell}$ in Form einer Kante erwartet, deren Position etwa bei der Massendifferenz zwischen den Neutralinos liegt. Der dominante Untergrund aus bekannten Standardmodellprozessen in Ereignissen mit der gesuchten Signatur ist die Paarproduktion von Top-Quarks. Die Flavors der Leptonen aus dileptonischen Zerfällen von Top-Quark Paaren sind unkorreliert. Daher werden Ereignisse mit Leptonen unterschiedlichen Flavors genutzt werden, um diesen Prozess und andere flavor-symmetrische Untergründe abzuschätzen. Kleine Korrekturen werden aus Daten bestimmt und angewandt, um experimentelle Effekte zu korrigieren, welche die Flavor-Symmetry beeinflussen. Nicht-flavor-symmetrische Untergründe stammen zumeist aus Prozessen die den Zerfall eines Z-Bosons enthalten. Hierbei müssen zwei Fälle berücksichtigt werden: Ereignisse in denen der fehlende Transversalimpuls von experimentellen Effekten, hauptsächlich der Fehlmessung von Jets, hervorgerufen wird, sowie seltene Prozesse bei denen Neutrinos die unausgeglichene Impulsbilanz verursachen. Erstere werden aus Kontrolldaten mit Photonen abgeschätzt, während für letztere simulierte Ereignisse genutzt werden, die in Kontrollregionen in Daten validiert werden. Bei einer Schwerpunktsenergie von 8 TeV beobachtete die CMS Kollaboration eine Abweichung von der Standardmodellerwartung mit einer lokalen Signifikanz von 2,5 Standardabweichungen. Diese war konsistent mit einer Kante in der $m_{\ell\ell}$-Verteilung bei etwa 80 GeV. Diese Abweichung kann in dieser Arbeit nicht bestätigt werden. Neue Suchregionen, unter Verwendung der $\mathrm{M_{T2}}$-Variable und einer neu definierten Wahrscheinlichkeitsverteilung, werden eingeführt, um den Untergrund aus Top-Quark Paarproduktion zu reduzieren, welcher durch den höheren Wirkungsquerschnitt bei 13 TeV Schwerpunktsenergie deutlich in seiner Bedeutung zugenommen hat. Weder ein Fit, um nach einer Kante in der $m_{\ell\ell}$-Verteilung zu suchen, noch ein Zählexperiment, in dem die beobachtete Anzahl an Ereignissen mit der erwarteten Anzahl verglichen wird, weisen eine signifikante Abweichung von der Erwartung aus Standardmodellprozessen auf. In der Abwesenheit von Hinweisen auf neue Physik werden die Ergebnisse genutzt, um Auschlussgrenzen von bis zu 1,2 TeV auf die Masse des bottom Squarks in vereinfachten supersymmetrischen Modellen zu setzen. Diese Auschlussgrenzen liegen 400–600 GeV oberhalb der Grenzen aus vorherigen Analysen.

Abstract

In this thesis, a search for new physics in final states with an oppositely-charged electron or muon pair, jets, and missing transverse momentum is presented. For this purpose, proton-proton collision data are used, which were recorded at a center-of-mass energy of 13 TeV with the CMS experiment at the LHC in 2016. The data set corresponds to an integrated luminosity of $35.9\,\mathrm{fb}^{-1}$. In supersymmetric models the targeted signature can result from cascade decays of strongly produced heavy particles into the lightest supersymmetric particle, here the lightest neutralino, which is assumed to be stable and leaves the experiment undetected. Correlated lepton pairs can arise from the decay of a heavier neutralino into a lighter one. In this case, the mass difference between the two neutralinos is an upper limit to the invariant mass of the dilepton system $m_{\ell\ell}$ and results in a characteristic edge shape in the $m_{\ell\ell}$ spectrum. The dominant background in the final state with at least two opposite-charge, same-flavor leptons, jets, and missing transverse momentum is the pair production of top quarks. Lepton flavors from a dileptonically decaying top quark pair are uncorrelated. Different-flavor lepton pairs can be used to estimate this process and other flavor-symmetric backgrounds. Small corrections have to be applied to account for detector effects that disturb the flavor symmetry. Non-flavor-symmetric backgrounds arise mainly from the decay of Z bosons. Two cases have to be considered: Events with purely instrumental missing transverse momentum due to jet mismeasurements and rare processes in which the momentum imbalance is caused by neutrinos. The former are estimated from a photon control sample, while simulated events validated in data control regions are used for the latter. At a center-of-mass energy of 8 TeV, the CMS collaboration observed a deviation from the standard model expectation with a local significance of 2.5 standard deviations consistent with an edge in the $m_{\ell\ell}$ distribution at about 80 GeV. This deviation cannot be confirmed in this thesis. New search regions, using the $\mathrm{M_{T2}}$ variable and a newly defined likelihood discriminator, are defined to reduce background from top quark pair production which increased significantly because of the higher cross section at 13 TeV center-of-mass energy. Neither a fit searching for a kinematic edge nor a counting experiment analysis, comparing the number of observed events to the estimated yield, show significant deviations from the standard model expectation. In absence of a signal, limits up to 1.2 TeV are set on the bottom squark mass in a simplified supersymmetric model expanding previous limits by 400–600 GeV.

Contents

1 Introduction

One of the main goals of science in general and physics in particular is to understand the fundamental principles of matter. Our current understanding of the known particles and their interactions is summarized in the standard model (SM) of particle physics. In the last decades, the SM was able to describe measurements to a high precision and even to predict the existence of new particles, which had not been observed before. The latest success of the SM was the discovery of the Higgs boson in 2012, nearly five decades after the initial proposals of the Higgs mechanism. However, there are several experimental observations and theoretical considerations that lead to the conclusion that the SM is incomplete and new physics is likely to manifest at the TeV-scale.

Several theories for physics beyond the standard model (BSM) exist to answer these open questions. One of the most promising of these theories is supersymmetry (SUSY), which introduces a symmetry between bosons and fermions and predicts partner particles for each SM particle.

The Large Hadron Collider (LHC) and its detectors were constructed to search for new physics at previously inaccessible energy scales, discover the Higgs boson, and perform precision measurements of the SM. In the first data-taking period from 2010 to 2012, proton-proton collision data at a center-of-mass energy ($\sqrt{s}$) of 7–8 TeV were taken. While the Higgs boson was already discovered in 2012 [1, 2] and the SM has been measured to a higher precision than ever before [3, 4], no BSM particles were observed in this first data-taking period. Nevertheless, some small deviations from the SM expectations were observed. While these results are still consistent with statistical fluctuations they might have been first hints of new physics.

One such deviation was observed in events with opposite-charge, same-flavor lepton (OCSF) pairs, jets, and missing transverse momentum recorded with the Compact Muon Solenoid (CMS) experiment in 2012 data [5, 6]. The data set, taken at a center-of-mass energy of 8 TeV and corresponding to an integrated luminosity of $19.4\,\text{fb}^{-1}$, shows an edge-like feature in the invariant dilepton mass spectrum $m_{\ell\ell}$ at about 80 GeV with a local significance of approximately 2.5 standard deviations.

In 2015, proton-proton collisions at the LHC reached a center-of-mass energy of 13 TeV. In most BSM scenarios, the production cross sections increase significantly with the center-of-mass energy. Thus, the increase in energy can help to clarify whether deviations like the one observed at 8 TeV are fluctuations or BSM physics and opens additional phase space for searches for new physics. Because of technical problems with the accelerator and the cooling system of the CMS magnet, the available integrated luminosity to repeat the search with 2015 data was only $2.3\,\text{fb}^{-1}$. Results with this data set disfavored the signal hypothesis [7] but more data were required to make a final statement about the nature of the deviation observed in 2012 data. In contrast to 2015, the data taking in 2016 was very successful and a data set of $35.9\,\text{fb}^{-1}$ of proton-proton collisions at 13 TeV is available for this analysis.

The purpose of this search is to investigate the deviation observed in 8 TeV data in an independent data set. If the excess is confirmed, the aim is to use the large amount of available data to further investigate the features of the deviation and to extract information about the new signature. If the result can not be confirmed, the analysis will be improved to increase

the sensitivity to new signal models.

This work builds upon the results of the doctoral theses by Niklas Mohr, Daniel Sprenger, and Jan-Frederik Schulte [6, 8, 9] based on the data taken in 2010 to 2012. The results of the present analysis have been published by the CMS collaboration [10], except for the investigation of the 8 TeV signal region. An update of the published result is presented here using slightly improved methods for the prediction of flavor-symmetric background processes and the determination of a likelihood discriminator used in the later parts of the analysis. The general principles of the methods, however, have not been changed and the results deviate very little from the published analysis.

This document is structured in the following way: After the introduction, chapter 2 discusses the theoretical foundations for the analysis, namely the standard model of particle physics, its shortcomings, and supersymmetry as a possible solution. A description of the LHC and the CMS detector are given in chapter 3, while the used data sets and physics objects are described in chapter 4. A check of the deviation observed in the counting experiment analysis at 8 TeV is given in chapter 5 including a detailed description of the background prediction methods used for the later parts as well. Chapter 6 discusses improvements made to increase the analysis sensitivity while chapter 7 contains the results of the counting experiment approach in the newly defined signal regions. The kinematic fit to search for an edge like structure is discussed in chapter 8 and the results are interpreted in chapter 9.

1.1 Conventions and variables

Natural units are used in this thesis. In this framework, the speed of light c and the reduced Planck constant $\hbar$ are set to one:

$$c = \hbar = 1. \tag{1.1}$$

Energies and momenta are therefore measured in GeV, while lengths are usually given in m for convenience, especially in the detector chapter. Cross sections (luminosities) are stated in (inverse) barn: $1\text{b} = 10^{-28}\ \text{m}^2$.

If not stated otherwise, particles and their antiparticles are referred to by the same name and symbol for simplicity and charge-indices are dropped. As an example, the decay of a Z boson into two leptons $Z^0 \to \ell^+\ell^-$ is abbreviated as $Z \to \ell\ell$.

A right-handed coordinate system is defined for the CMS detector with its origin at the nominal collision point in the center of the detector. The x axis points radially to the center of the LHC ring, the y axis upwards, and the z axis in the direction of a beam moving counterclockwise in the collider.

In most cases, these coordinates are transformed into a spherical coordinate system with radius $r = \sqrt{x^2 + y^2}$, azimuthal angle ϕ, and polar angle θ.

The pseudorapidity η is defined as

$$\eta = -\ln \tan\left(\frac{\theta}{2}\right). \tag{1.2}$$

In the limit of $E \approx |\vec{p}|$ it corresponds to the rapidity $y = \frac{1}{2} \ln\left(\frac{E+p_Z}{E-p_Z}\right)$. Using the pseudo-rapidity and the azimuthal angle, the geometrical distance between two objects is defined as

$$\Delta R = \sqrt{(\phi_1 - \phi_2)^2 + (\eta_1 - \eta_2)^2}. \tag{1.3}$$

In proton-proton collisions, the particles that actually interact are partons carrying an unknown fraction of the protons' momenta. Therefore, the total momentum along the beam axis is unknown. In contrast to this, the momenta in the transverse plane are negligible compared to those in longitudinal direction and the transverse plane can be used as a well defined initial state. Thus, the transverse momentum

$$p_\mathrm{T} = |\vec{p}_\mathrm{T}| = |\vec{p} \cdot \sin\theta| \tag{1.4}$$

is a widely used quantity. It is used to define the hadronic activity

$$H_\mathrm{T} = \sum_\mathrm{jets} p_\mathrm{T}, \tag{1.5}$$

a measure for the energy deposited by the hadronic jets in the event (see Section 4.2.6) and the missing transverse momentum

$$p_\mathrm{T}^\mathrm{miss} = \left|\vec{p}_\mathrm{T}^\mathrm{miss}\right| = \left| - \sum_\mathrm{particles} \vec{p}_\mathrm{T} \right|. \tag{1.6}$$

Because of momentum conservation, the missing transverse momentum is expected to be zero. Nonzero values are caused by particles leaving the experiment undetected, but also by mismeasurements and resolution effects. The term missing transverse energy $E_\mathrm{T}^\mathrm{miss}$ is frequently used in older publications and refers to the same quantity.

Another common quantity is the transverse mass of a lepton ℓ with respect to the missing transverse momentum. For negligible particle masses it is defined as

$$m_\mathrm{T}\left(\vec{\ell}, \vec{p}_\mathrm{T}^\mathrm{miss}\right) = \sqrt{2 p_\mathrm{T}^\mathrm{miss} p_\mathrm{T}^\ell \left(1 - \cos\left(\Delta\phi\right)\right)}, \tag{1.7}$$

where $\Delta\phi$ is the angle between $\vec{p}_\mathrm{T}^\mathrm{miss}$ and $\vec{p}_\mathrm{T}^\ell$ in the transverse plane. In case of two identical decay chains resulting each in a visible and an invisible particle, like the dileptonic decay of a top quark pair ($\mathrm{t\bar{t}}$), the $\mathrm{M_{T2}}$ variable [11, 12]

$$\mathrm{M_{T2}} = \min_{\vec{p}_\mathrm{T,1}^\mathrm{miss} + \vec{p}_\mathrm{T,2}^\mathrm{miss} = \vec{p}_\mathrm{T}^\mathrm{miss}} \left\{ \max\left[m_\mathrm{T}\left(\vec{\ell}_1, \vec{p}_\mathrm{T,1}^\mathrm{miss}\right), m_\mathrm{T}\left(\vec{\ell}_2, \vec{p}_\mathrm{T,2}^\mathrm{miss}\right) \right] \right\} \tag{1.8}$$

is a useful generalization that can be obtained via a numerical minimization (see Section 6.1).

2 Theoretical framework

The standard model of particle physics summarizes our current understanding of the fundamental forces of nature. It has been very successful at predicting undiscovered particles and describing experimental observations in the last decades, but there are observations indicating that the SM is incomplete and a more inclusive theory beyond the standard model is required.

In this chapter a short overview of the SM is given, followed by a discussion of the problems of the SM. Supersymmetry is introduced as a promising extension to the SM and the supersymmetric final state relevant for this analysis is discussed.

2.1 The standard model of particle physics

The standard model of particle physics describes particles and their interactions by a renormizable quantum field theory [13–19]. The particle content of the SM can be divided into two fundamental groups: fermions with half-integer spin and bosons with integer spin.

The fermions can further be subdivided into leptons and quarks, and both can be ordered into three generations with increasing mass. For the leptons each generation includes one lepton with a negative electrical elementary charge (e), namely the electron, muon, and tau lepton, and a corresponding neutrino without electrical charge. Neutrinos are massless in the SM. There are six quark flavors as well: up and down in the first, charm and strange in the second, and top and bottom in the third generation. The up-type quarks have an electrical charge of $+2/3\,e$, while the electrical charge of down-type quarks is $-1/3\,e$. A summary of the fermionic sector of the SM is shown in Tab. 2.1.

The interactions between particles are mediated via bosons, which couple to the charge that is associated with the corresponding interaction. The strong interaction couples to color charge, which is carried by the quarks (one color) and eight massless gluons (a color and an anticolor), the force carriers of the strong interaction. Quarks, electrically charged leptons, and the W boson carry an electrical charge and therefore couple to electrically neutral photons which mediate the electromagnetic interaction. The weak force couples to all fermions and is the only force that can change the lepton or quark flavor. It is mediated via the massive W ($m_{\mathrm{W}} = 80.4\,\mathrm{GeV}$) and Z bosons ($m_{\mathrm{Z}} = 91.2\,\mathrm{GeV}$) [20]. Gravity is not included in the SM and is much weaker than the other three forces at the energy scales that are reachable at colliders.

generation	leptons		quarks	
	flavor	charge [e]	flavor	charge [e]
1st	e	-1	d	$-\frac{1}{3}$
	ν_e	0	u	$+\frac{2}{3}$
2nd	μ	-1	s	$-\frac{1}{3}$
	ν_μ	0	c	$+\frac{2}{3}$
3rd	τ	-1	b	$-\frac{1}{3}$
	ν_τ	0	t	$+\frac{2}{3}$

Table 2.1: The fermionic sector of the SM

The mathematical description of the SM relies on the gauge group $SU(3)_C \times SU(2)_L \times U(1)_Y$. Here, $SU(3)_C$ describes the Quantum Chromodynamics (QCD) with C indicating the color charge. Gluons, in contrast to photons, carry the charge of the interaction they mediate. This leads to gluon self interactions and causes the strong force to increase with distance. Because of this color confinement, particles carrying color charge cannot exist as free particles and the observation of quarks is restricted to color neutral states, e.g. of three bound quarks (baryons) or of one quark and one antiquark (mesons). In collider experiments, QCD partons (quarks or gluons) hadronize and thereby produce a large number of particles, which eventually form jets. Jets are narrow cones of hadrons, which fly in the direction of the original parton. The unification of electromagnetic and weak interactions to the electroweak interaction is described in the $SU(2)_L \times U(1)_Y$ subgroup. The index L denotes that the weak isospin couples only to left handed particles while Y indicates the weak hypercharge. The $SU(2)_L$ group gives rise to three vector fields. Two of those mix to the mentioned $\mathrm{W}^{\pm}$ boson while the other mixes with the field from the $U(1)_Y$ group and results in photon and Z boson.

In the SM, gauge boson masses are generated by the Higgs mechanism [21–23]. By introducing a complex scalar doublet, the Higgs field, the $SU(2)_L \times U(1)_Y$ symmetry is spontaneoulsy broken and gives mass to the W and Z gauge bosons while the photon remains massless. Yukawa couplings to the Higgs field give mass to fermions. In addition to giving masses to other particles, the Higgs mechanism results in an additional massive boson, the so-called Higgs boson. In 2012, the ATLAS and CMS collaborations observed a new particle with a mass of approximately 125 GeV [1, 2, 24]. So far, the properties of this particle look very much like those expected of the SM Higgs boson [25], which has been the last unobserved elementary particle of the standard model.

2.2 Motivations for physics beyond the standard model

The standard model has been an extremely successful theory in the last decades. It was introduced in the 1960s and predicted the massive gauge bosons of the weak interaction and the top-quark which were discovered 1983 [26, 27] and 1995 [28, 29], respectively. Furthermore, the Higgs boson was found about five decades after the Higgs mechanism was proposed for the first time and the SM can predict current experimental results to a very high precision. Nevertheless, there are several reasons to assume the SM is incomplete and is in fact the low-energy limit of a more general theory:

- Gravity is not included in the SM although it is the dominant force at large distances. While gravity is much weaker than the other interactions at weak energy scales, it can no longer be neglected at the Planck scale $\mathcal{O}\left(10^{19}\ \mathrm{GeV}\right)$ and a formulation of gravity as a gauge mediated quantum field theory is required.

- In the SM, the loop corrections to the Higgs boson mass are much larger than the observed Higgs boson mass itself [30]. For fermion loops the correction to the Higgs boson mass is

$$\Delta m_H^2 = -\frac{|\lambda_f|^2}{8\pi^2}\Lambda_{UV}^2 + \dots , \tag{2.1}$$

  where λ_f is the coupling of the fermion to the Higgs boson mass and Λ_{UV} the ultraviolet cut-off scale. If the SM was valid up to the Planck scale, the cut-off scale would need to

be of the same order of magnitude. Thus, a very precise canceling of the loop corrections and the bare Higgs boson mass would be required to obtain the observed Higgs boson mass. This cancellation is regarded as an unnatural fine-tuning and is referred to as the hierarchy problem. Introducing scalars that couple to the Higgs boson mass could solve this problem. Each scalar would add another contribution

$$\Delta m_H^2 = \frac{\lambda_S}{16\pi^2}\left(\Lambda_{UV}^2 - 2m_S^2 ln\left(\Lambda_{UV}/m_S\right)\right) + ... \tag{2.2}$$

to the Higgs boson mass and if two scalars were added for each fermion with an identical coupling the quadratic divergences would cancel.

- In the 19th century, electricity and magnetism could be unified to electromagnetism, while in the 1960s electromagnetism and the weak interaction were combined to the electroweak interaction [14, 18]. A big step to a better understanding of nature would be the unification of the electroweak and strong forces and — if possible — later on gravity. In the SM, the extrapolation of the energy dependent coupling strengths to higher energies shows no common intersection point (see Fig. 2.1), excluding such a unification within the SM. In BSM models like the minimal supersymmetric extension of the standard model (MSSM) however, such a unification of the couplings is possible.
- The neutrinos are massless in the standard model, but observations of neutrino oscillations require a small mass that is greater than zero [31, 32].
- Measurements of the cosmic microwave background taken by the WMAP and Planck satellites indicate that baryonic matter contributes only about 5% to the energy content of the universe [33, 34]. Other contributions are dark matter (26%) and dark energy (69%). Further astrophysical observations like the rotation velocity distributions of galaxies [35] and the gravitational lensing of galaxy clusters [36] also hint at the fact that the mass of galaxies is larger than the mass of their luminous matter. This could be explained by dark matter, which interacts gravitationally but not via the electromagnetic force. The only dark matter candidates in the SM are neutrinos, if they indeed have a non-zero mass, but the contribution expected from neutrinos is too small [37, 38]. Furthermore, neutrinos would provide a candidate for hot (relativistic) dark matter while observations indicate cold (non-relativistic) particles.

2.3 Supersymmetry

A theory that might solve some of the problems stated above is supersymmetry (SUSY). By postulating a partner particle for each standard model particle with a spin that differs by 1/2 from the spin of the SM particle it might yield a solution to the hierarchy problem and lead to a unification of forces [30, 39]. Certain models also offer a candidate for dark matter.

In SUSY, a transformation is introduced to turn bosonic into fermionic states and vice versa. In principle, more than one superpartner per SM particle is possible, but only the MSSM is considered here. As a naming convention, superpartners of bosons are indicated with the suffix “-ino”, while for fermion partners an “s” is added as a prefix to the fermion name. The same convention is used for groups of particles like sfermions and gauginos as partners of fermions and gauge bosons, respectively, and sparticles for SUSY particles in general.

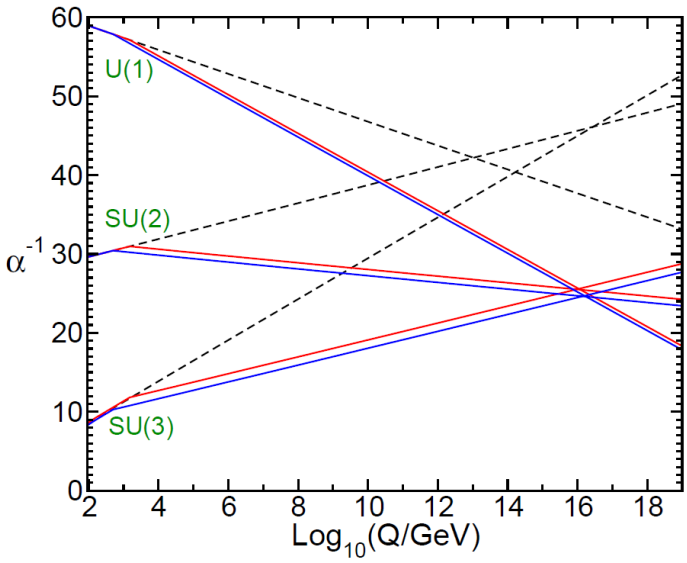

Figure 2.1: Evolution of the inverse of the three coupling strengths with increasing energy for the SM (dashed lines) and the MSSM (solid lines). In the MSSM, the masses of the SUSY particles are treated as a common threshold and varied between 500 GeV and 1.5 TeV while $\alpha_3(m_Z)$ is varied between 0.117 and 0.121 [30].

2.3.1 The minimal supersymmetric extension of the standard model

In the minimal supersymmetric extension of the standard model, SM particles and their superpartners form supermultiplets and all particles in a supermultiplet must have the same quantum numbers, except for the spin [30]. Two basic types of supermultiplets are possible: A chiral multiplet containing a single fermion with two spin helicity states and two real scalars that form a complex scalar field, and a gauge multiplet that contains a spin 1 boson and a spin 1/2 fermion, which are massless before the symmetry breaking.

Table 2.2 shows the particle content of the MSSM in which one superpartner is introduced for each degree of freedom of a SM particle. A second complex scalar doublet has to be added to the already existing one in the SM Higgs sector to avoid a gauge anomaly and to introduce the correct Yukawa couplings to fermions. One of those doublets gives mass to down type quarks and leptons while the other couples to up type quarks. In the electroweak symmetry breaking, three of those degrees of freedom give mass to the W and Z bosons. The remaining ones form an extended Higgs sector of five massive Higgs bosons: two neutral scalars h^0 and H^0, distinguished by their mass, a neutral pseudoscalar A^0, and two charged scalars $H^\pm$. The recently discovered Higgs boson can be identified as one of the two neutral scalars.

As for the electroweak gauge bosons in the SM, the gauge and mass eigenstates are not the same for the partners of the photon and the W, Z, and Higgs bosons. The four charged gauge eigenstates of the wino and higgsino couple to four charged gauginos, the charginos ($\tilde{\chi}^\pm_{1,2}$), and the four neutral SUSY gauge particles (bino, neutral wino, and higgsino) mix to four neutral gauginos, the neutralinos ($\tilde{\chi}^0_{1,2,3,4}$). As a convention, the index increases with the mass of the gauginos.

SM particle		Spin	SUSY particle		Spin
$5\times H$	Higgs boson	0	$4\times\tilde{H}$	higgsino	1/2
ℓ	lepton	1/2	$\tilde{\ell}$	slepton	0
q	quark	1/2	$\tilde{q}$	squark	0
g	gluon	1	$\tilde{g}$	gluino	1/2
B^0	B boson	1	$\tilde{B}^0$	bino	1/2
W^0, $W^\pm$	W boson	1	$\tilde{W}^0$, $\tilde{W}^\pm$	wino	1/2
(G	Graviton	2)	($\tilde{G}$	gravitino	3/2)

Table 2.2: SM particles and the corresponding superpartners in the MSSM.

Of the problems stated in Section 2.2, SUSY can solve the hierarchy problem and when extrapolating the coupling strengths to high energies it seems as if they intercept at one point (Fig. 2.1). Therefore, the unification of forces also seems possible. Another interesting feature of supersymmtery is that it can provide a good dark matter candidate if R-parity is conserved.

R-parity

In principle, SUSY could result in the violation of baryon and lepton number conservation [30]. Since no such violation has been observed, R-parity conservation is assumed in many SUSY models including the MSSM as an additional symmetry connected to a multiplicative quantum number P_R. It is defined as

$$P_\mathrm{R} = (-1)^{3B+L+2s}, \tag{2.3}$$

where B is the baryon number, L the lepton number and s the spin of the particle. By definition P_R is equal to $+1$ for SM and -1 for SUSY particles. If R-parity is conserved SUSY particles can only be produced in even numbers, usually in pairs and only decay into an odd number of lighter sparticles. The latter implies that the lightest supersymmetric particle (LSP) must be stable. If the LSP is neutral as well, it would be a promising dark matter candidate.

2.3.2 Symmetry breaking

No SUSY particles have been observed so far. Thus, SUSY needs to be broken and the sparticles must have higher masses than their SM partners. This results in a reduced version of the hierarchy problem, which still requires some fine-tuning but much less than in the SM. While the quadratic dependency on the cut-off scale cancels, a term remains, which depends on the mass of the SUSY particle and has a logarithmic dependency on the cut-off scale (see Section 2.2). Because of the fact that the Higgs boson mass has been found at the energy scale of the weak interaction, the masses of the superpartners are expected not to be several orders of magnitude larger than the Higgs boson mass to avoid large fine-tuning. Therefore, the TeV scale is a good candidate to search for SUSY particles. Especially, squarks of the third generation, which have the largest Yukawa couplings to the Higgs boson, are assumed to be light.

Supersymmetry is expected to be broken spontaneously, which means that the Lagrangian density of the underlying model is invariant under supersymmetric transformations while the vacuum of the model is not [30]. Because of this, SUSY is hidden at low energies like the electroweak symmetry in the SM.

In the MSSM, there are several approaches on how the symmetry breaking could be realized, e.g. gravity or gauge mediated symmetry breaking. In practice, extra terms are introduced into the effective MSSM Lagrangian that break the symmetry explicitly. The extra terms introduce in total 105 new free parameters like masses, phases and mixing angles.

2.3.3 Dileptonic final states in supersymmetry

Assuming R-parity conservation, SUSY particles have to be pair produced. The production of SUSY particles can either occur via strong interactions (squarks and gluinos) or via electroweak couplings (charginos, neutralinos, and sleptons). At hadron colliders like the LHC, the strong channel has a larger production cross section than the electroweak one if SUSY particles of a certain mass are assumed and this thesis focuses on the strong production mode.

SUSY particles decay in cascades into the LSP under the emission of SM particles. Starting from a squark or gluino one expects at least one quark or gluon from each cascade, which hadronizes into a jet and missing transverse momentum due if the LSP is a neutralino. The branching fraction into leptons is in general lower than into hadronic final states. Nevertheless, leptons are required in this analysis since they are easy to identify, can be measured precisely, and their presence significantly suppresses SM background processes, most importantly events which only contain jets produced through the strong interaction. These background processes are referred to as QCD multijet production. Only electrons and muons are considered in this analysis since tau leptons are harder to identify and provide less discrimination power against QCD multijet events.

The correlated production of a dilepton pair of the same flavor but opposite electric charge is of particular interest. This signature can arise in the decay of the next-to-lightest neutralino into the lightest neutralino and two leptons via a slepton or a Z boson:

$$\tilde{\chi}_2^0 \to \ell^{\pm}\tilde{\ell}^{\mp} \to \ell^{\pm}\ell^{\mp}\tilde{\chi}_1^0 \tag{2.4}$$

$$\tilde{\chi}_2^0 \to Z\tilde{\chi}_1^0 \to \ell^{\pm}\ell^{\mp}\tilde{\chi}_1^0. \tag{2.5}$$

The decays are illustrated in Fig. 2.2. Depending on the decay mechanism and the masses of the neutralinos, two kinds of characteristic shapes can arise in the invariant mass distribution of the dilepton system $m_{\ell\ell}$. If the decay is mediated by a Z boson and the mass difference between the neutralinos is larger than the Z boson mass, a resonant contribution at the Z boson mass is observed. For decays including an off-shell Z boson or a slepton, a characteristic edge like feature is introduced. This analysis focuses on signals producing an edge. These signals are of particular interest since the endpoint of the edge can provide information on the properties of the SUSY particles [40, 41]. A dedicated search for SUSY resulting in Z bosons is included in the published version of the CMS analysis [10].

The decay via an off-shell Z boson or slepton is performed as a three-body decay and the endpoint of the $m_{\ell\ell}$ distribution is given by the mass difference between the neutralinos:

$$m_{\ell\ell}^{\text{edge}} = m_{\tilde{\chi}_2^0} - m_{\tilde{\chi}_1^0}. \tag{2.6}$$

Two subsequent two-body decays occur if the slepton mass is in between the neutralino masses. In this case, the edge position is modified by the slepton mass $m_{\tilde{\ell}}$ and a lower value is observed:

$$m_{\ell\ell}^{\text{edge}} = \sqrt{\frac{\left(m_{\tilde{\chi}_2^0}^2 - m_{\tilde{\ell}}^2\right)\left(m_{\tilde{\ell}}^2 - m_{\tilde{\chi}_1^0}^2\right)}{m_{\tilde{\ell}}^2}}. \tag{2.7}$$

The exact shape of the distribution depends on the decay kinematics as well. For two subsequent two-body decays the shape is triangular with a maximum close to $m_{\ell\ell}^{\text{edge}}$. In case of three body decays, the distribution depends strongly on the parameters of the SUSY model. For neutralino mass differences below the Z boson mass, negative interference between the decay amplitudes via slepton and via Z boson can have an impact on the distribution and shift the maximum away from $m_{\ell\ell}^{\text{edge}}$ [41].

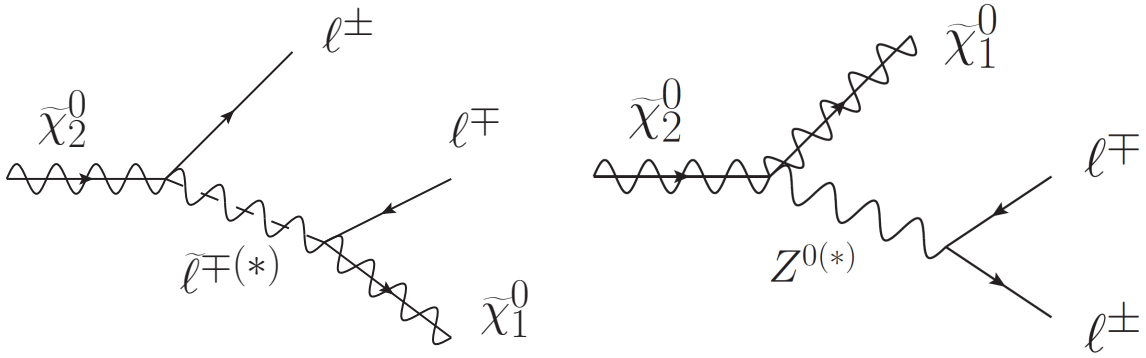

Figure 2.2: Decay of a $\tilde{\chi}_2^0$ into a $\tilde{\chi}_1^0$ and two leptons via an intermediate slepton (left) or a Z boson (right). The "(*)" indicates that intermediate particles can either be on-shell or off-shell.

2.3.4 Simplified model

As mentioned in Section 2.3.2, the symmetry breaking of the MSSM introduces 105 new free parameters. Experimental results restrict some of the parameters but nevertheless the model has to be simplified to be studied, since it is nearly impossible to scan a 105 dimensional parameter space effectively. Different models exist that restrict the number of free parameters. In the constrained MSSM, only five free parameters remain, but a large part of the phase space is already excluded especially for low sparticle masses [42]. The phenomenological MSSM is another simplification but it still requires 19 free parameters [43] and is therefore difficult to scan.

The so-called simplified model approach [44] is pursued in this work. In general, a full model introduces a lot of new particles and interactions, which makes it difficult to interpret it in the

context of experimental results. Simplified models are based on especially designed, effective theories, which include only the particles and interactions that are relevant to the signature of interest. Therefore, they contain only a few parameters, but might still be relevant as limits or special cases of a more general theory.

Two simplified models have been studied in a previous work in an attempt to describe the deviation observed at 8 TeV [45]. The model with less constraints on the resulting event kinematics is used in this analysis. It is sometimes referred to as "slepton model" and the corresponding diagram is shown in Fig. 2.3. The model is based on pair production of bottom squarks, which decay into a bottom quark and a $\tilde{\chi}_2^0$ with 100% branching fraction. Two decay modes are considered for the $\tilde{\chi}_2^0$ with 50% probability each: The decay into a Z boson and a $\tilde{\chi}_1^0$ and the decay into a lepton and a slepton that subsequently decays into a lepton and the lightest neutralino. Only selectrons and smuons are considered. The slepton masses are assumed to be degenerate and are fixed in between the neutralino masses: $m_{\tilde{\ell}} = 0.5(m_{\tilde{\chi}_2^0} + m_{\tilde{\chi}_1^0})$. The $m_{\tilde{b}}$-$m_{\tilde{\chi}_2^0}$ mass plane is scanned in 25 GeV steps for bottom squark masses below 800 GeV and in 50 GeV steps from 800 GeV upwards while $m_{\tilde{\chi}_1^0}$ is set to 100 GeV. The latter value is chosen to be moderately larger than the upper limits of about 50 GeV on $m_{\tilde{\chi}_1^0}$ in the MSSM assuming R-parity conservation, which are derived from the decay width of the Z boson into invisible particles and direct searches for charginos and sleptons [20]. The signal simulation is normalized to cross sections at next-to-leading order in the strong coupling including resummation of soft gluon emissions at next-to-leading-logarithmic accuracy (NLO+NLL) in QCD [46].

This setup allows for both mass edges below and above the Z boson mass. Figure 2.4 shows the $m_{\ell\ell}$ distribution for three example signal points. Events with an invariant dilepton mass above the edge position occur if there are more than two leptons in the event and the wrong combination is chosen. Since those leptons are uncorrelated, the same number of same-flavor (SF) and different-flavor (DF) events is expected and the DF events can be used to remove the contribution from incorrectly combined lepton pairs. A contribution at the Z boson mass is expected if the mass difference between the neutralinos allows for an on-shell production of the Z boson. This contribution is small compared to the edge shape since the Z boson decays according to its SM branching fractions producing light leptons only in approximately 7% of the cases while the slepton decay always produces a lepton pair. In case of the examples in Fig. 2.4, the fraction of events with an on-shell Z decay accounts only for about 5% of the total dilepton events if such a decay is possible.

2.4 Standard model background processes

Final states with an OCSF lepton pair, jets, and missing transverse momentum are not unique to supersymmetry or BSM physics in general. Three types of SM background processes can lead to this signature and constitute the background in this analysis.

Correlated lepton pairs without invisible particles escaping the detector mainly arise from the Drell-Yan (DY) process $pp \to \mathrm{Z}/\gamma^* \to \ell\ell$. Initial- and final-state radiation can result in jets and mismeasurements of these jets can give rise to events with a significant amount of $p_{\mathrm{T}}^{\mathrm{miss}}$. Further processes with a similar signature are Z boson production in association with another gauge boson or a top quark pair where the additional particles decay hadronically.

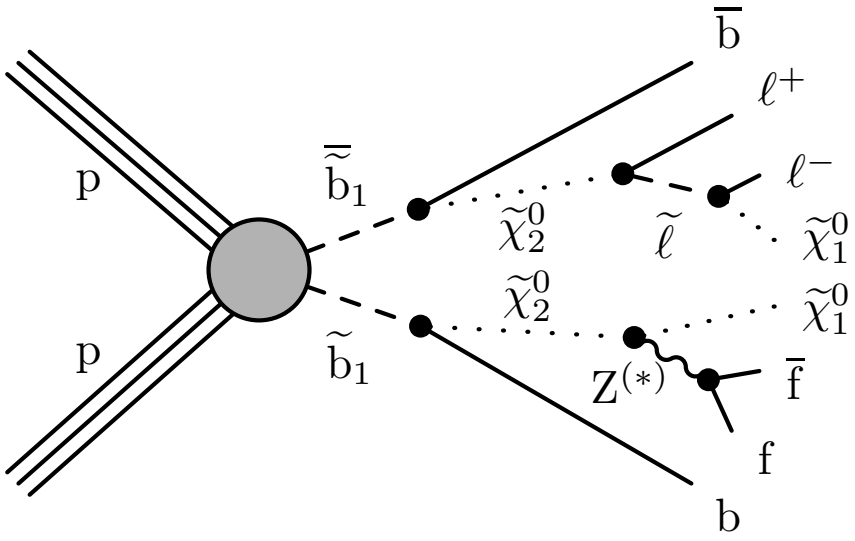

Figure 2.3: Graph for the slepton model. The "(*)" indicates that the Z boson can be off-shell.

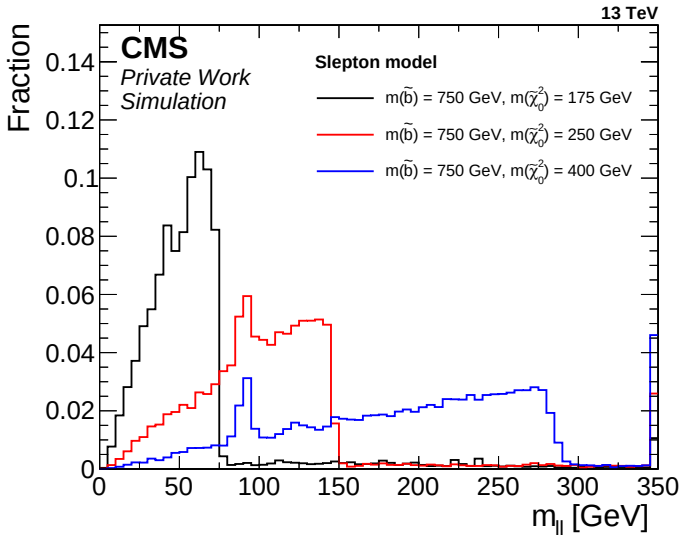

Figure 2.4: Distribution of $m_{\ell\ell}$ for three signal points of the slepton model, illustrating the edge shapes for different signal configurations.

For simplicity, all processes with this signature will be summarized as "DY+jets".

A second class of background processes with correlated lepton pairs originates from processes with a Z boson and genuine $p_{\mathrm{T}}^{\mathrm{miss}}$ due to neutrinos. Examples are diboson production (WZ$\rightarrow$ $3\ell\nu$, ZZ$\rightarrow$ $2\ell 2\nu$) and even rarer processes like $\mathrm{t\bar{t}Z}$ or triboson production. These processes are referred to as "Z+ν" and although the production cross sections are small they can account for a substantial fraction to the background at high values of $p_{\mathrm{T}}^{\mathrm{miss}}$ and $\mathrm{M_{T2}}$.

The third and most important background category summarizes all processes that produce uncorrelated lepton pairs and is referred to as "flavor-symmetric" background. These processes yield same-flavor and different-flavor dilepton pairs with the same probability. The dominant contribution comes from the dileptonic decay of a top quark pair $pp \rightarrow \mathrm{t\bar{t}} \rightarrow \mathrm{WbWb} \rightarrow \ell\nu\mathrm{b}\ell\nu\mathrm{b}$ and includes decays via intermediate tau leptons (W$\rightarrow \tau\nu \rightarrow \ell 3\nu$). Further contributions arise from the production of a single top quark in association with a W boson, DY decays with intermediate tau leptons ($\mathrm{Z}/\gamma^* \rightarrow \tau\tau \rightarrow 2\ell 4\nu$), diboson and triboson processes with more than two leptons or without a leptonically decaying Z boson, and leptons not originating from the hard interaction. Leptons that are not from the hard interaction can result from decays of b or c quarks inside jets or be jets that are misidentified as leptons.

Some processes contribute to more than one of these categories depending on the decay and the lepton pair that is chosen. For example, WZ diboson production can contribute to the DY+jets category (WZ$\rightarrow$ 2q2ℓ), the Z+ν background (WZ$\rightarrow$ $3\ell\nu$ if the lepton pair from the Z is chosen), and the flavor-symmetric background (WZ$\rightarrow$ $3\ell\nu$ if the lepton from the W boson is combined with a lepton from the Z boson). These cases need to be taken into account in the background prediction to avoid double counting of certain background processes.

3 Experimental setup

This analysis relies on data that were taken with the CMS experiment at the CERN LHC in 2016. Since both the collider and the experiment are very complex machines, only an introduction can be given here.

3.1 The Large Hadron Collider

The Large Hadron Collider (LHC) [47] is a synchrotron designed to collide protons at a center-of-mass energy of up to 14 TeV and accelerate heavy ion beams up to 2.76 TeV per nucleon. It is located in a tunnel of about 27 km circumference and about 100 m below the surface at the European Organization for Nuclear Research (CERN) near Geneva, in which the LEP collider was situated before.

Before the protons are injected into the LHC, they gain 450 GeV of kinetic energy in a chain of pre-accelerators, namely the Linac 2, the Proton Synchrotron Booster, the Proton Synchrotron, and the Super Proton Synchrotron. Superconducting magnets are operated at 1.9 K and can provide a magnetic field up to 8.3 T to bend the protons along the tunnel curvature and focus them at the interaction points. The LHC can be filled with up to 2808 proton bunches of about 10^{11} protons, which collide at the interaction points every 25 ns.

Four large experiments are located at the LHC (Fig. 3.1). ATLAS [48] and CMS [49] are multi-purpose detectors, while ALICE [50] examines the quark-gluon plasma in ion collisions and LHCb [51] is specialized on events containing b- or c-quarks to perform studies on CP-violation and to do precision measurements of the standard model.

While the design center-of-mass energy has not been reached yet, the instantaneous luminosity exceeded its design value of $10^{34}\,\mathrm{cm^{-2}s^{-1}}$ by about 50% in 2016, as can be seen in the left part of Fig. 3.2. A data set with an integrated luminosity of $40.8\,\mathrm{fb^{-1}}$ at a center-of-mass energy of 13 TeV was delivered to the CMS experiment in 2016, about ten times more than in 2015 and nearly twice as much as in 2012 with $\sqrt{s} = 8$ TeV (Fig. 3.2 right).

3.2 The Compact Muon Solenoid

The CMS experiment is one of the two multi-purpose detectors at the LHC [49] located at an interaction point of the LHC beams. It consists of several layers of subdetectors to precisely determine the properties of the produced particles. The subdetectors are arranged in a cylindrical symmetry around the beam pipe to provide a good coverage of the 4π solid angle. The CMS detector is divided in a barrel, which is sometimes referred to as the central region, and two endcaps. A main feature of the detector is the superconducting solenoid, which is cooled to about 4.5 K and generates an almost homogeneous magnetic field of 3.8 T in the inner part of the detector.

The beam pipe is surrounded by the tracking system consisting of the silicon pixel and silicon strip detectors. The former is used to identify the origin of charged particles while the latter measures the tracks and thereby the momenta of these particles. The electromagnetic and

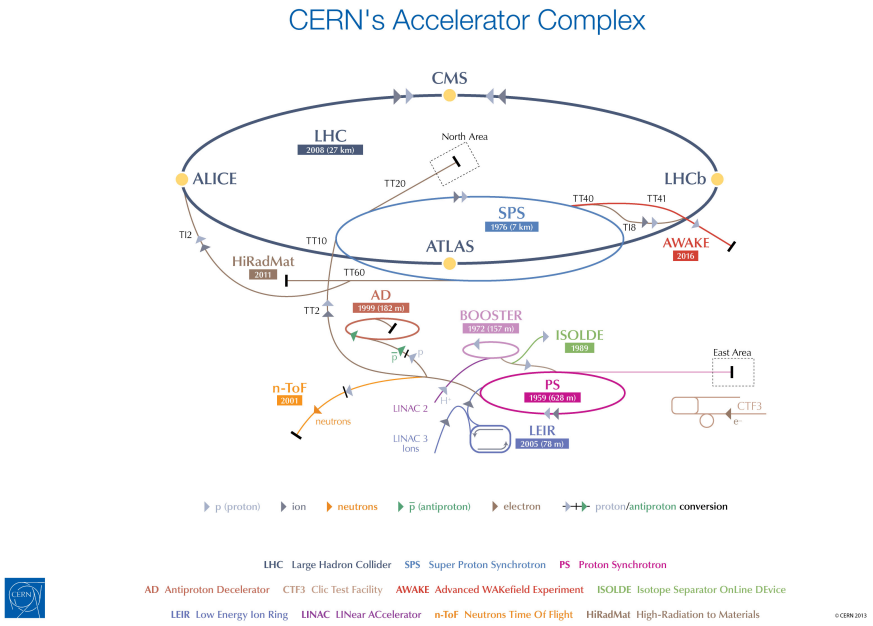

Figure 3.1: Sketch of the LHC, showing the four main experiments ALICE, ATLAS, CMS, and LHCb, and the pre-accelerators [52].

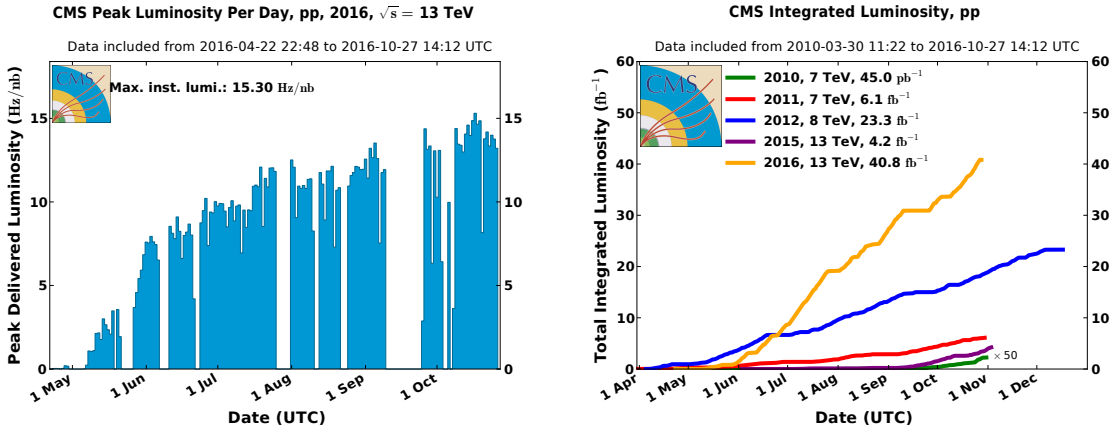

Figure 3.2: Maximal instantaneous (left) and integrated luminosity (right) delivered to the CMS experiment. The integrated luminosity is shown for all years of data taking while the instantaneous luminosity is displayed only for 2016 [53].

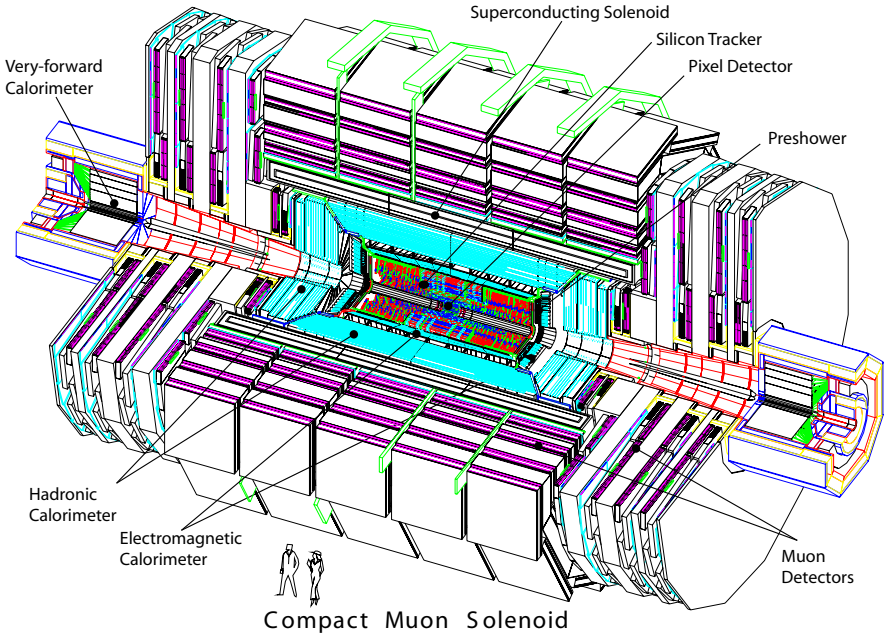

Figure 3.3: Sketch of the CMS detector with all subdetectors labeled [49].

hadron calorimeter to measure particle energies are located further outside, but still inside the volume of the solenoid. The iron return yoke and the muon system are situated outside of the solenoid and complete the detector setup. A sketch of the detector can be seen in Fig. 3.3.

The different subsystems are described in some detail in the following. A more complete description of the CMS experiment can be found in [49].

3.2.1 Tracking system

The tracking system is based on silicon detector technology. It has a diameter of 2.5 m and is 5.8 m long, thus providing the tracking information on charged particles with a pseudorapidity up to $|\eta| = 2.5$. Due to the magnetic field, the trajectories of charged particles bend, which allows for the determination of their charge signs and momenta. The CMS tracking system is shown in Fig. 3.4. It consists of the pixel detector and the strip tracker, which can be divided into several subsystems: Tracker Inner Barrel (TIB), Tracker Outer Barrel (TOB), Tracker Inner Discs (TID), and Tracker Endcaps (TEC). The pixel detector was replaced with an improved detector in the beginning of 2017 to cope with the expected higher luminosities in the next years. Since the data used in this work was still recorded with the previous pixel detector, the description here refers to the old setup.

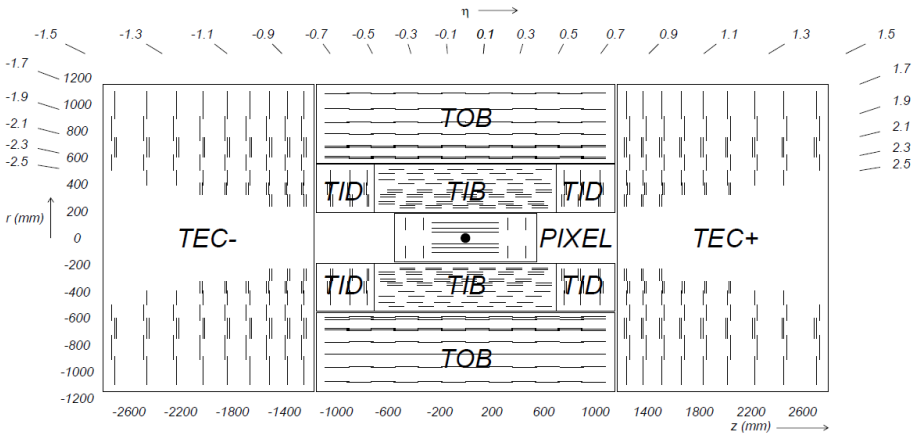

Figure 3.4: Schematic cross section through the CMS tracker in the r-z plane. Each line represents a detector module and double lines represent stereo modules [49].

Pixel detector

The pixel detector in 2016 surrounded the interaction point and consisted of three cylindrical layers of pixels at radii between 4.4 and 10.2 cm with a length of 53 cm in the barrel region. Two disks were located in each of the endcaps at z= $\pm$34.5 and z= $\pm$46.5 cm with radii between 6 and 15 cm. About 66 million pixels provided the high granularity required to maintain a low occupancy even at high particle densities close to the interaction point. Each pixel had a size of $100 \times 150\,\mu\text{m}^2$ resulting in a total active area of about $1\,\text{m}^2$. Simultaneous readout of neighboring pixels allowed for a spacial resolution between 15 and 20 μm. This resolution is required for a precise reconstruction of the interaction vertices, separating particles from different proton-proton interactions, as well as to provide the information for the secondary vertex reconstruction from heavy-flavor decays.

Strip tracker

About 15 000 strip modules with an active area of nearly $200\,\text{m}^2$ form the strip tracker at radii between 20 and 116 cm. The inner part of the strip tracker consists of the TIB and the TID. The former is made up of four cylindrical layers of silicon modules, while the latter is formed by three discs at each side. The TOB surrounds this part of the tracker and consists of six cylindrical layers of modules. Nine disks form the TECs, which complete the tracker in the forward and backward direction.

For low p_T tracks (1–10 GeV), the momentum resolution of the tracker system is about 1% in the central part and 2–3% in the endcaps. Higher momenta result in a reduced curvature in the magnetic field yielding a momentum resolution of 2–3% for tracks with $p_T = 100$ GeV and $|\eta| < 1.5$. At higher $|\eta|$, the resolution degrades significantly because of a shorter lever arm [54].

3.2.2 Electromagnetic calorimeter

The energy of electrons and photons is measured in the electromagnetic calorimeter (ECAL). The ECAL is made of lead tungstate ($PbWO_4$) crystals and is also divided in a barrel part ($|\eta| < 1.479$) and two endcaps ($1.479 < |\eta| < 3.0$). Lead tungstate is chosen because of its high density ($8.28\,\mathrm{g/cm^3}$), short radiation length (0.89 cm), and small Molière radius (2.2 cm). Additionally, it is radiation tolerant and a fast scintillator that emits about 80% of the light in 25 ns, which is the designed time between two proton-proton bunch crossings.

The light emitted by the scintillating crystals is detected by avalanche photodiodes in the barrel and vacuum phototriodes in the endcaps. The former are able to operate in the strong transverse magnetic field while the latter are less sensitive to the higher radiation in the endcaps.

The ECAL barrel (EB) consists of 61 200 crystals. These crystals have a front cross section of $2.2 \times 2.2\,\mathrm{cm^2}$, which is the square of the Moilère radius. The EB crystals are 23 cm long, which is equivalent to 25.8 times the radiation length. In each of the ECAL endcaps (EE) 7324 crystals are arranged in a rectangular x-y grid. The EE crystals have a larger front cross section ($2.86 \times 2.86\,\mathrm{cm^2}$) and are slightly shorter (22 cm) than those in the EB. In the range of $1.65 < |\eta| < 2.6$ preshower detectors are installed in front of the EE. These are made of lead absorber and silicon detector layers. The preshower detectors help to distinguish prompt photons and those from neutral pion decays. Furthermore, they improve the position measurement of electrons and photons and help to discriminate electrons from minimum ionizing particles.

The energy resolution in the ECAL can be parameterized in the following way:

$$\left(\frac{\sigma}{E}\right)^2 = \left(\frac{S}{\sqrt{E}}\right)^2 + \left(\frac{N}{E}\right)^2 + C^2.$$

In test beam measurements, the stochastic term is given by $S = 2.8\%$, the noise term by $N = 12\%$, and the constant term by $C = 0.3\%$ for E in GeV [49]. S is dominated by event-to-event fluctuations and photostatistics, N by noise due to electronics, digitization, and pileup. The main contributions to C are non-uniformity of the longitudinal light collection, intercalibration errors and energy leakage from the back of the crystal.

The mass resolution for $Z \to ee$ is about 1.7% if the electrons are measured in the ECAL barrel and 2.6% if both are reconstructed in the endcaps [55].

3.2.3 Hadron calorimeter

Energies of charged and neutral hadrons are measured in the hadron calorimeter (HCAL). The HCAL consists of several subdetectors, which are made of brass and stainless steel absorbers and plastic scintillators. The size of the ECAL with an outer radius of 1.77 m and the inner extent of the magnet coil at 2.95 m constrain the available space of the HCAL in the barrel region, and thus, the ability to fully contain the hadronic showers. The HCAL barrel (HB), which covers the pseudorapidity range $|\eta| < 1.3$ inside the superconducting solenoid, is therefore complemented by the outer hadronic calorimeter (HO), which uses the solenoid to

provide enough stopping power for sufficient containment of hadron showers. On each side, a HCAL endcap (HE) complements the HB for $1.3 < |\eta| < 3.0$. Hadron forward calorimeters (HF) extend the coverage up to $|\eta| = 5.0$.

HCAL barrel (HB) and outer hadronic calorimeter (HO)

The HB consists of alternating layers of absorber material and scintillators. The absorber plates are made of brass except for the innermost and outermost plates, which are made of stainless steel to increase the structural strength. The scintillator is divided into sectors of 0.087×0.087 in $\eta \times \phi$. Except for the two sectors closest to the HE at each side, all layers in an $\eta \times \phi$ sector are read out by the same photodiode. Thus, there is no segmentation in r and all scintillator layers in such a sector form a so-called calorimeter tower. The absorber material amounts to 5.82 hadronic interaction length λ_I at $|\eta| = 0$ and $10.6\,\lambda_\mathrm{I}$ at $|\eta| = 1.3$. The EB adds another $1.1\,\lambda_\mathrm{I}$ but the combination of HB and EB is insufficient to fully contain hadronic showers. The HO uses the solenoid as an additional absorber with one additional layer of scintillator except for the most central part where an additional layer of steel absorber and scintillator are used. The tiles of the HO scintillator roughly match the structure of the HB to make towers of a constant granularity in $\eta \times \phi$. Adding the HO increases the material budget of the calorimeter system to $> 11.8\,\lambda_\mathrm{I}$ except for the transition region between barrel and endcap.

HCAL endcap (HE)

The HEs cover the range of $1.3 < |\eta| < 3.0$ and are constructed from the same combination of absorber and scintillator layers as the HB. For $|\eta| < 1.6$ the granularity of the calorimeters in $\eta \times \phi$ is the same as in the HB, while it is reduced to 0.17×0.17 for larger $|\eta|$ to match the granularity in the EEs.

Hadron forward calorimeters (HF)

In a distance of about 11 m from the interaction point, the HCAL is completed by the HF to reconstruct jets with a very high $|\eta|$. Since most of the energy of a proton-proton interaction is deposited in this region, the HF must be very radiation tolerant. For this reason quartz fibers are chosen as the active medium instead of plastic scintillators. The fibers are inserted into grooves in steel plates, which function as absorber material. Charged particles passing these fibers emit Cherenkov light that is detected by photomultiplier tubes. Since there is no electromagnetic calorimeter in front of the HF, half of the fibers run over the full depth of the absorber of 165 cm while the other half starts at a depth of 22 cm. This setup makes it possible to distinguish between showers from electrons and photons, which deposit most of their energy in the first 22 cm, and those generated by hadrons.

3.2.4 Muon system

The muon system is required for the identification, triggering, and momentum measurement of muons. In general, muons are the only interacting particles that are not stopped by the calorimeters within the solenoid volume. Thus, muons can be well identified and measured outside of this volume. Therefore, the muon system is the outermost part of the detector, embedded into the return yoke of the magnet. Since the muon detector is positioned so far from the interaction point, it has to cover a large area, and thus, be relatively inexpensive in comparison to the technologies used in other subdetectors. Three types of gaseous particle detectors, with about $25\,000\,\mathrm{m}^2$ of detection planes in total, are used for the measurement of muon. The different detectors partially overlap in $|\eta|$ to ensure a high detector acceptance.

Drift tubes (DT)

In the barrel region, the muon rate is low and the magnetic field is uniform and mainly contained in the return yoke, which makes it possible to use drift chambers in this part of the muon system. Four layers of drift tube chambers, so-called muon stations, are located between the iron return yokes of the magnet and cover the pseudorapidity range $|\eta| < 1.2$. The first three stations consist of 60, the fourth of 70 drift chambers. Each drift chamber contains eight layers of DTs measuring in the r-ϕ plane while the chambers in the three inner stations also feature four layers sensitive in the z direction. Overall, there are about 172 000 DTs, each with a single anode wire and filled with a mixture of 85% Ar and 15% CO_2. The resolution in r-ϕ for a single DT is less than $250\,\mu$m and the combination of eight layers reduces the resolution to about $100\,\mu$m for one drift chamber.

Cathode strip chambers (CSC)

In the endcap regions the muon and background rates are higher, while the magnetic field is large and non-uniform. Cathode strip chambers are chosen for this environment because of their fast response time, radiation resistance, and fine segmentation. In each of the endcaps, four stations cover the range of $0.9 < |\eta| < 2.4$. Each station consists of trapezoidal shaped CSCs arranged in concentric rings around the beam pipe. The CSCs are filled with a mixture of CO_2, Ar, and CF_4 and each chamber consists of six layers of anode wire planes in r-ϕ direction interleaved with seven cathode strip panels with radial alignment.

Resistive plate chambers (RPC)

While DTs and CSCs can be used to trigger on the p_T of muons with a high efficiency, their timing resolution might not be good enough to assign a muon to the correct bunch crossing at high luminosity. For this reason, resistive plate chambers have been added as the third part of the muon system. A RPC is made of three parallel layers of bakelite with two gas filled gaps in between. A high voltage is applied between the layers to run in avalanche mode. Resistive plate chambers have a worse position resolution than DTs or CSCs but respond very fast and have a good timing resolution. Therefore, they can be used to associate muons to

bunch crossings and form a complementary trigger system for muons. Six RPC layers are used in the barrel part while three layers are installed in the endcaps for $|\eta| < 1.6$.

Muon momentum resolution

For muons with $10 < p_{\mathrm{T}} < 100\,\mathrm{GeV}$, the transverse momentum resolution of the muon system alone is about 10% in the barrel and 20% in the endcaps. Combining the information from the inner tracking system and the muon detector in a global muon fit can improve the resolution to 1.3–2.0% in the barrel and less than 6% in the endcaps [56]. The precision of the tracking measurement dominates in this momentum regime. Using both subdetectors, the $\mathrm{p_T}$ resolution of cosmic ray muons in the barrel is better than 10% for momenta up to 1 TeV [56].

3.2.5 Trigger system and data acquisition

A description of the trigger system during the data-taking period from 2010 to 2012 can be found in [57]. While the basic principles are still the same, the final output rate has increased because of improvements of the computing infrastructure.

In 2016, the LHC delivered proton bunch crossings at a frequency of 40 MHz. A readout of the full detector amounts to about 1 MB per bunch crossing. Since it is impossible to store and process events at such a rate with the available computer infrastructure, the amount of data has to be reduced by 4–5 orders of magnitude. The current rate at which events can be stored is about 1 kHz. A two-step trigger system is used to achieve the required reduction. The Level-1 (L1) trigger uses programmable electronics in the calorimeters and the muon system, allowing for a fast primitive reconstruction of physics objects. The L1 system accepts events with a rate of about 100 kHz. For these events, the data acquisition system (DAQ) collects the information from the subdetectors and passes it to the High-Level trigger (HLT). The HLT is a software trigger that is able to perform a full reconstruction of the events although fast approximations of the offline algorithms are frequently used to operate at a higher frequency.

Level-1 trigger

The data recorded in each subdetector are held in electronic pipelines until a first trigger decision is reached. Data from 128 bunch crossings can be stored in these pipelines, which requires the L1 trigger to accept or reject an event within 3.2 μs for a bunch spacing of 25 ns between two bunch crossings. Since the readout and track reconstruction from the inner tracker are too time consuming, only information from the calorimeters and the muon system is used. Both the calorimeter and the muon trigger consist of local, regional, and global components. Trigger towers are formed by a single HCAL tower and the 5×5 ECAL crystals in front of it. Regional electron and photon candidates and p_{T} sums based on 4×4 trigger towers are passed to the global calorimeter trigger (GCT). The GCT uses simple clustering algorithms to find jets and provides global quantities like $p_{\mathrm{T}}^{\mathrm{miss}}$. Muon candidates are formed from track segments and hit patterns in the three muon detectors. The global muon trigger merges candidates found by more than one subsystem and suppresses candidates with a low

quality. The global trigger collects the information from muon and calorimeter trigger and decides based on up to 128 L1 physics trigger algorithms whether to accept an event [58].

Data acquisition system (DAQ)

If an event is accepted by the L1 trigger, the DAQ gathers the event data from the buffers of the different subdetectors, combines it to whole events and passes them on to the HLT. If the event rate passed from the L1 exceeds the processing capability of the DAQ, the DAQ can reduce the rate, introducing a dead time, to prevent data corruption and buffer overflows.

High level trigger system (HLT)

The HLT is a software system in a filter farm, which reduces the data rate by about 2 orders of magnitude. The HLT tests if an event fulfills one or several HLT paths, taking the data from all subdetectors into account. Each HLT path consists of algorithmic processing steps run in a predefined order. These steps reconstruct physics objects and apply selections based on these objects. The steps in an HLT path increase in complexity, starting with requirements on the calorimeters and muon detectors to reduce the rate before applying computing intensive track reconstructions.

The actual thresholds for both L1 and HLT are adapted during the data taking based on the current instantaneous luminosity. To keep the total output rate constant, some HLT paths that are available at low luminosity are either switched off or prescaled at higher luminosity. If a path is prescaled with a factor n, only every nth event that fulfills the HLT path is actually recorded.

4 Data analysis and event selection

This chapter gives an overview of the event processing and the used data sets, both from collision data and simulations. Furthermore, the reconstruction of the physical objects from the data provided by the CMS experiment, relying mainly on the particle-flow algorithm, is discussed and the basic event selection in this work is given.

4.1 Event processing and data sets

Events accepted by the HLT are transferred to the Tier-0 computing center at CERN for offline reconstruction and permanent storage. Events are grouped into non-exclusive primary data sets based on the HLT decisions. These primary data sets are distributed over several Tier-1 and Tier-2 centers worldwide and can be accessed via tools like the CMS Remote Analysis Builder (CRAB) [59] to perform data analysis. A first event reconstruction is done directly after data taking, making the data accessible for analyses within a few days using the CMS software (CMSSW) framework [60]. In September 2016, the full detector calibration and alignment was updated for the rest of the 2016 data-taking period and the already taken data were reconstructed a second time with these conditions.

The events are stored in the mini analysis data object (miniAOD) format [61]. The format contains only a reduced selection of high level objects like leptons and jets. No detailed detector information, like energy deposits in calorimeter cells, is included, which is of little interest to most analyses. While this allows for a reduction of the event size from approximately 2 MB to 40–50 kB, effects were discovered in data that could not be recovered from this final data format and required a new reproduction from a previous step in February 2017. This reproduction was done in the software version "CMSSW 8.0.26 patch 1".

The events in the miniAOD format are processed using the worldwide LHC computing grid [62, 63]. The computing centers in the grid provide the necessary storage and computing capacities for the LHC experiments. Data sets stored at the storage sides are accessed via CRAB. Using tools provided in CMSSW, events containing a dilepton pair that fulfills a set of selection criteria (see Section 4.2.5) are identified and the properties of the lepton pair and further important event features are stored. Because of the reduced number of events and the further reduced event size of about 0.5 kB per event, the analysis of the selected events can be performed on a normal desktop computer. Both the CMSSW framework and the final analysis rely on the ROOT framework [64].

4.1.1 Data sets

This analysis uses the CMS proton-proton collision data taken in 2016. The 2016 data taking has been divided into several data-taking periods. While Run2016A was dedicated to detector and collider commissioning as well as cosmics data taking, proton-proton collision data were taken from Run2016B to Run2016H. Since Run2016H is split into two parts, eight subsets of each primary data set are used.

The most important primary data sets for this analysis are the DoubleEG, DoubleMu, and MuEG data sets containing, among others, events triggered with double electron, double muon, and muon electron triggers, respectively. The maximal instantaneous luminosity per run increased during the data taking and the trigger thresholds were adapted accordingly. Thus, a variety of dilepton triggers with different transverse momentum, identification, and isolation requirements have been used. The dilepton triggers can be divided into two basic categories. Triggers in the first category require the leptons to fulfill loose isolation criteria and have a p_{T} threshold of at least 17 or 23 GeV for the first and 8 or 12 GeV for the second lepton, depending on the lepton flavor and time of data taking. Some of these triggers also have a constraint on the longitudinal impact parameter. The isolation criteria in these triggers use a constant isolation cone size, in contrast to the isolation variable applied in the analysis (see Section 4.2.5). Leptons that originate from a very high momentum ("boosted") mother particle, e.g. a Z boson or SUSY particle, often have a high p_{T} and small spatial separation from the other lepton or additional jets. In such cases, the isolated triggers frequently discard the event because of the proximity of a lepton to another object. To regain sensitivity to these decays, a set of non-isolated triggers with higher p_{T} thresholds forms a second category. An overview of the exact primary data sets and trigger definitions is given in Appendix A.

Primary data sets and HLT paths based on the scalar sum of the p_{T} of the jets, H_{T}, are used to perform efficiency measurements of the dilepton triggers. Since the trigger rates at low and moderate H_{T} are very high, all but the trigger with the highest H_{T} requirement are prescaled. Similarly, primary single lepton data sets and prescaled low p_{T}, single lepton trigger paths provide data to study non-prompt leptons.

4.1.2 Monte Carlo simulation and simulated data sets

Simulated data sets of SM and signal processes are useful tools to design and validate analysis methods before looking at the collision data. Furthermore, they can be used directly to predict background contributions and to interpret results in terms of potential signals. The event generation is done in several steps: First, the hard scattering process is simulated with a Monte Carlo (MC) event generator to obtain a list of particles and their momenta. In a second step partons from the hard process are hadronized. Several simulated soft QCD events are overlaid to emulate pileup effects. Finally, the detector response is simulated to mimic the measurements in data. The same object reconstruction procedures as on data are applied for simulated events.

Hard scattering process and parton distribution functions

Monte Carlo event generators are used to simulate the interaction of two protons into the final state of interest for a given physical process. This requires the calculation of the cross section of the hard scattering using perturbation theory. At proton colliders, the cross section for the hard scattering has to be convolved with the parton distribution functions (PDFs) to account for the inner structure of the proton. For an interaction at the momentum scale Q^2, the PDF $f_i^p\left(x, Q^2\right)$ gives the probability that a parton i with a fraction x of the proton's momentum

is found in the proton. The total cross section for a proton-proton collision into a final state C is given by:

$$\sigma\left(pp \to C\right) = \sum_{i,j} \int dx_1 dx_2 f_i^p\left(x_1, Q^2\right) f_j^p\left(x_2, Q^2\right) \hat{\sigma}\left(ij \to C\right). \tag{4.1}$$

The sum takes all possible combinations of partons into account (three valence quarks, sea quarks, and gluons), while $\hat{\sigma}\left(ij \to C\right)$ is the cross section of the hard scattering of the partons i and j into the final state.

Parton distribution functions cannot be calculated analytically but need to be determined from data using perturbative calculations. The samples used in this analysis were produced with the NNPDF3.0 [65] PDF set, which is based on electron-proton collision data from HERA [66], but also takes data from fixed target experiments and LHC data into account. NNPDF3.0 uses QCD calculations up to NLO and includes electroweak corrections as well. Parton distribution functions that are determined at a certain collider can be extrapolated to the momentum regimes of other colliders using the DGLAP (Dokshitzer, Gribov, Lipatov, Altarelli, Parisi) equations [67–69].

Standard model processes are either simulated with the Powheg event generator [70–77] at next-to-leading order (NLO) perturbative QCD or with MadGraph5_aMC@NLO [78], referred to as MadGraph. MadGraph samples are either generated at NLO or at leading order (LO) with additional partons in the matrix element.

The inclusion of these additional parton emissions at matrix element level allows for the modeling of the initial- or final-state radiation. For highly energetic partons, this works well, but at low energies and for collinear emissions, this treatment breaks down because of the confinement of QCD and parton shower models are required to describe these emissions.

Hadronization and parton showers

Strongly interacting particles that are produced in the hard interaction or in parton showers fragment into hadrons. The hadronization is a non-perturbative process that needs to be described by phenomenological models. In this analysis, the matrix element calculations from Powheg or MadGraph are interfaced with Pythia 8 [79] to simulate parton showers and hadronization. Pythia uses a string fragmentation model in which color strings connect color-charged particles. The energy, stored in the potential represented by the string, increases linearly with the distance between the particles until the string breaks and a quark-antiquark pair is produced to form color-singlets. Depending on the energy, several subsequent breaks may occur until the remaining energy is no longer sufficient to continue this process. If the resulting hadrons are unstable, further decays into (almost) stable particles are simulated as well. The phenomenological hadronization model needs to be tuned to describe collision data. The CTUEP8M1 and CTUEP8M2 tunes [80], obtained from underlying event and multi-parton scattering measurements, are used here.

To achieve a smooth translation from the regime of hard initial- or final-state emissions, simulated in Powheg or MadGraph, to parton showers from soft emissions, modeled with

Pythia, a matching algorithm needs to be applied. The MLM and FxFx matching schemes are used for MadGraph samples at LO [81, 82] and NLO precision [78], respectively, while Powheg uses matching procedures that are tuned for the corresponding process [70–77].

Pileup

On average, about 27 proton-proton interactions occurred per bunch crossing during 2016 data taking (in-time pileup), as can be seen in Fig. 4.1. Additionally, the high frequency of bunch crossings every 25 ns can cause overlaps in the detector readout (out-of-time pileup). To account for these effects, each simulated event is overlaid with a certain number of additional events. The number of additional events for individual hard interactions is determined from a probability density function that is expected to match the pileup distribution in data. This distribution is determined by multiplying the total inelastic proton-proton cross section with the instantaneous luminosity per bunch crossing. To account for out-of-time pileup, bunch crossings before and after the main interaction are simulated as well, using a number of pileup events according to a Poisson distribution with the same mean as the bunch crossing that contains the main interaction. The MC samples were produced before the end of data taking. Therefore, the distribution of additional interactions had to be estimated beforehand and differs from the one observed in data. A reweighting procedure is introduced to account for this, which is described in more detail at the end of this section.

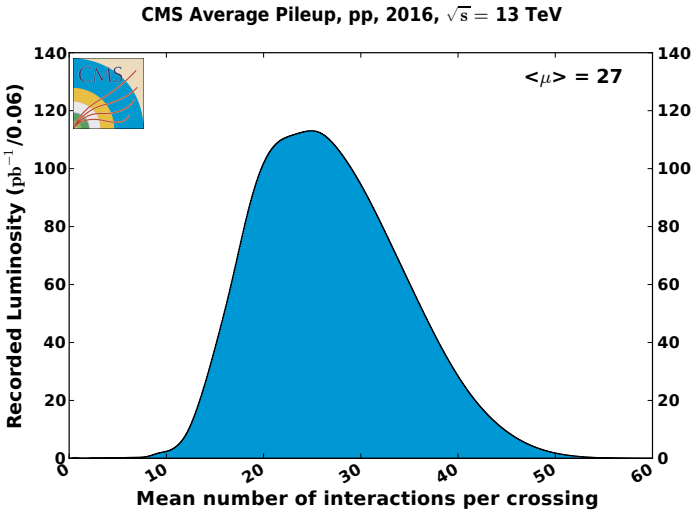

Figure 4.1: Mean number of interactions per bunch crossing in 2016 data taking [53]. The term "mean number" reflects the fact that the number of interactions per bunch crossing is not measured for each bunch crossing directly. Instead, the total inelastic cross section and the instantaneous luminosity in a time interval of about 23 s, called lumi section, are used to determine an average number of interactions per bunch crossing. This value is assigned to the data recorded in the lumi section.

Interaction with the detector

Two types of simulations of the interaction of particles with the detector material are available for the CMS experiment. A detailed model of the CMS detector within GEANT4 [83] is used for the simulation of background processes at a high accuracy. It includes a description of the detector geometry and the material budget. The particles from previous simulation steps are interfaced to GEANT4 and the interaction of these particles with the detector material is modeled, taking into account the propagation inside different materials and the magnetic field of the CMS solenoid. The response of the detector electronics is simulated as well and the same reconstruction algorithms as for data are applied, including a simulation of the HLT triggers.

While the underlying theory for background processes is well known and many analyses require the same background samples, signal models are often customized for one or a few analyses and the uncertainties in the theory are large, especially for simplified models. Furthermore, signal scans usually consist of several hundred signal points and for each of the points a sufficiently large number of events has to be generated. Thus, a fast simulation of the CMS detector has been developed [84], which is less precise than the full detector simulation but about 2 orders of magnitude faster. The fast simulation relies on a simplified description of the detector like homogeneous tracker layers instead of thousands of individual modules as well as simplified reconstruction algorithms. Scale factors are applied to account for differences in the efficiencies compared to the full detector simulation, although a similar accuracy is achieved for most physics objects. No trigger simulation is applied for the fast simulation.

The miniAODSIM data format, which is used to store simulated events, contains all information that is stored in the miniAOD format for real collisions as well as additional information about the generated particles. Thus, simulated data sets can be processed with the same software that is used in the analysis of data events.

Simulated data sets

Standard model processes producing a lepton pair or a lepton and additional particles that might be misidentified as a second lepton can contribute to the background in this analysis. Simulated samples of these processes are used to define signal and control regions as well as to develop or validate background estimation techniques. A variety of SM processes is considered in this work. In most cases, these processes are divided into several samples according to final states. This is of particular interest if the branching fraction into the dileptonic final state is small compared to other decay channels. In this way, a large amount of events can be directly produced for the final state of interest instead of spending computing resources to generate events for the inclusive final state and discarding most of the events in the selection afterwards. Powheg was used to generate samples for top quark pair production ($t\bar{t}$), t- and tW-channel single top quark production, some diboson decay channels, and $t\bar{t}$+Higgs boson production. The remaining diboson decays, s-channel single top quark production, triboson production, $t\bar{t}$+V (V=W or Z boson), $t\bar{t}$+photon, VH, and $t\bar{t}t\bar{t}$ were simulated using MadGraph at NLO while DY processes and W boson production were generated at LO with up to four additional partons in the matrix element using the same MC generator. The

generated samples need to be scaled to the integrated luminosity in data. For this purpose, the number of generated events $N_{\text{events}}^{\text{gen}}$ and the cross section σ need to be taken into account. For many processes, total cross section calculations are available at a higher precision than the integrated differential cross sections used in the event generators. The simulated samples are normalized to these higher order cross sections. The top quark pair production cross section has been calculated at next-to-next-to leading order (NNLO) in QCD including soft-gluon resummation at next-to-next-to-leading logarithmic order (NNLL) with Top++ [85]. FEWZ [86–88] was used to calculate the W and Z boson cross section, including electroweak corrections in NLO and QCD corrections in NNLO. MCFM [89] calculations at NLO order are used for the diboson cross sections. Single top quark contributions in the tW-channel are normalized to approximate NNLO [90], while Hathor is used at NLO precision to normalize the single top quark s- and t-channel samples [91, 92]. For the remaining processes, the NLO MC generator cross sections are used.

In case of MadGraph samples at NLO accuracy, additional generator weights $w_{\text{gen}} = \pm 1$ are assigned to each event. Events obtain negative generator weights if they contain parton emissions already taken into account in the NLO matrix element calculation [78, 93]. The fraction of events with a negative generator weight $f_{\text{events}}^{\text{neg}}$ can range up to more than 30%, and thereby reduce the available statistical precision. In regions of the phase space the sample barely contributes to, statistical fluctuations can result in more events with negative w_{gen} than events with positive w_{gen}, and thus a negative contribution of the corresponding sample, which is unphysical. Powheg is able to avoid negative generator weights [70, 94, 95] and always gets assigned $w_{\text{gen}} = 1$. Therefore, Powheg samples are preferred if they are available for the process of interest and do not contain much fewer events than the MadGraph sample.

The final event weight is given by

$$w = \frac{w_{\text{gen}} \cdot L \cdot \sigma}{N_{\text{events}}^{\text{gen}} \cdot (1 - 2 \cdot f_{\text{events}}^{\text{neg}})},$$

where w_{gen} stands for the generator weight of the event, L is the integrated luminosity, σ the cross section of the process, $N_{\text{events}}^{\text{gen}}$ the number of generated events, and $f_{\text{events}}^{\text{neg}}$ the fraction of events which have a negative generator weight. The factor $(1 - 2 \cdot f_{\text{events}}^{\text{neg}})$ is included to take the sum of the generator weights into account in the overall normalization.

A complete list of all SM background samples used in the main part of the analysis can be found in Tab. 4.1, while the database paths of the samples can be found in Appendix B. The background from QCD multijet events is heavily suppressed by requiring two well identified and isolated leptons and is therefore negligible in all dilepton selections. Nevertheless, the simulation of QCD multijet events with Pythia is used as a reference in the study of non-prompt leptons and a list of the corresponding samples can be found in Appendix B as well.

Signal samples containing the pair production of bottom squarks were simulated using MadGraph at LO accuracy with up to two additional partons in the matrix element calculation. The decay chain into the LSP is simulated in Pythia together with the parton shower generation. Signal cross sections were calculated at NLO+NLL accuracy [46].

All MC samples are reweighted according to the number of simultaneous interactions in data. Additionally, scale factors are applied to account for differences in the lepton identification

efficiencies and b-tagging efficiencies between data and simulation [96–98]. In most cases, the lepton identification efficiencies are larger for simulation than for data, resulting in average scale factors of about 92% for electrons and 97% for muons with the exact values depending on the lepton p_T and η as well as the number of pileup vertices.

While the trigger simulation is used for the background samples, the signal samples are normalized to the trigger efficiencies measured in data, since no trigger simulation is available for the fast simulation of the detector. If systematic uncertainties in the background simulation are shown, these include uncertainties in the jet energy scale, trigger efficiencies, cross sections, and the pileup reweighting. For samples containing a decay of a top quark pair, events are reweighted to account for differences in the p_T spectrum of the top quarks between data and simulation [99, 100]. In these cases, the uncertainty in the reweighting is used as an additional uncertainty. Both the flavor-symmetric and DY+jets background processes are estimated from data and the simulated samples are only used to define signal and control regions and to validate the background estimation methods. The only background contributions that are directly taken from simulation are the processes in the Z+ν category containing the dileptonic decay of a Z boson and genuine missing transverse momentum due to neutrinos. Special multi-lepton control regions have been defined to study the agreement between data and simulation for the most important of these processes and to assign scale factors and systematic uncertainties based on the agreement (see Section 5.2.3). Therefore, further systematic uncertainties in the background simulation are neglected here and the displayed uncertainties represent a lower bound for the actual systematic uncertainties in the simulation. A detailed description of the uncertainties of the signal simulation can be found in Section 9.2.

4.2 Physics objects reconstruction and basic event selections

The important physical objects in this analysis are electrons, muons, jets, and the missing transverse momentum p_T^{miss}. All of these are reconstructed by combining information of several subdetectors using the particle-flow approach [101]. Isolation requirements are added in the lepton selection to remove leptons originating from a heavy-flavor decay instead of the hard interaction.

4.2.1 Particle-flow algorithm

In general, most particles are expected to give rise to measurements in more than one subdetector. Combining the different measurements can help to improve the reconstruction precision and the identification efficiency. The particle-flow (PF) algorithm [101] uses information from all subdetectors to provide a consistent description of the event in terms reconstructed particles. The PF algorithm consists of three steps: At first, basic PF elements are reconstructed in each subdetector. In a second step, a link algorithm combines geometrically connected elements into blocks. Finally, identification algorithms provide the final PF candidates.

The basic track elements are determined using Kalman filter techniques [102] both in the inner tracker and the muon system [54, 103]. Assuming tracks that start in the center of

category	process	generator	σ [pb]	$f_{\text{events}}^{\text{neg}}$	$N_{\text{events}}^{\text{gen}}$	$\lvert w\rvert$
$t\bar{t}$	$t\bar{t} \to 2b2\ell2\nu$	Powheg	87.31	-	78 958 408	0.040
	$t\bar{t} \to 2b2q\ell\nu$	Powheg	271.15	-	152 720 976	0.064
DY+jets	$Z/\gamma^* \to \ell\ell$, $m_{\ell\ell} \in [10, 50]\,\text{GeV}$	MadGraph LO	18 610	-	35 291 544	18.9
	$Z/\gamma^* \to \ell\ell$, $m_{\ell\ell} > 50\,\text{GeV}$	MadGraph LO	6025	-	49 144 292	4.40
	WZ$\to 2\ell$2q	MadGraph NLO	5.60	0.22	26 517 278	0.014
	ZZ$\to 2\ell$2q	MadGraph NLO	3.22	0.20	15 345 572	0.013
	ZZ$\to 4\ell$	Powheg	1.21	-	6 669 988	0.007
Z+ν	WZ$\to 3\ell\nu$	Powheg	4.43	-	11 887 464	0.013
	ZZ$\to 2\ell2\nu$, $m_{\ell\ell} > 40\,\text{GeV}$	Powheg	0.56	-	8 842 475	0.002
	WWZ	MadGraph NLO	0.17	0.06	250 000	0.028
	WZZ	MadGraph NLO	0.055	0.06	246 800	0.009
	ZZZ	MadGraph NLO	0.014	0.07	249 237	0.002
	$t\bar{t}$Z, Z$\to 2\ell/2\nu$	MadGraph NLO	0.25	0.25	1 992 438	0.009
	tZ, Z$\to \ell\ell$	MadGraph NLO	0.076	0.37	14 509 520	< 0.001
	VH, H$\to$non b$\bar{\text{b}}$	MadGraph NLO	0.95	0.24	1 007 898	0.065
Single t	t/$\bar{\text{t}}$ s-channel, t$\to$ b$\ell\nu$	MadGraph NLO	3.36	0.18	1 000 000	0.188
	t t-channel	Powheg	136.02	-	67 240 800	0.073
	$\bar{\text{t}}$ t-channel	Powheg	80.95	-	38 811 008	0.075
	t tW-channel, tW$\to$ b$2\ell2\nu$/b$\ell\nu$2q	Powheg	19.57	-	3 256 650	0.180
	$\bar{\text{t}}$ tW-channel, tW$\to$ b$2\ell2\nu$/b$\ell\nu$2q	Powheg	19.57	-	3 256 407	0.180
Other SM	W$\to \ell\nu$	MadGraph LO	61 530	-	29 705 752	74.4
	WW$\to 2\ell2\nu$	Powheg	12.18	-	1 999 000	0.219
	WW$\to \ell\nu$2q	Powheg	50.00	-	6 998 600	0.256
	WZ$\to \ell\nu$2q	MadGraph NLO	10.71	0.22	24 221 924	0.028
	$t\bar{t}\gamma$	MadGraph NLO	3.70	0.34	9 885 348	0.042
	$t\bar{t}$W, W$\to \ell\nu$	MadGraph NLO	0.20	0.24	2 160 168	0.006
	$t\bar{t}$W, W$\to$ 2q	MadGraph NLO	0.41	0.24	833 298	0.034
	$t\bar{t}$Z, Z$\to$ 2q	MadGraph NLO	0.53	0.26	749 400	0.053
	$t\bar{t}$H, H$\to$ b$\bar{\text{b}}$	Powheg	0.29	-	3 845 992	0.003
	$t\bar{t}$H, H$\to$ non b$\bar{\text{b}}$	Powheg	0.22	-	3 981 250	0.002
	$t\bar{t}t\bar{t}$	MadGraph NLO	0.009	0.29	2 456 040	< 0.001

Table 4.1: Summary of the simulated background data sets used in the analysis except for the QCD multijet samples, which can be found in Tab. B.2. The samples are grouped by phenomenological background contributions. The flavor-symmetric background is split into three subcategories: top quark pair production, single top quark production, and other SM processes. Some processes might contribute to more than one category and are assigned according to their main contribution. For each process, information about the generator, the cross section, the fraction of events with negative generator weight, the number of processed events, and the absolute value of the resulting weight used to scale the simulation to the recorded luminosity are given.

the detector, the algorithm starts with track seeds in the inner part of the subdetector and extrapolates to the next layer or station. Uncertainties due to energy losses and interactions with the material are taken into account and a certain fraction of missing hits is tolerated. In case of the silicon tracker, the procedure is iterated several times, each time relaxing the track seed requirements and removing hits associated to track candidates from previous iterations.

Calorimeter clusters are another type of basic PF elements and are formed in three steps. At first, cluster seeds, local calorimeter-cell energy maxima above a certain threshold, are identified. As a second step, topological clusters are grown from these seeds by iteratively adding neighboring cells as long as these exceed a given energy threshold. Finally, PF clusters are defined for each seed. If there is more than one seed in a topological cluster, the energy of each cell in the topological cluster is shared between the PF clusters according to the distances between the cell and the PF clusters.

An algorithm combines basic PF elements to blocks of elements depending on their geometrical position. Particle-flow candidates are reconstructed from the objects in these blocks iteratively, removing the objects associated to the PF candidate after each step to avoid double counting of measurements. At first, muons are reconstructed. In the second step, electrons are selected, for which bremsstrahlung photons are taken into account. In the same step, isolated photons are identified as well. Finally, charged hadrons are extracted from the remaining calorimeter clusters compatible with tracks while at the same time clusters without corresponding tracks are either identified as non-isolated photons or neutral hadrons, depending on the fraction of energy that is deposited in the ECAL.

Several types of muon objects are produced in the event reconstruction. Tracker muons are tracks in the inner tracker that can be matched to an entry, though not necessarily a full track, in the muon system. Particle flow elements from the muon system alone are referred to as standalone muons. If a standalone muon can be associated to a charged particle track in the tracker, a combined fit to all hits from both objects is performed. If the fit returns an acceptable χ^2, a global muon is returned. In cases where standalone muons can be matched to more than one tracker track, the global muon with the lowest χ^2 is chosen. For any of the aforementioned muon objects to be identified as a muon by the PF algorithm, they need to fulfill additional requirements on the isolation or track quality [101, 104].

To reconstruct electrons, tracks from the tracking system have to be associated to clusters in the ECAL. Photons from bremsstrahlung need to be taken into account since the material budget of the tracker amounts to 0.4–2.0 radiation lengths depending on the pseudorapidity [105]. On average, this corresponds to radiative emissions of 33–86% of the electrons momentum. Additionally, the strong magnetic field bends the electron trajectory away from the emitted photon in ϕ direction. Thus, roughly squared calorimeter clusters and tracks from Kalman filters are insufficient to account for bremsstrahlung. Special algorithms determine ECAL superclusters (SC), which are wider in ϕ than in η, and a Gaussian sum filter (GSF) algorithm [106] is used to refit electron candidates. The GSF tracking is either triggered if a SC can be extrapolated back to a track seed in the inner tracker layers or if a charged-particle track either directly points to an ECAL cluster or is of poor quality with only a few tracker hits indicating photon radiation.

4.2.2 Vertex reconstruction and pileup

On average, about 27 proton-proton collisions occurred within one bunch crossing during 2016 data taking. To distinguish the particles from the interaction of interest from the remaining ones, the so-called pileup, an association of particles to interaction vertices is required.

Charged PF candidates are clustered into vertices using a deterministic annealing algorithm [54, 107]. An adaptive vertex fitter [108] is used to find the vertex position, assigning a weight between 0 and 1 to each track according to the likelihood of the track being correctly assigned to the vertex. An anti-k_t jet clustering algorithm [109, 110] is applied to the PF candidates from a vertex to provide physics objects and the missing transverse momentum associated to the vertex. More details on jet clustering and missing transverse momentum reconstruction can be found in Sections 4.2.6 and 4.2.7, respectively. The vertex with the largest p_{T} sum of associated objects is chosen as the primary vertex. Tracks can afterwards be classified as coming from the primary vertex or a pileup vertex. Neutral hadrons from pileup vertices cannot be identified directly and indirect corrections are required when the leptons and jets are selected (see Sections 4.2.5 and 4.2.6).

4.2.3 Electron identification

A multivariate approach is chosen to identify electrons, taking track quality criteria, the matching of geometry and momentum between the track and the SC, the shower shapes in the ECAL, and the energy fractions in the ECAL and HCAL into account to distinguish between electrons, photons, and jets from charged hadrons. The identification efficiency increases with the electron p_{T} and is in general higher in the barrel than in the endcaps [96, 105]. For the chosen working point typical efficiencies to identify electrons from the primary interaction are 85–90% at $p_{\mathrm{T}} = 20\,\mathrm{GeV}$ and about 95% above 40 GeV. To reject electrons from photon conversion, electron candidates are vetoed if a hit in the inner tracker layers is missing or the candidate can be fitted with neighboring tracks to a common vertex that indicates a conversion. For electrons from the primary interaction the probability of these fits is small and all electron candidates with a fit probability above 10^{-6} are vetoed.

To suppress electrons originating from secondary interactions, the impact parameter of the electron track with respect to the primary vertex must not exceed 0.5 mm in the transverse plane (d_{xy}) and 1 mm in z direction (d_z). Furthermore, the ratio of the three dimensional impact parameter divided by its uncertainty (SIP3D) must be smaller than 8. The most basic electron selection requires $p_{\mathrm{T}} > 10\,\mathrm{GeV}$ and $|\eta| < 2.5$ and is summarized in Tab. 4.2.

4.2.4 Muon identification

A muon in this analysis is required to be either a global or a tracker muon. The track in the inner tracker needs to have a fraction of valid hits above 0.8. For global muons, the χ^2 per degree of freedom of the global muon fit is required to be less than 3 and the matching between the tracker and the standalone tracks computed on a common surface has to have a local position χ^2 smaller than 12. Furthermore, a kink finder is applied in the inner tracker

Criterion	Selection
Kinematics	
p_{T}	$> 10\,\mathrm{GeV}$
$\lvert\eta\rvert$	< 2.5
Identification	
electron MVA Id	Tight working point
missing hits	$= 0$
conversion fit probability	$< 10^{-6}$
Impact parameter	
d_{xy}	$< 0.5\,\mathrm{mm}$
d_z	$< 1\,\mathrm{mm}$
SIP3D	< 8

Table 4.2: Summary of the electron selection requirements

by splitting the track into an inner and an outer part at several points of the trajectory and the maximal χ^2 per degree of freedom for the compatibility of the two parts must not exceed 20. Finally, the segment compatibility, which is computed by propagating the inner track to the muon system and evaluating the number of matched segments in all muon stations and the quality of the matching, is required to be greater than 0.303. Global muons that fail one of the requirements stated above and tracker muons are accepted, if they fulfill a tighter segment compatibility requirement of 0.451.

The same requirements on the impact parameter as for electrons are applied. Beside removing muons from secondary interactions these requirements effectively suppress muons of cosmic origin. Muons with $p_{\mathrm{T}} > 10\,\mathrm{GeV}$ and $|\eta| < 2.4$ are considered and a summary of all selection criteria is given in Tab. 4.3.

4.2.5 Lepton isolation

The lepton identification requirements stated above reject backgrounds from particles misidentified as leptons. Further requirements need to be added to make sure the leptons originate from the primary interaction vertex and not from the decay of heavy-flavor quarks in a jet.

Heavy-flavor decays are suppressed by requiring the amount of activity around the lepton to be small. For this purpose, the uncorrected lepton isolation is defined by the p_{T} sum of all PF candidates in a cone around the lepton, excluding the lepton itself:

$$\mathrm{Iso}^{\mathrm{uncor}} = \sum_{\text{charged hadrons}} p_{\mathrm{T}} + \sum_{\text{neutral hadrons}} p_{\mathrm{T}} + \sum_{\text{photons}} p_{\mathrm{T}}. \tag{4.2}$$

A p_{T} dependent cone size around the lepton is used to recover leptons with high momenta and small separation from other objects, e.g. from boosted decays:

$$\Delta R = \begin{cases} 0.2 & p_{\mathrm{T}} < 50\,\mathrm{GeV} \\ \frac{10\,\mathrm{GeV}}{p_{\mathrm{T}}} & 50 \leq p_{\mathrm{T}} \leq 200\,\mathrm{GeV} \\ 0.05 & p_{\mathrm{T}} > 50\,\mathrm{GeV}. \end{cases} \tag{4.3}$$

Criterion	Selection	
Kinematics		
p_{T}	$> 10\,\mathrm{GeV}$	
$\lvert\eta\rvert$	< 2.4	
Identification		
required to be	PF muon	
	global muon	global muon or tracker muon
global track χ^2/N_{dof}	< 3	-
local position χ^2	< 12	-
kink finder χ^2/N_{dof}	< 20	-
segment compatibility	> 0.303	> 0.451
fraction of valid tracker hits	> 0.8	
Impact parameter		
d_{xy}	$< 0.5\,\mathrm{mm}$	
d_z	$< 1\,\mathrm{mm}$	
SIP3D	< 8	

Table 4.3: Summary of the muon selection requirements

The presence of PF candidates originating from pileup vertices in the isolation cone can significantly increase the isolation sum. Charged hadrons from pileup interactions can be associated to a different vertex and are neglected in the calculation. For neutral hadrons and photons no such matching is possible. The contribution of neutral pileup is estimated using the average energy density in the event ρ, determined using the k_t jet clustering algorithm [111] with a distance parameter of 0.6, and the effective area of the isolation cone $A^{\mathrm{eff}}_{\mathrm{lepton}}$:

$$\sum_{\text{neutral PU}} p_{\mathrm{T}} = \rho \cdot A^{\mathrm{eff}}_{\mathrm{lepton}}. \tag{4.4}$$

The resulting isolation variable is given by:

$$\mathrm{Iso} = \sum_{\text{charged hadrons from PV}} p_{\mathrm{T}} + \max\left(0, \sum_{\text{neutral hadrons}} p_{\mathrm{T}} + \sum_{\text{photons}} p_{\mathrm{T}} - \sum_{\text{neutral PU}} p_{\mathrm{T}}\right). \tag{4.5}$$

The relative isolation $\mathrm{Iso}_{\mathrm{rel}} = \mathrm{Iso}/p_{\mathrm{T}}$ must not exceed 10% for electrons and 20% for muons (see Section 4.3).

4.2.6 Jets

An anti-k_t algorithm in a fast implementation [109, 110] is used to cluster the particles from the hadronization of quarks or gluons into jets. It takes all PF candidates as an input for a sequential clustering and treats them as pseudo jets. Two quantities are introduced as distance measures, the first one between a pseudo jet i and the beam axis and the second one between two pseudo jets i and j:

$$d_{iB} = p_{\mathrm{T},i}^{-2}, \tag{4.6}$$

$$d_{ij} = \min\left(p_{\mathrm{T},i}^{-2}, p_{\mathrm{T},j}^{-2}\right) \frac{(y_i - y_j)^2 + (\phi_i - \phi_j)^2}{R^2}, \tag{4.7}$$

where $p_{\mathrm{T},i}$, y_i, and ϕ_i stand for the transverse momentum, rapidity, and azimuthal angle of pseudo jet i. The distance parameter R is a measure for the size of the resulting jets and is set to 0.4 in this analysis. In each step, the distances are calculated for each pseudo jet and combination of pseudo jets, respectively. If the minimal distance is a d_{ij} the two corresponding pseudo jets are merged into a new one. Any pseudo jet with a d_{iB} smaller than the minimal d_{ij} is considered a final jet and removed from the collection of objects to cluster.

The measured jet momentum p^{raw} is subject to several effects, which cause the reconstructed momentum to be different from the momentum of the true particle jet. Nonuniform and nonlinear calorimeter responses have the largest impact, but offset corrections due to pileup and electronic noise need to be taken into account as well. A multiplicative jet energy correction (JEC) is applied to the measured momentum [112]:

$$p^{\mathrm{cor}} = C\left(p_{\mathrm{T}}, \eta\right) \cdot p^{\mathrm{raw}}. \tag{4.8}$$

A factorized approach was chosen where each factor accounts for a different effect:

$$C\left(p_{\mathrm{T}}, \eta\right) = C_{\mathrm{offset}}\left(p_{\mathrm{T}}^{\mathrm{raw}}\right) \cdot C_{\mathrm{MC}}\left(p_{\mathrm{T}}', \eta\right) \cdot C_{\mathrm{rel}}\left(\eta\right) \cdot C_{\mathrm{abs}}\left(p_{\mathrm{T}}''\right), \tag{4.9}$$

where p_{T}' and p_{T}'' are the transverse momenta after applying the respective previous corrections.

The offset corrections are applied to the raw jet and account for pileup effects and electronics noise. Similarly to the lepton isolation, the energy density in the event ρ is determined and compared to the average energy density in the underlying event $\langle\rho_{\mathrm{UE}}\rangle$ measured in events without pileup interactions. Using the jet area A_j, the offset correction is given as

$$C_{\mathrm{offset}}\left(p_{\mathrm{T}}^{\mathrm{raw}}\right) = 1 - \frac{\left(\rho - \langle\rho_{\mathrm{UE}}\rangle\right) \cdot A_j}{p_{\mathrm{T}}^{\mathrm{raw}}}. \tag{4.10}$$

After applying the offset correction, the jet momentum is in principle independent of the instantaneous luminosity. As a second step, a correction based on the ratio of the generated and reconstructed jet momenta in MC simulation is applied to account for nonuniform and nonlinear detector response in η and p_{T}. Residual corrections between data and simulation are the final corrections to be applied. Relative residual corrections depending on η are derived using a dijet p_{T}-balancing method. One jet in the barrel region ($|\eta| < 1.3$) is used to measure the detector response of a jet at arbitrary η relative to the response in the central region. The method relies on the assumption that a dijet system is balanced in p_{T} and therefore energy corrections for non-central jets with respect to central jets can be derived. Absolute residual corrections are derived from events containing a central jet and a photon or a leptonically decaying Z boson. The energy of the photon or the decay products of the Z boson can be measured to a higher precision using the tracker and the ECAL than the jet in the HCAL.

Jet correction factors are derived by assuming that the events are balanced in the transverse plane and correct the jet momentum to the recoil of the photon or Z boson.

Jets in this analysis are required to fulfill $p_T > 35\,\text{GeV}$ and $|\eta| < 2.4$ to be taken into account for the jet multiplicity and hadronic activity.

Because of their life time, hadrons containing b-quarks decay at a measurable distance from the primary vertex and produce a secondary vertex. The CSVv2 algorithm [113] is used in this analysis to find secondary vertices. Information of displaced tracks and secondary vertices associated to the jet are combined using a multivariate technique and a discriminating variable is extracted. The medium CSVv2 working point is chosen, which has a b-tagging efficiency of about 70% while the probability to misidentify a jet from a light squark as a b jet is 1–2% for jets with $p_T < 600\,\text{GeV}$ and can range up to 3.5% at even higher transverse momenta.

4.2.7 Missing transverse momentum $\mathbf{p_T^{miss}}$

Before the interaction, the initial state of the collision has negligible momentum in the plane transverse to the beam direction. After the interaction, weakly interacting particles that leave the experiment undetected can cause missing transverse momentum p_T^{miss}, defined in Equation 1.6. Since the momentum imbalance is the only experimental signature of these particles, a precise measurement of p_T^{miss} is crucial to the discovery of processes that include such particles.

The negative vectorial sum of all PF particles is used to determine p_T^{miss} [114]. The jet energy corrections are propagated to p_T^{miss} for all jets with $p_T > 15\,\text{GeV}$ and less than 90% of their energy deposited in the ECAL. If a muon is present in a jet, its momentum is removed from the jet before the correction and added again afterwards.

To veto events in which a muon is poorly reconstructed and causes a momentum imbalance, calorimetric (calo) p_T^{miss} is used (see Section 4.3.1). Calorimetric p_T^{miss} is calculated as the negative vector sum of the energy deposits in the calorimeter towers. Since muons deposit only a small energy fraction in the calorimeters, these energy deposits are replaced by the measured momentum in case of well reconstructed muons.

4.3 Basic event selection

Several selection criteria are applied to find signal-like events among the vast number of events from known SM processes. One of the main objectives of this analysis is to check if the deviation observed in 8 TeV data can be confirmed. Thus, many event selection criteria as well as control region definitions are the same as in the 8 TeV analysis except for cases in which trigger requirements made increased thresholds necessary.

4.3.1 Event filters

To ensure good data quality and remove events with large p_T^{miss} not originating from the proton-proton interaction, several quality requirements are applied. The data quality is mon-

itored during data taking and validated afterwards by the CMS data quality monitoring [115]. Only data for which all subdetectors were fully operational and no problems occurred during the event reconstruction are used in this work.

Events that do not originate from the collision, like cosmic rays, can be vetoed using requirements on the vertex. A primary vertex with a distance to the nominal interaction point of less than 2 cm in the transverse plane and 24 cm in z direction is required. Furthermore, the number of degrees of freedom, defined as:

$$n_{\text{dof}} = -3 + 2 \sum_{i=1}^{\#\text{ assoc. tracks}} w_i \tag{4.11}$$

is required to be greater than four [54]. The weights w_i are assigned to each track based on the likelihood to be correctly associated to the vertex, as described in Section 4.2.2.

Several phenomena causing anomalous high $p_{\text{T}}^{\text{miss}}$ have been identified during data taking and filters are applied to veto such signatures [114]. These include detector effects like noise in the HCAL, dead ECAL cells, and supercrystals in the ECAL endcaps that give anomalously high pulses in several channels at once. Further phenomena are protons interacting with gas molecules in the beam pipe or the detector infrastructure and failures of the tracking algorithms. Figure 4.2 shows the impact of these filters on the $p_{\text{T}}^{\text{miss}}$ distribution in dijet events. The filters reject most of the events with $p_{\text{T}}^{\text{miss}} > 600\,\text{GeV}$ and improve the agreement between data and simulation significantly.

After the end of 2016 data taking, a problem in the muon reconstruction was discovered that caused muons to be reconstructed twice in some cases. The duplicated muons usually feature low track quality criteria and are in some cases regarded as a jet. A new version of the data in miniAOD format was produced to remove this effect but some suspicious cases remained. To veto these signatures, two additional filters are applied in this analysis. Events are vetoed if the $p_{\text{T}}^{\text{miss}}$ from the PF algorithm is more than five times larger than the calo $p_{\text{T}}^{\text{miss}}$ which only takes well reconstructed muons into account. Additionally, events are vetoed if they contain a jet with $p_{\text{T}} > 200\,\text{GeV}$ and a muon fraction larger than 50%, which points in the opposite direction of the missing transverse momentum vector ($|\Delta\phi\left(\vec{p}_{\text{T}}^{\,\text{jet}}, -\vec{p}_{\text{T}}^{\,\text{miss}}\right)| < 0.4$).

4.3.2 Inclusive dilepton selection

Two basic principles drive the determination of selection thresholds for the leptons. Firstly, the offline lepton p_{T} thresholds need to be at least as strict as the trigger requirements. An exception are the non-isolated triggers with higher p_{T} thresholds. These triggers target leptons from boosted decays, which usually have a higher p_{T}. The non-isolated triggers are therefore ignored at this point. Secondly, the estimation of the main background component relies on the symmetry between the lepton flavors. Thus, detector parts for which this symmetry is potentially violated are excluded.

The most inclusive dilepton selection used in this work contains two isolated electrons or muons with opposite electric charge. The lepton p_{T} is required to be larger than 25 GeV for the lepton with the higher p_{T} and larger than 20 GeV for the second one. The former lepton

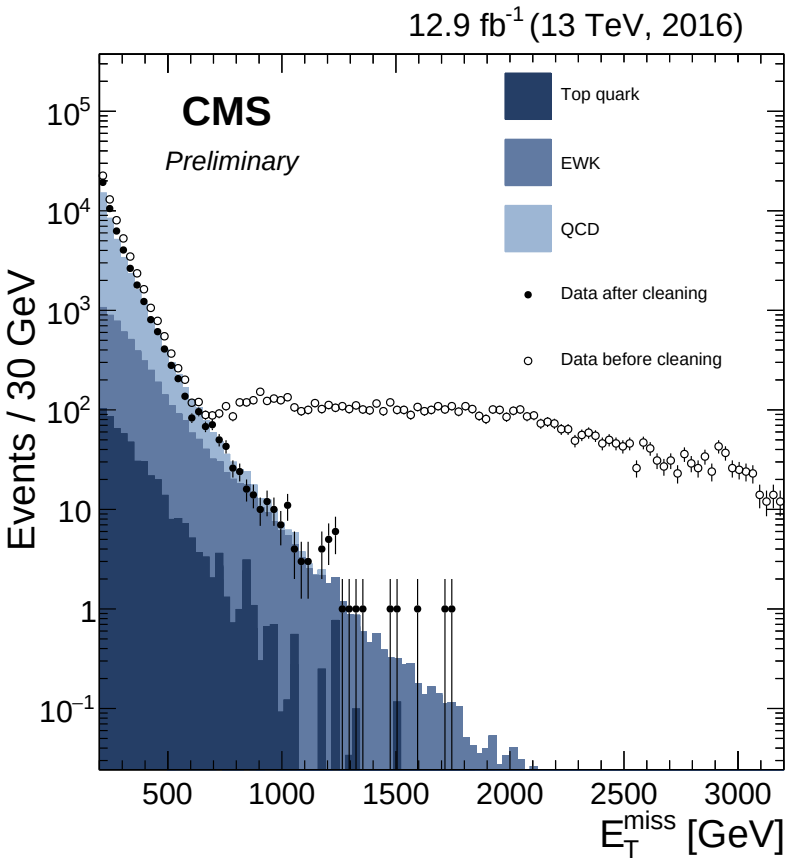

Figure 4.2: Distribution of missing transverse momentum in dijet events in the first 12.9 fb^{-1} of 2016 data. Open and filled markers show the events before and after applying the filters for phenomena with anomalous high $p_{\mathrm{T}}^{\mathrm{miss}}$, respectively. Simulated samples are shown for comparison. The top quark contribution consists of top quark pair production and single top quark production processes. The EWK background includes $\mathrm{Z}\to\ell\ell$, $\mathrm{Z}\to\nu\nu$, $\mathrm{W}\to\ell\nu$, and diboson processes [114].

Criterion	Selection
Event filters	Pass
Leading lepton p_{T}	$> 25\,\mathrm{GeV}$
Subleading lepton p_{T}	$> 20\,\mathrm{GeV}$
Lepton $\lvert\eta\rvert$	< 2.4 excl. $[1.4, 1.6]$
Charge and flavor	Opposite-charge, same-flavor pair
$p_{\mathrm{T}}^{\ell\ell}$	$> 25\,\mathrm{GeV}$
$m_{\ell\ell}$	$> 20\,\mathrm{GeV}$,
$\Delta R_{\ell\ell}$	> 0.1

Table 4.4: Requirements in the inclusive dilepton selection selection.

is sometimes referred to as the leading lepton and the latter as the subleading or trailing one. Both leptons need to be reconstructed within $|\eta| < 2.4$, excluding those leptons with $1.4 < |\eta| < 1.6$. If more than two leptons fulfilling the basic requirements are present, the two leptons with the largest p_{T} are chosen as the relevant dilepton pair. The dilepton system is required to have a transverse momentum of $p_{\mathrm{T}}^{\ell\ell} > 25\,\mathrm{GeV}$, $m_{\ell\ell} > 20\,\mathrm{GeV}$, and the leptons need to be spatially separated by $\Delta R_{\ell\ell} > 0.1$. A trigger corresponding to the flavor combination of the leptons is required to have fired, e.g. an event in the dimuon selection requires one of the dimuon triggers to have triggered. No explicit matching of a lepton to the object that has fired the trigger is performed. The requirements are summarized in Tab. 4.4 and a motivation for the selection thresholds is given in the following.

The lepton p_{T} requirements are driven by the thresholds of the triggers and will be discussed in more detail in Section 5.2.1.

The distribution of $|\eta|$ for the leading and trailing lepton in simulated dielectron and dimuon pairs from decays of top quark pairs is shown in Fig. 4.3. Events fulfilling the inclusive dilepton selection except for the $|\eta|$ requirement are considered. Although the tracker geometry allows for an electron reconstruction up to $|\eta| = 2.5$, only electrons up to $|\eta| = 2.4$ are selected to ensure a symmetric selection between electrons and muons. Similarly, the pseudorapidity window $1.4 < |\eta| < 1.6$ around the transition region between the ECAL barrel and endcaps is excluded for both lepton flavors, because the electron reconstruction efficiency is reduced in this regime while the muon efficiency is not. Since the ratio of dielectron to dimuon events differs between leptons in the barrel part of the detector and those reconstructed in the endcaps, the 8 TeV analysis was split into two $|\eta|$ bins [5, 6] (see Section 5.1): Events labeled as central were required to have both leptons reconstructed within $|\eta| < 1.4$, whereas forward events contained at least one lepton with $|\eta| > 1.6$. While the event yields in this work are not split into $|\eta|$ regions, except for the investigation of the 8 TeV excess region, the prediction of flavor-symmetric backgrounds will still use these $|\eta|$ bins to provide a more accurate description (see Section 5.2.1). In principle, splitting the forward bin into two parts by requiring either one or both leptons to be reconstructed at $|\eta| > 1.6$ might be desirable, but in some control selections only about 2% of the events fall into the latter category, which results in a sample size that is too small for an accurate prediction. Other detector structures can be observed in the $|\eta|$ distribution as well. Most prominently, a transition between DT chambers results in the drop of the muon efficiency at $|\eta| = 0.25$. Since these effects are much less pronounced than the asymmetry in the ECAL transition region, no further $|\eta|$

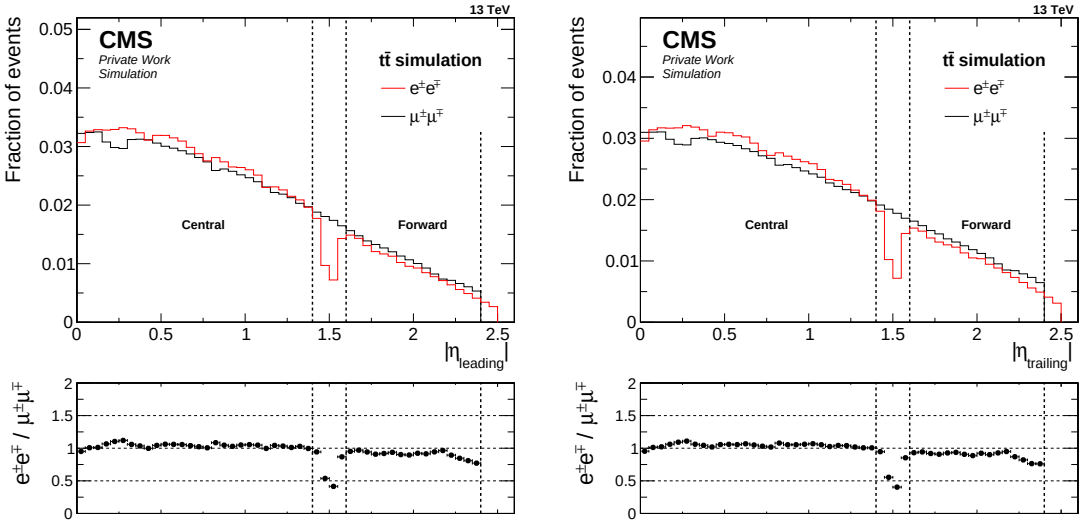

Figure 4.3: Distribution of $|\eta|$ of the leading (left) and trailing lepton (right) for $\mu^{\pm}\mu^{\mp}$ (black line) and $e^{\pm}e^{\mp}$ events (red line) in $\mathrm{t\bar{t}}$ simulation. The histograms have been normalized to 1 and the bottom panel shows the ratio between $e^{\pm}e^{\mp}$ and $\mu^{\pm}\mu^{\mp}$ events. Dashed lines indicate the $|\eta|$ range excluded in the analysis.

requirements or correction bins are used.

Studies with different isolation requirements have been performed on a simulated sample of $\mathrm{t\bar{t}}$ events. The dielectron and dimuon events in this sample are split into three categories depending on the lepton with lower p_{T}: Leptons originating from a decay of a W boson or a tau lepton are labeled as prompt leptons. Non-prompt leptons are further split into leptons from decays of charm or bottom quarks, summarized as heavy-flavor decays, or jets that were misidentified as leptons. Figure 4.4 shows the relative isolation, $\mathrm{Iso_{rel}}$, of the subleading lepton for dielectron (left) and dimuon events (right) fulfilling the inclusive dilepton selection. Since the number of jets that are misidentified as leptons is higher in case of electrons, asymmetric thresholds on $\mathrm{Iso_{rel}}$ are required to achieve a similar fraction of prompt leptons in both flavors. Requirements of $\mathrm{Iso_{rel}} < 0.1$ for electrons and < 0.2 for muons are used to achieve a purity of prompt leptons of 99.7% in both samples.

A threshold on the invariant dilepton mass $m_{\ell\ell}$ of at least 20 GeV is used to avoid contamination of low mass resonances and possible reconstruction problems.

The DY+jets background is estimated from a γ+jets sample under the assumption that $p_{\mathrm{T}}^{\mathrm{miss}}$ mainly originates from jet mismeasurements in both cases. Thus, similar $p_{\mathrm{T}}^{\mathrm{miss}}$ distributions for γ+jets and DY+jets events are expected if the bosons have the same momenta. The most inclusive and highly prescaled photon trigger allows to use photons with $p_{\mathrm{T}} > 25$ GeV and the same requirement is used for the dilepton system.

At 8 TeV, an asymmetry was observed in $\mathrm{t\bar{t}}$ simulation between dielectron and dimuon events with small spatial separation between the leptons (upper left plot in Fig. 4.5) [6]. Furthermore, leptons too close to each other can interfere with each others isolation, which used a constant

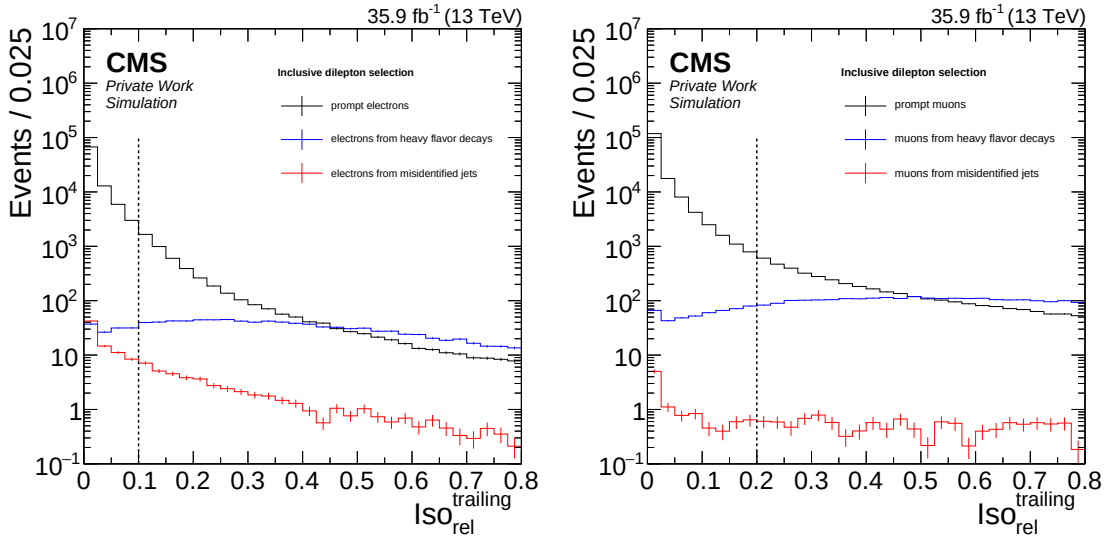

Figure 4.4: Distribution of the relative isolation of the subleading lepton for $e^{\pm}e^{\mp}$ (left) and $\mu^{\pm}\mu^{\mp}$ events (right) in $\mathrm{t\bar{t}}$ simulation. Dashed black lines indicate the chosen cut values.

isolation cone of $\Delta R = 0.3$ at the time. This motivated the introduction of a requirement on the spatial resolution of $\Delta R_{\ell\ell} > 0.3$. The upper right plot in Fig. 4.5 shows the same distribution for 13 TeV simulation, when not requiring $m_{\ell\ell} > 20\,\mathrm{GeV}$. A similar discrepancy between the lepton flavors is observed at small values of $\Delta R_{\ell\ell}$. Requiring $m_{\ell\ell} > 20\,\mathrm{GeV}$ reduces the fraction of events with $\Delta R_{\ell\ell} < 0.3$ by about an order of magnitude and removes most of the discrepancy between the flavors (lower plot in Fig. 4.5). The introduction of a p_{T} dependent cone size reduces the impact on the isolation and makes a smaller requirement on the spatial resolution possible. To regain sensitivity to leptons from decays of highly boosted particles and since the fraction of affected events in flavor-symmetric processes is small, the requirement on the spatial resolution is reduced to $\Delta R_{\ell\ell} > 0.1$ to remove only the most extreme cases. An exception is the investigation on the deviation observed at 8 TeV where the old threshold is applied. In both analyses, an asymmetry between dielectron and dimuon events can be observed at very high values of $\Delta R_{\ell\ell}$ as well. Since the number of affected events is small, no requirement is introduced to veto these events.

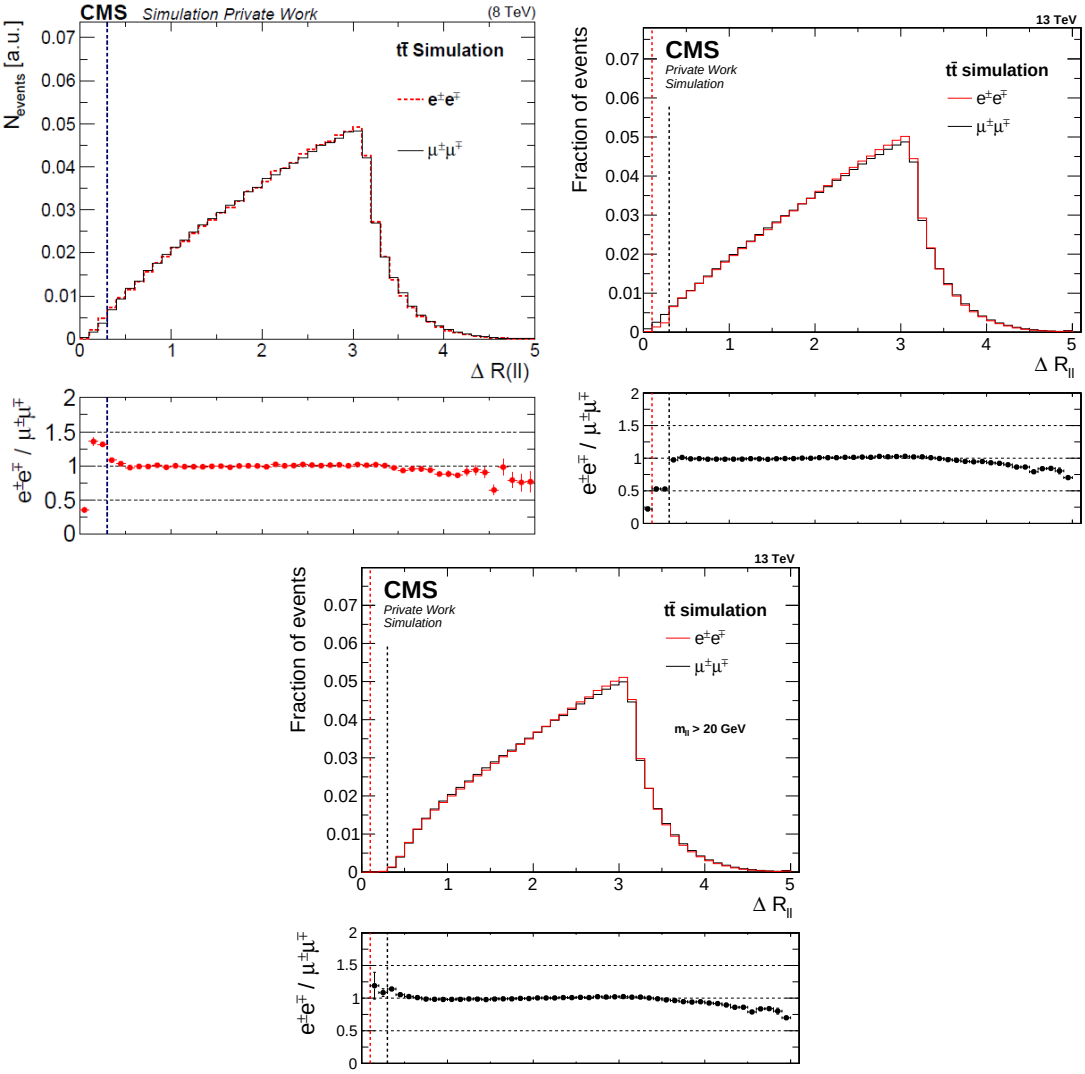

Figure 4.5: Distribution of $\Delta R_{\ell\ell}$ for $\mu^{\pm}\mu^{\mp}$ (black line) and $e^{\pm}e^{\mp}$ events (red line) in $t\bar{t}$ simulation at 8 TeV (top left, taken from [6]) and 13 TeV (top right and bottom). No requirements on $m_{\ell\ell}$ are applied in the upper plots, while only events with $m_{\ell\ell} > 20$ GeV are selected in the lower plot. The histograms have been normalized to 1 and the bottom panels show the ratio between $e^{\pm}e^{\mp}$ and $\mu^{\pm}\mu^{\mp}$ events. Dashed black lines indicate the cut value at 8 TeV, while the cut value at 13 TeV is given by a red dashed line in the top right and bottom plot.

5 Analyzing the deviation observed at 8 TeV with 13 TeV data

Using 19.4 fb^{-1} of 8 TeV data taken in 2012, the CMS collaboration observed a deviation of about 2.5 standard deviations in a signal region with two OCSF leptons, jets, and missing transverse momentum at low invariant dilepton mass [5, 6]. Although the deviation could not be confirmed using 13 TeV data taken in 2015 [7], another investigation is performed here since the data set taken by the CMS experiment in 2015 was not very large and only 2.3 fb^{-1} could be used for this purpose. The data set taken in 2016 amounts to 35.9 fb^{-1} and is therefore well suited for an investigation with large statistical power.

For simplicity, only the "counting experiment" approach of the 8 TeV analysis is repeated in this chapter, which compares the number of observed events to the expectation from background processes. In the first part of this chapter, the 8 TeV signal region, in which the deviation was observed, will be defined along with the control regions for the background prediction. Afterwards, a detailed description of the background prediction methods and the results in the signal region will be given. The background prediction methods will be used in later parts of the analysis as well.

5.1 Signal and control regions

Supersymmetric models that include the strong production of gluinos or squarks and R-parity conservation predict final states with several jets and missing transverse momentum. In most cases, the jet multiplicity N_{Jets} and the amount of $p_{\text{T}}^{\text{miss}}$ is larger than for SM background processes. Signal regions are therefore defined at high values in these variables, while control regions, dominated by background processes, are defined at lower values.

Figure 5.1 shows the distribution of simulated $\text{t}\bar{\text{t}}$ (left) and DY+jets events (right) in the $p_{\text{T}}^{\text{miss}}$-$N_{\text{Jets}}$ plane. The lines indicate the signal and control regions used in the 8 TeV analysis. Figure 5.2 shows the same distribution for two example signal points of the slepton model discussed in Section 2.3.4. For both signal points, the bottom squark mass ($m_{\tilde{b}}$) is 1000 GeV. The left plot, in which the mass of the $\tilde{\chi}_2^0$ is 200 GeV, shows a high amount of $p_{\text{T}}^{\text{miss}}$ and a very high jet multiplicity. In the right plot, which features a more compressed scenario ($m_{\tilde{\chi}_2^0} = 900$ GeV), the average jet multiplicity is lower while the amount of $p_{\text{T}}^{\text{miss}}$ is even larger. In comparison to the background processes, both signal points have a tendency towards higher values of N_{Jets} and $p_{\text{T}}^{\text{miss}}$. Most importantly, there are only few signal events with $N_{\text{Jets}} < 2$.

The signal selection in the analysis at 8 TeV required either $N_{\text{Jets}} \geq 2$ and $p_{\text{T}}^{\text{miss}} > 150$ GeV or $N_{\text{Jets}} \geq 3$ and $p_{\text{T}}^{\text{miss}} > 100$ GeV. The first selection is more sensitive to signal points where more energy is carried away by invisible objects and less is distributed to the jets while it is the other way around for the second selection.

Two control regions are defined to provide samples enriched either in events from DY+jets processes or top quark pair production. Events from DY+jets processes usually have a low jet multiplicity and little $p_{\text{T}}^{\text{miss}}$ (figure 5.1, right). To obtain a high statistics control sample of lepton pairs from the Drell-Yan process to perform efficiency measurements, events with $N_{\text{Jets}} \geq 2$ and $p_{\text{T}}^{\text{miss}} < 50$ GeV are selected. The requirement on the jet multiplicity reduces the sample size significantly but allows to study events with jet kinematics similar to the

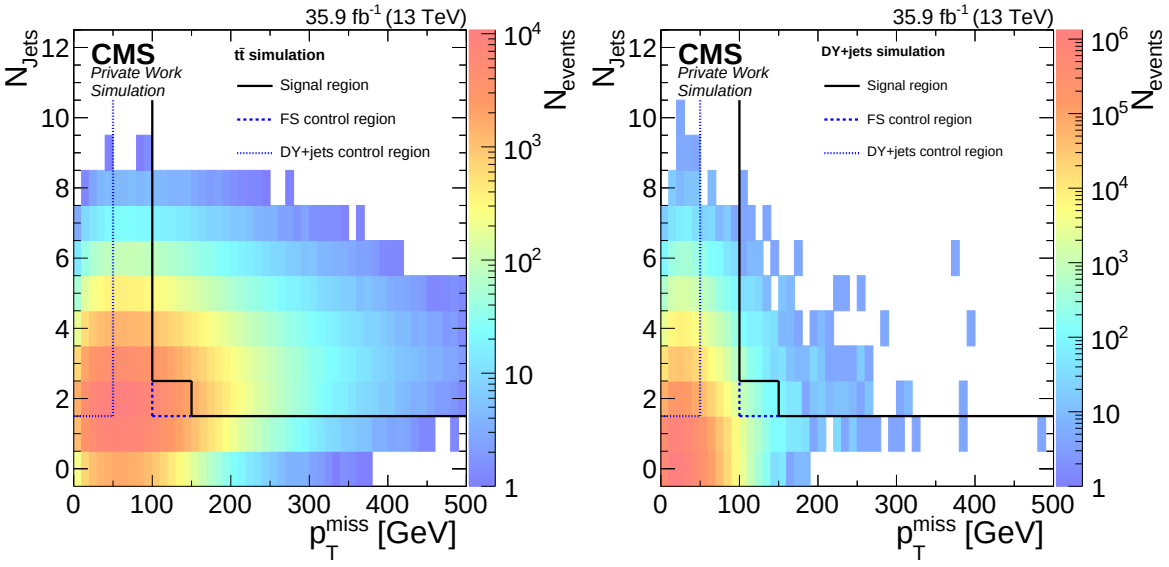

Figure 5.1: Distribution of backgrounds events with SF leptons in the $p_{\mathrm{T}}^{\mathrm{miss}}$-$N_{\mathrm{Jets}}$ plane for $\mathrm{t\bar{t}}$ (left) and DY+jets (right) events from simulation. The events are weighted according to the cross section of the process and the size of the generated event sample, assuming an integrated luminosity of $35.9\,\mathrm{fb}^{-1}$. The signal and control regions defined in the plane are indicated by lines.

signal region. Even after this requirement, the number of DY+jets events is still sufficient for the purpose of this analysis and about 2 orders of magnitude larger than the number of events from $\mathrm{t\bar{t}}$ production. Top quark pair production dominates at medium values of N_{Jets} and $p_{\mathrm{T}}^{\mathrm{miss}}$. To achieve a sufficient suppression of DY+jets events and to be close to the signal region, the control region for flavor-symmetric backgrounds requires exactly two jets and $100 < p_{\mathrm{T}}^{\mathrm{miss}} < 150\,\mathrm{GeV}$.

The signal region in the 8 TeV analysis was further subdivided into three regions in $m_{\ell\ell}$ and two selections depending on the $|\eta|$ values of the two leptons [5, 6]. The deviation of about 2.5 standard deviations was observed in the signal bin with $20 < m_{\ell\ell} < 70\,\mathrm{GeV}$ and $|\eta| < 1.4$ for both leptons. Since none of the other signal bins showed any significant deviation in the 8 TeV analysis or in the results with 13 TeV data taken in 2015 [7] they are not considered here. A summary of the requirements in the control regions and the 8 TeV signal region is given in Tab. 5.1.

5.2 Background estimation

While it is possible to get a good prediction of the data from the simulation of these processes for most of the phase space, the simulation might not be so accurate in more extreme phase space regions. Furthermore, using the simulation for the description of the background introduces a number of uncertainties in the modeling of both the physical process itself and the detector response. Therefore, most of the background processes are estimated from data to achieve a higher precision.

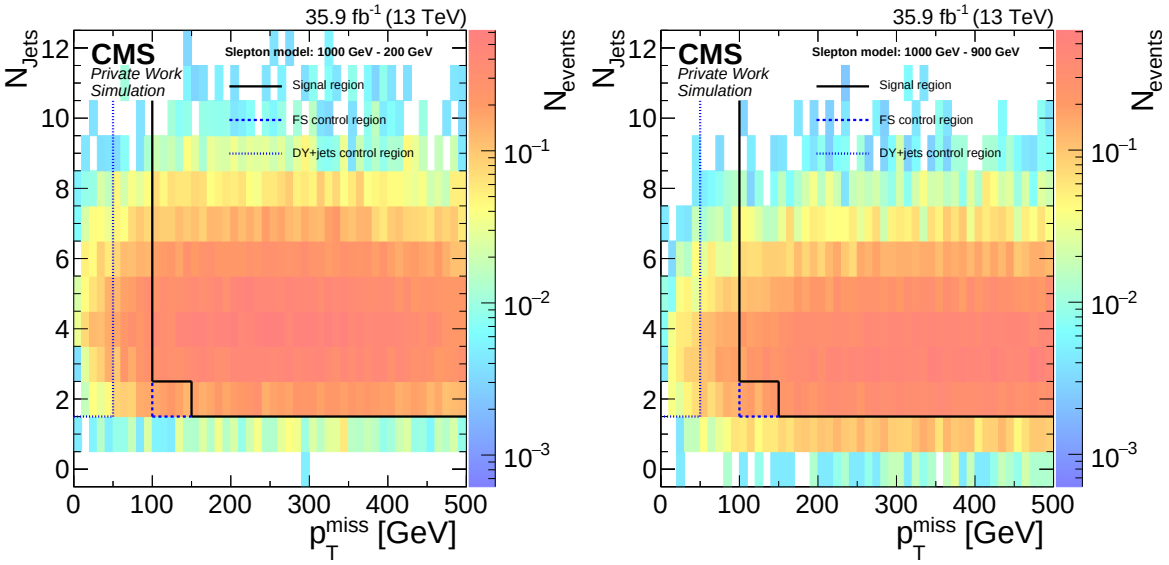

Figure 5.2: Distribution of signal events with SF leptons in the $p_{\mathrm{T}}^{\mathrm{miss}}$-$N_{\mathrm{Jets}}$ plane for points of the slepton model with $m_{\tilde{b}} = 1000\,\mathrm{GeV}$ and $m_{\tilde{\chi}_2^0} = 200\,\mathrm{GeV}$ (left) or $m_{\tilde{\chi}_2^0} = 900\,\mathrm{GeV}$ (right). The events are weighted according to the cross section and the size of the generated event sample, assuming an integrated luminosity of $35.9\,\mathrm{fb}^{-1}$. The signal and control regions defined in the plane are indicated by lines.

Region	Selection
DY+jets control region	Inclusive dilepton selection $N_{\mathrm{Jets}} \geq 2$ $p_{\mathrm{T}}^{\mathrm{miss}} < 50\,\mathrm{GeV}$
Flavor-symmetric control region	Inclusive dilepton selection $N_{\mathrm{Jets}} = 2$ $100 < p_{\mathrm{T}}^{\mathrm{miss}} < 150\,\mathrm{GeV}$
8 TeV signal region	Inclusive dilepton selection both leptons $\lvert\eta\rvert < 1.4$ $\Delta R(\ell\ell) > 0.3$, $20 < m_{\ell\ell} < 70\,\mathrm{GeV}$ $N_{\mathrm{Jets}} \geq 2$ and $p_{\mathrm{T}}^{\mathrm{miss}} > 150\,\mathrm{GeV}$ or $N_{\mathrm{Jets}} \geq 3$ and $p_{\mathrm{T}}^{\mathrm{miss}} > 100\,\mathrm{GeV}$

Table 5.1: Summary of the control regions and the 8 TeV signal region. The requirements on N_{Jets} and $p_{\mathrm{T}}^{\mathrm{miss}}$ in the control and signal regions are applied on top of the inclusive dilepton selection defined in Tab. 4.4.

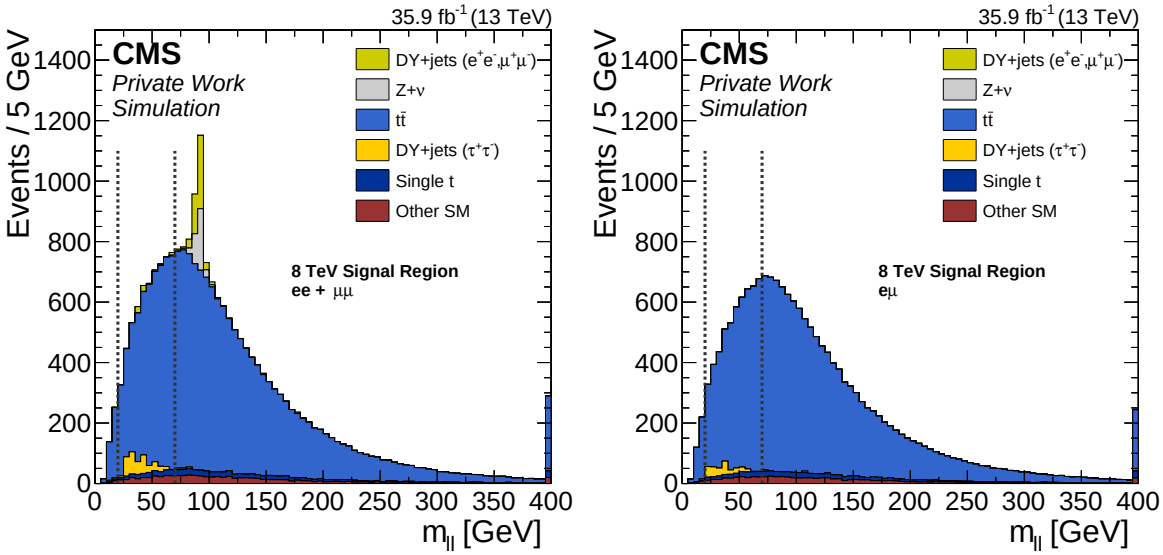

Figure 5.3: Distribution of $m_{\ell\ell}$ in SM simulation in the 8 TeV signal region omitting the $m_{\ell\ell}$ requirement. The left plot shows the distribution of SF events while DF events are displayed in the right plot. The simulation is normalized to an integrated luminosity of 35.9 fb^{-1}. The mass bin used in the signal region definition is indicated by dashed lines.

Figure 5.3 shows the $m_{\ell\ell}$ distribution in SM simulation for the 8 TeV signal region (left) and the corresponding control sample of different flavor events (right). The requirements on the mass are indicated by dashed lines. Top quark pair production accounts for most of the SM background in this selection and the DF sample can be used to predict the contribution from $\text{t}\bar{\text{t}}$ and other flavor symmetric processes like the associated production of a top quark and a W boson or the decay of a Z/γ^* into two τ leptons. While these processes produce SF and DF lepton pairs with the same abundance, the detector response and the ability to trigger, reconstruct, and identify these events differ slightly. Correction factors need to be derived to account for these differences to obtain a prediction of the SF data from the DF sample.

Non-flavor symmetric are mainly processes that contain the decay of a Z/γ^* boson into a dilepton pair. These processes can further be subdivided in those that produce a lepton pair and jets but contain no genuine $p_{\text{T}}^{\text{miss}}$ from neutrinos, labeled as DY+jets, and those with prompt neutrinos in addition to the Z/γ^* boson, labeled as Z+ν.

5.2.1 Flavor-symmetric background estimation

The flavor-symmetric background estimation accounts for all SM processes that produce SF and DF lepton pairs symmetrically, which allows to use the DF event yield for the prediction of the number of SF events. The contributing processes have been discussed in Sections 2.4 and 5.2. An additional contribution originates from non-prompt leptons, as will be discussed later.

Due to the mass difference between electron and muon, decays of a τ lepton slightly favor de-

cays into electrons. The ratio of branching fractions of decays into $\mu+\nu$ and $e+\nu$ has been measured to be $\frac{\mathrm{BF}(\tau \to \mu+2\nu)}{\mathrm{BF}(\tau \to \mathrm{e}+2\nu)} = 0.9762 \pm 0.028$ [20]. In contrast to this, no deviation of the flavor-symmetry has been observed in the decays of the W boson $\frac{\mathrm{BF}(\mathrm{W} \to \mu+\nu)}{\mathrm{BF}(\mathrm{W} \to \mathrm{e}+\nu)} = 0.991 \pm 0.018$ [20]. Since backgrounds including τ leptons are subdominant compared to the contribution from W boson decays and the deviation from unity is small, these backgrounds are considered flavor-symmetric on particle level.

Deviations from the flavor-symmetry can be introduced if the efficiencies to trigger, reconstruct, and identify electrons and muons with the CMS experiment differ. Therefore, the number of events in the DF sample cannot be used as a prediction directly but needs to be corrected for the differences in efficiencies. A multiplicative correction $R_{\mathrm{SF/DF}}$ is applied to the DF yield N_{DF}:

$$N_{SF}^{\mathrm{pred}} = R_{SF/DF} \cdot N_{DF}. \tag{5.1}$$

Two independent methods are used to derive $R_{\mathrm{SF/DF}}$ on data. The first approach is a direct measurement of the ratio of SF to DF events in the flavor-symmetric control region defined in Section 5.1, while the second method is a factorized approach that uses the lepton trigger efficiencies as well as the efficiencies to reconstruct and select the leptons to determine $R_{\mathrm{SF/DF}}$.

In principle, $R_{\mathrm{SF/DF}}$ can depend on the lepton or event kinematics. As was mentioned in Section 4.3.2, the correction factor is estimated separately for events with both leptons reconstructed within $|\eta| < 1.4$, called central, and those with at least one lepton with $|\eta| > 1.6$, labeled forward. One ingredient of the factorization method shows an additional dependency on the lepton p_{T}, which motivates the usage of a parameterization of this factor with respect to the p_{T} of the trailing lepton and thereby makes a correction on an event-by-event basis necessary.

Direct measurement of $R_{\mathrm{SF/DF}}$

The flavor-symmetric control region is used to estimate $R_{\mathrm{SF/DF}}$ directly from data by measuring the number of SF and DF events in a part of the phase space that is dominated by $\mathrm{t\bar{t}}$ events. To reduce the number of DY events even further and thereby increase the flavor-symmetry, dilepton masses around the Z boson mass from 70 to 110 GeV are excluded.

Table 5.2 summarizes the obtained SF and DF event yields and the values for $R_{\mathrm{SF/DF}}$ in the central and forward selection. Data and simulation agree within 2%. The extrapolation into the signal region is tested in simulation by determining $R_{\mathrm{SF/DF}}$ in the 8 TeV signal region as well and calculating the ratio to the value obtained in the control region. The obtained ratios agree with unity within 1%. The difference between the values obtained in the central and forward selection of approximately 5% justifies the use of separate correction factors.

The dependency of $R_{\mathrm{SF/DF}}$ on properties of the lepton pair and other relevant observables is studied on data and simulation. Figure 5.4 shows the ratio of SF to DF events in the central lepton selection as a function of $m_{\ell\ell}$, the p_{T} of the higher and lower energetic lepton, jet multiplicity, $p_{\mathrm{T}}^{\mathrm{miss}}$, and $\mathrm{M_{T2}}$. Since the control and signal region are defined in terms of jet multiplicity and p_{T}^{miss}, the corresponding plots show data points only within the boundaries of the control region while the ratio estimated from MC is shown for the full range. Dashed

	N_{SF}	N_{DF}	$R_{SF/DF} \pm \sigma_{stat}$	SR / CR $\pm\sigma_{stat}$
	Central			
Data	9242	8464	1.092±0.016	–
MC	9112.2	8463.5	1.077±0.006	1.006±0.006
	Forward			
Data	4196	3674	1.142±0.026	–
MC	4226.0	3767.8	1.122±0.010	1.006±0.009

Table 5.2: Observed event yields in the control region for flavor-symmetric backgrounds and the resulting values of $R_{SF/DF}$. The results are shown separately for the central and forward lepton selection and the same quantities derived on simulation are shown for comparison. For simulation, the ratio between the values of $R_{\mathrm{SF/DF}}$ in the 8 TeV signal region to the flavor-symmetric control region is shown as well.

lines indicate the boundaries of the control region and the excluded $m_{\ell\ell}$ window. The distributions in data show some fluctuations due to limited statistics in the control region. Neither distributions in data nor in MC exhibit strong trends and a systematic uncertainty of 4% is assigned to cover a possible small dependency in the jet multiplicity observed in MC as well as the discrepancy between the values obtained in data and MC. The corresponding figure for the forward selection can be found in Appendix C. The number of events in the forward region is smaller than in the central lepton selection, but no clear trends can be observed in data or simulation and the same systematic uncertainty is assigned.

Factorization method

Distortions of the flavor symmetry in measurements of flavor-symmetric backgrounds can be introduced by different efficiencies to trigger, reconstruct, and select leptons. Measurements of these efficiencies can therefore be used to determine $R_{\mathrm{SF/DF}}$.

The following naming convention is used here: ϵ_ℓ and $\epsilon_{\ell\ell}$ indicate a single lepton and dilepton efficiency, respectively. If no upper index is used, the quantity includes all efficiencies (trigger, selection, and reconstruction). In contrast to this, $\epsilon^{\mathrm{T}}_{\ell\ell}$ denotes a dilepton trigger efficiency and a "*" indicates that only reconstruction and selection efficiencies are included, while the index "hard" stands for the quantity on particle level. Furthermore, the assumption is made that the correlation between the efficiencies of the two leptons in an event is negligible and the dilepton efficiency can be factorized, i.e. $\epsilon_{\ell\ell} \approx \epsilon_\ell \cdot \epsilon_\ell$.

For processes that produce the same number of dielectron and dimuon events on particle level, the efficiency ratio

$$r_{\mu/e} = \frac{\epsilon_\mu}{\epsilon_e} \approx \sqrt{\frac{\epsilon_{\mu\mu}}{\epsilon_{ee}}} = \sqrt{\frac{N_{\mu\mu}}{N_{ee}}} \tag{5.2}$$

can be determined by measuring the number of ee and $\mu\mu$ events. $r_{\mu/e}$ can be rewritten as:

$$r_{\mu/e} \approx \sqrt{\frac{\epsilon_{\mu\mu}}{\epsilon_{ee}}} = \sqrt{\frac{\epsilon^*_{\mu\mu}\epsilon^{\mathrm{T}}_{\mu\mu}}{\epsilon^*_{ee}\epsilon^{\mathrm{T}}_{ee}}} \approx \frac{\epsilon^*_\mu}{\epsilon^*_e}\sqrt{\frac{\epsilon^{\mathrm{T}}_{\mu\mu}}{\epsilon^{\mathrm{T}}_{ee}}} = r^*_{\mu/e}\sqrt{\frac{\epsilon^{\mathrm{T}}_{\mu\mu}}{\epsilon^{\mathrm{T}}_{ee}}} \tag{5.3}$$

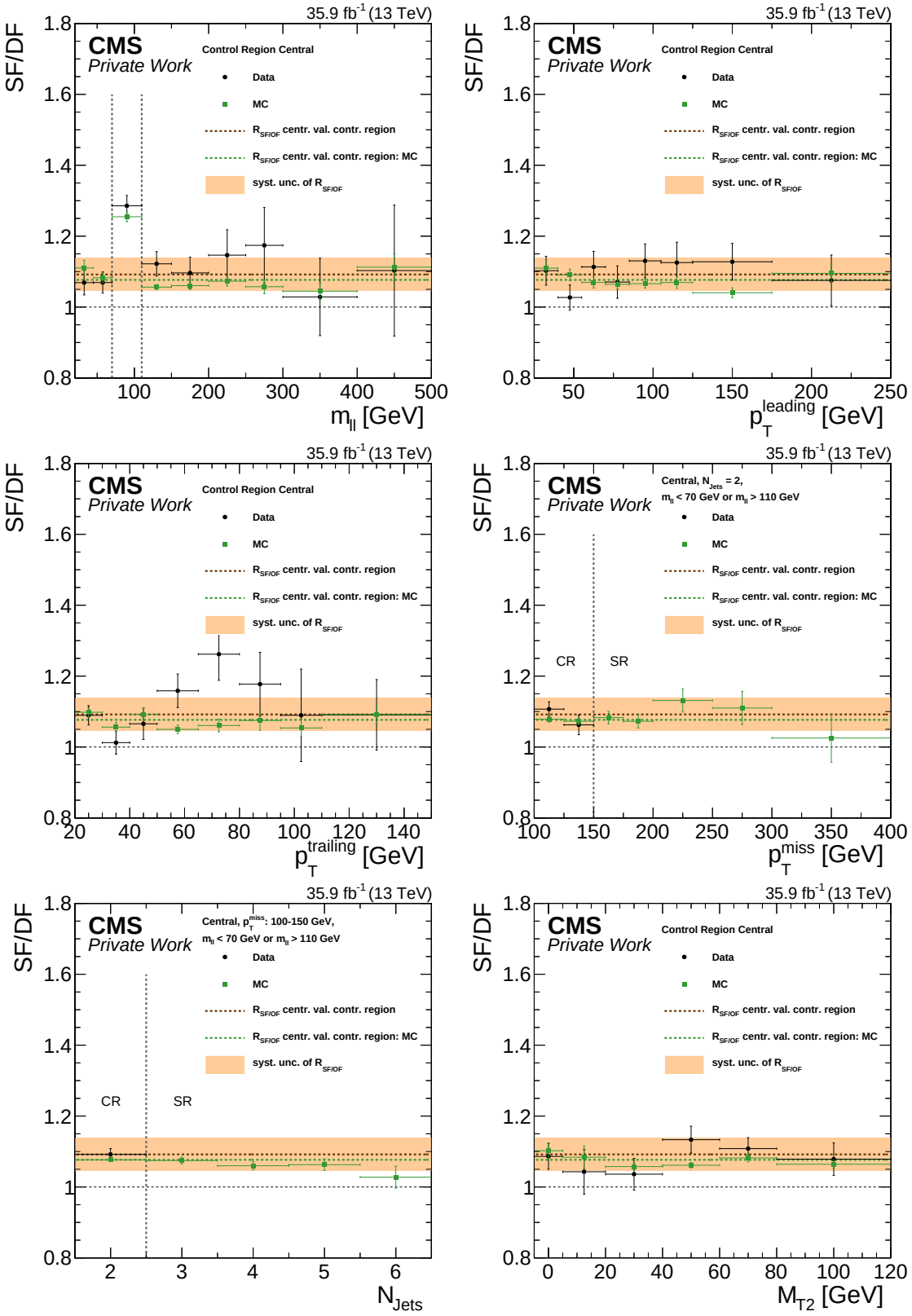

Figure 5.4: $R_{\mathrm{SF/DF}}$ as a function of $m_{\ell\ell}$ (top left), leading lepton p_{T} (top right), subleading lepton p_{T} (center left), jet multiplicity (center right), $p_{\mathrm{T}}^{\mathrm{miss}}$ (bottom left), and $\mathrm{M_{T2}}$ (bottom right) in the flavor-symmetric control region for the central lepton selection for data and simulation. Dashed gray lines indicate the boundaries of the flavor symmetric control region and the excluded mass window. The assigned systematic uncertainty of 4% is indicated as an orange band.

and be used to predict the dielectron and dimuon event yield from the number of observed $e\mu$ events:

$$N_{ee}^{\text{pred}} = \epsilon_{ee}^{\text{T}} N_{ee}^{*} \approx \epsilon_{ee}^{\text{T}} \left(\epsilon_{e}^{*}\right)^{2} N_{ee}^{\text{hard}} = \frac{1}{2}\epsilon_{ee}^{\text{T}} \left(\epsilon_{e}^{*}\right)^{2} N_{DF}^{\text{hard}} = \frac{1}{2}\epsilon_{ee}^{\text{T}} \frac{\epsilon_{e}^{*}}{\epsilon_{\mu}^{*}} N_{DF}^{*} \tag{5.4}$$
$$= \frac{1}{2}\frac{1}{r_{\mu/e}^{*}} \frac{\epsilon_{ee}^{\text{T}}}{\epsilon_{e\mu}^{\text{T}}} N_{DF} = \frac{1}{2}\frac{1}{r_{\mu/e}} \frac{\sqrt{\epsilon_{ee}^{\text{T}}\epsilon_{\mu\mu}^{\text{T}}}}{\epsilon_{e\mu}^{\text{T}}} N_{DF}$$

and

$$N_{\mu\mu}^{\text{pred}} = \epsilon_{\mu\mu}^{\text{T}} N_{\mu\mu}^{*} \approx \epsilon_{\mu\mu}^{\text{T}} \left(\epsilon_{\mu}^{*}\right)^{2} N_{\mu\mu}^{\text{hard}} = \frac{1}{2}\epsilon_{\mu\mu}^{\text{T}} \left(\epsilon_{\mu}^{*}\right)^{2} N_{DF}^{\text{hard}} = \frac{1}{2}\epsilon_{\mu\mu}^{\text{T}} \frac{\epsilon_{\mu}^{*}}{\epsilon_{e}^{*}} N_{DF}^{*} \tag{5.5}$$
$$= \frac{1}{2} r_{\mu/e}^{*} \frac{\epsilon_{\mu\mu}^{\text{T}}}{\epsilon_{e\mu}^{\text{T}}} N_{DF} = \frac{1}{2} r_{\mu/e} \frac{\sqrt{\epsilon_{ee}^{\text{T}}\epsilon_{\mu\mu}^{\text{T}}}}{\epsilon_{e\mu}^{\text{T}}} N_{DF}.$$

The combined prediction for the number of SF events is given by

$$N_{SF}^{\text{pred}} = N_{\mu\mu}^{\text{pred}} + N_{ee}^{\text{pred}} = \frac{1}{2}\left(r_{\mu/e} + \frac{1}{r_{\mu/e}}\right) \frac{\sqrt{\epsilon_{ee}^{\text{T}}\epsilon_{\mu\mu}^{\text{T}}}}{\epsilon_{e\mu}^{\text{T}}} N_{DF}. \tag{5.6}$$

Abbreviating the factor including the trigger efficiencies as

$$R_{\text{T}} = \frac{\sqrt{\epsilon_{ee}^{\text{T}}\epsilon_{\mu\mu}^{\text{T}}}}{\epsilon_{e\mu}^{\text{T}}} \tag{5.7}$$

and comparing Equation 5.6 to Equation 5.1, $R_{\text{SF/DF}}$ can be identified as

$$R_{\text{SF/DF}} = \frac{1}{2}\left(r_{\mu/e} + \frac{1}{r_{\mu/e}}\right) R_{\text{T}}. \tag{5.8}$$

Measurement of R_{T}

A data sample collected with H_{T} triggers (see Section 4.1.1 and Appendix A.1) is used to measure the dilepton trigger efficiencies. All triggers except for the one with the highest threshold are prescaled. Events containing a lepton pair with the flavor combination of interest are selected. The H_{T} definition on trigger level is different from the one on analysis level and in general more inclusive, taking lower energetic jets and in some cases energy deposits from leptons into account. Events are required to have $H_{\text{T}} > 200\,\text{GeV}$ on analysis level to make sure that the events are well reconstructed and that their properties do not differ too much between trigger and analysis level. Furthermore, events with $N_{\text{Jets}} \geq 2$ and $p_{\text{T}}^{\text{miss}} > 100\,\text{GeV}$ are rejected to determine R_{T} in a region that is orthogonal to the signal region and the flavor-symmetric control region, resulting in a statistical independence of the two background prediction methods. In general, the offline lepton selection has stricter requirements than the selection applied by the HLT. Therefore, the triggers should have accepted all events fulfilling

the dilepton selection requirements. An exception are the non-isolated dilepton triggers, which have lepton p_{T} thresholds of 27–33 GeV. These additional triggers are included to increase the sensitivity to leptons pairs from decays of boosted particles. Such leptons have a high momentum and small spatial separation which might cause the isolated triggers to fail since those do not feature the p_{T} dependent isolation cone size that recovers such events in the offline selection. At low lepton momentum ($p_{\mathrm{T}} < 40$ GeV) nearly all events that are triggered by the non-isolated triggers and fulfill the offline selection are triggered by the isolated triggers as well.

The trigger efficiency is defined as the fraction of selected events in the H_{T} triggered sample that is also accepted by a dilepton trigger:

$$\epsilon^{\mathrm{T}}_{\ell\ell} = \frac{N_{\mathrm{events}}\left(H_{\mathrm{T}}\text{ trigger} \cap \ell\ell\text{ selection} \cap \ell\ell\text{ trigger}\right)}{N_{\mathrm{events}}\left(H_{\mathrm{T}}\text{ trigger} \cap \ell\ell\text{ selection}\right)}. \tag{5.9}$$

In all cases, a combination of several dilepton triggers is used, since different triggers were active at different instantaneous luminosity or data taking periods. Therefore, the combined efficiency is measured by requiring any trigger for a certain flavor combination. On simulation, the H_{T} triggers are not prescaled, which allows for an increased statistics to measure the efficiencies much more precisely.

Figure 5.5 shows the trigger efficiencies for the three lepton flavor combinations as a function of the p_{T} of the leading and trailing lepton for data and for simulation. The events are not split into the central and forward lepton selection, since the effects are similar in both categories. The dielectron triggers show turn-on effects up to 50(40) GeV for the leading(trailing) lepton. A similar, although somewhat weaker, trend can be observed for DF lepton pairs, while the dimuon triggers are fully efficient above 30 GeV. These broad turn-ons in electron trigger and identification efficiencies are known effects [96], which need to be taken into account in the analysis design. In principle, it would be desirable only to use leptons with p_{T} above the end of the turn-ons. This is not feasible and actually not necessary in this analysis for several reasons:

- The 8 TeV analysis used thresholds of $p_{\mathrm{T}} > 20$ GeV for both leptons. Increasing this to 40–50 GeV would change the event kinematics and reduce the statistical precision significantly. For thresholds of 50(40) GeV for the leading(subleading) lepton about 85% of the events in the $m_{\ell\ell}$ range of 20–70 GeV, used in the 8 TeV signal region, would be rejected and even above the Z boson mass peak more than 30% of the events would be discarded.
- Asymmetric thresholds with lower requirements for dimuon events could recover some of these events but would disturb the flavor-symmetry and thereby make the prediction of flavor-symmetric background processes more difficult and less precise.
- A parameterization of turn-on effects can be used to regain sensitivity. This is done in case of $r_{\mu/e}$, as will be discussed later on. For R_{T} and the direct measurement of $R_{\mathrm{SF/DF}}$ such a parameterization is not necessary since for both ratios nominator (ee events) and denominator ($e\mu$ events) are affected and most of the effect cancels.

The resulting efficiencies are summarized in Tab. 5.3. In the dielectron case, data and simulation are in good agreement with trigger efficiencies of approximately 96% in both lepton

Central

	Data			MC		
	nominator	denominator	$\epsilon^{\mathrm{T}}_{\ell\ell} \pm \sigma_{stat}$	nominator	denominator	$\epsilon^{\mathrm{T}}_{\ell\ell} \pm \sigma_{stat}$
ee	9313	9708	0.959±0.002	77222	80370	0.961±0.001
$\mu\mu$	6163	6467	0.953±0.003	123007	125833	0.978±0.001
eμ	1855	2036	0.911±0.007	30268	32303	0.937±0.001
R_T		1.049±0.042			1.034±0.040	

Forward

	Data			MC		
	nominator	denominator	$\epsilon^{\mathrm{T}}_{\ell\ell} \pm \sigma_{stat}$	nominator	denominator	$\epsilon^{\mathrm{T}}_{\ell\ell} \pm \sigma_{stat}$
ee	2757	2876	0.959±0.004	34348	36003	0.954±0.002
$\mu\mu$	2578	2763	0.933±0.005	66474	68246	0.974±0.001
eμ	582	654	0.890±0.014	12100	13362	0.906±0.001
R_T		1.063±0.060			1.065±0.056	

Table 5.3: Trigger efficiencies in the central and forward selection on data measured using H_{T} baseline triggers. Results on simulation without any baseline trigger requirement are shown for comparison.

selections. The obtained agreement between data and simulation is worse for the other two lepton flavor combinations. In these cases, the efficiencies in simulation are 2–4% higher than those measured in data and the efficiencies in data, ranging from 89 to 95%, are lower than in the dielectron sample. A systematic uncertainty of 3(4)% is assigned to each trigger efficiency in the central(forward) selection, which corresponds to the maximally observed deviation between data and simulation. The systematic uncertainties in the trigger efficiencies are propagated to R_{T} and are added in quadrature to the statistical uncertainties. The obtained values for R_{T} are 1.049 ± 0.042 for central leptons and 1.063 ± 0.60 in the forward selection and agree with those estimated from simulation within 2%.

Figure 5.6 shows R_{T} as a function of several important observables in the central selection. A small dependency on the lepton p_{T} remains, which also influences the $m_{\ell\ell}$ distribution since in general low values of $m_{\ell\ell}$ correspond to low lepton momenta. These dependencies are fully covered by the systematic uncertainty, however, and no trends are observed in the jet multiplicity, $p_{\mathrm{T}}^{\mathrm{miss}}$, or $\mathrm{M_{T2}}$. The corresponding studies in the forward selection can be found in Appendix D.

Measurement of $r_{\mu/e}$

To measure $r_{\mu/e}$ to a high precision, a process is required that produces a large number of dielectron and dimuon events with the same abundance on particle level. The Drell-Yan process is the ideal production mechanism for this purpose. Therefore, $r_{\mu/e}$ is measured on the Z boson mass peak, requiring $60 < m_{\ell\ell} < 120\,\mathrm{GeV}$, in the DY+jets control region, defined in Section 5.1. As can be observed in Fig. 5.7, DY+jets is by far the dominant process in this selection. A good agreement between data and simulation is obtained for both lepton flavors, indicating that this kinematic region is well described by the CMS simulation.

Figure 5.8 shows $r_{\mu/e}$ as a function of the p_{T} of the leading and subleading lepton, as well as the invariant mass and p_{T} of the dilepton system. A significant dependency of $r_{\mu/e}$ on the lepton

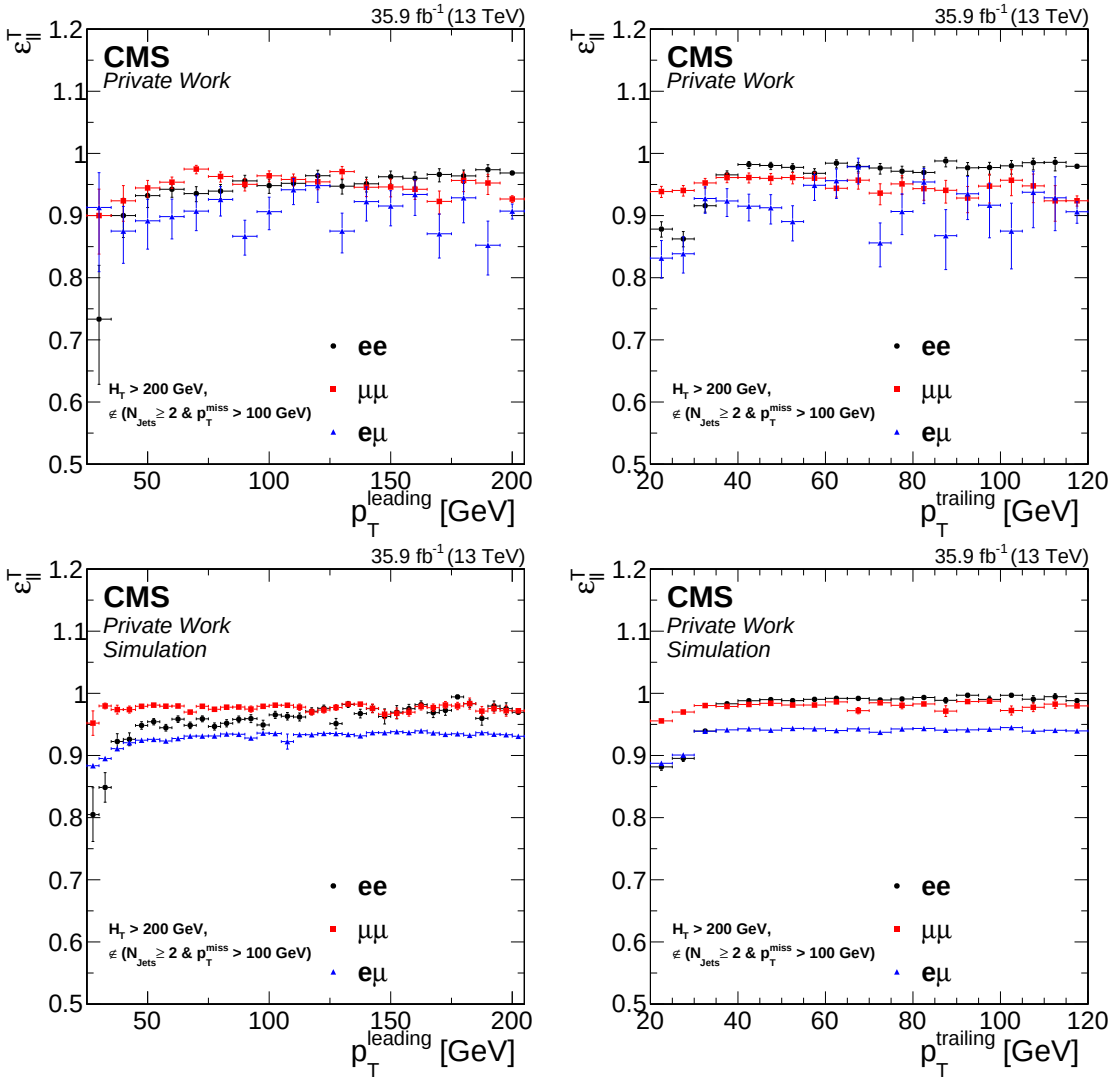

Figure 5.5: Trigger efficiencies as a function of the leading lepton p_{T} (left) and subleading lepton p_{T} (right) for data (top) and simulation (bottom). The efficiencies for ee, $\mu\mu$, and $e\mu$ events are shown as black dots, red squares, and blue triangles, respectively.

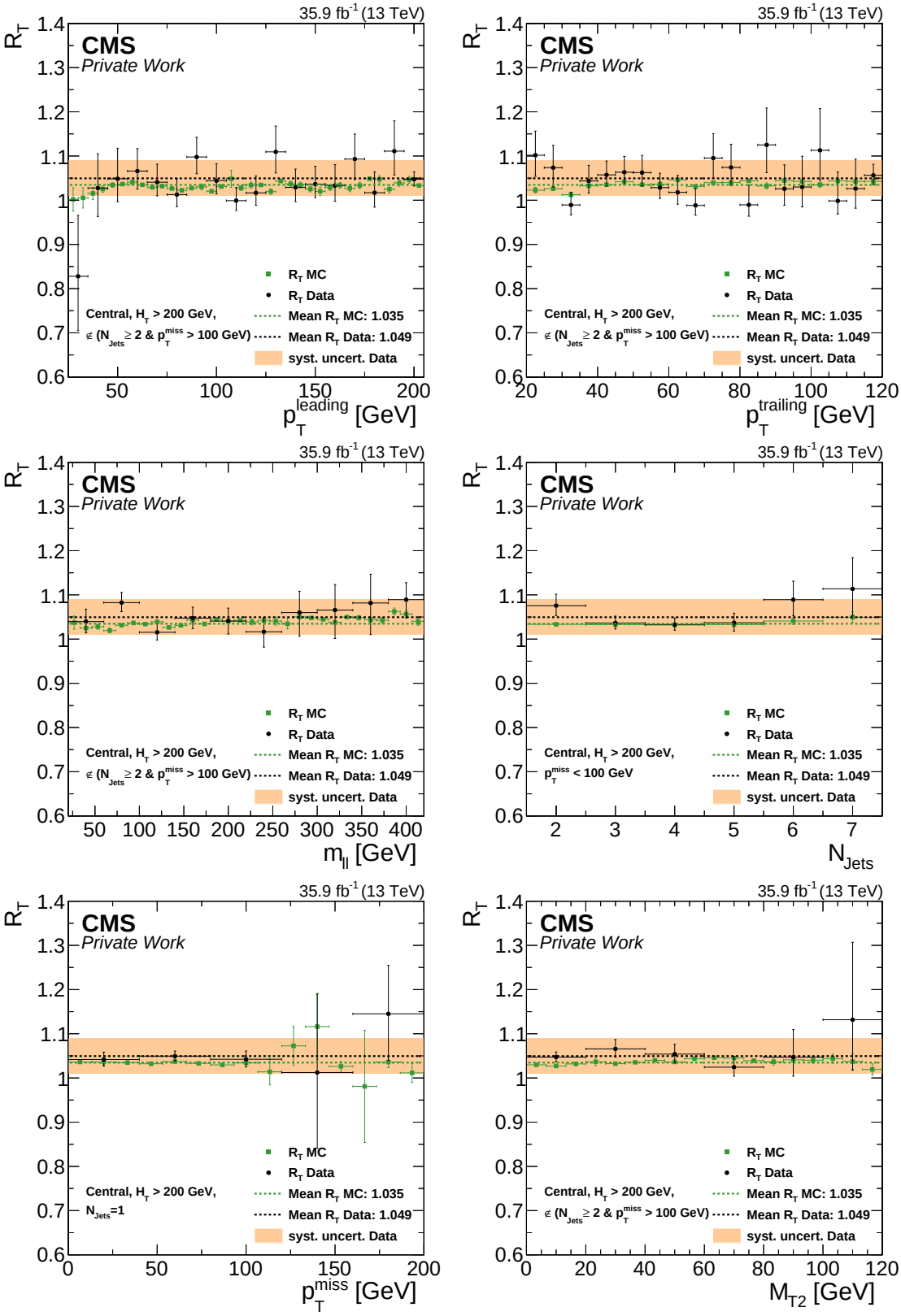

Figure 5.6: R_{T} as a function of leading lepton p_{T} (top left), subleading lepton p_{T} (top right), $m_{\ell\ell}$ (center left), jet multiplicity (center right), $p_{\mathrm{T}}^{\mathrm{miss}}$ (bottom left), and $\mathrm{M_{T2}}$ (bottom right) for the central lepton selection in data (black) and simulation (green). The central value obtained in data (simulation) is shown as a black (green) dashed line, while the systematic uncertainty of approximately 4% is indicated as an orange band around the central value in data.

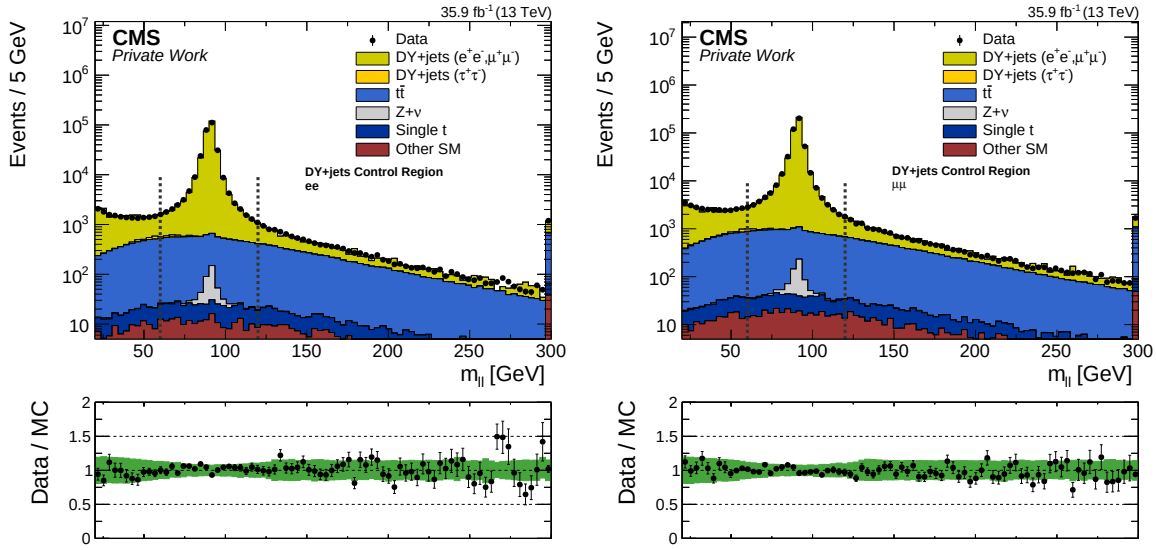

Figure 5.7: Distribution of $m_{\ell\ell}$ for dielectron events (left) and dimuon events (right) in the DY+jets control region. The data are shown as black points, while the simulation of SM processes is displayed as a stacked histogram. Dashed lines indicate the $m_{\ell\ell}$ range used in the determination of $r_{\mu/e}$.

	Central		Forward	
	$r^{c}_{\mu/e}$	$r^{p_\mathrm{T}}_{\mu/e}$ [GeV]	$r^{c}_{\mu/e}$	$r^{p_\mathrm{T}}_{\mu/e}$ [GeV]
Data	1.117±0.006	4.57±0.19	1.230±0.009	4.81±0.30
MC	1.144±0.012	4.43±0.43	1.231±0.020	5.18±0.65

Table 5.4: Result of the fit of $r_{\mu/e}$ as a function of $p_\mathrm{T}^{\text{trailing}}$ in the DY+jets control region. The fit parameters are given separately for the central and forward lepton selection and the same quantities derived from simulation are shown for comparison. Only the statistical uncertainties in the fit parameters are given.

p_T is observed, which also affects observables correlated to the lepton momenta like $m_{\ell\ell}$. The effect is present in data and simulation. Studies on simulation, given in Appendix E, indicate that the trend is mainly caused by differences in the trigger and identification efficiencies between electrons and muons at low p_T, while the asymmetric isolation requirements (see Section 4.3.2) have an additional small impact. The same trend is observed in the forward selection and the corresponding studies are shown in Appendix E as well. To account for this effect, a parameterization of $r_{\mu/e}$ as a function of the trailing lepton p_T is introduced:

$$r_{\mu/e} = r_{\mu/e}\left(p_\mathrm{T}^{\text{trailing}}\right) = r^{c}_{\mu/e} + \frac{r^{p_\mathrm{T}}_{\mu/e}}{p_\mathrm{T}^{\text{trailing}}}. \tag{5.10}$$

The parameters $r^{c}_{\mu/e}$ and $r^{p_\mathrm{T}}_{\mu/e}$ are determined by a fit to data, which is shown in the top right plot of Fig. 5.8. Table 5.4 summarizes the obtained factors for data and simulation in the central and forward lepton selection.

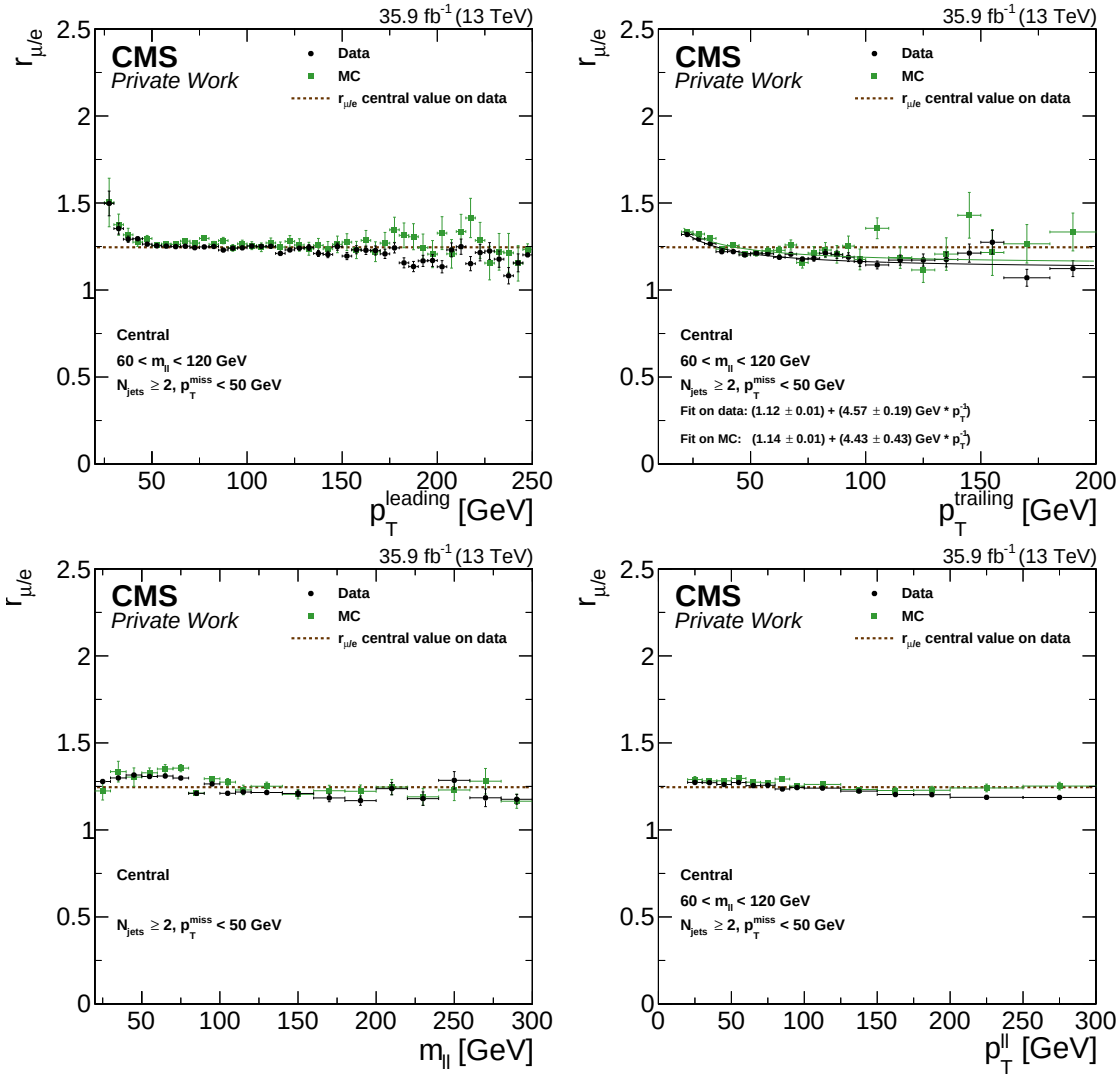

Figure 5.8: $r_{\mu/e}$ as a function of the p_{T} of the leading (top left) and trailing lepton (top right) and the invariant mass (bottom left) and p_{T} of the dilepton system (bottom right) in the central lepton selection for data and simulation. The central value indicates the $r_{\mu/e}$ value that would be used without the parameterization. The fit values of the parameterization are shown in the top right plot.

To validate the parameterization, each dielectron event is weighted by $r^2_{\mu/e}\left(p_{\mathrm{T}}^{\mathrm{trailing}}\right)$ to correct each of the electrons to a "muon efficiency level". A new ratio $r^{\mathrm{corr.}}_{\mu/e}$ is calculated by dividing the number of dimuon events by the number of reweighted dielectron events. Figure 5.9 shows this new ratio as a function of the p_{T} of the leading and trailing lepton, invariant mass and p_{T} of the dilepton system, jet multiplicity, and $p_{\mathrm{T}}^{\mathrm{miss}}$. Per definition, $r^{\mathrm{corr.}}_{\mu/e}$ is expected to be close to unity and to correct the trend in the p_{T} of the lower energetic lepton. The dependencies on the invariant mass and p_{T} of the dilepton system are reduced as well, while a small trend on the p_{T} of the higher energetic lepton remains. Since the remaining effect is mainly at very low leading lepton p_{T} and affects less than 5% of the total number of events, no attempt is made to use an additional parameterization on the p_{T} of the leading lepton. A systematic uncertainty of 10% is assigned to $r_{\mu/e}$ to account for the remaining fluctuations and dependencies with respect to the transverse lepton momenta and $m_{\ell\ell}$. This uncertainty is combined with the statistical uncertainty of the fit parameters.

The factorization method uses $0.5\left(r_{\mu/e} + 1/r_{\mu/e}\right)$ to determine $R_{\mathrm{SF/DF}}$. Because of the combination of $r_{\mu/e}$ with its inverse, any remaining dependencies and the uncertainty of the method are significantly reduced. As the measurement of $r_{\mu/e}$ is performed in a region different from the signal selection, the dependency of $0.5\left(r^{\mathrm{corr.}}_{\mu/e} + 1/r^{\mathrm{corr.}}_{\mu/e}\right)$ on several important observables is studied in Fig. 5.10 to make sure the extrapolation into the signal region does not introduce any additional trends. No such trends are observed and all deviations are well covered by the systematic uncertainty. The resulting systematic uncertainty in $R_{\mathrm{SF/DF}}$ is approximately 1% and thereby subdominant compared to the uncertainties originating from the trigger efficiencies and the systematic uncertainty assigned to the direct measurement of $R_{\mathrm{SF/DF}}$.

Combined flavor-symmetric background prediction and resulting background estimate

Because of the parameterization of $r_{\mu/e}$, the factorization method has to be applied on an event-to-event basis. No result for $R_{\mathrm{SF/DF}}$ can be given, which is valid in all signal regions. Instead, the factorization method is applied in each signal region and the obtained prediction is divided by the number of DF events to get an $R_{\mathrm{SF/DF}}$ factor for the factorization method in this region. This factor is combined with $R_{\mathrm{SF/DF}}$ from the control region method by a weighted average to obtain a single correction factor and thereby a combined flavor-symmetric background prediction for the signal region.

The number of DF events, the prediction from the factorization methods, the resulting $R_{\mathrm{SF/DF}}$ factors, and the background estimation for flavor-symmetric processes in the 8 TeV signal region are summarized in Tab. 5.5. The $R_{\mathrm{SF/DF}}$ factors obtained with the two different methods agree within approximately 1%. Since the methods are performed on independent data sets and under the assumption that their uncertainties follow a Gaussian distribution, a weighted average can be used to combine the two $R_{\mathrm{SF/DF}}$ factors. The combined prediction has a precision of about 3% and $5862 \pm 80 \pm 185$ SF events from flavor-symmetric background processes are expected in the 8 TeV signal region. Here and in the following, if the uncertainty is split into two terms, the first one accounts for the statistical uncertainty and the second

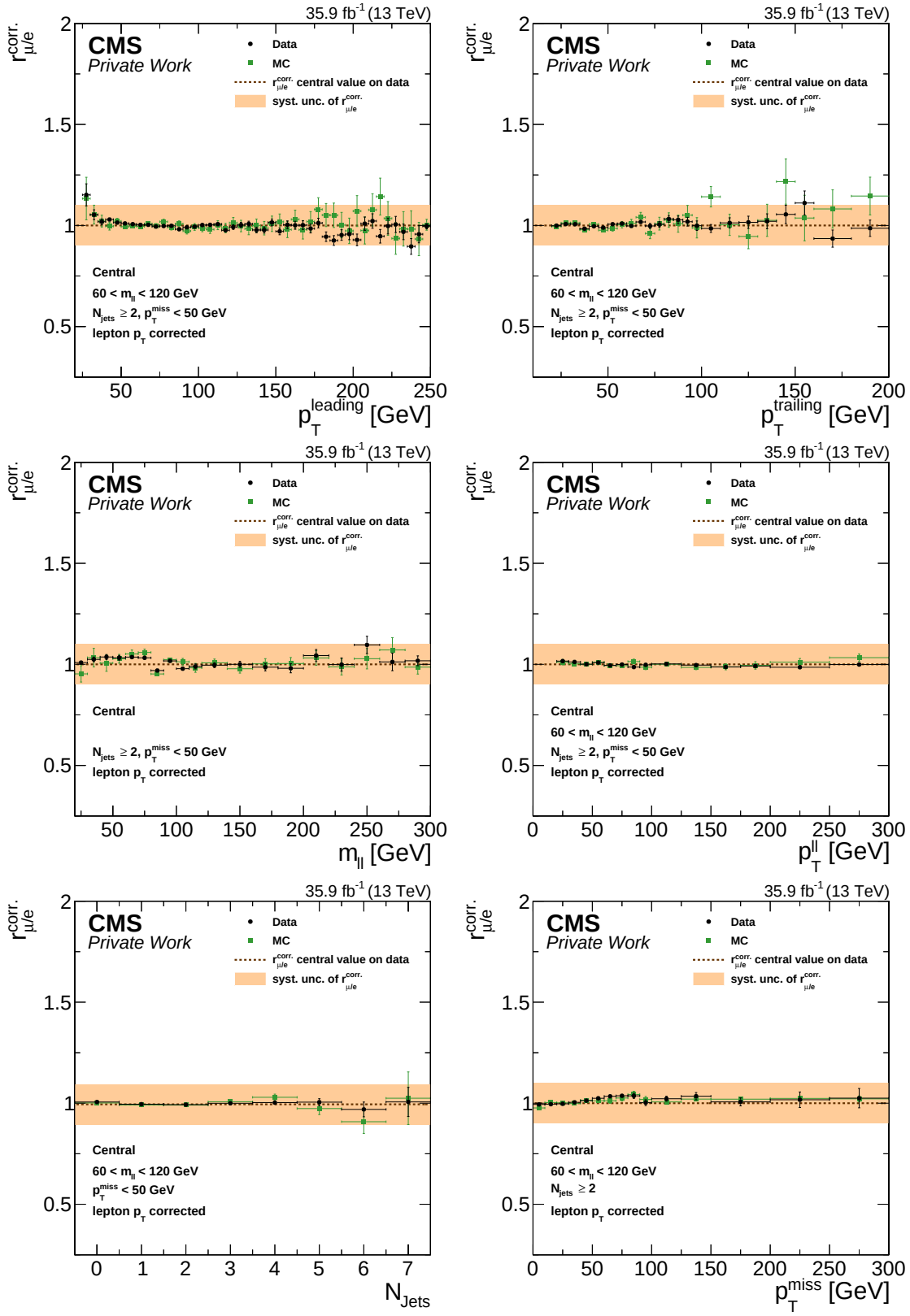

Figure 5.9: $r_{\mu/e}^{\text{corr.}}$ as a function of the p_{T} of the leading (top left) and trailing lepton (top right), invariant mass (center left) and p_{T} of the dilepton system (center right), jet multiplicity (bottom left), and $p_{\text{T}}^{\text{miss}}$ (bottom right) in the central lepton selection for data and simulation. The central value on data is indicated by a dashed line while the systematic uncertainty is shown by an orange band.

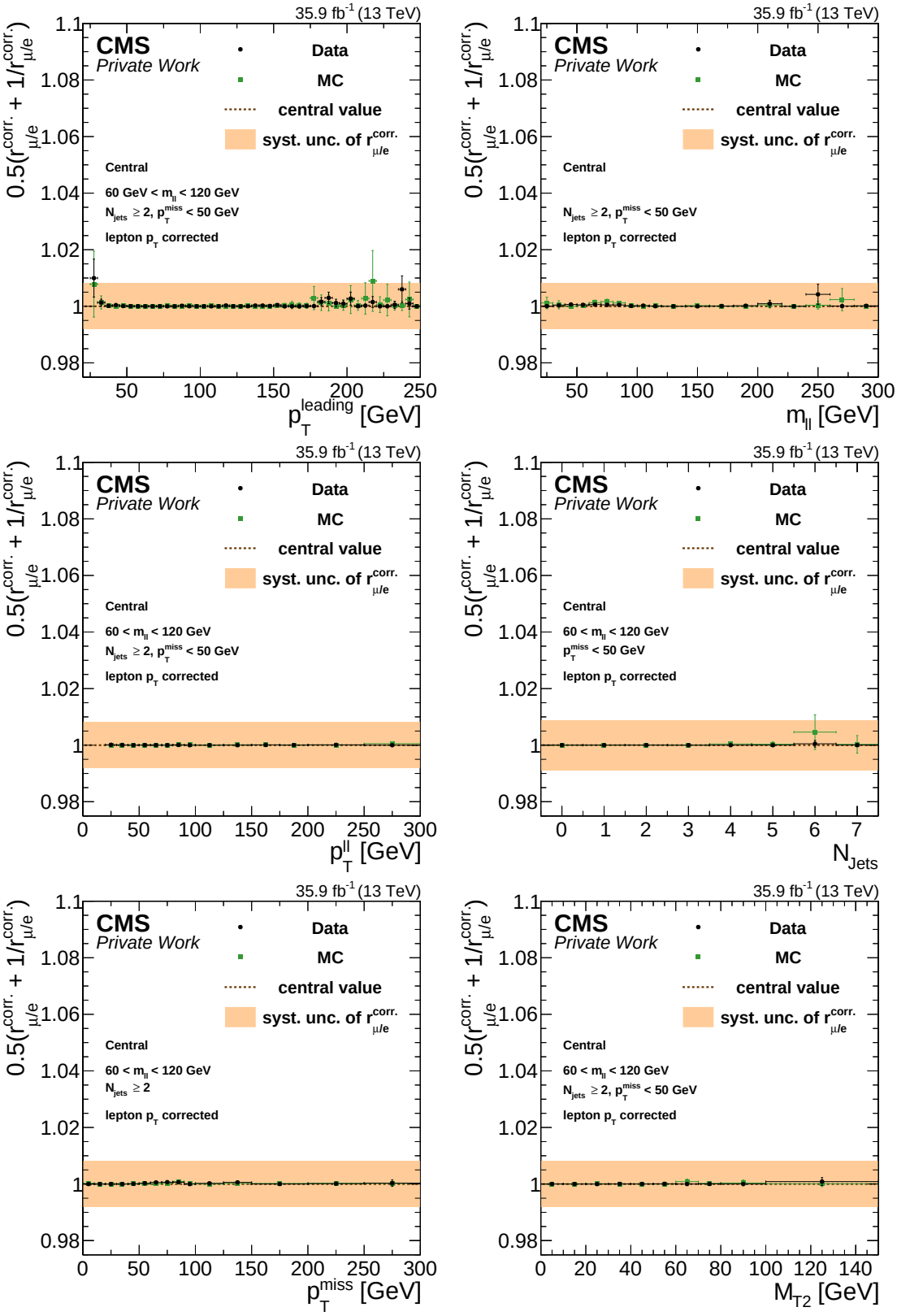

Figure 5.10: $0.5\left(r^{\text{corr.}}_{\mu/e} + 1/r^{\text{corr.}}_{\mu/e}\right)$ as a function of the leading lepton p_{T} (top left), invariant mass (top right) and p_{T} of the dilepton system (center left), jet multiplicity (center right), $p_{\text{T}}^{\text{miss}}$ (bottom left), and M_{T2} (bottom right) in the central lepton selection for data and simulation. The central value on data is indicated by a dashed line while the systematic uncertainty is shown by an orange band.

DF events	$SF^{pred}_{fact.\ meth.}$	$R^{fact}_{SF/DF}$	$R^{direct}_{SF/DF}$	$R^{combined}_{SF/DF}$	SF^{pred}
5393	5830±79±274.1	1.08±0.05	1.09±0.05	1.09±0.03	5862±80±185

Table 5.5: Resulting estimate for flavor-symmetric backgrounds in the 8 TeV signal region. Given is the observed $e^{\pm}\mu^{\mp}$ event yield, the estimate in the SF channel using the event-by-event reweighting of the factorization method, $R_{\mathrm{SF/DF}}$ for the factorization method and from the direct measurement, the combination of both values, and the final prediction. Statistical and systematic uncertainties of the predictions are given separately.

one for the systematic uncertainty of the method.

Validation of the flavor-symmetric background estimation methods

To test the performance of the flavor-symmetric background estimation methods, the methods are applied to SM simulation. The number of simulated SF and DF events in the 8 TeV signal region are shown in Tab. 5.6 together with the flavor-symmetric background estimation, SF^{pred}. The given uncertainty in the SF and DF yield include only the statistical uncertainty of the simulation, while the systematic uncertainty of the method is included for SF^{pred}. Other systematic uncertainties affecting the simulation are not considered here, since the effects on SF and DF events are the same. The relative statistical uncertainty can get quite large if only a few simulated events with large event weights are present. This is the case for the DY+jets background contributions, which mainly originate from a sample of simulated $Z/\gamma* \to \ell\ell$ events. Although the sample statistics of nearly 50 million generated events is not small, the large cross section of about 6000 pb results in an event weight of 4.4 (see Tab. 4.1).

As expected, deviations from the flavor-symmetry are observed for processes containing the direct decay of a Z boson into a dielectron or dimuon pair, namely processes in the DY+jets ($e^+e^-, \mu^+\mu^-$) and Z+ν categories. Similarly, for most of the processes that produce as many SF as DF lepton pairs on particle level, namely $t\bar{t}$, single top quark production, and processes in the "other SM" category, the difference between SF and SF^{pred} is compatible with zero within the given uncertainty. An exception is the DY+jets ($\tau^+\tau^-$) category where 123 ± 51 more SF events are obtained from the direct simulation than from the prediction. Because of the large cross section of the $Z/\gamma* \to \ell\ell$ process, 47 simulated DF and 83 SF events in the signal region get reweighted to values of about 200 and 340, respectively. Note that the exact weights differ from the factor of 4.4 stated in Tab. 4.1 due to the impact of additional scale factors to perform the pileup reweighting and account for lepton identification efficiency differences between data and simulation (see Section 4.1.2).

To investigate the deviation observed for the DY+jets ($\tau^+\tau^-$) background, the same quantities as in Tab. 5.6 are determined in the inclusive dilepton selection, the DY+jets control region, and the control region for flavor-symmetric backgrounds for this background process (see Tab. 4.4 and 5.1 for the exact requirements of these selections). The numerical results in these selections and the 8 TeV signal region are shown in Tab. 5.7. No overall underprediction of the DY+jets ($\tau^+\tau^-$) background by the flavor-symmetric background estimation method can be observed. While the difference between SF and SF^{pred} is compatible with zero for the two control regions within the uncertainties, a slight overprediction is observed in the

	SF	DF	SF^{pred}	$SF - SF^{pred}$
$t\bar{t}$	5205 ± 14	4876 ± 13	5311 ± 172	-106 ± 172
DY+jets $(e^+e^-, \mu^+\mu^-)$	62 ± 27	< 1	< 1	62 ± 27
DY+jets $(\tau^+\tau^-)$	338 ± 40	198 ± 30	215 ± 31	123 ± 51
Single t	151 ± 4	141 ± 4	153 ± 6	-2 ± 8
Z+ν	12 ± 1	< 1	< 1	12 ± 1
Other SM	191 ± 5	178 ± 5	194 ± 8	-3 ± 9
Flavor-symmetric backgrounds	5856 ± 40	5372 ± 31	5851 ± 192	5 ± 196
Not-flavor-symmetric backgrounds	74 ± 28	< 1	< 1	74 ± 28
Total simulation	5929 ± 48	5372 ± 31	5851 ± 192	78 ± 198

Table 5.6: Event yield in the 8 TeV signal region in simulation. SF^{pred} is obtained by multiplying the DF yield with $R_{SF/DF}$. For the number of SF and DF events the uncertainty is given by the MC statistics, while the uncertainty in SF^{pred} additionally includes the systematic uncertainty of $R_{SF/DF}$.

	SF	DF	SF^{pred}	$SF - SF^{pred}$
Inclusive dilepton selection	$13\,950 \pm 250$	$13\,170 \pm 240$	$14\,570 \pm 560$	-620 ± 610
DY+jets control region	875 ± 64	798 ± 60	882 ± 72	-7 ± 96
Flav.-sym. control region	225 ± 32	175 ± 27	193 ± 31	32 ± 44
8 TeV signal region	338 ± 40	198 ± 30	215 ± 31	123 ± 51

Table 5.7: Event yield for the DY+jets $(\tau^+\tau^-)$ background category in simulation in different selections. SF^{pred} is obtained by multiplying the DF yield with $R_{SF/DF}$. For the number of SF and DF events the uncertainty is given by the MC statistics, while the uncertainty in SF^{pred} additionally includes the systematic uncertainty of $R_{SF/DF}$.

inclusive dilepton selection. Comparing the differences in the four selections, there might be a dependency on p_T^{miss}, which is the main difference in the definitions of the control and signal regions. Such an effect would occur if $R_{SF/DF}$ or the flavor-symmetry in the simulation depended on p_T^{miss}. In Fig. 5.12, the number of simulated SF is events compared to SF^{pred} for the DY+jets $(\tau^+\tau^-)$ background in the inclusive dilepton selection and when requiring at least two jets and two central leptons. Good agreement is observed up to 100 GeV, while more SF events than expected are obtained for higher values of p_T^{miss}. Neither any of the more important flavor-symmetric background processes, like $t\bar{t}$, nor the direct measurements of $R_{SF/DF}$ or the ingredients of the factorization method show such a trend, therefore a dependency of $R_{SF/DF}$ on p_T^{miss} seems unlikely. Since DY+jets $(\tau^+\tau^-)$ background processes only account for about 5% of the total background contribution in the 8 TeV signal region and is negligible in later parts of the analysis after applying a requirement on M_{T2}, no further investigation is performed. Neither a possible dependency of the flavor-symmetry on p_T^{miss} in the simulation nor a statistical fluctuation in a part of the phase space with little MC statistics can be ruled out by these studies, which underlines the importance to estimate the background from data if possible.

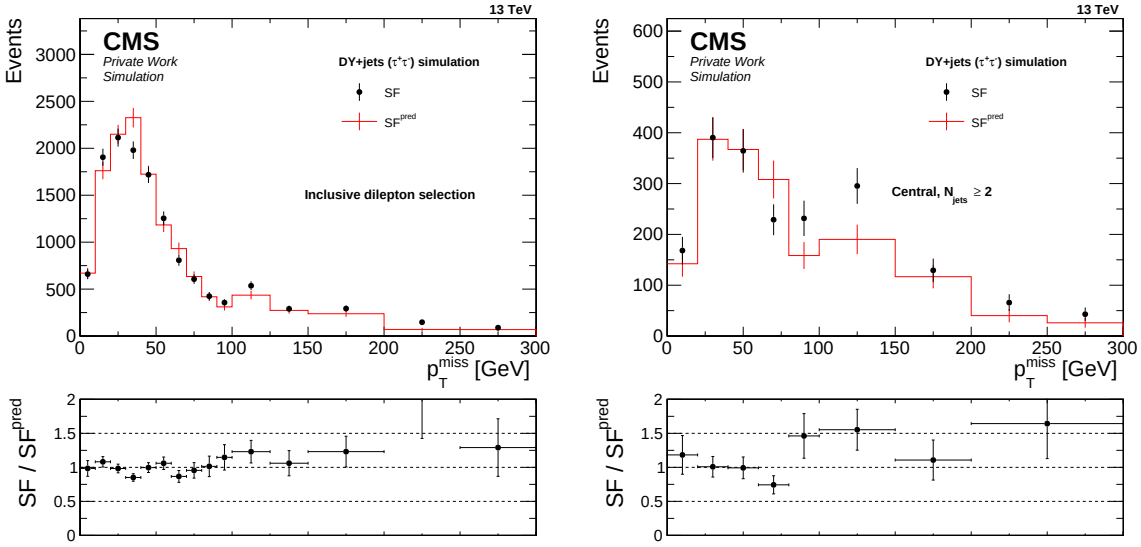

Figure 5.11: Distribution of $p_{\mathrm{T}}^{\mathrm{miss}}$ for the simulation of the DY+jets $(\tau^+\tau^-)$ background in the inclusive dilepton selection (left) and for central events with at least two jets. The contribution of SF is shown as black dots, while the prediction obtained by applying the flavor-symmetric background prediction methods to DF events $\mathrm{SF}^{\mathrm{pred}}$ is indicated as a red line. The bottom panel shows the ratio between SF events and the prediction, taking the statistical uncertainties of numerator and denominator into account.

Study of non-prompt leptons

An additional background contribution can arise from leptons, which are not produced in the hard interaction. These can be real leptons from decays of heavy-flavor quarks or jets that are misidentified as leptons. In general, the modeling of such leptons in simulation is not as precise as for leptons from the hard process. Additional studies are performed on data and simulation to ensure that the flavor-symmetry applies for the small contribution of non-prompt leptons. In a first step, the generator information of the simulation is used to examine the flavor-symmetry of non-prompt leptons in simulated $\mathrm{t\bar{t}}$ events. Afterwards, a data driven estimate is derived using leptons with relaxed isolation criteria.

Non-prompt leptons in $\mathrm{t\bar{t}}$ simulation: In simulation, the information on the direction and momentum of a reconstructed lepton can be used to match it to a generated particle and thereby determine whether the lepton originates from the decay of W or Z boson or a τ lepton and can thus be classified as a prompt lepton. Non-prompt leptons can result from decays of heavy-flavor quarks inside of jets or be jets that are misidentified as leptons. The matching is performed by considering all generated particles in a cone of $\Delta R = 0.1$ around the lepton for which the difference between the p_{T} of the generated particle and the reconstructed lepton does not exceed twice the p_{T} of the generated particle. The generated particle with the smallest spatial separation to the reconstructed lepton that fulfills these criteria is selected.

Simulated $\mathrm{t\bar{t}}$ events are used to study the contribution of non–prompt leptons to the inclusive

	Inclusive dilepton selection		8 TeV signal region	
	all leptons	non-prompt	all leptons	non-prompt
$e^{\pm}e^{\mp}$	$90\,962 \pm 58$	244 ± 3	1873 ± 8	5.7 ± 0.4
$\mu^{\pm}\mu^{\mp}$	$156\,538 \pm 80$	684 ± 5	3332 ± 12	18.3 ± 0.9
SF	$247\,500 \pm 99$	928 ± 6	5205 ± 14	24.0 ± 1.0
$e^{\pm}\mu^{\mp}$	$229\,245 \pm 94$	797 ± 6	4876 ± 13	19.0 ± 0.9
$R_{\mathrm{SF/DF}}$	1.081 ± 0.001	1.164 ± 0.011	1.067 ± 0.004	1.26 ± 0.08

Table 5.8: Number of events with non-prompt leptons in the inclusive dilepton selection and the 8 TeV signal region compared to the total number of dilepton events in $\mathrm{t\bar{t}}$ simulation. Only statistical uncertainties are given.

dilepton selection and the 8 TeV signal region. The two b jets from the decays of the top quarks are sources for leptons from heavy-flavor decays. Figure 5.12 shows the $m_{\ell\ell}$ distribution of events containing at least one non-prompt lepton in the inclusive dilepton selection and the 8 TeV signal region. The corresponding event yields are stated in Tab. 5.8 and compared to the total number of reconstructed leptons in each selection. The fraction of events containing a non-prompt lepton amounts to 0.3–0.5% in all cases with slightly higher values for non-prompt muons than for non-prompt electrons. The ratio of SF to DF events is slightly higher for non-prompt leptons than the one for prompt lepton pairs, indicating a small underprediction of this background, at least in simulation.

Non-prompt leptons in data: A "tight-to-loose" ratio method is applied to obtain an estimate for the contribution of non-prompt leptons to the signal selection. The method applied here follows the principles used by recent CMS searches for SUSY in final states with a same-sign dilepton pair [116] or at least three leptons [117].

Two control regions in data enriched in non-prompt leptons are used for this purpose. These are obtained by relaxing the isolation requirement on the leptons from $\mathrm{Iso_{rel}} < 0.1$ for electrons and $\mathrm{Iso_{rel}} < 0.2$ for muons to $\mathrm{Iso_{rel}} < 0.4$ for both flavors. Furthermore, loose working points for the lepton identification requirements are chosen. Leptons fulfilling the nominal (relaxed) requirement are referred to as "tight" ("loose") leptons. By this definition, every tight lepton is also a loose lepton. The probability for a non-prompt lepton that passes the loose selection to also pass the tight selection is referred to as "fake rate" (f). The contribution of non-prompt leptons to the signal region is determined by weighting all events by $f/(1-f)$ for each loose lepton. This is done in a sample populated by events that contain at least one lepton that satisfies the loose requirements but fails the tight selection while all other requirements are the same as in the signal selection.

The fake rate is determined on a sample recorded with prescaled low p_{T} single lepton triggers (see Section 4.1.1 and Appendix A). Exactly one loose lepton and at least one jet is required. Events from W or Z boson decays are suppressed by requiring $p_{\mathrm{T}}^{\mathrm{miss}}$ and the transverse mass, $m_{\mathrm{T}}\left(\vec{\ell}, \vec{p}_{\mathrm{T}}^{\mathrm{miss}}\right)$, both to be below 20 GeV. The remaining contributions from these processes are estimated from simulation, normalized in an orthogonal sample with $p_{\mathrm{T}}^{\mathrm{miss}} > 20\,\mathrm{GeV}$ and $70 < m_{\mathrm{T}}\left(\vec{\ell}, \vec{p}_{\mathrm{T}}^{\mathrm{miss}}\right) < 120\,\mathrm{GeV}$, and subtracted from the sample.

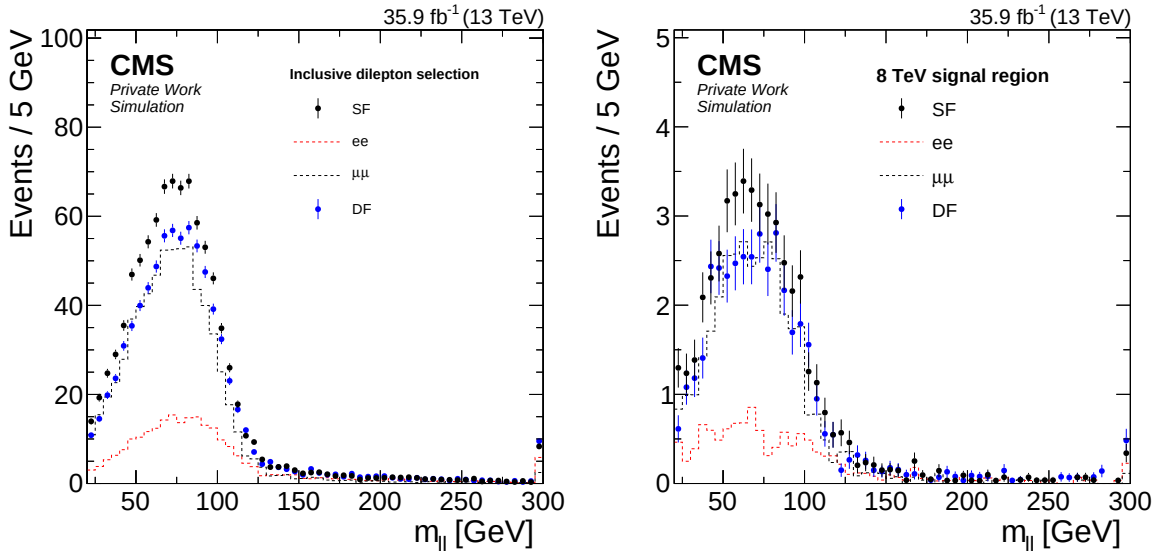

Figure 5.12: Distribution of $m_{\ell\ell}$ in $\mathrm{t\bar{t}}$ simulation for lepton pairs with at least one non-prompt lepton in the inclusive dilepton selection (left) and the 8 TeV signal region (right). The contributions of dielectron and dimuon events are shown as red and black lines, while SF and DF pairs are shown as black and blue points.

Figure 5.13 shows the fake rate as a function of the p_{T} and η of the lepton for electrons and muons. The corresponding rates in QCD multijet simulation are shown for comparison. To account for dependencies on these observables, the fake rate is measured and applied as a function of these variables. On average, fake rates of approximately 17% for electrons and 36% for muons are determined. A relative uncertainty of 30% is assigned to account for the observed differences between the fake rates in data and simulation, which are most prominent for leptons with low momentum in the central parts of the detector.

The number of events with one or two loose leptons that fail the tight criteria and the resulting contribution of non-prompt leptons in the 8 TeV signal region are summarized in Tab. 5.9. Note that applying the fake rate as a function of lepton p_{T} and η results in a prediction that differs from the one obtained when multiplying the average values of $f/(1-f)$ to the event numbers stated in Tab. 5.9 for each loose-not-tight lepton. The ratio of SF to DF events is given as well. The uncertainty in the fake rate is propagated to the prediction under the assumption of fully correlated uncertainties between leptons of the same flavor and no correlations between leptons of different flavor. Therefore, a large fraction of the systematic uncertainty in the predicted non-prompt SF and DF yield cancels when calculating $R_{\mathrm{SF/DF}}$. The obtained prediction for DF events is higher than for SF events resulting in a ratio of $R_{\mathrm{SF/DF}} = 0.76 \pm 0.13$. This indicates an overprediction of this background by the flavor-symmetric background estimation methods, which provide therefore a conservative estimate for background events from non-prompt leptons. The relative contribution of non-prompt leptons to the flavor-symmetric background prediction is small and accounts for less than 2% of the total prediction.

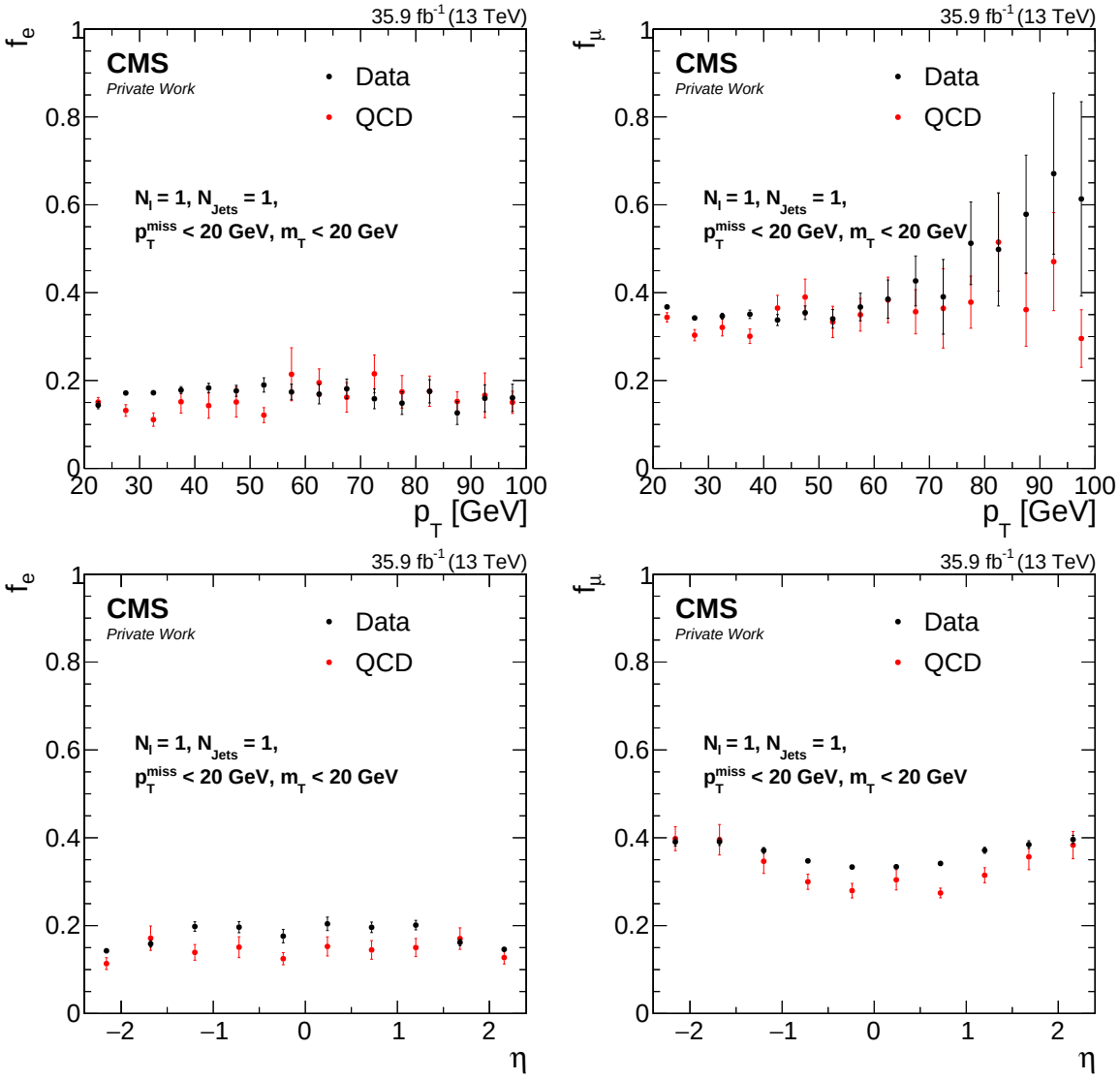

Figure 5.13: Fake rate as a function of lepton p_{T} (top) and η (bottom) for electrons (left) and muons (right). The fake rates in data and QCD multijet simulation are shown in black and red, respectively.

8 TeV signal region	$e^{\pm}e^{\mp}$	$\mu^{\pm}\mu^{\mp}$	SF	$e^{\pm}\mu^{\mp}$	$R_{\mathrm{SF/DF}}$
1 loose-not-tight lepton	96	68	164	171	0.96±0.10
2 loose-not-tight leptons	9	4	13	9	1.44 ± 0.63
non-prompt prediction	24±10	41±22	64±24	85±39	0.76±0.13

Table 5.9: Number of events with at least one loose lepton that fails the tight criteria and the resulting prediction of events with non-prompt leptons in the 8 TeV signal region. The ratio of SF to DF flavor events is given as well. All uncertainties include statistical and systematic components except for the uncertainties in $R_{\mathrm{SF/DF}}$ calculated directly from the event yields with 1 or 2 loose-not-tight leptons for which only the statistical uncertainty is given.

5.2.2 Drell-Yan+jets background prediction

Since the development and application of the DY+jets background prediction method was not part of the work covered in this thesis only a short overview is given here.

One of the key features of the DY+jets background is the fact that no prompt neutrinos are present. Therefore, mismeasurements of observables are the only way to produce a significant amount of $p_{\mathrm{T}}^{\mathrm{miss}}$ in these processes. In general, the CMS experiment is able to measure leptons to a much higher precision than jets, which makes mismeasurements of the hadronic system recoiling against the Z boson the main source of $p_{\mathrm{T}}^{\mathrm{miss}}$ for these backgrounds. The same is true for γ+jets events. Therefore, a sample of γ+jets events can be used to predict the contribution of DY+jets events at high $p_{\mathrm{T}}^{\mathrm{miss}}$. This is referred to as the $p_{\mathrm{T}}^{\mathrm{miss}}$-template method [10, 118].

A photon control region is defined according to the signal region definition. The kinematic distributions of the hadronic system differ between γ+jets and DY+jets events because of the different boson masses. Therefore, a reweighting is applied such that the p_{T} distribution of the photon matches that of the dilepton system in a dilepton sample. This sample is identical to the signal sample except for requiring $m_{\ell\ell}$ to be within 5 GeV of the Z boson mass. This sample is referred to as "on-Z region". Contributions from SM processes with photons and genuine $p_{\mathrm{T}}^{\mathrm{miss}}$ are taken from simulation and subtracted from the event yield in the photon control region. The background prediction is obtained by normalizing the resulting $p_{\mathrm{T}}^{\mathrm{miss}}$ distribution to the observed data yield in the on-Z region in the range $50 < p_{\mathrm{T}}^{\mathrm{miss}} < 100\,\mathrm{GeV}$ after subtracting other background contributions.

Variables like $\mathrm{M_{T2}}$ and angular differences between the leptons rely on two visible objects and thus cannot be calculated for the photon sample. Since some of these observables become important in later parts of the analysis they are emulated by simulating the decay of the photon into two leptons. The decay is performed under the assumption that the mother particle has the mass of the Z boson. A reference system is introduced in which the mother particle is at rest and the decay into leptons takes the angular dependence of spin correlations in the matrix element into account. Afterwards, a Lorentz transformation is performed to the simulated dilepton system to match it to the momentum of the photon reconstructed in data. The emulated leptons need to fulfill the same requirements on p_{T} and η as the reconstructed leptons.

The systematic uncertainty of the prediction takes the statistical uncertainty of the photon sample and the normalization region into account. Further uncertainties are assigned based on tests of the method on simulation and others arise from tests of the subtraction of events from processes with genuine $p_{\mathrm{T}}^{\mathrm{miss}}$ performed in a data control region.

Extrapolation to off-Z regions

The method described above results in a prediction for the on-Z region with $86 < m_{\ell\ell} < 96\,\mathrm{GeV}$. Contributions outside of this mass window can arise from off-shell Z bosons or the Drell-Yan continuum. The background estimation for these contributions is determined by applying an extrapolation factor $R_{\mathrm{out/in}}$ to the prediction in the on-Z region. $R_{\mathrm{out/in}}$ is measured in the DY+jets control region and is defined as the ratio of the event yield in the

	N_{out}	N_{in}	$R_{\text{out/in}} \pm \sigma_{\text{stat}} \pm \sigma_{\text{syst}}$
Data	48070±551	591079±782	0.081±0.001±0.020
MC	39347±509	519187±733	0.076±0.001±0.019

Table 5.10: Results of the calculation of $R_{\text{out/in}}$ in the mass region of the 8 TeV signal region ($20 < m_{\ell\ell} < 70\,\text{GeV}$) for data and simulation.

	Estimate on-Z	$R_{\text{out/in}}$	$20 < m_{\ell\ell} < 70\,\text{GeV}$
8 TeV signal region	549 ± 162	0.08 ± 0.02	45 ± 17

Table 5.11: Drell-Yan+jets prediction obtained with the $p_{\text{T}}^{\text{miss}}$-template method for the 8 TeV region at the Z boson mass and extrapolation to the signal mass region.

mass region of interest (out) to that in the Z boson mass window (in). To increase the purity of DY+jets events, the contribution from flavor-symmetric processes is determined from the DF sample and subtracted:

$$R_{\text{out/in}} = \frac{N_{\text{out}}}{N_{\text{in}}} = \frac{N_{SF}^{\text{out}} - N_{DF}^{\text{out}} R_{\text{SF/DF}}}{N_{SF}^{\text{in}} - N_{DF}^{\text{in}} R_{\text{SF/DF}}}. \tag{5.11}$$

The event yields and the resulting extrapolation factors are summarized in Tab. 5.10. Values of approximately 8% are determined for both data and simulation.

This approach relies on the assumption that the shape of the $m_{\ell\ell}$ distribution and especially the extrapolation factor does not depend on $p_{\text{T}}^{\text{miss}}$ when extrapolating from the DY+jets control region to the signal region. Figure 5.14 shows $R_{\text{out/in}}$ as a function of $p_{\text{T}}^{\text{miss}}$ and the jet multiplicity in the mass range of the 8 TeV signal region for data and simulation. No dependency on $p_{\text{T}}^{\text{miss}}$ is observed. In contrast to this, $R_{\text{out/in}}$ clearly increases with the number of jets for jet multiplicities up to three jets. For higher jet multiplicities the available number of events decreases and while the trend seems to continue in data it does not do so in simulation. This confirms the chosen control region definition to require at least two jets, which discards a significant amount of statistics in favor of event kinematics that are more similar to those in the signal region. Because of this similarity between the DY+jets control region and the signal region in terms of jet multiplicity, the applicability of the method in the signal region is not restricted. A systematic uncertainty of 25% is assigned to cover the trends at high jet multiplicity in data.

The estimated background prediction with the $p_{\text{T}}^{\text{miss}}$-template method in the 8 TeV signal region is shown in Tab. 5.11. In the Z boson mass window, 549±162 events are predicted, resulting in an estimation of 45 ± 17 events in the signal mass region.

5.2.3 Background prediction for processes with Z bosons and genuine $p_{\text{T}}^{\text{miss}}$ (Z+ν)

The $p_{\text{T}}^{\text{miss}}$-template method discussed in Section 5.2.2 only accounts for processes with instrumental $p_{\text{T}}^{\text{miss}}$ from jet mismeasurements. Therefore, it does not include contributions from rare processes which include a dileptonic decay of a Z boson and genuine $p_{\text{T}}^{\text{miss}}$ from prompt

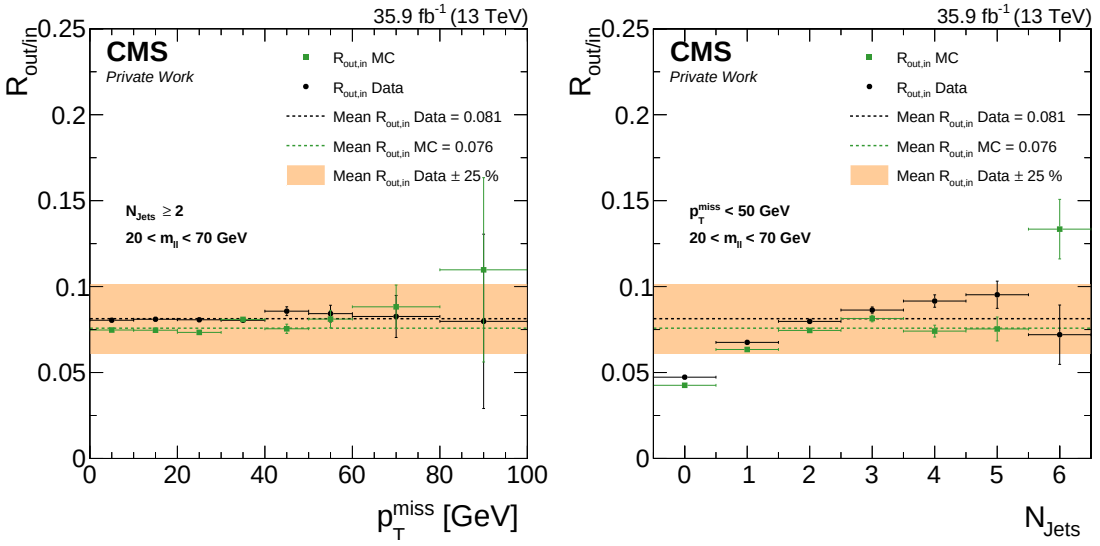

Figure 5.14: $R_{\text{out/in}}$ as a function of the p_{T}^{miss} (left) and jet multiplicity (right) for data (black) and simulation (green). The central value obtained in data (simulation) is shown as a black (green) dashed line, while the systematic uncertainty of 25% is indicated as an orange band around the central value in data.

neutrinos. The most important of these processes are WZ$\rightarrow 3\ell\nu$, ZZ$\rightarrow 2\ell 2\nu$, and t$\bar{\text{t}}$Z. While the relative contribution of these processes to the background composition in the 8 TeV signal region is small, it can be significant in signal regions that are less dominated by top quark pair production or use an $m_{\ell\ell}$ range closer to the Z boson mass.

Determining all of the background processes in the Z+ν category from data would require a large effort and would not necessarily yield more precise results than a prediction from simulation. Since it is a minor background contribution in most signal bins, the effort is not undertaken and simulated events are used for the prediction. Control regions in data, requiring either three or four leptons, are used to validate the simulation of the three most important processes and to derive scale factors to account for differences. A region enriched in WZ events is obtained by requiring exactly three leptons, at least two jets, no b-tagged jet, $p_{\text{T}}^{\text{miss}} > 60\,\text{GeV}$, and an OCSF lepton pair with $86 < m_{\ell\ell} < 96\,\text{GeV}$. The t$\bar{\text{t}}$Z control region requires three leptons and at least two jets as well, two b-tagged jets, $p_{\text{T}}^{\text{miss}} > 30\,\text{GeV}$, and an OCSF pair as in the WZ control region.

The third important process ZZ$\rightarrow 2\ell 2\nu$ does not produce additional leptons that could be used to suppress backgrounds with larger production cross sections. Furthermore, the $p_{\text{T}}^{\text{miss}}$ distributions in events with dilepton pairs from top quark pair production and ZZ$\rightarrow 2\ell 2\nu$ decays are very similar. A veto on b-tagged jets and restriction to a $m_{\ell\ell}$ range around the Z boson mass could reduce the contribution from t$\bar{\text{t}}$ but would also enrich the sample in events from the DY process. Since the cross section for $\text{Z}/\gamma^* \rightarrow \ell\ell$ events is about 4 orders of magnitude larger than for ZZ$\rightarrow 2\ell 2\nu$ (see Tab. 4.1), DY events with large $p_{\text{T}}^{\text{miss}}$ due to jet mismeasurements would dominate such a selection. In contrast to this, the ZZ$\rightarrow 4\ell$ process provides two OCSF lepton pairs, a very rare signature in the SM. Mismodelings in simulation often depend on the event generator and affect the hadronic system more strongly than the

	WZ control region	$t\bar{t}Z$ control region	ZZ control region
signal process	111.5 ± 3.0	19.3 ± 0.6	8.1 ± 0.2
remaining background	46.4 ± 3.3	8.2 ± 0.5	5.1 ± 0.4
data	163	34	17
data−background	116.6 ± 13.2	25.8 ± 5.9	11.9 ± 4.1
(data−bkg)/signal	1.05 ± 0.12	1.33 ± 0.31	1.47 ± 0.51

Table 5.12: Data yields and estimated background contributions from simulation in the multi lepton control regions.

generated leptons. Since both decay modes of Z boson pairs are simulated with the same event generator and differ only in the lepton kinematics, a difference already accounted for in the cross sections in Tab. 4.1, it can be assumed that both samples would be impacted by the same sources for mismodeling. A control region with four leptons is used to validate the simulation of ZZ production. The four leptons need to form two OCSF lepton pairs of which one has to lie within $86 < m_{\ell\ell} < 96\,\text{GeV}$, while $m_{\ell\ell} > 20\,\text{GeV}$ is required for the second pair to reject contributions from low mass resonances. At least two jets are required to obtain a sample similar to the signal region in terms of jet multiplicity.

Figure 5.15 shows the $m_{\ell\ell}$ distribution of the OCSF pair closest to the Z boson mass for the three control regions. Each of the three backgrounds is the dominant contribution in the corresponding control region and in all cases, more events are observed in data than expected from simulation. The yields in data and predictions from simulation are summarized in Tab. 5.12. Only statistical uncertainties due to the sample sizes are taken into account.

The WZ control region contains the most events and shows the smallest relative deviation with 112 WZ events expected and 117 events observed after subtracting the remaining background contributions. This translates into a scale factor of 1.05, calculated as the ratio of the yield in data, after subtracting the remaining background processes, to the expected contribution from the process of interest. Scale factors of 1.33 and 1.47 are obtained in the $t\bar{t}Z$ and ZZ control regions, respectively. The limited number of events in the control regions does not allow for detailed dependency studies. Uncertainties of 30%, 40%, and 60% are assigned to the scale factors for the WZ, $t\bar{t}Z$, and ZZ processes, respectively, to account for the limited statistics in the control regions and possible differences in the kinematics when extrapolating to the dilepton sample. The relative contribution of processes in the Z+ν category to the background estimation is small in most signal regions, which reduces the impact of these uncertainties in the total prediction. A 70% uncertainty is assigned to the contribution of the remaining even rarer processes also contributing to the Z+ν background, like triboson production.

5.3 Results in the 8 TeV signal region

The observed yields in the 8 TeV signal region and the SM background prediction are summarized in Tab. 5.13. Very good agreement is observed between the yields in data and the prediction. The flavor-symmetric background processes account for 99% of the total estimated background. The corresponding $m_{\ell\ell}$ distribution is therefore shown twice in Fig. 5.16, once

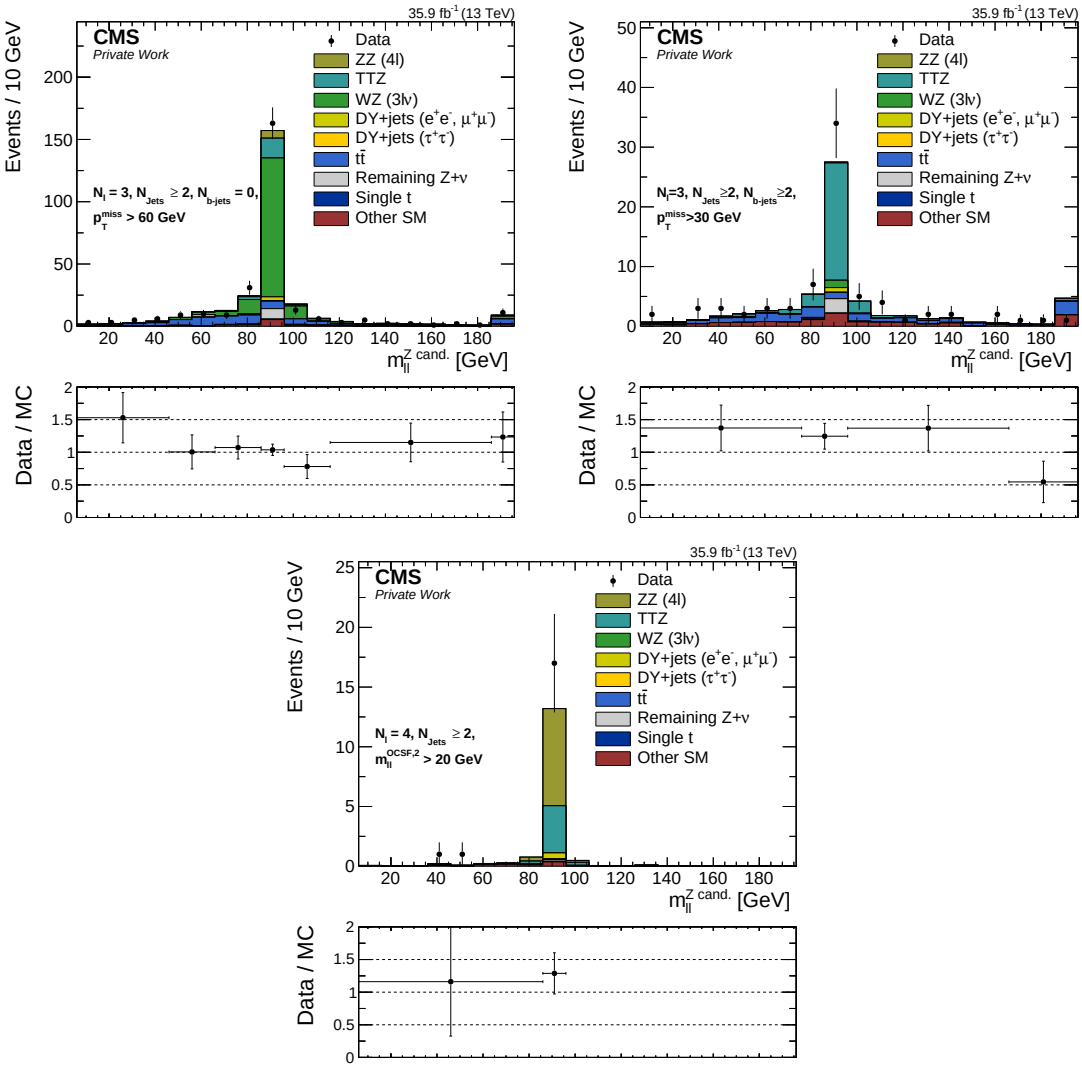

Figure 5.15: $m_{\ell\ell}$ distribution for the OCSF pair closest to the Z boson mass in the WZ (top left), $t\bar{t}Z$ (top right), and ZZ control region (bottom). The data, shown as black points, is compared to the simulation of SM processes, displayed as a stacked histogram of the contributing processes. The ratio of data to simulation is shown in the lower panel. Only statistical uncertainties are taken into account for the error bars in the ratio.

	Flavor-symmetric	DY+jets	Z+ν	Total estimate	Observed
8 TeV signal region	$5862 \pm 80 \pm 185$	45 ± 17	11 ± 4	5917 ± 203	5894

Table 5.13: Data yields and estimated background contributions in the 8 TeV signal region.

with a linear scale to study the overall shape and once with a logarithmic scale to visualize the relative background contributions. At low invariant dilepton masses, the data yield lies slightly above the prediction while the opposite is the case for the highest mass bins. The overall effect is small and is mostly covered by the assigned uncertainty in the background prediction.

The deviation observed in the 8 TeV analysis could not be confirmed in this work. The integrated luminosity in 2016 was nearly twice as large as in 2012 while the production cross section of top quark pair production, the main background process, increases by more than a factor of 3 when changing the energy from 8 to 13 TeV. The greater center-of-mass energy also increases the available energy for jets and leptons from the decays of the top quarks and all effects combined lead to a sample size in the signal region that is about 8 times larger than the corresponding sample in the 8 TeV data set. Since the production cross sections for most SUSY or other BSM physics scenarios also get larger with the center-of-mass energy and the increase for most signal scenarios that are not yet excluded is even stronger than for $\mathrm{t\bar{t}}$, it is highly unlikely that the deviation in the 8 TeV analysis, where 860 events were observed and 730^{+49}_{-48} were expected [5], was caused by a new physics process. It is much more likely that an upward fluctuation in the data caused an excess of about 2.5 standard deviations. Therefore, the rest of this work is dedicated to improving the analysis sensitivity by applying or developing new discriminators to distinguish between lepton pairs that most likely originate from the dominant $\mathrm{t\bar{t}}$ background and those that might be produced in the decay chains of SUSY particles.

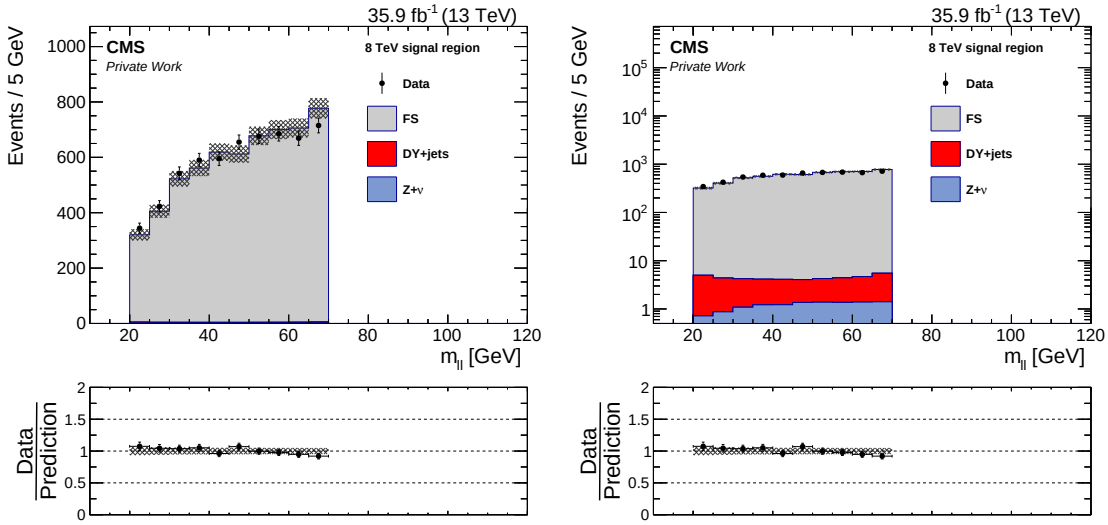

Figure 5.16: $m_{\ell\ell}$ distribution in the 8 TeV signal region using a linear (left) and logarithmic scale (right). The data, shown as black points, is compared to the total background estimate. The ratio of data to simulation is shown in the lower panel. The hashed band shows the total uncertainty of the background prediction, including statistical and systematic sources.

6 Improving the analysis' sensitivity

The signal region requirements in Section 5 followed the 8 TeV analysis closely to investigate a deviation observed in the aforementioned search. These criteria were optimized for a smaller sample size and lower background cross sections. Since the deviation could not be confirmed and many models with SUSY particles of moderate mass have been excluded by previous searches of the ATLAS and CMS collaborations, more refined methods and selections are required to be sensitive to signal models with lower production cross sections or rarer signatures.

As a first step, the requirements and signal bins that were used in previous versions of this analysis on data taken in 2012 and 2015 are examined to decide whether the discrimination power they offer motivates a further use. Comparisons are made to other observables, which can be used to distinguish between the dominant background from top quark pair production and the signal signature. In the second part of this section, new signal regions for a counting experiment approach as well as a shape analysis are defined before checking if the background prediction methods described in Section 5.2 can still be used or need to be adapted.

6.1 Observables to distinguish between top quark pair production and signal scenarios

The signal selection in the 8 TeV [5, 6] and first 13 TeV version [7] of the CMS search for SUSY in events with an OCSF dilepton pair, jets, and $p_{\mathrm{T}}^{\mathrm{miss}}$ required at least two jets and at least 150 GeV of $p_{\mathrm{T}}^{\mathrm{miss}}$ or at least three jets and 100 GeV of $p_{\mathrm{T}}^{\mathrm{miss}}$. In the counting experiment analysis, the event yields were further subdivided into bins of the invariant dilepton mass, lepton $|\eta|$, and, in case of the 13 TeV data taken in 2015, b jet multiplicity. The mass bins were introduced to increase the sensitivity to scenarios with varying mass differences between the neutralinos, while the bins in b jet multiplicity separated the sample into parts that are more or less likely to result from the decay of a top quark pair. The assumption of new heavy particles to be produced more centrally and the better detector performance in the central part of the detector motivated the bins in lepton $|\eta|$. All of these bins are discarded for now to check in a more inclusive selection which variables are most suitable to distinguish between possible signals and the dominant $\mathrm{t\bar{t}}$ background that is expected to contribute about 20 000 events to this selection.

The upper left plot in Fig. 6.1 shows the $p_{\mathrm{T}}^{\mathrm{miss}}$ distribution for simulation of the $\mathrm{t\bar{t}}$ background and five mass scenarios of the simplified model introduced in Section 2.3.4. The mass scenarios are chosen in a range not yet excluded by previous versions of this analysis but within the sensitivity of this work. The combinations of $\tilde{b}$ and $\tilde{\chi}_2^0$ masses are selected to feature examples for both small and large differences between the two masses as well as scenarios in between. By excluding the events with at least three jets and 100–150 GeV of $p_{\mathrm{T}}^{\mathrm{miss}}$, about half of the $\mathrm{t\bar{t}}$ background events can be discarded while only a small fraction of signal events is removed in all scenarios. This change of the requirements also removes the discontinuity in the $p_{\mathrm{T}}^{\mathrm{miss}}$ distribution at 150 GeV, which will be important later on. Requiring more $p_{\mathrm{T}}^{\mathrm{miss}}$ or introducing bins at higher $p_{\mathrm{T}}^{\mathrm{miss}}$ could improve the signal to background ratio significantly.

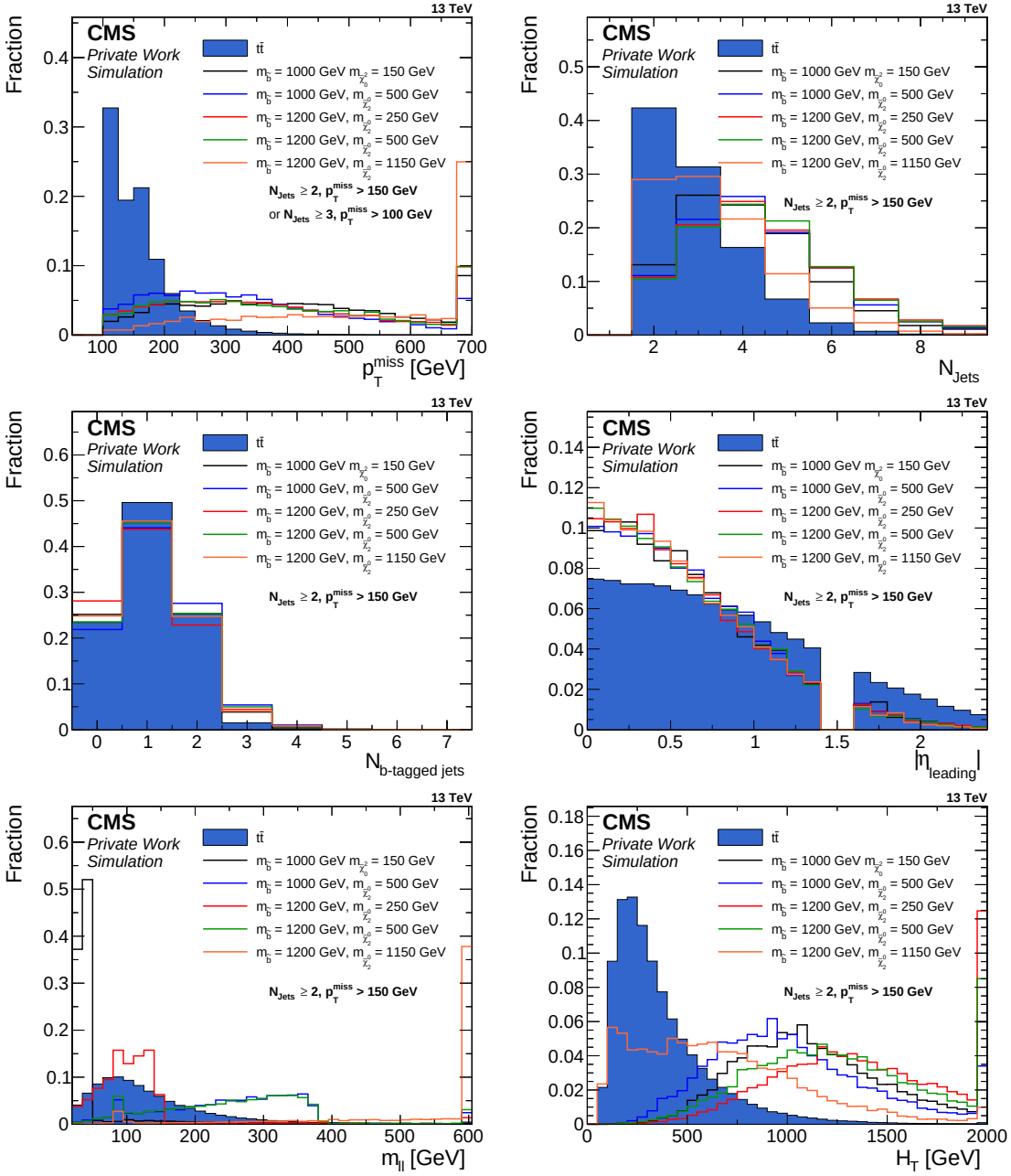

Figure 6.1: Distributions of $p_{\mathrm{T}}^{\mathrm{miss}}$ in the 8 TeV signal region without $m_{\ell\ell}$ and $|\eta|$ requirements (top left) and jet multiplicity (top right), b jet multiplicity (center left), $|\eta|$ of the leading lepton (center right), $m_{\ell\ell}$ (bottom left), and hadronic activity (bottom right) after requiring 150 GeV of $p_{\mathrm{T}}^{\mathrm{miss}}$ and at least two jets. The simulated shape of the $\mathrm{t\bar{t}}$ background is compared to five mass scenarios of the simplified model. All distributions are normalized to 1.

Previous versions of this analysis [5–7] or corresponding searches by the ATLAS collaboration [119, 120] use requirements on or bin in jet multiplicity, b jet multiplicity, $|\eta|$ of the leptons, $m_{\ell\ell}$, or H_{T}. The distributions of these observables for $\mathrm{t\bar{t}}$ simulation and the signal scenarios after requiring at least two jets and 150 GeV of $p_{\mathrm{T}}^{\mathrm{miss}}$ are shown in the remaining plots of Fig. 6.1. All of the shown signal scenarios feature a higher jet multiplicity and hadronic activity than the $\mathrm{t\bar{t}}$ background. This effect is weaker if the mass difference between the bottom squark and the $\tilde{\chi}_2^0$ is small. In contrast to this, the b jet multiplicities of the $\mathrm{t\bar{t}}$ process and the signal scenarios are quite similar, which reduces the usability of b-tagging requirements at least for this signal model. Overall, the signal scenarios deposit a larger event fraction in the central part of the detector, but since the leptons from top quark pair production are mainly recorded in the barrel as well, the effect on the signal-to-background ratio is small. Due to their small impact on the sensitivity, requirements on the lepton $|\eta|$ and b jet multiplicity are no longer considered although the corrections for the flavor-symmetric background prediction are still estimated separately for events with both leptons in the central part of the detector and those with at least one lepton in the endcaps.

Since both leptons in the signal signature originate from the decay of the same $\tilde{\chi}_2^0$ while the leptons in $\mathrm{t\bar{t}}$ events come from different decay branches, the kinematics of the dilepton system differ significantly between signal events and those from top quark pair production. The most prominent features are the mass edges observed in the signal $m_{\ell\ell}$ distributions. This motivates the continued usage of invariant dilepton mass bins. Two other characteristic dilepton observables are shown in the upper plots of Fig. 6.2, namely the p_{T} of dilepton system, $p_{\mathrm{T}}^{\ell\ell}$, and the absolute value of the azimuthal distance between the two leptons, $\Delta\phi_{\ell\ell}$. The latter is highly correlated to the geometrical distance between the leptons $\Delta R_{\ell\ell}$ but provides a slightly better separation between signal and background scenarios. The dilepton p_{T} spectra of the signal scenarios are higher energetic than the spectrum for top quark pair production. But they can differ significantly depending on the mass scenario with more $\mathrm{t\bar{t}}$-like distributions for lower particle masses. In contrast to this, signal points with low $m_{\tilde{\chi}_2^0}$ feature small azimuthal distances between the leptons while the $\Delta\phi_{\ell\ell}$ distributions for the highest particle masses are more similar to $\mathrm{t\bar{t}}$. This indicates that a requirement on one observable might increase the sensitivity to some mass scenario while it reduces the sensitivity to others. Introducing a binning in such variables can avoid this problem. Adding a binning in several observables increases the number of signal regions significantly making it hard to decide whether a deviation is just a fluctuation in one of many signal regions or a sign for new physics. Combining the information of several observables can be a way to determine the likelihood of an event to originate from the decay of a top quark pair.

The highest potential for background suppression is offered by observables in which events from dileptonic $\mathrm{t\bar{t}}$ decays feature a clear cut-off with no events above or below a certain value. The most important of these observables is the $\mathrm{M_{T2}}$ variable [11, 12] already defined in Section 1.1. $\mathrm{M_{T2}}$ is a generalization of the transverse mass to four particles. In case of two identical two-body decays of a mother particle, the $\mathrm{M_{T2}}$ distribution formed of the four decay products features an upper limit at the mass of the mother particle. For dileptonic decays of top quark pairs, $\mathrm{M_{T2}}$ formed from the two leptons and the two neutrinos has a cut-off at the W boson mass of about 80 GeV. Since single neutrinos cannot be identified experimentally and contribute to the missing transverse momentum, $\vec{p}_{\mathrm{T}}^{\,\mathrm{miss}}$ needs to be split into two parts. A

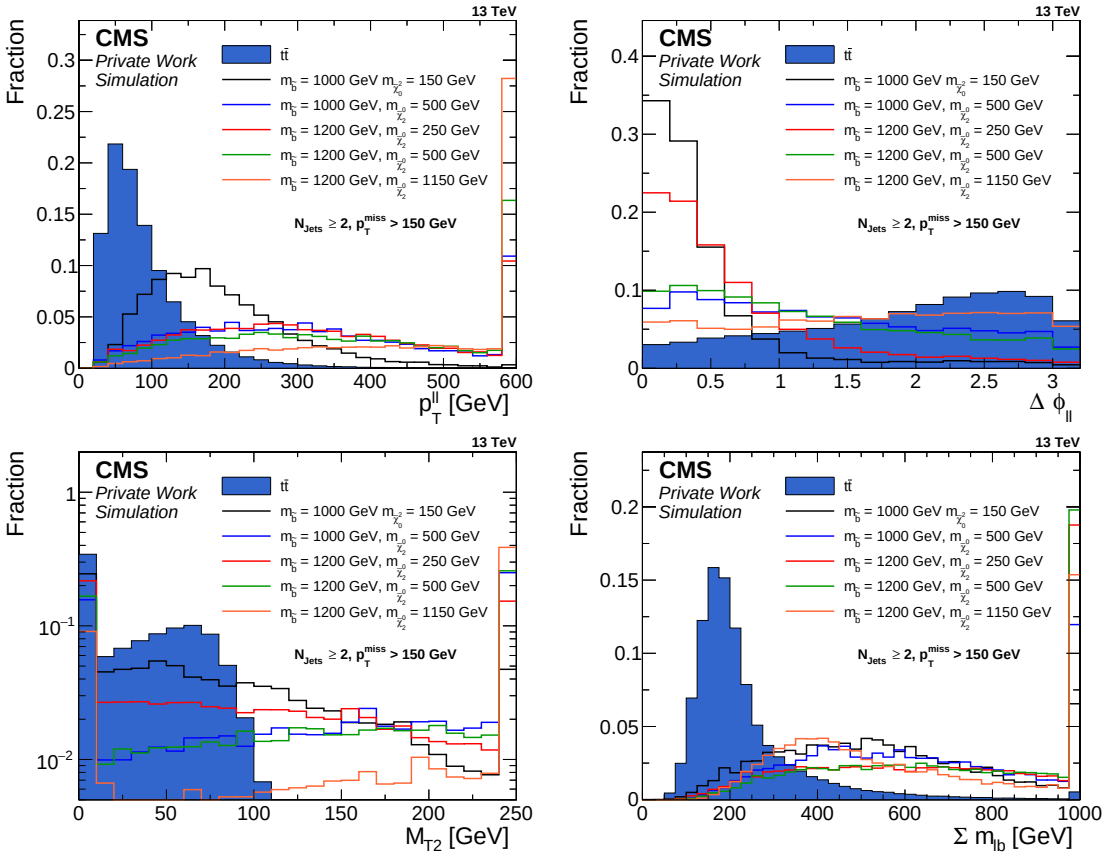

Figure 6.2: Distributions of the p_T of the dilepton system (top left), $\Delta\phi$ between the leptons (top right), M_{T2} (bottom left), and $\Sigma m_{\ell b}$ (bottom right) after requiring 150 GeV of p_T^{miss} and at least two jets. The simulated shape of the $t\bar{t}$ background is compared to five mass scenarios of the simplified model. All distributions are normalized to 1.

numerical minimization is performed to find the ideal separation and the resulting M_{T2} value. The lower left plot in Fig. 6.2 shows the M_{T2} distribution for $t\bar{t}$ simulation and the same five signal scenarios as before. Because of the experimental resolution, some $t\bar{t}$ contribution above the W boson mass remains but the distribution falls off rapidly. The signal event fraction above the W boson mass depends on the chosen mass point, ranging from 40 to 90%, but no sharp upper value is observed in any of the cases. The large fraction of events in the first M_{T2} bin originates from events in which the vector of the missing transverse momentum lies in between the transverse components of the lepton vectors. In these cases, the correct separation of the transverse momentum in the numeric minimization cannot be performed and the events get assigned a M_{T2} value of 0 GeV.

A second observable, called $\Sigma m_{\ell b}$, with an upper limit for dileptonic decays of top quark pairs is shown in the lower right plot of Fig. 6.2. It is formed by considering all possible combinations of a lepton and a b-tagged jet in an event. If no b-tagged jets are present non-tagged jets are considered. The pairing with the minimal invariant mass is selected and the procedure is repeated for the remaining lepton and jets, again preferring b-tagged jets. The sum of those two invariant masses is defined as $\Sigma m_{\ell b}$ and should have an endpoint at $2\sqrt{M(\mathrm{t})^2 - M(\mathrm{W})^2} \approx 300\,\mathrm{GeV}$ for $t\bar{t}$ events. Because of the limited jet-resolution and the possibility of incorrect jet-lepton combinations, the upper limit is less stringent than in case of M_{T2}. Signal scenarios feature higher values of $\Sigma m_{\ell b}$.

Overall, M_{T2} is the observable that provides the best suppression of events from the dominant background from dileptonic decays of top quark pairs.

6.2 Signal region definitions and $t\bar{t}$ likelihood

Events in the new signal regions need to contain more than 150 GeV of $p_{\mathrm{T}}^{\mathrm{miss}}$ and at least two jets. To suppress most of the background from top quark pair production $M_{T2} > 80\,\mathrm{GeV}$ is required as well. Increasing this requirement further could reduce the $t\bar{t}$ background contribution even more, but the kinematic fit to search for an edge in the invariant dilepton mass distribution needs several hundred events in the signal region to work reliably. An additional requirement on the azimuthal distance between the two jets with the highest p_{T} and $\vec{p}_{\mathrm{T}}^{\,\mathrm{miss}}$ of $\Delta\phi\left(\vec{p}_{\mathrm{T}}^{\,\mathrm{jet\ 1,2}}, \vec{p}_{\mathrm{T}}^{\,\mathrm{miss}}\right) > 0.4$ is introduced to reduce backgrounds where the $p_{\mathrm{T}}^{\mathrm{miss}}$ in the event originates from mismeasured jets. This mainly affects the DY+jets background. Figure 6.3 shows the invariant dilepton mass distribution for background simulation when requiring 150 GeV of $p_{\mathrm{T}}^{\mathrm{miss}}$ and at least two jets and for the newly defined signal region, referred to as edge fit region. More than 90% of the background events are rejected by requiring $M_{T2} > 80\,\mathrm{GeV}$ and $\Delta\phi\left(\vec{p}_{\mathrm{T}}^{\,\mathrm{jet\ 1,2}}, \vec{p}_{\mathrm{T}}^{\,\mathrm{miss}}\right) > 0.4$. Besides reducing the number of events from top quark pair production, the DY+jets background is suppressed nearly completely. This is the case for decays into τ leptons as well as light lepton pairs. An additional effect of the M_{T2} requirement is a change of the shape of the invariant dilepton mass distribution, which impacts the extrapolation factor $R_{\mathrm{out/in}}$ for the DY+jets background estimation (see Section 6.3).

About 1000 expected events remain in the edge fit region. To increase the sensitivity of the counting experiment analysis even further, additional bins can be introduced for this part of the analysis. As discussed in Section 6.1, several observables besides M_{T2} offer potential to

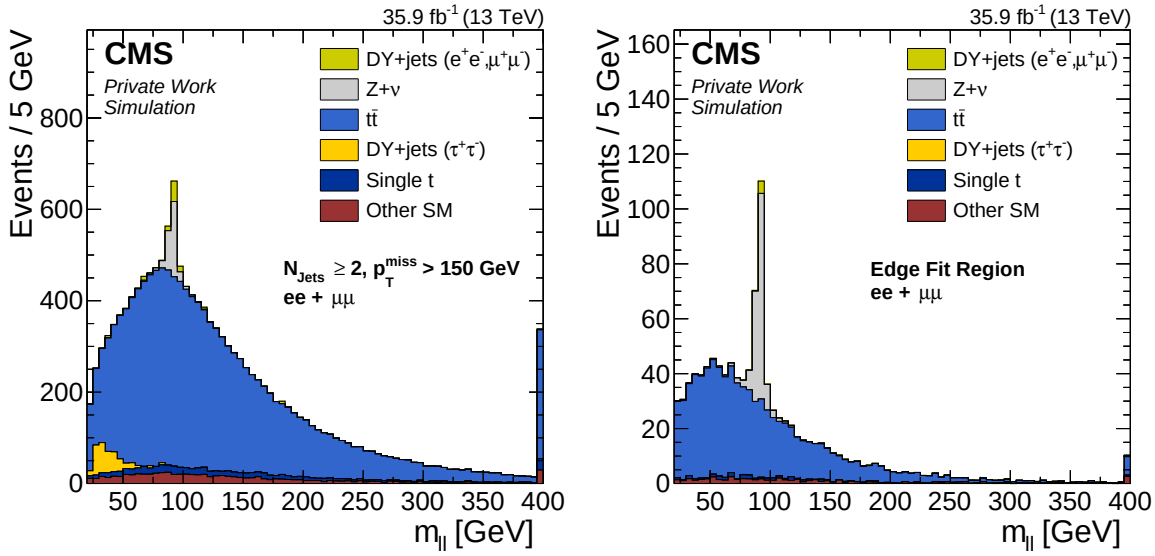

Figure 6.3: Distribution of $m_{\ell\ell}$ in SM simulation when requiring at least two jets and 150 GeV of $p_{\mathrm{T}}^{\mathrm{miss}}$ (left) and in the signal region for the kinematic fit (right). The simulation is normalized to an integrated luminosity of 35.9 fb^{-1}.

distinguish between events from top quark pair production and the signal signature. Since none of the variables offers significantly more potential than the remaining ones and bins in several of them would increase the number of signal regions significantly, a different approach is chosen here. The information of some of these observables is combined into a likelihood to determine how likely it is that an event originates from top quark pair production. To avoid using too many observables as input, it is desirable to use the variables with the highest discrimination power between top quark pair production and a possible signal and to avoid large correlations between the chosen observables. Thereby, each of the observables adds important information to the likelihood discriminator on top of the other included variables.

As a first step, the correlations between eight observables in $\mathrm{t\bar{t}}$ simulation are shown in Fig. 6.4. These observables are the jet multiplicity, H_{T}, $p_{\mathrm{T}}^{\mathrm{miss}}$, $\Delta R_{\ell\ell}$, $\Delta\phi_{\ell\ell}$, $p_{\mathrm{T}}^{\ell\ell}$, $\Sigma m_{\ell b}$, and $\mathrm{M_{T2}}$. To increase the available statistics and observe the correlations to $\mathrm{M_{T2}}$, the signal requirement on $\mathrm{M_{T2}}$ is removed for this check. Strong correlations are observed between $\Delta R_{\ell\ell}$ and $\Delta\phi_{\ell\ell}$ and between the jet multiplicity and H_{T}. This motivates to disregard the less sensitive variable of each pair, namely $\Delta R_{\ell\ell}$ and the number of jets. The hadronic activity shows further moderate correlations to other observables related to the energy scale of the event, mainly $p_{\mathrm{T}}^{\mathrm{miss}}$ and $p_{\mathrm{T}}^{\ell\ell}$, with correlation coefficients up to 0.44. Since especially $p_{\mathrm{T}}^{\mathrm{miss}}$ offers a higher potential to distinguish between signal and background events, H_{T} is discarded as a possible input to the likelihood discriminator. No correlation of $\mathrm{M_{T2}}$ to any of the variables is observed, which supports the decision to use a likelihood discriminator formed from these observables in addition to the $\mathrm{M_{T2}}$ requirement.

The four remaining variables $p_{\mathrm{T}}^{\mathrm{miss}}$, $\Delta\phi_{\ell\ell}$, $p_{\mathrm{T}}^{\ell\ell}$, and $\Sigma m_{\ell b}$ are nearly uncorrelated, with absolute values of the correlation coefficients of less than 0.32, and are used as an input to the $\mathrm{t\bar{t}}$-likelihood discriminator. Figure 6.5 shows the shapes of each of these observables for SF

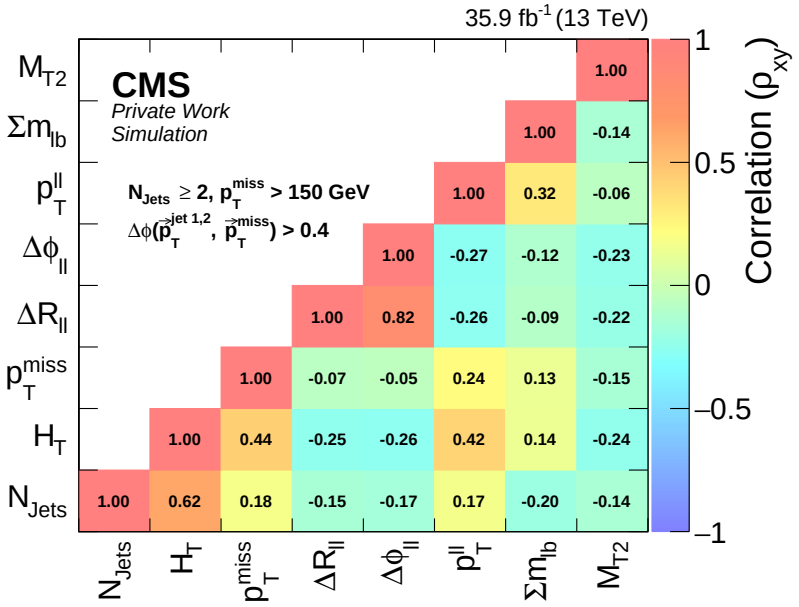

Figure 6.4: Correlation coefficients between jet multiplicity, H_{T}, $p_{\mathrm{T}}^{\mathrm{miss}}$, $\Delta R_{\ell\ell}$, $\Delta\phi_{\ell\ell}$, $p_{\mathrm{T}}^{\ell\ell}$, $\Sigma m_{\ell b}$, and $\mathrm{M_{T2}}$ in $\mathrm{t\bar{t}}$ simulation. Simulated events with at least two jets and 150 GeV of $p_{\mathrm{T}}^{\mathrm{miss}}$ are taken into account.

and DF events in simulation of top quark pair production and for DF events in data. The same selection is used as for the determination of the correlations. To produce the likelihood discriminator, an analytical function is fitted to each of these distributions to obtain the probability density function. The respective fit functions are a sum of two exponentials for $p_{\mathrm{T}}^{\mathrm{miss}}$, a fourth order polynomial for $\Delta\phi_{\ell\ell}$, and a Crystal Ball function [121] for both the dilepton p_{T} and $\Sigma m_{\ell b}$. The fitted functions describe the data and simulation well, except for some deviations around the peak in the $\Sigma m_{\ell b}$ distribution. The discrepancy amounts only to a few percent of the fitted value and has a negligible effect on the final likelihood discriminator. No deviation from flavor-symmetry is observed in top quark pair production and the fitted functions are very similar for $\mathrm{t\bar{t}}$ simulation and DF data.

The negative logarithms of the probability density functions are added up and taken as a discriminator value. Approximately 95% of the $\mathrm{t\bar{t}}$ events have a likelihood discriminator value below 21 and this value is used to split the signal region into two parts: "$\mathrm{t\bar{t}}$-like" events with a discriminator value below 21 and the remaining "not-$\mathrm{t\bar{t}}$-like" events. Figure 6.6 shows the shape of the distribution of the likelihood discriminator value for DF data compared to simulated SF and DF events from top quark pair production. The used samples in the left plot require at least two jets and 150 GeV of $p_{\mathrm{T}}^{\mathrm{miss}}$, while the edge fit signal selection is applied in the right one. Simulated SF distributions are shown for the Z+ν background contribution and several signal points as well. The chosen signal mass scenarios are the same as in Section 6.1.

A very good flavor symmetry is observed for $\mathrm{t\bar{t}}$ events, while the likelihood discriminator on DF data is slightly shifted towards higher values due to small contributions of other SM processes. The event fraction in the not-$\mathrm{t\bar{t}}$-like selection in the more inclusive selection is

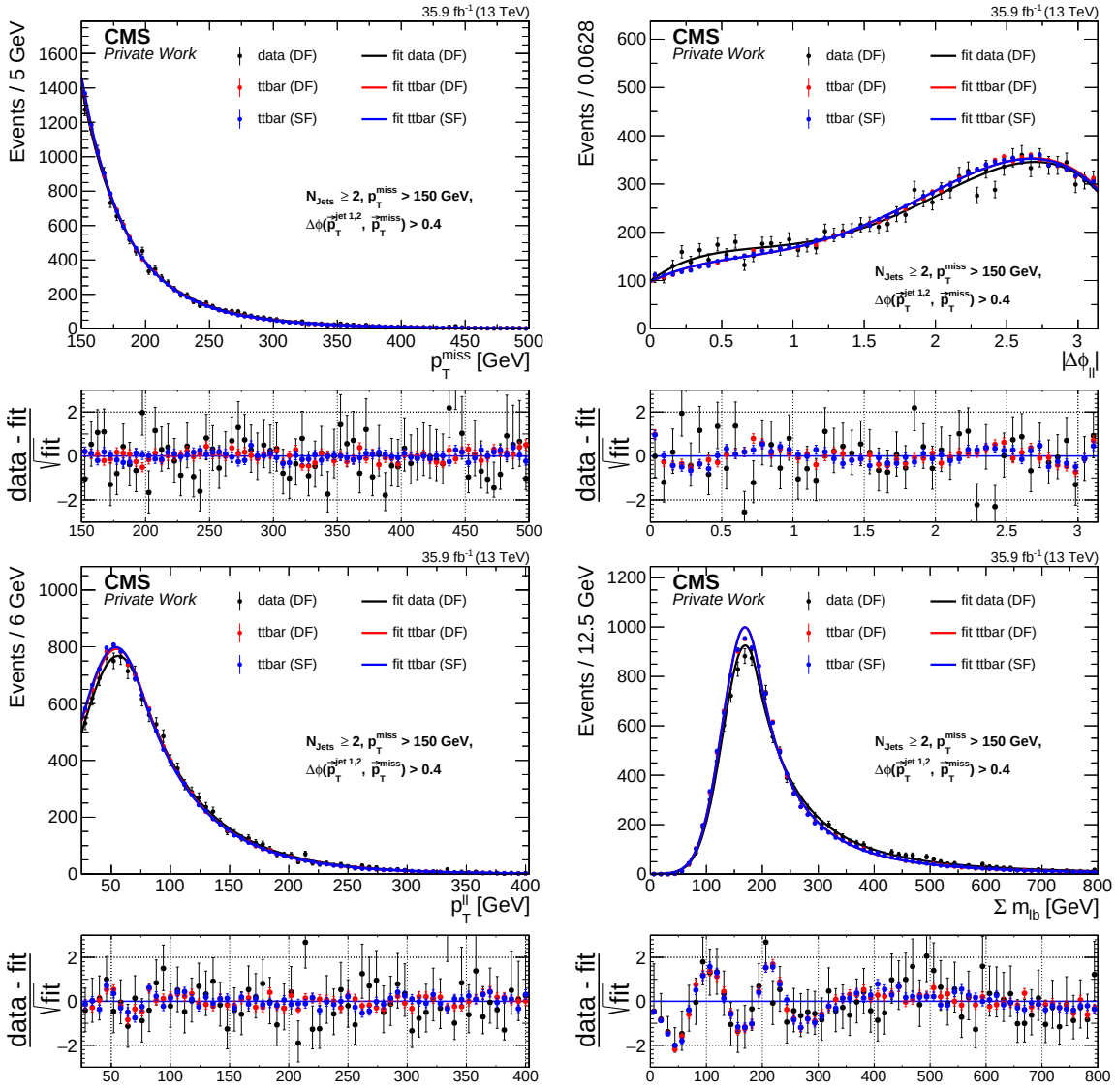

Figure 6.5: Distributions of $p_{\mathrm{T}}^{\mathrm{miss}}$ (top left), $\Delta\phi_{\ell\ell}$ (top right), $p_{\mathrm{T}}^{\ell\ell}$ (bottom left), and $\Sigma m_{\ell b}$ (bottom right) in the signal selection for the kinematic fit. Different-flavor pairs in data are compared to SF and DF yields in $\mathrm{t\bar{t}}$ simulation. An analytic function is fitted to each of these distributions and the lower panel in each plot shows the difference between the observation and the fit, divided by the square root of the number of fitted events, for each of the three samples.

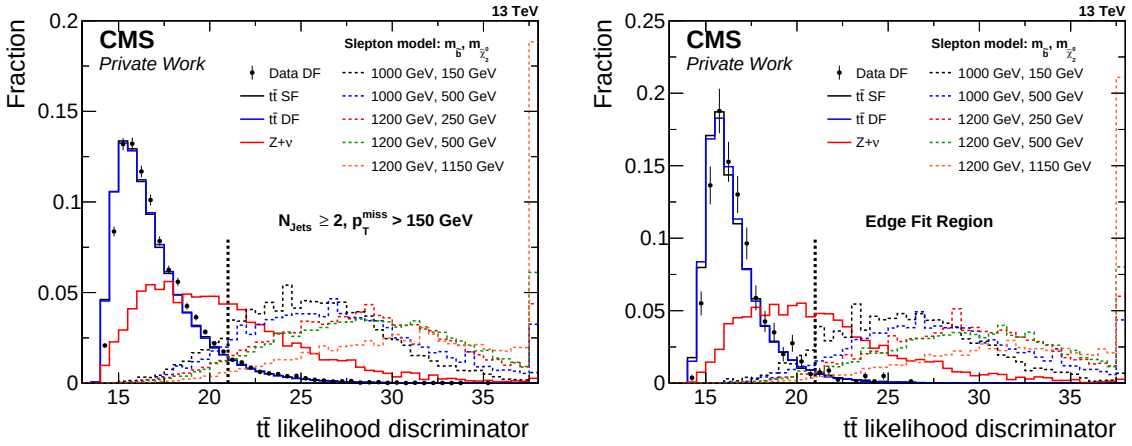

Figure 6.6: Shape of the $t\bar{t}$ likelihood discriminator distribution for events with at least two jets and at least 150 GeV of $p_{\mathrm{T}}^{\mathrm{miss}}$ (left) and in the edge fit signal region (right). The shape for DF events in data is shown as black dots and compared to the shapes in simulated DF and SF events of top quark pair production displayed as blue and black solid lines, respectively. Simulated SF events for the Z+ν background (red solid line) and five signal scenarios indicated by dashed lines are shown as well. The cut value to distinguish between the $t\bar{t}$-like and not-$t\bar{t}$-like selection is marked by a vertical dashed line. Each distribution is normalized to unity.

7.0% in data and 6.4% in $t\bar{t}$ simulation, while it is reduced to 3.3% and 2.8% respectively in the edge fit region. In contrast to this, 40–50% of the simulated Z+ν background events are categorized as not-$t\bar{t}$-like, while the fraction ranges from 85% to more than 95% for the considered signal scenarios.

As was shown in Section 6.1, the invariant dilepton mass distributions can differ quite strongly between signal scenarios and top quark pair production as well as different mass scenarios of the slepton model. To be sensitive to different scenarios of neutralino mass differences, the invariant dilepton mass has not been incorporated into the likelihood discriminator and additional bins in $m_{\ell\ell}$ are used instead. In total, seven mass bins are defined, excluding the on-Z mass range to avoid overlap with an existing specialized CMS SUSY on-Z search that is included in [10] as well. The mass bins are chosen to obtain similar flavor-symmetric contributions in each not-$t\bar{t}$-like mass bin.

The signal region requirements and sub selections in the counting experiment analysis are summarized in Tab. 6.1.

Simulated event yields for top quark pair production and the five signal scenarios used above for certain selection requirements are stated in Tab. 6.2. Expected dilepton events refers to the value obtained by multiplying integrated luminosity, production cross section, and branching fraction into the final state with at least one SF lepton pair. In the upper third of the table, the requirements are added subsequently. The simulated event yields in the lower parts of the table refer to the 14 signal bins and all requirements in the first part of the table are applied as well. Only the statistical uncertainties in the simulated samples are given. The lepton selection and signal region requirements reduce the number of events from top quark pair

	Selection
Edge fit region	Inclusive dilepton selection $N_{\text{Jets}} \geq 2$ and $p_{\text{T}}^{\text{miss}} > 150\,\text{GeV}$ $\text{M}_{\text{T2}} > 80\,\text{GeV}$ $\Delta\phi\left(\vec{p}_{\text{T}}^{\text{ jet 1,2}}, \vec{p}_{\text{T}}^{\text{miss}}\right) > 0.4$
sub selections for counting experiment analysis	
$\text{t}\bar{\text{t}}$-like	$\text{t}\bar{\text{t}}$-likelihood < 21
not-$\text{t}\bar{\text{t}}$-like	$\text{t}\bar{\text{t}}$-likelihood > 21
$m_{\ell\ell}$ binning [GeV]	20–60, 60–86, 96–150, 150–200, 200–300, 300–400, > 400

Table 6.1: Summary of signal regions selections. The basic signal region selection is used for the kinematic fit while the sub selections are used in the counting experiment analysis.

production by 3 orders of magnitude to about 840 events. Most of these events contribute to the $\text{t}\bar{\text{t}}$-like selection at low invariant dilepton mass. In contrast to this, 10–25% of the expected SF events enter the signal selection for the displayed signal scenarios, contributing mainly to the not-$\text{t}\bar{\text{t}}$-like signal bins. The mass of the $\tilde{\chi}_2^0$ and thereby the difference to the mass of the lightest neutralino, which is set to 100 GeV, determines to which mass bins a signal point mainly contributes. The number of signal events in these bins are of a similar size or larger than the expected contribution from top quark pair production, indicating that the analysis is sensitive to such signal scenarios.

6.3 Background prediction methods for the newly defined signal regions

The background prediction methods from data rely on the extrapolation from control regions to the signal region. The additional requirements on M_{T2} and the likelihood discriminator could disturb this extrapolation and might make redefinitions of control regions or adaptions of the methods necessary. Since the probability density function for the $p_{\text{T}}^{\text{miss}}$ distribution takes only events with $p_{\text{T}}^{\text{miss}} > 150\,\text{GeV}$ into account, the likelihood discriminator is not well defined in the control regions and the input observables need to be investigated instead.

The dependency of the direct $R_{SF/DF}$ measurement and the input factors of the factorization method, R_{T} and $r_{\mu/e}$, on M_{T2} and the input variables for the likelihood discriminator have either been studied in Section 5.2.1 or are shown in Appendix C–E. No dependency on any of these variables can be observed which indicates that the methods for the prediction of the flavor-symmetric background component do not need to be adapted. The flavor-symmetric background estimates are summarized in Tab. 6.3. The $R_{SF/DF}$ values obtained by the factorization method show a trend towards smaller values for higher mass bins. This is expected since a larger value of $m_{\ell\ell}$ usually correspond to larger lepton momenta and thereby lower values of $r_{\mu/e}$. The uncertainty in the flavor-symmetric background prediction is driven by the limited number of DF events, which ranges from only a few events in the not-$\text{t}\bar{\text{t}}$-like bins up to several hundred events in the $\text{t}\bar{\text{t}}$-like cases at low invariant dilepton masses.

Due to the emulated decay of a photon into two leptons, the $p_{\text{T}}^{\text{miss}}$-template method can be used to provide predictions in the Z boson mass window for the signal selection in both likelihood bins. As discussed in Section 6.2, the requirement on M_{T2} changes the shape of

	SF events					
	top quark pair	Slepton model $m_{\tilde{b}}$, $m_{\tilde{\chi}_2^0}$ [GeV]				
Selection	production	1000, 150	1000, 500	1200, 250	1200, 500	1200, 1150
Expected SF events	963 000	173	173	45	45	45
OCSF, $p_{\mathrm{T}}^{\ell} > 25/20\,\mathrm{GeV}$	278 463±100	64.2±0.5	82.0±0.5	20.6±0.1	21.6±0.1	21.4±0.1
$m_{\ell\ell} > 20\,\mathrm{GeV}$	271 768±99	56.5±0.4	82.0±0.5	20.4±0.1	21.6±0.1	21.4±0.1
$\mathrm{p}_{\mathrm{T}}^{\ell\ell} > 25\,\mathrm{GeV}$	245 908±94	56.3±0.4	81.5±0.5	20.3±0.1	21.5±0.1	21.3±0.1
jet-multiplicity ≥ 2	42 637±39	50.3±0.4	67.4±0.5	17.6±0.1	18.5±0.1	16.5±0.1
$\Delta\phi(\mathrm{jet}_{1,2}, p_{\mathrm{T}}^{\mathrm{miss}}) > 0.4$	37 282±37	46.7±0.4	58.2±0.4	15.6±0.1	16.2±0.1	13.7±0.1
$p_{\mathrm{T}}^{\mathrm{miss}} > 150\,\mathrm{GeV}$	10 573±20	46.2±0.4	57.2±0.4	15.4±0.1	15.9±0.1	13.6±0.1
$\mathrm{M_{T2}} > 80\,\mathrm{GeV}$	844.2±5.5	18.1±0.2	38.2±0.4	7.8±0.1	10.4±0.1	10.8±0.1
$\mathrm{t\bar{t}}$-like						
$20 < m_{\ell\ell} < 60\,\mathrm{GeV}$	284.5±3.2	1.6±0.1	<0.1	<0.1	<0.1	<0.1
$60 < m_{\ell\ell} < 86\,\mathrm{GeV}$	179.8±2.6	<0.1	<0.1	<0.1	<0.1	<0.1
$96 < m_{\ell\ell} < 150\,\mathrm{GeV}$	177.1±2.5	<0.1	0.25±0.03	0.11±0.01	<0.1	<0.1
$150 < m_{\ell\ell} < 200\,\mathrm{GeV}$	67.4±1.6	<0.1	0.27±0.03	<0.1	<0.1	<0.1
$200 < m_{\ell\ell} < 300\,\mathrm{GeV}$	41.6±1.2	<0.1	0.76±0.05	<0.1	<0.1	<0.1
$300 < m_{\ell\ell} < 400\,\mathrm{GeV}$	9.4±0.6	<0.1	0.49±0.04	<0.1	<0.1	<0.1
$m_{\ell\ell} > 400\,\mathrm{GeV}$	4.9±0.4	<0.1	<0.1	<0.1	<0.1	0.12±0.01
Not-$\mathrm{t\bar{t}}$-like						
$20 < m_{\ell\ell} < 60\,\mathrm{GeV}$	3.9±0.4	16.4±0.2	1.0±0.1	1.25±0.03	0.24±0.01	<0.1
$60 < m_{\ell\ell} < 86\,\mathrm{GeV}$	3.2±0.3	<0.1	1.4±0.1	1.48±0.04	0.42±0.02	0.14±0.01
$96 < m_{\ell\ell} < 150\,\mathrm{GeV}$	5.6±0.5	<0.1	4.2±0.1	3.76±0.06	1.16±0.03	0.26±0.02
$150 < m_{\ell\ell} < 200\,\mathrm{GeV}$	3.6±0.4	<0.1	4.6±0.1	<0.1	1.29±0.03	0.24±0.01
$200 < m_{\ell\ell} < 300\,\mathrm{GeV}$	3.5±0.4	<0.1	11.6±0.2	<0.1	3.24±0.05	0.66±0.02
$300 < m_{\ell\ell} < 400\,\mathrm{GeV}$	2.0±0.3	<0.1	10.2±0.2	<0.1	2.79±0.05	0.88±0.03
$m_{\ell\ell} > 400\,\mathrm{GeV}$	2.0±0.3	<0.1	1.1±0.1	<0.1	0.29±0.02	7.87±0.08

Table 6.2: Simulated event yields for top quark pair production and five signal scenarios for different selection requirements. Expected SF events refers to the value obtained by multiplying luminosity, production cross section, and branching fraction into the final state with at least two same-flavor leptons. The requirements in the first part of the table are added subsequently and applied for the signal bins in the lower parts as well. Only statistical uncertainties in the simulated samples are given.

$m_{\ell\ell}$ range [GeV]	DF	Pred. fact. meth.	$R^{\text{fact.}}_{\text{SF/DF}}$	$R^{\text{direct}}_{\text{SF/DF}}$	$R^{\text{comb.}}_{\text{SF/DF}}$	FS pred.
$t\bar{t}$-like						
20-60	264	$287.9^{+18.3}_{-17.2}\pm14.3$	1.09±0.05	1.10±0.05	1.10±0.04	$289.5^{+18.4}_{-17.3}\pm9.4$
60-86	164	$178.8^{+14.5}_{-13.4}\pm8.8$	1.09±0.05	1.10±0.05	1.10±0.04	$180.1^{+14.6}_{-13.5}\pm5.9$
96-150	160	$173.7^{+14.3}_{-13.2}\pm8.4$	1.09±0.05	1.11±0.05	1.10±0.04	$175.5^{+14.4}_{-13.3}\pm5.7$
150-200	67	$72.8^{+10.0}_{-8.9}\pm3.5$	1.09±0.05	1.11±0.05	1.10±0.04	$73.7^{+10.1}_{-9.0}\pm2.4$
200-300	43	$46.4^{+8.2}_{-7.0}\pm2.2$	1.08±0.05	1.11±0.05	1.10±0.04	$47.1^{+8.3}_{-7.2}\pm1.5$
300-400	17	$18.2^{+5.6}_{-4.4}\pm0.8$	1.07±0.05	1.11±0.05	1.09±0.03	$18.5^{+5.7}_{-4.4}\pm0.6$
>400	4	$4.2^{+3.4}_{-2.0}\pm0.2$	1.06±0.05	1.09±0.05	1.08±0.03	$4.3^{+3.4}_{-2.1}\pm0.1$
not-$t\bar{t}$-like						
20-60	3	$3.2^{+3.1}_{-1.8}\pm0.2$	1.08±0.05	1.11±0.05	1.09±0.03	$3.3^{+3.2}_{-1.8}\pm0.1$
60-86	3	$3.2^{+3.1}_{-1.7}\pm0.1$	1.06±0.05	1.09±0.05	1.08±0.03	$3.2^{+3.1}_{-1.8}\pm0.1$
96-150	6	$6.5^{+3.9}_{-2.6}\pm0.3$	1.09±0.05	1.12±0.05	1.10±0.04	$6.6^{+4.0}_{-2.6}\pm0.2$
150-200	5	$5.3^{+3.6}_{-2.3}\pm0.2$	1.07±0.05	1.09±0.05	1.08±0.03	$5.4^{+3.7}_{-2.3}\pm0.2$
200-300	3	$3.2^{+3.1}_{-1.7}\pm0.1$	1.06±0.05	1.09±0.05	1.08±0.03	$3.2^{+3.1}_{-1.8}\pm0.1$
300-400	3	$3.2^{+3.1}_{-1.8}\pm0.1$	1.07±0.05	1.11±0.05	1.09±0.03	$3.3^{+3.2}_{-1.8}\pm0.1$
>400	1	$1.1^{+2.4}_{-0.9}\pm0.0$	1.06±0.05	1.09±0.05	1.07±0.03	$1.1^{+2.5}_{-0.9}\pm0.0$

Table 6.3: Resulting estimates for the flavor-symmetric background contribution. The factorization method is applied on an event-by-event basis to the DF event yields. The corresponding value of $R_{\text{SF/DF}}$ is obtained by dividing the background estimation from the factorization method by the DF event yield. The $R_{\text{SF/DF}}$ values from the direct measurement take the event fractions in the central and forward lepton selection into account. A weighted average is used to combine both $R_{\text{SF/DF}}$ values. This value is applied to the DF event yield to obtain the combined prediction.

the $m_{\ell\ell}$ distribution and thereby also the factor $R_{\text{out/in}}$ to extrapolate from the on-Z mass window to the respective mass bin. Figure 6.7 shows $R_{\text{out/in}}$ as a function of M_{T2} for data and simulation in the DY+jets control region. The mass bins below and above the Z boson mass are combined for simplicity. An upward trend is observed for the high mass selection and a downward trend for low invariant masses.

Due to the dependency on M_{T2}, the requirement of $\text{M}_{\text{T2}} > 80\,\text{GeV}$ is added to the DY+jets control region when determining $R_{\text{out/in}}$ for the new signal regions. The resulting event yields and extrapolation factors for the seven mass bins are summarized in Tab. 6.4. Because of the small statistics after adding the M_{T2} requirement, no additional dependency studies are possible and a systematic uncertainty of 50% is assigned to $R_{\text{out/in}}$ for the $m_{\ell\ell}$ bins below 150 GeV. In case of the mass bins above 150 GeV, the available statistics and thus the $R_{\text{out/in}}$ values are even smaller and the systematic uncertainty is increased to 100%. The $p_{\text{T}}^{\text{miss}}$-template method predicts only about 20 events in the Z mass window of the edge fit region with a fraction of approximately 65% in the not-$t\bar{t}$-like selection. The extrapolated predictions amount to less than two events in each individual signal region for the counting experiment analysis making the DY+jets background the least significant background contribution in all signal bins.

Since the Z+ν background is taken directly from simulation, the emulated event yields can be obtained directly for each signal region.

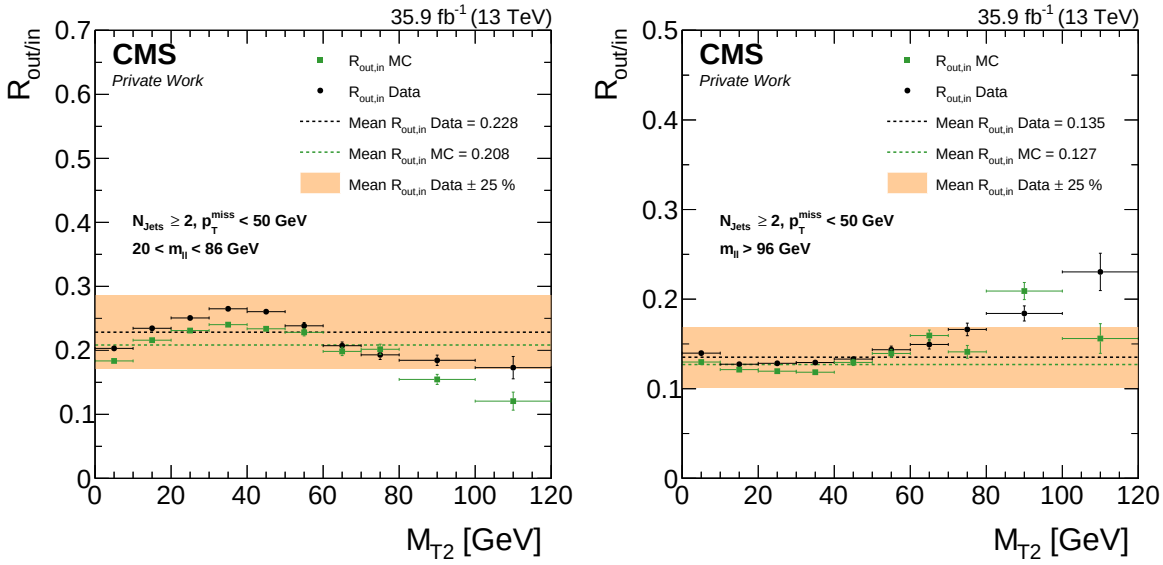

Figure 6.7: $R_{\mathrm{out/in}}$ as a function of $\mathrm{M_{T2}}$ in the DY+jets control region for the combined mass bins below (left) and above the Z boson mass (right) for data (black) and simulation (green). The central value obtained in data (simulation) is shown as a black (green) dashed line, while the systematic uncertainty of 25% used in Section 5.2.2 is indicated as an orange band around the central value in data.

	Data		MC	
	N_{in} 4295±65		N_{in} 3923±62	
mass range [GeV]	N_{out}	$R_{\mathrm{out/in}}$	N_{out}	$R_{\mathrm{out/in}}$
20-60	229±15	0.053±0.027	136±12	0.035±0.018
60-86	551±23	0.128±0.064	451±21	0.115±0.058
96-150	671±26	0.156±0.078	622±25	0.159±0.080
150-200	74±9	0.017±0.017	53±8	0.014±0.014
200-300	52±9	0.012±0.012	50±8	0.013±0.013
300-400	22±5	0.005±0.005	19±5	0.005±0.005
>400	23±5	0.006±0.006	25±5	0.007±0.007

Table 6.4: Results of the calculation of $R_{\mathrm{out/in}}$ in the seven mass regions for data and simulation.

7 Counting experiment analysis

In the counting experiment approach, the number of observed SF events is compared to the estimate from flavor-symmetric, DY+jets, and Z+ν backgrounds in fourteen signal regions defined in $m_{\ell\ell}$ and the likelihood discriminator. The results of the counting experiment analysis are presented and discussed in this chapter.

The background predictions and observed data yields for all signal regions are summarized in Tab. 7.1. To visualize the shapes and account for the differing bin widths, the $m_{\ell\ell}$ distributions for $t\bar{t}$-like and not-$t\bar{t}$-like events are given in events per GeV on a linear scale in Fig. 7.1. A second visualization of the results in Fig. 7.2 uses a logarithmic scale and the event yields in each bin to emphasize the relative background contributions and to increase the visibility of signal regions with small event yields. Flavor-symmetric processes are the dominant background contribution in all signal regions except for the two invariant dilepton mass bins closest to the Z boson mass in the not-$t\bar{t}$-like case. In these two bins the Z+ν background is at least of similar size. The statistical uncertainty in the number of DF events is the driving uncertainty in all other cases.

$m_{\ell\ell}$ range [GeV]	FS	DY+jets	Z+ν	Total background	Data	Significance [s. d.]
$t\bar{t}$-like						
20–60	290^{+21}_{-20}	0.4±0.3	1.4±0.6	291^{+21}_{-20}	273	-0.4
60–86	180^{+16}_{-15}	0.9±0.7	8.9±3.9	190^{+16}_{-15}	190	0.0
96–150	175^{+16}_{-15}	1.1±0.9	6.4±2.9	183^{+16}_{-15}	193	0.5
150–200	74^{+10}_{-9}	0.1±0.1	0.5±0.2	74^{+10}_{-9}	66	-0.6
200–300	$47.1^{+8.5}_{-7.3}$	< 0.1	0.3±0.1	$47.5^{+8.5}_{-7.3}$	42	-0.5
300–400	$18.5^{+5.7}_{-4.5}$	< 0.1	< 0.1	$18.6^{+5.7}_{-4.5}$	11	-1.2
> 400	$4.3^{+3.4}_{-2.1}$	< 0.1	0.1±0.1	$4.5^{+3.4}_{-2.1}$	4	-0.1
Not-$t\bar{t}$-like						
20–60	$3.3^{+3.2}_{-1.8}$	0.7±0.5	1.4±0.5	$5.3^{+3.3}_{-1.9}$	6	0.2
60–86	$3.2^{+3.1}_{-1.8}$	1.6±1.3	6.4±2.9	$11.3^{+4.5}_{-3.6}$	19	1.4
96–150	$6.6^{+4.0}_{-2.6}$	1.9±1.5	6.1±2.9	$14.7^{+5.1}_{-4.2}$	27	1.9
150–200	$5.4^{+3.7}_{-2.3}$	0.2±0.3	0.6±0.3	$6.2^{+3.7}_{-2.4}$	7	0.2
200–300	$3.2^{+3.1}_{-1.8}$	0.2±0.2	0.4±0.2	$3.8^{+3.2}_{-1.8}$	4	0.1
300–400	$3.3^{+3.2}_{-1.8}$	< 0.1	0.1±0.1	$3.5^{+3.2}_{-1.8}$	0	-2.2
> 400	$1.1^{+2.5}_{-0.9}$	< 0.1	0.4±0.2	$1.5^{+2.5}_{-0.9}$	5	1.4

Table 7.1: Predicted and observed yields in each of the 14 signal bins of the counting experiment approach. The given uncertainties include statistical and systematic sources.

The agreement between expected and observed event yield in each signal region is quantified using a profile likelihood ratio. In Section 9.3, the results of all signal bins will be combined to provide exclusion limits and observed significances for the slepton model. Since the determination of both the exclusion limits and the agreement between observation and expectation use similar methods, a combined description is given here. The methods rely on the modified

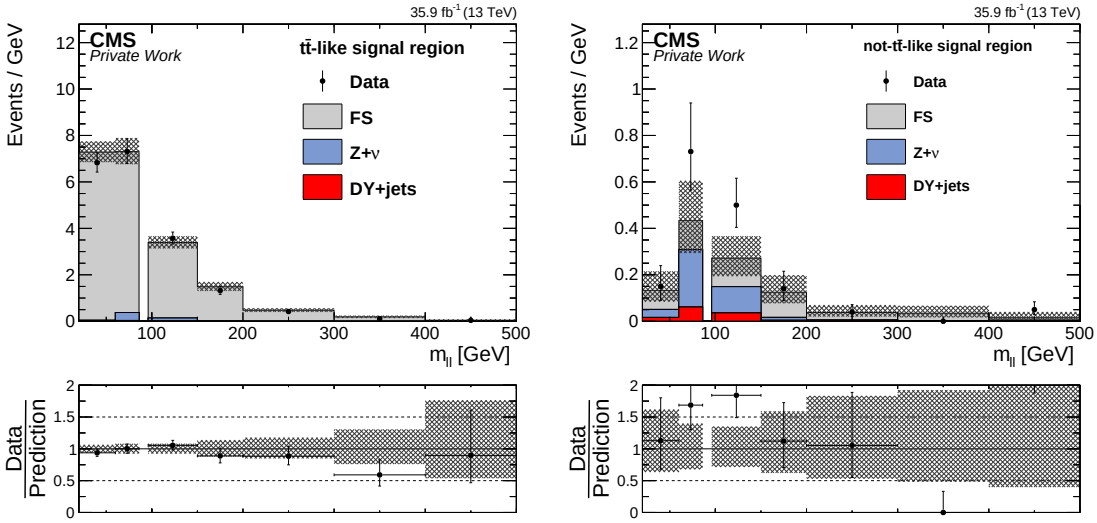

Figure 7.1: Distribution of $m_{\ell\ell}$ in the $\mathrm{t\bar{t}}$-like (left) and not-$\mathrm{t\bar{t}}$-like (right) signal regions of the counting experiment analysis. A 5 GeV window around the Z boson mass is excluded. The number of data events, shown as black dots, is compared to the total background estimate. The flavor-symmetric background component is indicated as a gray area, while the non-flavor-symmetric contributions from Z+ν and DY+jets processes are shown as light blue and red areas respectively. In the lower panels, the ratio of data to the background prediction is displayed. The total uncertainty in the background prediction is indicated as a hatched band.

frequentist CL_s method [122, 123] and were established by the combination of the Higgs boson searches of the ATLAS and CMS collaborations [24, 124]. An asymptotic formulation [125] implemented in the RooStats framework [126] is used to obtain the results. For a few signal points, the exclusion limits obtained with the asymptotic formulation are cross checked with a more accurate but also more resource intensive method relying on a large number of toy data sets. The results deviate very little from the approximate formulation and thereby justify the use of the asymptotic approach.

Both the observed significances and the exclusion limits rely on a likelihood function defined as

$$\mathcal{L}\left(\text{data}|\mu,\theta\right) = \prod_i \frac{\left(\mu s_i + b_i\right)^{n_i}}{n_i!} e^{-(\mu s_i + b_i)} p\left(\tilde{\theta}|\theta\right), \tag{7.1}$$

where "data" represents either the observation or pseudo-data (toy data). The signal strength parameter μ, is used to scale the signal cross section, and thus the signal yield, simultaneously in all signal bins. A signal strength of $\mu = 0$ corresponds to the background-only hypothesis. The systematic uncertainties θ on both background and signal are sometimes referred to as nuisance parameters, and $p\left(\tilde{\theta}|\theta\right)$ is the parameterization of these parameters, taking the nominal values $\tilde{\theta}$ into account. The different systematic uncertainties are assumed to be uncorrelated among each other but fully correlated between the different signal bins. In Section 9.3, s_i refers to the number of simulated signal events in each signal region i. When looking at the agreement between observation and expectation in this chapter, each signal

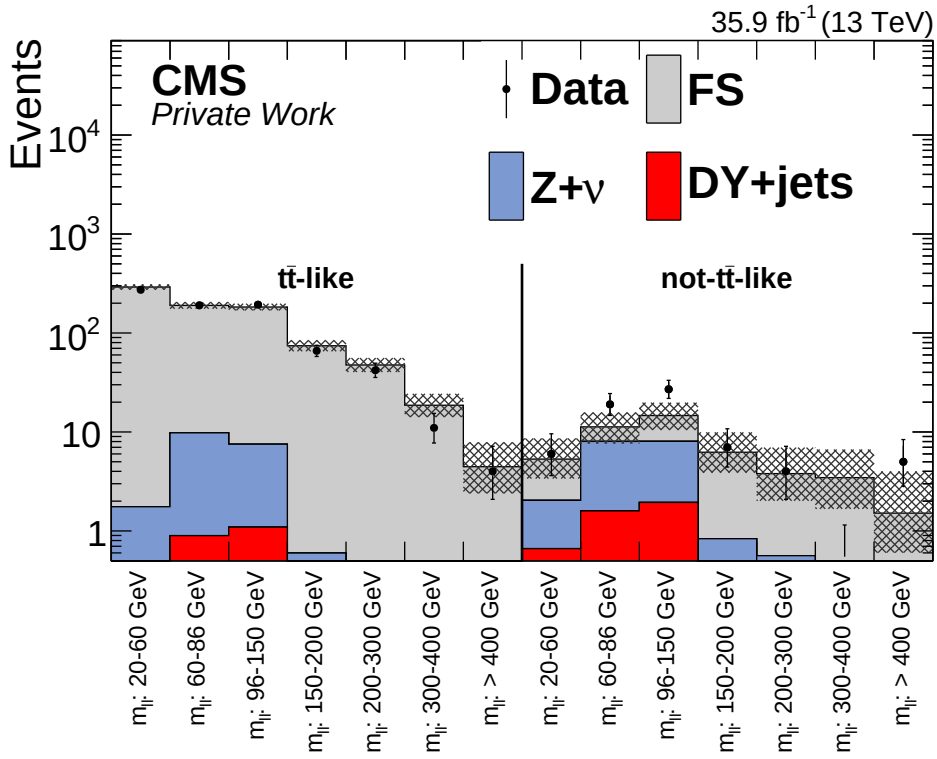

Figure 7.2: Results of the counting experiment analysis in each signal region. The number of data events, shown as black dots is compared to the total background estimate. The flavor-symmetric background component is indicated as a gray area, while the non-flavor-symmetric contributions from Z+ν and DY+jets processes are shown as light blue and red areas respectively. The total uncertainty in the background prediction is displayed as a hatched band.

region i is treated individually and the s_i are arbitrarily set to 1. In this case, the signal contribution is modified by μ when the global maximum is determined and set to 0 for the background-only hypothesis. Similarly, b_i and n_i stand for the background prediction and the number of observed events in bin i, respectively.

A test statistics $\tilde{q}_\mu$, to distinguish between the background-only and signal+background hypothesis, is defined as the likelihood ratio

$$\tilde{q}_\mu = -2 \ln \frac{\mathcal{L}\left(\text{data}|\mu, \hat{\theta}_\mu\right)}{\mathcal{L}\left(\text{data}|\hat{\mu}, \hat{\theta}\right)}, \tag{7.2}$$

where $\hat{\theta}_\mu$ refers to the nuisance parameters for a given signal strength, while $\hat{\mu}$ and $\hat{\theta}$ are the parameters for the global maximum of the likelihood. The probabilities to obtain a value of $\tilde{q}_\mu$ that is larger than the one for a given signal strength are referred to as:

$$CL_{s+b}(\mu) = P\left(\tilde{q}_\mu \geq \tilde{q}_\mu^{obs}|\text{signal} + \text{background}\right), \tag{7.3}$$

$$CL_b(\mu) = P\left(\tilde{q}_\mu \geq \tilde{q}_\mu^{obs}|\text{background-only}\right), \tag{7.4}$$

for the signal+background and background-only hypothesis. The upper limit on the signal cross section is given by the value of μ for which

$$CL_s(\mu) = \frac{CL_{s+b}(\mu)}{CL_b(\mu)}. \tag{7.5}$$

is equal to 0.05, corresponding to a 95% confidence level (CL).

The agreement between observation and expectation is quantified by converting the p-value of the background only hypothesis $CL_b(\mu)$ into a significance, expressed in standard deviations (s. d.). The observed agreement in Tab. 7.1 is as expected for 14 signal regions dominated by statistical uncertainties. An upward or downward deviation of more than 1 s. d. is obtained in five signal bins. The largest discrepancies with a magnitude of about 2 s. d. are observed in the not-$t\bar{t}$-like regions with $m_{\ell\ell}$ between 96 and 150 GeV and between 300 and 400 GeV. In the former $15.3^{+5.4}_{-4.6}$ events are predicted and 27 are observed, while the latter shows a downward fluctuation of the SF data resulting in 0 observed events.

8 Search for a kinematic edge

As a second approach, a fit to the invariant dilepton mass distribution is performed to search for an edge signature which is characteristic for OCSF lepton pairs from a decay of a $\tilde{\chi}_2^0$ into a $\tilde{\chi}_1^0$ via an intermediate slepton or an off-shell Z boson. The fit is performed simultaneously on $e^{\pm}e^{\mp}$, $\mu^{\pm}\mu^{\mp}$, and $e^{\pm}\mu^{\mp}$ data using the RooFit toolkit [127].

Different analytic functions are used to model the contributions of flavor-symmetric backgrounds, backgrounds containing the decay of a Z/γ^* boson, and the potential signal. Like the background from Z boson decays, the signal is expected to only contribute to the SF samples. The DF sample is used as a constraint for the flavor-symmetric background model.

After introducing the background and signal models that are used in the combined fit, the procedure is validated on simulation and in a data control region before applying it to the data in the signal region.

The basic principles and the implementation of the fit are based on the developments for previous versions of this analysis [6, 9] and similar validation steps are undertaken. The main differences are a newly defined signal region with different event kinematics and an improved parameterization of the flavor-symmetric background component.

8.1 Background and signal models

The parameterizations of the two background components and the signal contribution are discussed in this section.

8.1.1 Flavor-symmetric background model

Most of the events in the signal region of the edge fit originate from flavor-symmetric processes. To ensure the validity of the description of this important background contribution several different parameterizations are studied. Beside the nominal parameterization, which is used in most cases, two alternatives are used to cross check the results.

Nominal parameterization

The flavor-symmetric background contribution is modeled using a Crystal Ball function [121], $\mathcal{P}_{FS}(m_{\ell\ell})$, which contains a Gaussian part to model the peak of the distribution and one of the flanks, and a power-law tail at the other side:

$$\mathcal{P}_{FS}(m_{\ell\ell}) = \begin{cases} \exp\left(-\frac{(m_{\ell\ell}-\mu_{FS})^2}{2\sigma_{FS}^2}\right) & \text{if } \frac{m_{\ell\ell}-\mu_{FS}}{\sigma_{FS}} < \alpha_{FS} \\ A\left(B + \frac{m_{\ell\ell}-\mu_{FS}}{\sigma_{FS}}\right)^{-n_{FS}} & \text{if } \frac{m_{\ell\ell}-\mu_{FS}}{\sigma_{FS}} > \alpha_{FS}, \end{cases} \tag{8.1}$$

with

$$A = \left(\frac{n_{FS}}{|\alpha_{FS}|}\right)^{n_{FS}} \quad \text{and} \quad B = \frac{n_{FS}}{|\alpha_{FS}|} - |\alpha_{FS}| \ . \tag{8.2}$$

Since the function and its derivative need to be continuous, the model for the FS background has five free parameters: the overall normalization, the mean μ_{FS} and width σ_{FS} of the Gaussian part, the transition point α_{FS} between the Gaussian part and the power low tail, and the power law parameter n_{FS}. While the normalization differs for the three lepton flavor combinations, they use the same shape parameters:

$$\mathbf{p}_{FS} = (\mu_{FS}, \sigma_{FS}, \alpha_{FS}, n_{FS}) \,. \tag{8.3}$$

Parameterization from 2012 analysis

In a previous version of analysis on 8 TeV data [5, 6] the parameterization of the flavor-symmetric background component contained three parts: The rising flank was modeled by a power law, the peak region by a third order polynomial, and the falling part by an exponential:

$$\mathcal{P}_{FS}\left(m_{\ell\ell}\right) = \begin{cases} c_1 \cdot m_{\ell\ell}^{\alpha} & \text{if } m_{\ell\ell} < m_{\ell\ell}^{(1)} \\ \sum_{i=0}^{3} c_{2,i} \cdot m_{\ell\ell}^{i} & \text{if } m_{\ell\ell}^{(1)} < m_{\ell\ell} < m_{\ell\ell}^{(2)} \\ c_e \cdot e^{-\beta m_{\ell\ell}} & \text{if } m_{\ell\ell}^{(2)} < m_{\ell\ell}. \end{cases} \tag{8.4}$$

Assuming again continuity of the function and its derivative at the transition points $m_{\ell\ell}^{(1)}$ and $m_{\ell\ell}^{(2)}$, five shape parameters and the overall normalization remain as free parameters. The shape was found to describe the flavor-symmetric background contribution well in most cases. Because of the additional free parameter, the fit requires notably more time to converge than with the nominal shape and in some rare cases the fit does not converge at all. For these reasons, the shape was abandoned except to perform cross-checks of the results.

Kernel density estimator (KDE)

Instead of using an analytical function, the binned invariant dilepton mass distribution in the DF channel can be used directly to predict the distribution in the SF data. The advantage of this approach is, not to require any prior knowledge of the flavor-symmetric background shape. A large disadvantage is the susceptibility towards statistical fluctuations if the distribution is used directly. To avoid these large statistical fluctuations, a smoothed version of the distribution in DF data can be used.

A kernel density estimator is utilized to predict the background shape in SF data from the distribution in the DF sample. Gaussian distributions for each DF event are summed up to construct the shape in SF data. The mean of each Gaussian is set to the $m_{\ell\ell}$ value of the event. The RooFit implementation of one-dimensional kernel probability density functions, summarized in the RooKeysPdf class, is used for this purpose. The kernel density

$$\hat{f}_h\left(m_{\ell\ell}\right) = \frac{1}{nh} \sum_{i=1}^{n} K\left(\frac{m_{\ell\ell} - m_{\ell\ell,i}}{h}\right) \tag{8.5}$$

is used to estimate the probability density function for the random variable $m_{\ell\ell}$ using the n entries in the DF sample, a smoothing parameter h, and the kernel K, which is a Gaussian distribution in this analysis [128]. Depending on the density of events, the widths of

the Gaussian distributions are adapted. In case of high densities a narrow width offers the potential to preserve details of the distribution, while at low densities, larger widths allow to smooth the resulting shape. The method is not suitable to provide quantitative results since the background shape needs to be fixed on the DF sample and no shape uncertainties can be included in the fit, but it can be used as a cross-check for the nominal shape.

8.1.2 Model for Z/γ^* boson backgrounds

In contrast to the counting experiment analysis, the non-flavor-symmetric backgrounds are not split into contributions with and without genuine $p_{\mathrm{T}}^{\mathrm{miss}}$ from neutrinos. Therefore, the Z/γ^* boson background in the fit corresponds to the combination of the DY+jets and Z+ν background processes in the counting experiment approach.

The shape for backgrounds containing a dileptonic decay of a Z/γ^* boson has two components: a model for the Z boson mass peak and one for the Drell-Yan continuum. The latter is described by an exponential function $\mathcal{P}_{exp}$, while the peak model consists of a Breit-Wigner function $\mathcal{P}_{BW}$, with mean and width fixed to the nominal values of the Z boson mass peak [20], convolved with a double-sided Crystal Ball function, $\mathcal{P}_{DSCB}\left(m_{\ell\ell}\right)$. The Breit-Wigner function accounts for the physical Z boson lineshape, while the double-sided Crystal Ball function models the effects of the detector resolution and radiative corrections to the Z boson line shape. In comparison to the normal Crystal Ball function, the Gaussian part of the double-sided Crystal Ball function models only the core of the distribution while exponential terms are used for both sides of the peak instead of only one:

$$\mathcal{P}_{DSCB}\left(m_{\ell\ell}\right) = \begin{cases} A_1 \left(B_1 + \frac{m_{\ell\ell}-\mu_{DSCB}}{\sigma_{DSCB}}\right)^{-n_1} & \text{if } \frac{m_{\ell\ell}-\mu_{DSCB}}{\sigma_{DSCB}} < -\alpha_1 \\ \exp\left(-\frac{(m_{\ell\ell}-\mu_{DSCB})^2}{2\sigma_{DSCB}^2}\right) & \text{if } -\alpha_1 < \frac{m_{\ell\ell}-\mu_{DSCB}}{\sigma_{DSCB}} < \alpha_2 \\ A_2 \left(B_2 + \frac{m_{\ell\ell}-\mu_{DSCB}}{\sigma_{DSCB}}\right)^{-n_2} & \text{if } \frac{m_{\ell\ell}-\mu_{DSCB}}{\sigma_{DSCB}} > \alpha_2. \end{cases} \tag{8.6}$$

A_i and B_i are defined according to Equation 8.2, thereby defining two power law parameters n_i, μ_{DSCB} and σ_{DSCB} are the mean and width of the Gaussian part and the α_i are the transition points to the power law tails.

Adding the exponential contribution to the convolution of the Breit-Wigner and double-sided Crystal Ball, the description of Z/γ^* boson backgrounds is given by

$$\mathcal{P}_{Z/\gamma*} = f_{exp}\mathcal{P}_{exp}\left(m_{\ell\ell}\right) + \left(1 - f_{exp}\right) \int \mathcal{P}_{DSCB}\left(m_{\ell\ell}\right) \mathcal{P}_{BW}\left(m_{\ell\ell} - m'\right) dm', \tag{8.7}$$

where f_{exp} is the fraction that the exponential part contributes to the probability density function.

The model is fit separately for dielectron and dimuon pairs in a region enriched in events containing Z boson decays. As discussed in Sections 6.2 and 6.3, the requirement on $\mathrm{M_{T2}}$ changes the invariant dilepton mass distribution. Therefore, the same control region is used as for the determination of $R_{\mathrm{out/in}}$ in Section 6.3, e.g. requiring at least two jets, less than 50 GeV of $p_{\mathrm{T}}^{\mathrm{miss}}$, and $\mathrm{M_{T2}} > 80\,\mathrm{GeV}$. The fitted contributions in $e^{\pm}e^{\mp}$ and $\mu^{\pm}\mu^{\mp}$ events are

	Parameter	Status	Initial value	Range
$\mathbf{p}^{ee}_{Z/\gamma*}$, $\mathbf{p}^{\mu\mu}_{Z/\gamma*}$	m_{Z}[GeV]	fixed	91.1876	-
	σ_{Z} [GeV]	fixed	2.4952	-
$\mathbf{p}^{ee}_{Z/\gamma*}$	μ^{ee}_{DSCB} [GeV]	floating	3.0	[-10, 10]
	σ^{ee}_{DSCB} [GeV]	floating	1.6	[0, 20]
	α^{ee}_1	floating	1.2	[0, 10]
	α^{ee}_2	floating	2.5	[0, 10]
	n^{ee}_1	floating	3.0	[0, 20]
	n^{ee}_2	floating	1.0	[0, 100]
	f^{ee}_{exp}	floating	0.003	[0, 1]
	μ^{ee}_{exp} [GeV^{-1}]	floating	-0.02	[-0.1, 0]
$\mathbf{p}^{\mu\mu}_{Z/\gamma*}$	$\mu^{\mu\mu}_{DSCB}$ [GeV]	floating	3.0	[-10, 10]
	$\sigma^{\mu\mu}_{DSCB}$ [GeV]	floating	1.6	[0, 20]
	$\alpha^{\mu\mu}_1$	floating	1.2	[0, 10]
	$\alpha^{\mu\mu}_2$	floating	2.5	[0, 10]
	$n^{\mu\mu}_1$	floating	3.0	[0, 20]
	$n^{\mu\mu}_2$	floating	1.0	[0, 100]
	$f^{\mu\mu}_{exp}$	floating	0.003	[0, 1]
	$\mu^{\mu\mu}_{exp}$ [GeV^{-1}]	floating	-0.02	[-0.1, 0]

Table 8.1: Summary of all parameters of the model for the Z/$\gamma*$ background fit in the Z boson enriched control region. Given are the status of the parameter, either floating or fixed, the initial value, and the allowed range.

shown in Fig. 8.1. All fit parameters of the model as well as their allowed ranges and starting values are summarized in Tab. 8.1.

After the fit in the control region, all shape parameters of the model are fixed and the normalizations in the signal region are the only parameters left floating in the main fit. The invariant dilepton mass resolution is extracted from the fitted width of the Gaussian part of the double-sided Crystal Ball function, $\sigma_{DSCB}$and is used as an input for the modeling of potential signals (see Section 8.8). The obtained resolution is $1.58 \pm 0.08\,\mathrm{GeV}$ for dielectron and 1.64 ± 0.16 GeV for dimuon events.

8.1.3 Signal model

The signal component is based on an edge model of two subsequent two body decays. The signal model consists of a triangular shape, convolved with a Gaussian distribution to account for the experimental resolution, $\sigma_{\ell\ell}$, for which the values of σ_{DSCB} are used that are obtained in the fit to the Z boson mass peak described in Section 8.1.2. The parameterization is given by

$$\mathcal{P}_S\left(m_{\ell\ell}\right) = \frac{1}{\sqrt{2\pi\sigma^2_{\ell\ell}}} \int_0^{m^{edge}_{\ell\ell}} y \cdot \exp\left(-\frac{(m_{\ell\ell}-y)^2}{2\sigma^2_{\ell\ell}}\right) dy. \tag{8.8}$$

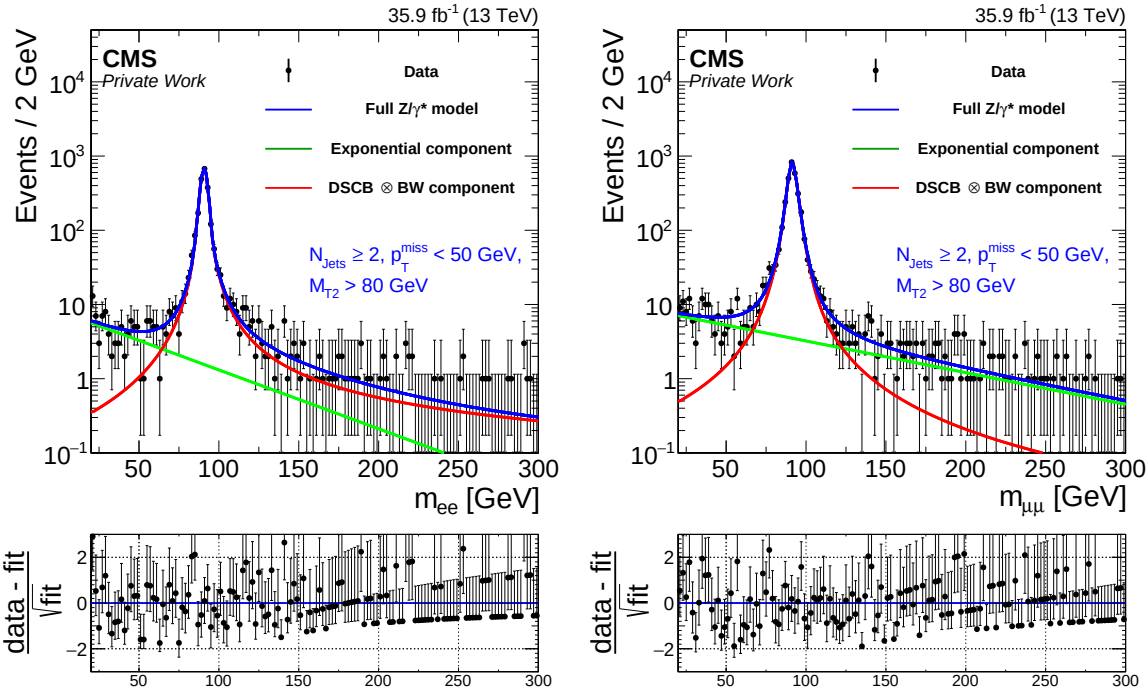

Figure 8.1: Fit to the invariant dilepton mass distribution in the Z/γ^* enriched control region for dielectron (left) and dimuon events (right). The data are shown as black points while the combined fit is displayed as a blue line. The contributions of the exponential part and the convolution of the Breit-Wigner with the double sided Crystal Ball are shown as green and red lines, respectively.

Since the triangle always starts at 0, the edge position $m_{\ell\ell}^{edge}$ is the only free parameter besides the normalization and the same position is used in the dielectron and dimuon sample.

8.2 Combined model and fitting procedure

The combined fit model is obtained by adding a yield parameter N_x to each component x. In case of different-flavor events the flavor-symmetric background is the only contribution and the model is given by

$$\mathcal{P}_{DF}\left(m_{\ell\ell}\right) = N_{FS}^{DF} \cdot \mathcal{P}_{FS}\left(m_{\ell\ell}\right). \tag{8.9}$$

For the same-flavor samples all three components need to be taken into account:

$$\begin{aligned}
\mathcal{P}_{ee}\left(m_{\ell\ell}\right) &= N_{FS}^{ee} \cdot \mathcal{P}_{FS}\left(m_{\ell\ell}\right) + N_{Z/\gamma*}^{ee} \cdot \mathcal{P}_{Z/\gamma*}^{ee}\left(m_{\ell\ell}\right) + N_{S}^{ee} \cdot \mathcal{P}_{S}\left(m_{\ell\ell}, \sigma_{DSCB}^{ee}\right) \\
\mathcal{P}_{\mu\mu}\left(m_{\ell\ell}\right) &= N_{FS}^{\mu\mu} \cdot \mathcal{P}_{FS}\left(m_{\ell\ell}\right) + N_{Z/\gamma*}^{\mu\mu} \cdot \mathcal{P}_{Z/\gamma*}^{\mu\mu}\left(m_{\ell\ell}\right) + N_{S}^{\mu\mu} \cdot \mathcal{P}_{S}\left(m_{\ell\ell}, \sigma_{DSCB}^{\mu\mu}\right),
\end{aligned} \tag{8.10}$$

where N_S^{ee} and $N_S^{\mu\mu}$ are fixed to zero for the background-only hypothesis.

The lepton efficiencies do not depend on the production process of the leptons. Additionally, all considered background processes and the slepton model produce the same number of electrons and muons. Therefore, the number of free parameters can be reduced by introducing universal lepton fractions for dielectron and dimuon pairs: $f_{\mu\mu} = 1 - f_{ee}$ and $0 < f_{ee} < 1$. Connecting the flavor-symmetric contributions in the SF and DF channels via $R_{\mathrm{SF/DF}}$ yields the relations:

$$\begin{array}{rclcrcl}
N_{FS}^{ee} & = & f_{ee} \cdot R_{\mathrm{SF/DF}} \cdot N_{FS}^{DF}, & & N_{FS}^{\mu\mu} & = & (1 - f_{ee}) \cdot R_{\mathrm{SF/DF}} \cdot N_{FS}^{DF}, \\
N_{Z/\gamma*}^{ee} & = & f_{ee} \cdot N_{Z/\gamma*}, & \text{and} & N_{Z/\gamma*}^{\mu\mu} & = & (1 - f_{ee}) \cdot N_{Z/\gamma*}, \\
N_{S}^{ee} & = & f_{ee} \cdot N_{S}, & & N_{S}^{\mu\mu} & = & (1 - f_{ee}) \cdot N_{S}.
\end{array} \tag{8.11}$$

The systematic uncertainty in $R_{\mathrm{SF/DF}}$ is included in the fit as a constraint. Since $R_{\mathrm{SF/DF}}$ can depend on the event kinematics, the flavor-symmetric background prediction methods introduced in Section 5.2.1 are applied on the DF data sample to obtain $R_{\mathrm{SF/DF}}$ and its uncertainty. For the edge fit region, values of 1.097 ± 0.035 and 1.079 ± 0.032 are obtained on data and simulation, respectively. The constraint is added to the likelihood model in form of a Gaussian function with mean and width at the measured value:

$$\mathcal{G}\left(R_{\mathrm{SF/DF}};\, R_{\mathrm{SF/DF}}^{\mathrm{measured}}, \sigma_{R_{\mathrm{SF/DF}}^{\mathrm{measured}}}\right). \tag{8.12}$$

The full likelihood model as a function of $m_{\ell\ell}$ is obtained by multiplying the probability density functions $\mathcal{P}_x$ of the three dilepton samples. For a set of parameters $\mathbf{p}$ it is given by

$$\begin{aligned}
\mathcal{L}\left(m_{\ell\ell}, \mathbf{p}\right) = \; & \mathcal{N}_{ee} \times \mathcal{N}_{\mu\mu} \times \mathcal{N}_{DF} \\
& \times \textstyle\prod_{e^{\pm}e^{\mp}} \left[N_{FS}^{ee} \cdot \mathcal{P}_{FS}\left(m_{\ell\ell}; \mathbf{p}_{FS}\right) + N_{Z/\gamma*}^{ee} \cdot \mathcal{P}_{Z/\gamma*}^{ee}\left(m_{\ell\ell}; \mathbf{p}_{Z/\gamma*}^{ee}\right) + N_{S}^{ee} \cdot \mathcal{P}_{S}\left(m_{\ell\ell}; \mathbf{p}_{S}^{ee}\right) \right] \\
& \times \textstyle\prod_{\mu^{\pm}\mu^{\mp}} \left[N_{FS}^{\mu\mu} \cdot \mathcal{P}_{FS}\left(m_{\ell\ell}; \mathbf{p}_{FS}\right) + N_{Z/\gamma*}^{\mu\mu} \cdot \mathcal{P}_{Z/\gamma*}^{\mu\mu}\left(m_{\ell\ell}; \mathbf{p}_{Z/\gamma*}^{\mu\mu}\right) + N_{S}^{\mu\mu} \cdot \mathcal{P}_{S}\left(m_{\ell\ell}; \mathbf{p}_{S}^{\mu\mu}\right) \right] \\
& \times \textstyle\prod_{\mu^{\pm}\mu^{\mp}} \left[N_{FS}^{DF} \cdot \mathcal{P}_{FS}\left(m_{\ell\ell}; \mathbf{p}_{FS}\right) \right] \\
& \times \mathcal{G}\left(R_{\mathrm{SF/DF}}\right),
\end{aligned} \tag{8.13}$$

	Parameter	Status	Initial value	Range
	N_{FS}^{DF}	floating	$0.7N_{DF}$	[0, $2N_{DF}$]
	$N_{Z/\gamma*}$	floating	$0.5N_{SF}^{Z}$	[0, N_{SF}^{Z}]
	N_S	floating	0	[-2 $(N_{SF} - 0.8N_{DF})$, 2 $(N_{SF} - 0.8N_{DF})$]
	$R_{\mathrm{SF/DF}}$	constrained	$R_{\mathrm{SF/DF}}^{\mathrm{measured}}$	$R_{\mathrm{SF/DF}}^{\mathrm{measured}} \pm 4\sigma_{R_{\mathrm{SF/DF}}^{\mathrm{measured}}}$
	f_{ee}	floating	0.5	[0, 1]
$\mathbf{p}_{FS}$	μ_{FS} [GeV]	floating	50	[0, 200]
	σ_{FS} [GeV]	floating	20	[0, 100]
	α_{FS}	floating	1	[0, 10]
	n_{FS}	floating	1	[0, 100]
$\mathbf{p}_S$	$m_{\ell\ell}^{edge}$ [GeV]	floating	varying	[35, 500]

Table 8.2: Summary of all parameters varied in the final fit.

where $\mathcal{N}_{\ell\ell}$ are Poisson factors for the normalization in each sample. For dielectron and dimuon pairs they are of the form

$$\mathcal{N}_{\ell\ell} = \frac{\left(N_{FS}^{\ell\ell} + N_{Z/\gamma*}^{\ell\ell} + N_{S}^{\ell\ell}\right)^{N_{\ell\ell}} e^{-\left(N_{FS}^{\ell\ell} + N_{Z/\gamma*}^{\ell\ell} + N_{S}^{\ell\ell}\right)}}{N_{\ell\ell}!},$$

while they are given by

$$\mathcal{N}_{DF} = \frac{\left(N_{FS}^{DF}\right)^{N_{\ell\ell}} e^{-(N_{FS}^{DF})}}{N_{\ell\ell}!}$$

for $e^{\pm}\mu^{\mp}$ events. In each case, $N_{\ell\ell}$ is the number of observed events in the corresponding channel.

A summary of all parameters that are being varied in the final fit is shown in Tab. 8.2. The number of observed SF (N_{SF}) and DF events (N_{DF}) and the number of SF events in a range of 20 GeV around the Z boson mass $\left(N_{SF}^{Z}\right)$ are taken as an input to determine the starting value and range for the normalizations. The fit is performed in an invariant dilepton mass range up to 500 GeV, but since very few events with values above 300 GeV are present (see Tab. 7.1), the fits are only displayed up to 300 GeV to avoid plotting too many bins without data content and increase the visibility of effects at lower masses.

8.3 Fit validation

To validate the performance of the fit, several studies are performed on simulation and a data control region before applying it to the signal selection. Since the results on simulation might be subject to fluctuations in the used MC samples, additional tests are performed using toy data sets generated from the fitted model itself.

8.3.1 Tests on MC simulation

As a first step, the ability of the fit to correctly describe a data set is tested on SM simulation and examples of the slepton model. The simulation is normalized to $35.9\,\mathrm{fb}^{-1}$ and the full set of background processes is considered. The fits are performed either with or without the injection of a signal point.

The result of the fit to the simulation of the background processes without an injected signal can be observed in Fig. 8.2. The combined fit describes the simulation well. A χ^2-test to quantify the agreement between the simulation and the fit yields a probability of about 34% to achieve a worse agreement if the fit is repeated on an independent sample and the data follows the assumed distributions (χ^2-probability) [129]. In the absence of signal simulation, a small negative signal yield of -46 ± 46 events is fitted with an upper edge at about 100 GeV. To verify that the global minimum was found, a scan of the likelihood as a function of $m_{\ell\ell}^{edge}$ is performed. The result of this test can be observed in Fig. 8.3. Two main minima can be observed, the global minimum above the Z boson mass, which was fitted in Fig. 8.2, and a second one at about 70 GeV. Above the global minimum, the result depends little on $m_{\ell\ell}^{edge}$ and only features an insignificant minimum at about 180 GeV. In the absence of a signal, the overall differences in the likelihood are small. It can therefore occur that the fit does not find the global minimum if the starting point of the fitted edge position is far away from the global minimum or close to a local minimum.

Two signal points of the slepton model are used to test the ability of the fit to find a signal and reproduce its parameters. In both cases, the mass of the bottom squark is 850 GeV, while the mass of the $\tilde{\chi}_2^0$ is either 150 or 300 GeV. As discussed in Section2.3.4, the mass of the $\tilde{\chi}_1^0$ is always set to 100 GeV in the slepton model. These signal models are referred to as S1 and S2. According to Equation 2.7 for two subsequent two-body decays, this corresponds to generated values of 49.7 and 193.6 GeV for $m_{\ell\ell}^{edge}$. The fits for the background-only and background+signal hypothesis can be observed in Fig. 8.4. The full fit describes the simulation well, while the background-only hypothesis is unable to account for the contribution of the signal simulation.

The generated and fitted parameters for these two scenarios and the fits on background-only simulation for the signal+background and background-only hypothesis are summarized in Tab. 8.3. While the generated positions of $m_{\ell\ell}^{edge}$ are well reconstructed, the fitted signal yields of 48 ± 24 and 95 ± 29 events are about 10 events lower than the 59 and 106 generated signal events for scenarios S1 and S2, respectively. The comparison of the fit of the background-only hypothesis to the other cases shows that the fit can absorb some real signal events in an increased background prediction. For the Z/$\gamma*$ contribution, this is only possible if $m_{\ell\ell}^{edge}$ is larger than the Z boson mass. In case of the flavor-symmetric component, the increase of the prediction can occur for any position of $m_{\ell\ell}^{edge}$ and is caused by increasing the flavor-symmetric component in the DF sample N_{FS}^{DF} or $R_{\mathrm{SF/DF}}$. In scenario S1 both are shifted simultaneously and account for a similar fraction of the change, while only N_{FS}^{DF} is increased in scenario S2. If no signal is injected, the fit can simultaneously vary signal and background components to improve the likelihood. In the fit to the background-only simulation more than half of the fitted negative signal yield is compensated by increased background components.

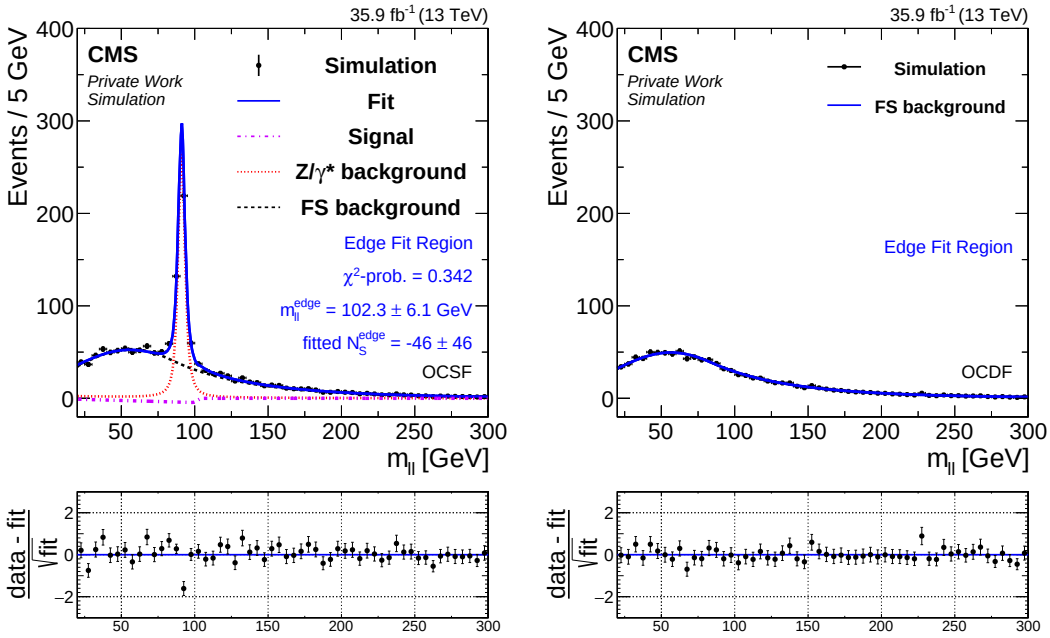

Figure 8.2: Fit to the background-only simulation for SF (left) and DF lepton pairs (right). The simulated data, shown as black points, are compared to the combined fit which is displayed as a solid blue line. The separate fit components for the flavor-symmetric component, the Z/γ^* background, and the signal model are shown as dashed black, dotted red, and dash-dotted violet lines, respectively. The difference between the observation in data and the fit, divided by the square root of fitted events, is shown in the lower panels.

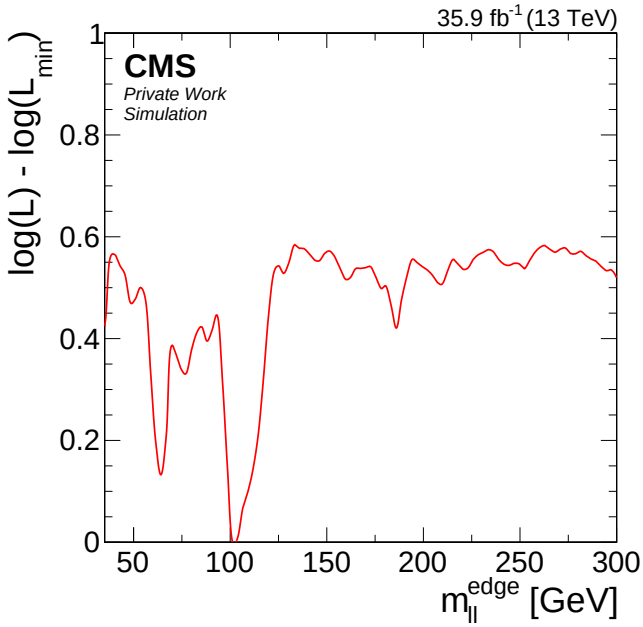

Figure 8.3: Scan of the observed log-likelihood as a function of $m_{\ell\ell}^{edge}$ in the edge fit region on simulation. The minimal observed value is subtracted.

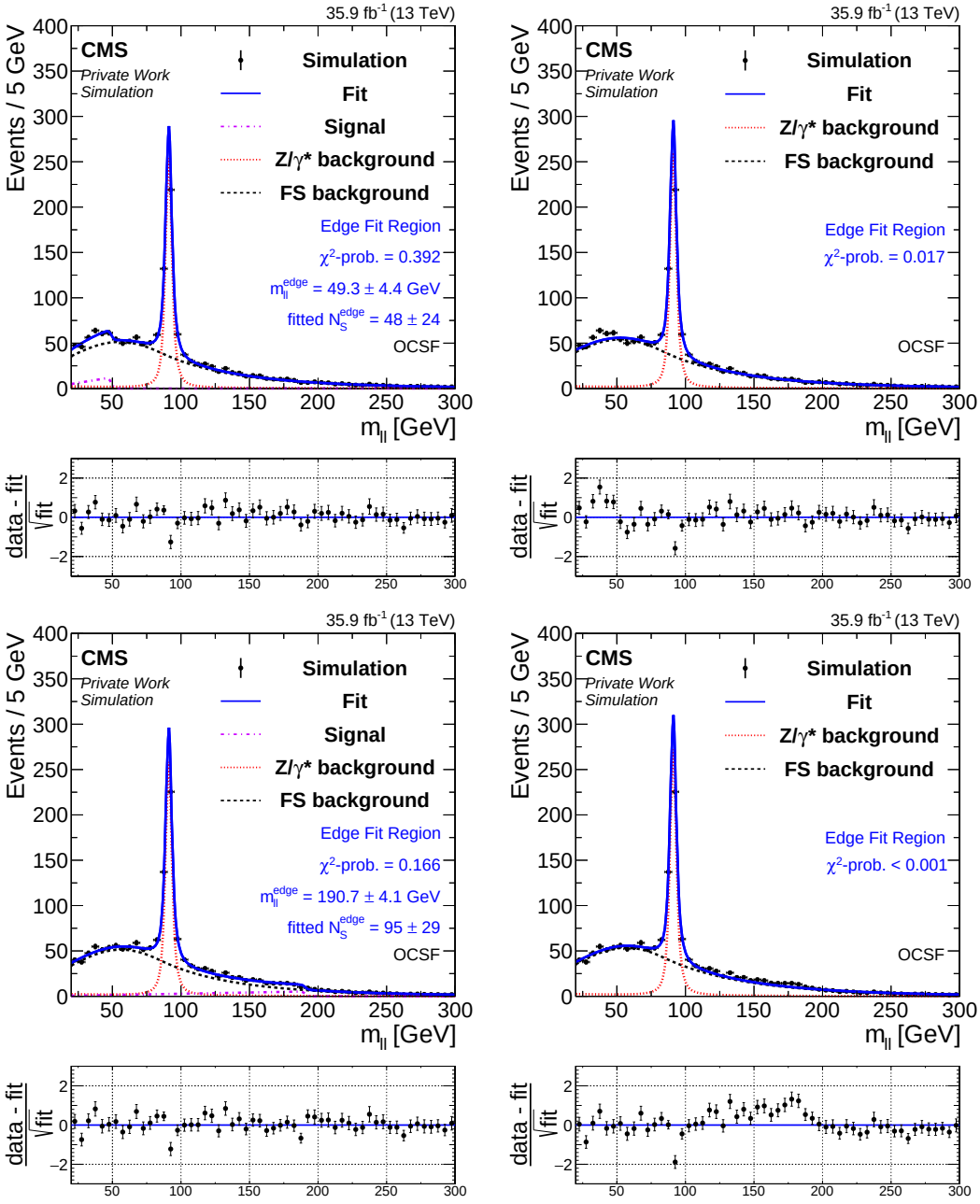

Figure 8.4: Fit of the signal+background (left) and background-only hypothesis (right) to the combination of background and signal simulation. The slepton model S1 is used in the upper and the model S2 in the lower plots. The simulated data, shown as black points, are compared to the combined fit which is displayed as a solid blue line. The separate fit components for the flavor-symmetric component, the Z/γ^* background, and the signal model are shown as dashed black, dotted red, and dash-dotted violet lines, respectively. The difference between the observation in data and the fit, divided by the square root of fitted events, is shown in the lower panels.

fit hypothesis simulated samples	BG-only BG	signal+BG BG	signal+BG BG+S1	signal+BG BG+S2
gen. $m_{\ell\ell}^{edge}$[GeV]	-	-	49.7	193.6
gen. N_S	-	-	58.9	105.8
fitted $m_{\ell\ell}^{edge}$ [GeV]	-	102.3 ± 6.1	49.3 ± 4.4	190.7 ± 4.1
fitted N_S	-	-46 ± 46	48 ± 24	95 ± 29
fitted N_{Z/γ^*}	420 ± 27	433 ± 30	420 ± 27	429 ± 27
fitted N_{FS}^{DF}	1027 ± 27	1038 ± 29	1031 ± 28	1032 ± 29
fitted $R_{\mathrm{SF/DF}}$	1.079 ± 0.028	1.089 ± 0.030	1.083 ± 0.029	1.079 ± 0.029
fitted N_{FS}^{SF}	1108 ± 39	1130 ± 43	1117 ± 41	1113 ± 42

Table 8.3: Fit results on simulation. The results of the full fit for two cases in which a signal point of the slepton model is added to the background processes are compared to the fit of the background-only and signal+background hypothesis on background-only simulation. The generated number of signal events is defined as the SF yield subtracted by the number of DF events for the signal process. N_S and N_{Z/γ^*} refer to the fitted signal and Z/γ^* components in the SF sample, while N_{FS}^{DF} is the background component in the DF sample and N_{FS}^{SF} the obtained contribution on SF data using the fitted value of $R_{\mathrm{SF/DF}}$.

8.3.2 Fit performance on toy data sets

Toy data sets are used to study the performance of the fit. The different-flavor samples in these data sets are obtained by fitting the background shape to DF events in simulation and varying these using a Poisson distribution. For dielectron and dimuon data sets, a combination of the shape for flavor-symmetric backgrounds and the Z/$\gamma*$ model is used. For the former, the shape and normalization from the DF sample are modified by $R_{\mathrm{SF/DF}}$, which is measured in data. Furthermore, $R_{\mathrm{SF/DF}}$ is split according to the dielectron and dimuon fractions in the flavor-symmetric control region to provide the contributions to the individual samples. The simulated dielectron and dimuon yields from non-flavor-symmetric background processes are used to normalize the shapes of the Z/$\gamma*$ model. Signal contributions for a given edge position and number of signal events can be added if desired. Fractions of the SF signal yield in each sample are again formed according to the contributions in the flavor-symmetric control region. Toy data sets for both SF samples are obtained by independently fluctuating the different contributions according to a Poisson distribution. For each considered scenario 1000 toy data sets are generated.

Data sets without injected signal

The results of two configurations of the fit applied to toy data sets of the background-only model are shown in Fig. 8.5. In the first configuration, the edge position is allowed to float, in the second one it is fixed to 150 GeV. The left plot in Fig. 8.5 shows the number of fitted signal events divided by its uncertainty. In case of a fixed edge position the results follow a Gaussian distribution centered around zero with a width of approximately one, which is expected in the absence of a signal. If $m_{\ell\ell}^{edge}$ is allowed to float, two peaks above and below

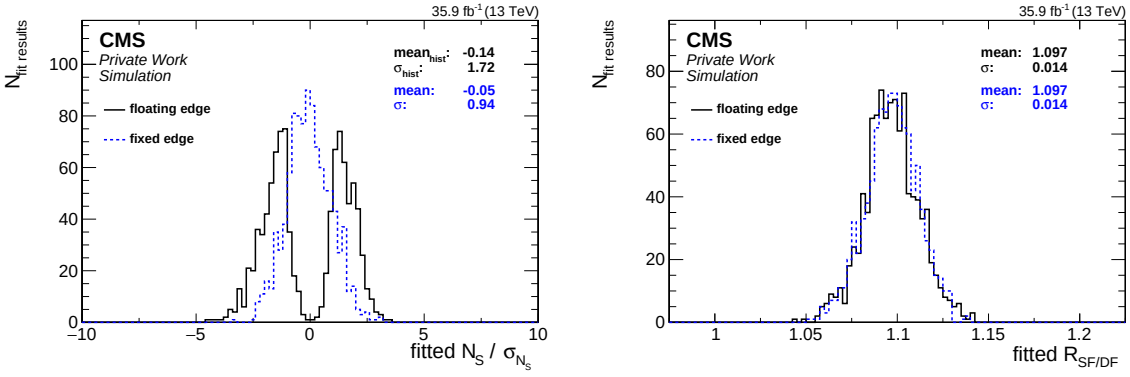

Figure 8.5: Distribution of the number of fitted signal events divided by the uncertainty (left) and fitted $R_{\mathrm{SF/DF}}$ values (right) in toy studies without injected signal. The results for a floating edge position are shown as a black solid line and a blue dashed line indicates those with a fixed edge position.

zero are obtained while nearly no fit results exhibit a negligible signal yield. Since a single Gaussian fit is unable to describe the double peak structure, the average value and standard deviation of the plotted histogram are given instead. This distribution is a result of the "look-elsewhere-effect" [130], caused by the degree of freedom introduced by the floating edge position, which allows the fit to find an edge position where a signal contribution improves the likelihood because of a statistical fluctuation in the data set. Depending on the fluctuations that are present, the fitted signal yield can either be negative or positive and slightly more negative values are obtained in the studied toy data. Compared to a fit with a fixed edge position, a bias is introduced towards edge positions where a signal component can reduce the negative log-likelihood.

The distribution of the fitted $R_{\mathrm{SF/DF}}$ value is shown on the right plot in Fig. 8.5. Both the fits with a fixed and a floating edge position reproduce the value of 1.097 used in the generation of the toy data sets very well. The widths of the two distributions are identical as well, indicating that the floating edge position does not introduce an additional bias on $R_{\mathrm{SF/DF}}$.

Figure 8.6 shows the distribution of the fitted edge position as a function of the initial value if $m_{\ell\ell}^{edge}$ is allowed to float. The initial edge positions have been randomized between 35 and 300 GeV. The lower value is chosen to ensure that $m_{\ell\ell}^{edge}$ is not too close to the lower boundary. In the absence of a signal, the initial and final values are strongly correlated. This indicates that the fit tends to converge in a local minimum of the negative log-likelihood. For fits on data it is therefore necessary to generate a likelihood scan, as shown in Fig. 8.3, and choose a starting value close to the global minimum. In case of toys it is not feasible to produce such a scan for each toy data set. To eliminate this bias, a constant initial value is chosen for each data set produced with the same conditions. For toy data sets with an injected signal, the value of $m_{\ell\ell}^{edge}$ used in the generation is chosen as the initial value. If no signal is injected, the starting value is set to 150 GeV.

To investigate how a mismeasurement of $R_{\mathrm{SF/DF}}$ can influence the fit, toy data sets are generated with $R_{\mathrm{SF/DF}}$ shifted by $\pm 1\sigma$ from the value measured in data. Fits to these toys

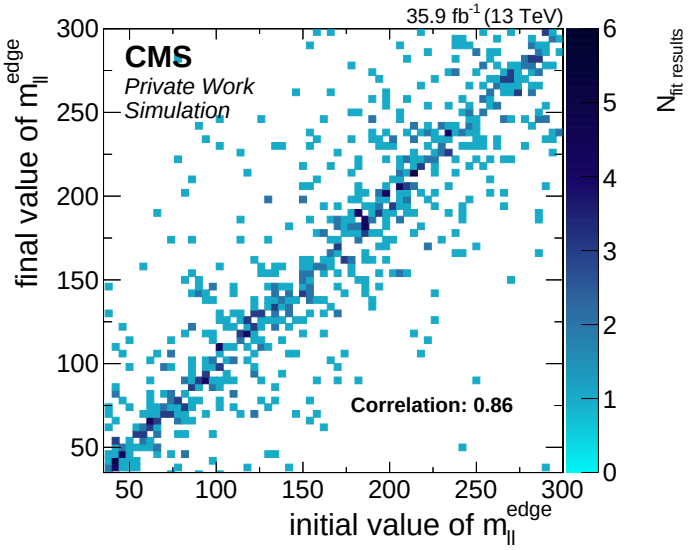

Figure 8.6: Distribution of the generated and fitted values of $m_{\ell\ell}^{edge}$ for toys with randomized initial edge positions without injected signal.

are applied afterwards using the nominal value of $R_{\mathrm{SF/DF}}$ and its uncertainty as a Gaussian constraint. The resulting number of signal events divided by its uncertainty and the fitted $R_{\mathrm{SF/DF}}$ values are shown in Fig. 8.7. Applying the fit with $R_{\mathrm{SF/DF}}$ constrained to the nominal value to toys generated with a larger value causes the fit to initially underestimate the flavor-symmetric background contribution. The obtained values of $R_{\mathrm{SF/DF}}$, with a mean shifted only by 0.007–0.008 from the nominal value instead of the introduced shift of 0.035, indicate that the fit is not able to correct for a biased initial value of $R_{\mathrm{SF/DF}}$ completely. The main part of the systematic shift is absorbed by introducing a signal. The double peak structure in the number of signal events observed in the nominal configuration is shifted to the negative (positive) peak for the toys generated with lower (higher) values of $R_{\mathrm{SF/DF}}$.

The ability to partially correct for mismeasured values of $R_{\mathrm{SF/DF}}$ is more than is possible in the counting experiment analysis, but the fact that a remaining bias directly affects the fitted signal underlines the necessity to derive $R_{\mathrm{SF/DF}}$ as precisely as possible. This is taken into account by producing an individual value of $R_{\mathrm{SF/DF}}$ for each signal region in dependence of the lepton kinematics in the DF sample.

Data sets with signal injected

A signal with an edge position of 150 GeV is used to test the performance of the fit in the presence of a signal. A signal yield of 70 events is added to the background contribution and all components are fluctuated individually according to a Poisson distribution when producing the toys. Several distributions of fit results are shown in Fig. 8.8. The number of fitted signal events is described by a Gaussian with a mean of approximately 76 events which is slightly higher than the number of injected events. At the same time the fitted $R_{\mathrm{SF/DF}}$ value of 1.093 ± 0.014 is 0.4% smaller than the value obtained for background-only toys in

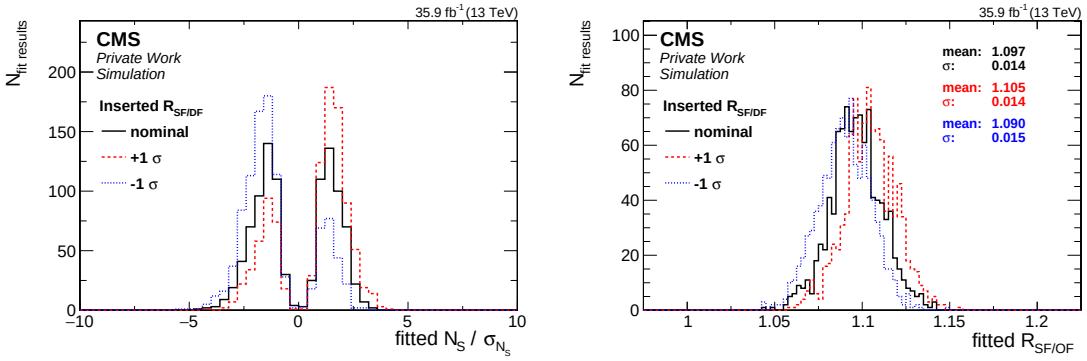

Figure 8.7: Distribution of the number of fitted signal events divided by the uncertainty (left) and fitted $R_{\mathrm{SF/DF}}$ values (right) in toy studies without injected signal. The fits to toys generated with the nominal value of $R_{\mathrm{SF/DF}}$ are shown as a black line while those fitted to toys with $R_{\mathrm{SF/DF}}$ systematically shifted up and down are displayed as dashed red and dotted blue lines, respectively.

Fig. 8.5. Comparing this to the number of flavor-symmetric background events, which is about 1000 events, indicates that most of the difference between injected and fitted signal events can be related to the change of the flavor-symmetric background prediction due to the reduced value of $R_{\mathrm{SF/DF}}$. In comparison to the tests on MC simulation where the fitted number of signal events was lower than the injected number and the fitted values of $R_{\mathrm{SF/DF}}$ higher than the injected ones, the trends are reversed. This originates from the fact that the $m_{\ell\ell}$ distribution in the slepton model does not perfectly agree with the fitted signal shape and other background components are increased to improve the agreement. In contrast to this, the signal component in the toy data sets is generated with the signal model that is fitted later on fluctuated by a Poisson distribution. In both cases, the number of fitted signal events and the background contributions agree within their uncertainties with the injected values. A Gaussian with a mean of about 2.6 and a width of 0.8 is obtained when the number of fitted signal events is divided by its uncertainty (upper right plot of Fig. 8.8). This width is smaller than expected for a normalized Gaussian distribution and suggests slightly overestimated uncertainties. The fitted edge position of $149.6 \pm 4.2\,\mathrm{GeV}$ agrees very well with the generated value. While no results with a number of fitted signal events between -10 and 10 are present, a few fit results with a negative fitted signal component of up to 50 events are obtained. This contradicts the expectation of a larger likelihood for 0 signal events than for a negative signal contribution if a positive number of signal events is injected and demonstrates the bias of the fit towards non-negligible signal yields.

The impact of the edge position on the fit results is studied by generating toys with 70 signal events, fluctuated by a Poisson distribution, at different values of $m_{\ell\ell}^{edge}$ between 40 and 300 GeV in 10 GeV steps. For each configuration 1000 toy data sets are created and fits to these performed. The left plot in Fig. 8.9 shows the distributions of the fitted value of $m_{\ell\ell}^{edge}$ as a function of the generated edge position. As for the test performed for a single scenario above, the generated edge position is recovered very well in most cases. The Z boson mass peak has two effects on the results. For generated edge positions of 80 and 100 GeV, a small but notable fraction of fits features a fitted edge position close to the Z boson mass.

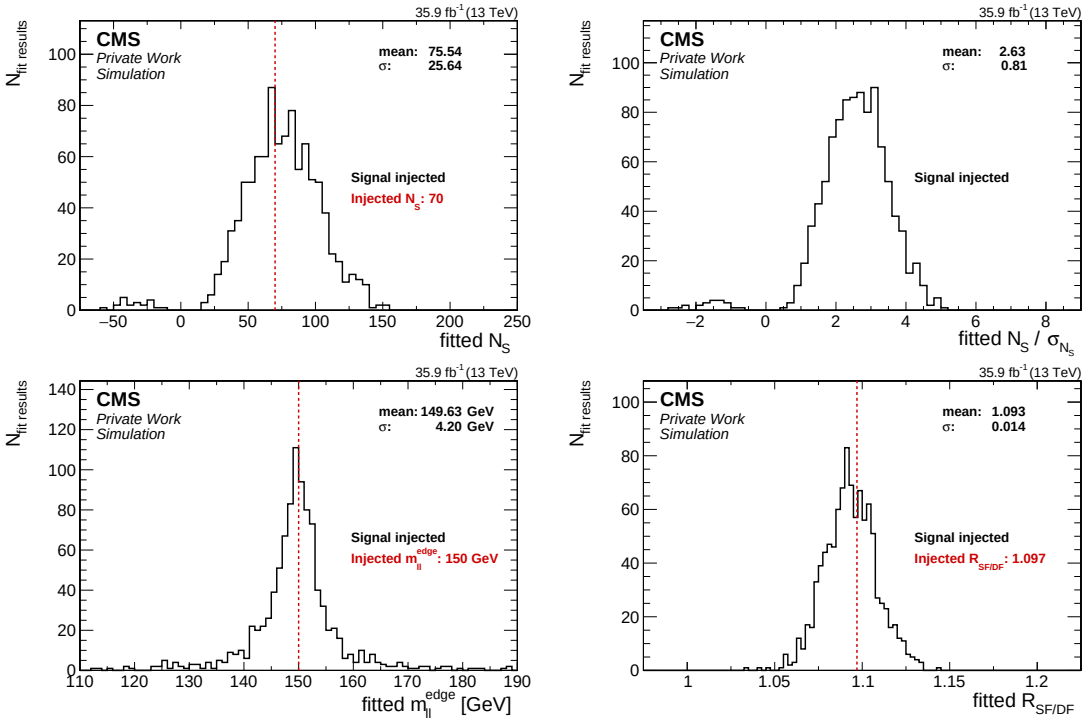

Figure 8.8: Distribution of the number of fitted signal events (top left) the number of fitted signal events divided by the uncertainty (top right), the fitted edge position (bottom left), and the fitted $R_{\mathrm{SF/DF}}$ values (right) in toy studies with an injected signal. The signal has a generated edge position of 150 GeV.

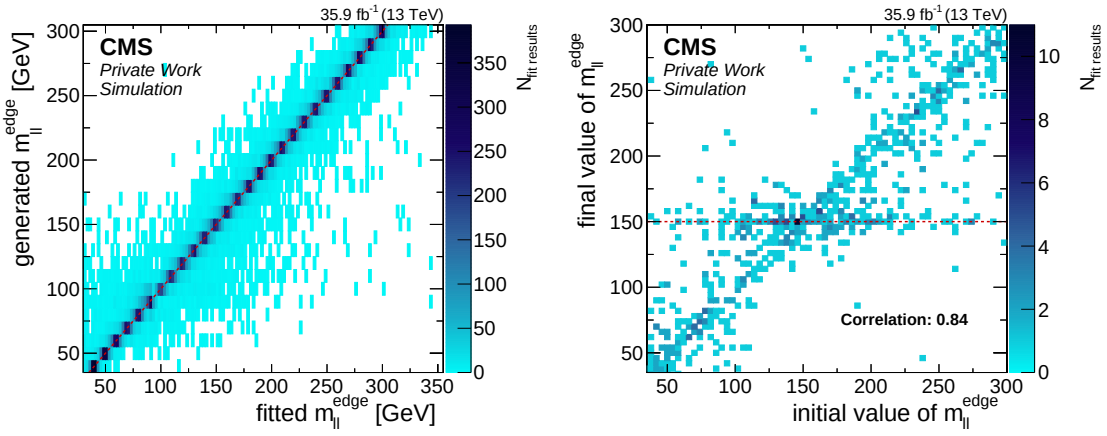

Figure 8.9: The left plots shows the distribution of the generated value of $m_{\ell\ell}^{edge}$ as a function of the fitted value of $m_{\ell\ell}^{edge}$ for toys with the initial value of $m_{\ell\ell}^{edge}$ set to the correct value. In the right plot, the fitted value of $m_{\ell\ell}^{edge}$ is shown in dependency of the initial value for fits with a randomized initial value of $m_{\ell\ell}^{edge}$ to toy data sets with an injected signal at 150 GeV. The abundance of fitted results is indicated by the color, with darker colors indicating higher values. Points where the fitted value matches the generated one are indicated by a red dashed line.

Furthermore, the overall spread of the results and the probability for large deviation are maximal for generated $m_{\ell\ell}^{edge}$ values close to the Z boson mass and decrease for large and very small values of the generated edge position. Comparing these toy results to fits where the starting position of the edge fit is randomized shows that fixing the initial value to the correct edge position introduces a bias towards a better performance. The right plot in Fig. 8.9 demonstrates this for an injected signal of 70 events at 150 GeV, where the initial and fitted value of $m_{\ell\ell}^{edge}$ are compared. This underlines the importance to perform a likelihood scan before fitting to data to ensure that the global minimum is found.

The number of fitted signal events and the fitted value of $R_{\mathrm{SF/DF}}$ are shown in Fig. 8.10 for the scan with 70 injected events and an initial value of $m_{\ell\ell}^{edge}$ fixed to the generated one. In both cases, the mean of the fitted values is close to the one used in the generation of the toys, while the distributions show relatively large deviations from the generated value. The latter reflects the fluctuated event yields in the generation of the toys. For the number of fitted signal events, the deviations are again larger for generated edge positions close to the Z boson mass. The fit nearly never fits approximately 0 signal events, while in a small fraction of cases negative signal yields are obtained, again emphasizing the bias towards non-negligible signal contributions.

Overall, the fit shows a good performance when trying to reproduce injected signal properties if the initial value of the edge position is set to the generated one. This underlines once more the importance to perform a scan of the log-likelihood as a function of the edge position to make sure that the global minimum is obtained. If the edge position is left floating, the look-elsewhere-effect needs to be taken into account as it biases the fit towards a non-negligible signal component. Smaller values of $R_{\mathrm{SF/DF}}$ or the number of fitted DF events can correlate

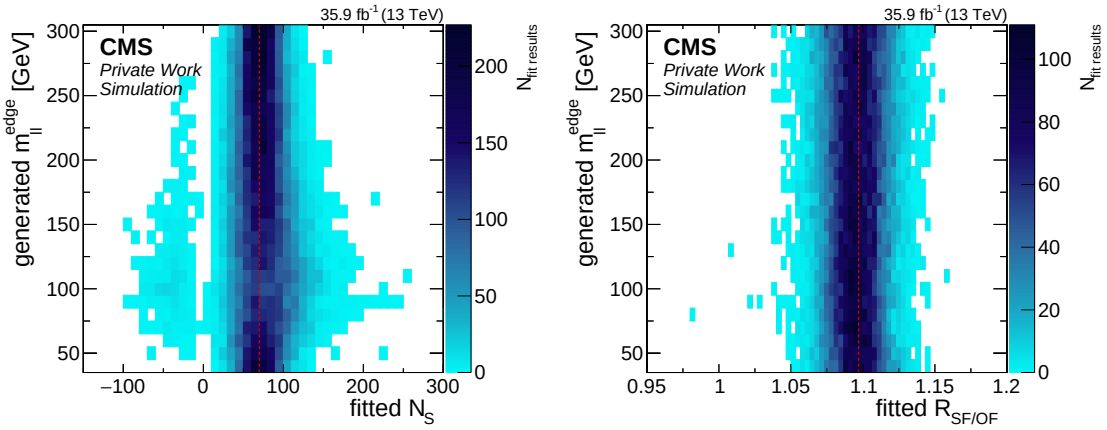

Figure 8.10: Distribution of the number of fitted signal events (left) and fitted $R_{\mathrm{SF/DF}}$ values (right) for the generated values of $m_{\ell\ell}^{edge}$. The abundance of fitted results is indicated by the color, with darker colors indicating higher values. The points where the fitted value matches the generated one is indicated by a red dashed line.

with positive signal contribution and vice versa. In comparison to the previous version of this analysis performed on the 8 TeV data set, the impact of the look-elsewhere-effect increased resulting in less cases with negligible fitted signal component. There are two reasons for this increase. The first is the split of the data into a central and forward selection in the 8 TeV analysis that is no longer performed. The number of data sets on which the fit is performed is therefore reduced from six (dielectron, dimuon, and electron-muon in central and forward) to three. The likelihood to have simultaneous fluctuations in all data sets that favor a signal with a certain edge position decreases with an increasing number of data sets. The second reason is the reduction of the event number in the signal region for the fit by about a factor of 3 to 4, due to the requirement on $\mathrm{M_{T2}}$ that was not used at 8 TeV, as smaller data sets are more susceptible towards statistical fluctuations.

8.3.3 Fit in data control region

A control region in data, referred to as high-$\mathrm{M_{T2}}$ control region, is defined by relaxing the requirements on $p_{\mathrm{T}}^{\mathrm{miss}}$ of the edge fit region to 100–150 GeV. The fit is applied in this region and the result shown in Fig. 8.11. A negative signal yield of -159 ± 77 is fitted for an edge position of about 100 GeV. Again, the tendency of the fit to use non-negligible signal components to compensate fluctuations in data biases the result. The scan of the log-likelihood is displayed in Fig. 8.12. The obtained edge position corresponds to the global minimum, with no other minima of similar likelihood.

8.4 Fit results on data

The resulting $m_{\ell\ell}$ distributions in the SF and DF channel of the fit performed in the edge fit signal region are shown in Fig. 8.13. The best fit features 62 ± 26 signal events for an

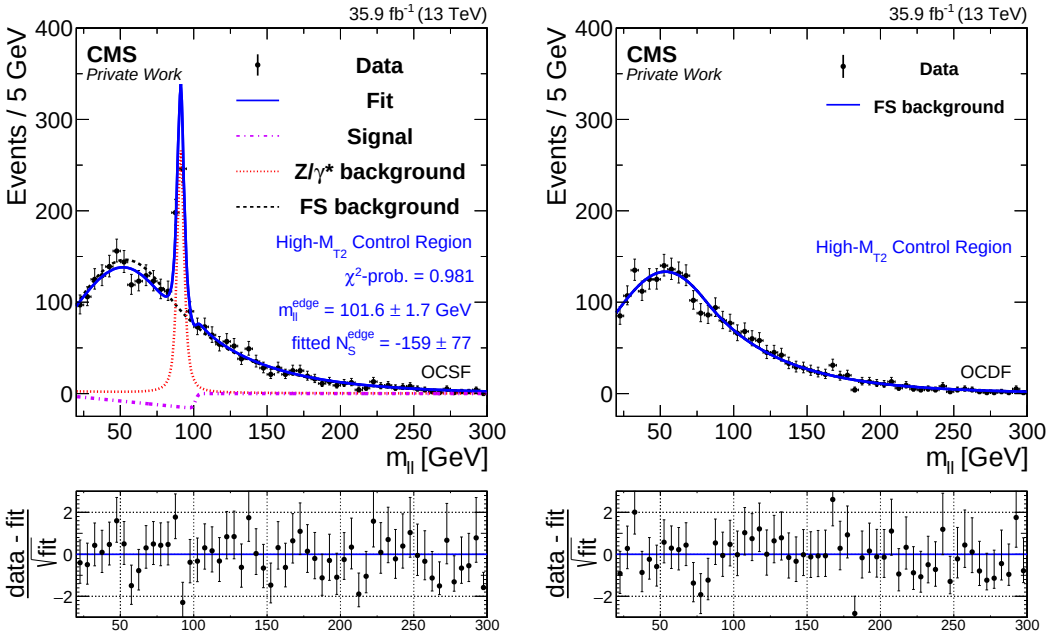

Figure 8.11: Fit to SF (left) and DF lepton pairs (right) in the high M_{T2} control region. The data, shown as black points, are compared to the combined fit which is displayed as a solid blue line. The separate fit components for the flavor-symmetric component, the Z/γ^* background, and the signal model are shown as dashed black, dotted red, and dash-dotted violet lines, respectively. The difference between the observation in data and the fit, divided by the square root of fitted events, is shown in the lower panels.

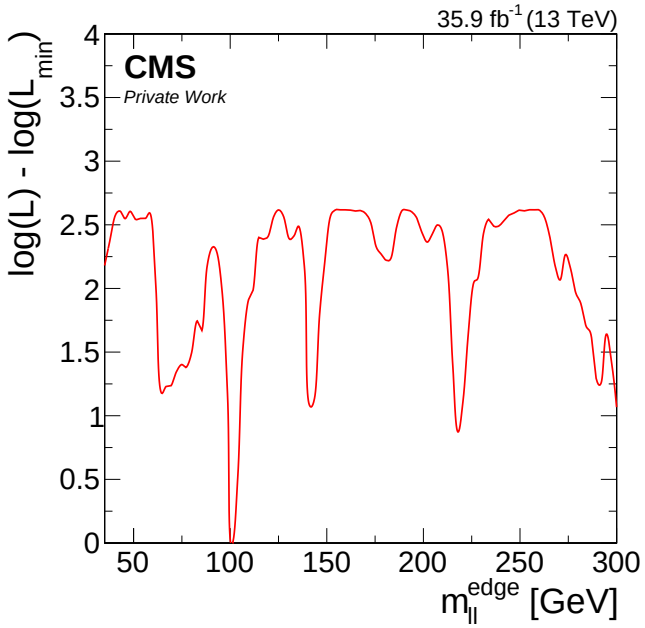

Figure 8.12: Scan of the observed log-likelihood as a function of $m_{\ell\ell}^{edge}$ in the high M_{T2} control region. The minimal observed value is subtracted.

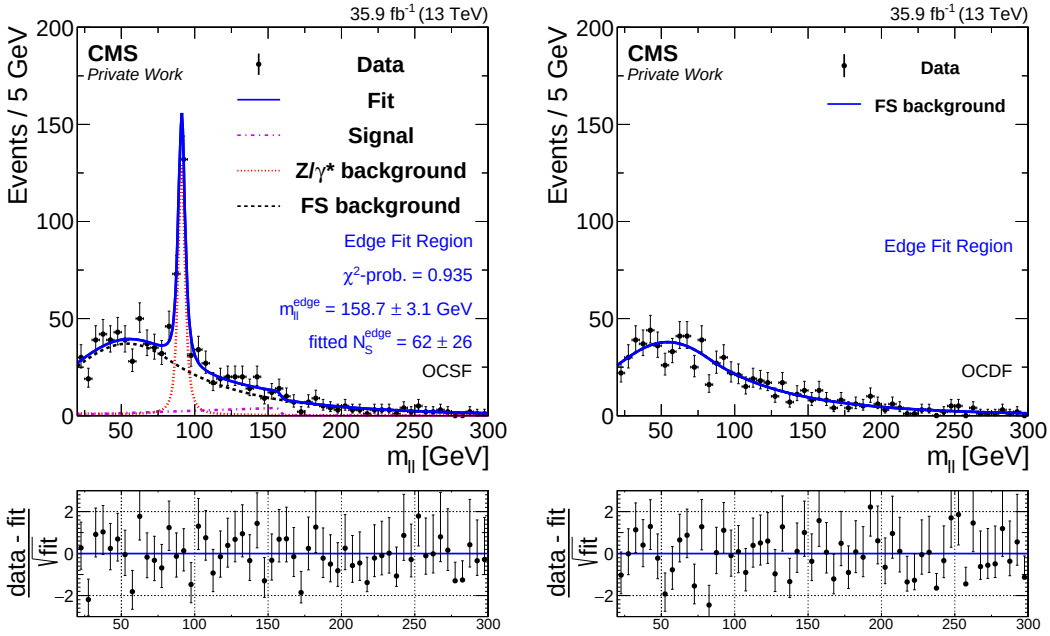

Figure 8.13: Fit to SF (left) and DF lepton pairs (right) in the edge fit region. The data, shown as black points, is compared to the combined fit which is displayed as a solid blue line. The separate fit components for the flavor-symmetric component, the Z/γ^* background, and the signal model are shown as dashed black, dotted red, and dash-dotted violet lines, respectively. The difference between the observation in data and the fit, divided by the square root of fitted events, is shown in the lower panels.

edge position of approximately 159 GeV. A scan of the log-likelihood as a function of $m_{\ell\ell}^{edge}$ is displayed in Fig. 8.14 and confirms that the fitted edge position is indeed the global minimum. Beside a nearby local minimum at about 145 GeV, no other mass range exhibits a minimum of similar size. Table 8.4 summarizes the obtained parameters for the background-only and signal+background hypothesis. The fitted value of $R_{\mathrm{SF/DF}}$ in the signal+background hypothesis is about 3% smaller than the initial value and 2% smaller than the value in the fit of the background-only hypothesis. The fitted contribution in the DF sample for the signal+background hypothesis is about 20 events smaller than in the background-only hypothesis and the combination with the reduced value of $R_{\mathrm{SF/DF}}$ results in a background contribution that is reduced by about 40 events compared to the background-only model. This indicates that the fit has compensated a smaller background component with a signal contribution.

A comparison to the results of the counting experiment analysis, which use the same signal region split into invariant dilepton mass and $\mathrm{t\bar{t}}$-likelihood bins, underlines this conclusion. In Tab. 8.5, the yields in the two likelihood bins in each of the three lowest mass regions of the counting experiment approach are added up and compared to the fitted contributions in these mass ranges. The observed signal yield in the counting experiment analysis is about 20 events less than expected in the first mass bin from 20 to 60 GeV. In the next two mass bins, from 60 to 86 GeV and 96 to 150 GeV, the observation exceeds the expectation by 6 and 21 events, respectively. For such a result in the counting experiment analysis, it is to be expected that

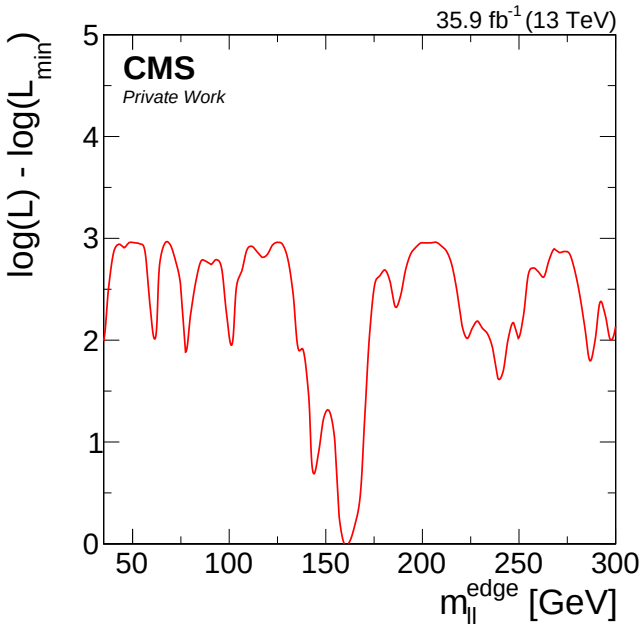

Figure 8.14: Scan of the observed log-likelihood as a function of $m_{\ell\ell}^{edge}$ in the edge fit region region. The minimal observed value is subtracted.

	Background-only hypothesis	Signal+background hypothesis
N_{Z/γ^*}	206 ± 22	205 ± 20
N_{FS}^{DF}	788 ± 23	767 ± 24
$R_{\mathrm{SF/DF}}$	1.087 ± 0.029	1.064 ± 0.031
N_{FS}^{SF}	857 ± 32	816 ± 34
N_S	-	62 ± 26
$m_{\ell\ell}^{edge}$ [GeV]	-	158.7 ± 3.1
Local significance	-	2.4 s. d.
Global significance	-	1.5 s. d.

Table 8.4: Results of the fit to search for a kinematic edge in the edge fit signal region for the background-only and signal+background hypothesis.

	N_{Z/γ^*}	N_{FS}^{DF}	$R_{\mathrm{SF/DF}}$	N_{FS}^{SF}	SF	N_S
$20 < m_{\ell\ell} < 60\,\mathrm{GeV}$						
Fit	8.1 ± 0.8	263 ± 8	1.064 ± 0.031	280 ± 12	288 ± 12	8 ± 3
Count. exp. analysis	4.3 ± 1.1	267	1.097	293 ± 20	279	-18 ± 26
$60 < m_{\ell\ell} < 86\,\mathrm{GeV}$						
Fit	19.3 ± 1.9	167 ± 5	1.064 ± 0.031	177 ± 7	197 ± 8	9 ± 4
Count. exp. analysis	19.5 ± 5.9	167	1.098	183 ± 16	209	6 ± 22
$96 < m_{\ell\ell} < 150\,\mathrm{GeV}$						
Fit	23.9 ± 2.4	157 ± 5	1.064 ± 0.031	167 ± 7	191 ± 8	33 ± 14
Count. exp. analysis	16.9 ± 5.1	166	1.097	182 ± 15	220	21 ± 22

Table 8.5: Comparison of the results of the fit and the counting experiment analysis in the three lowest mass bins of the counting experiment approach without split into $\mathrm{t\bar{t}}$-likelihood bins. The probability density functions contributing to the fit model are integrated in the three mass bins to evaluate the fitted yields in these bins. The $\mathrm{Z}/\gamma*$, N_{FS}^{DF}, and N_{FS}^{SF} contributions in the counting experiment analysis correspond to the combination of the DY+jets and Z+ν backgrounds, the event yield in the DF sample, and the flavor-symmetric background prediction, respectively. The number of SF events in the counting experiment analysis and the sum of $N_{\mathrm{Z}/\gamma^*}^{SF}$ and N_{FS}^{SF} in the fit are referred to as SF. N_S stands for the difference between the observed and predicted event yields in the counting experiment approach.

the fit reduces N_{FS}^{DF} and $R_{\mathrm{SF/DF}}$ to improve the agreement at low $m_{\ell\ell}$ and adds a signal that mainly contributes to the next two mass ranges.

The local significance stated in Tab. 8.4 stands for the significance without correction for the look-elsewhere-effect, e.g. without a floating edge position, and is obtained in two ways. The first approach is to apply Wilk's theorem [131]. The theorem states that the distribution of $-2\Delta\left(\log\left(L\right)\right) = -2\left(\log\left(L_1\right) - \log\left(L_0\right)\right)$, where L_0 and L_1 are the likelihoods of the background-only and signal+background hypotheses, respectively, follows a χ^2 distribution with the same number of degrees of freedom n as there are free parameters in the fitted signal model. In case of a fixed edge position, the only degree of freedom of the signal model is the number of signal events. Integrating this χ^2 distribution for values larger than the one obtained in data yields the p-value, which can be translated into a significance. The second approach is to generate a sufficiently large number of toy data sets without injected signal and fix the edge position in the fit to the value observed in data. The p-value can be determined by calculating the fraction of fits on toy data sets that exhibits a larger value of $-2\Delta\left(\log\left(L\right)\right)$ than the value obtained in data. Both methods yield a consistent local significance of 2.4 standard deviations.

Since Wilk's theorem does not hold if a parameter of the signal model, beside the normalization, is not included in the background only model, the theorem cannot be used to obtain a global significance, which takes the floating edge position into account [130]. Therefore, only toy data sets are used to calculate the global significance. Figure 8.15 shows the $-2\Delta\left(\log\left(L\right)\right)$ distributions for fits to toy data sets with fixed and floating edge position. The χ^2 distributions for 1 and 2 degrees of freedom are shown for comparison. The fit results for the fixed edge position follow the distribution for 1 degree of freedom, validating the applicability of

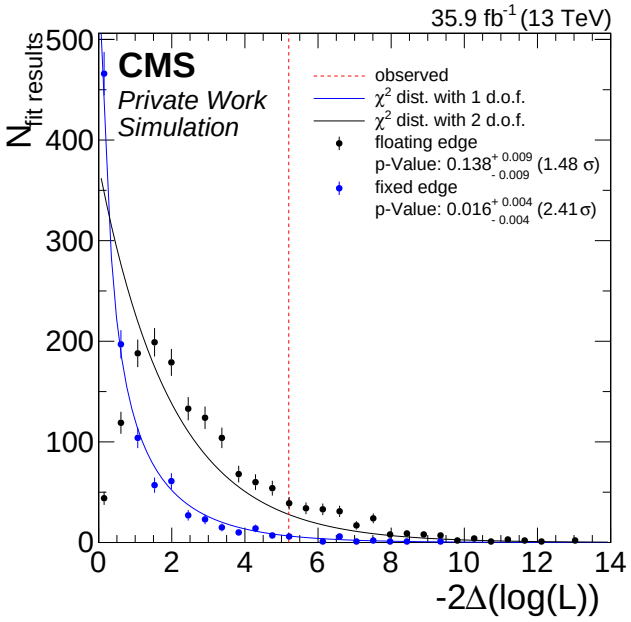

Figure 8.15: Determination of the fit significance using background only toy data sets. The distribution of $-2\Delta\left(\log\left(L\right)\right)$ is displayed for fits with a floating (black) and fixed edge position (blue). The χ^2 distributions for one and two degrees of freedom are shown as blue and black lines, respectively. The red line indicates the value of $-2\Delta\left(\log\left(L\right)\right)$ obtained in data using a floating edge position.

Wilk's theorem in this scenario. The floating edge position shifts the results to higher values of $-2\Delta\left(\log\left(L\right)\right)$ and does not follow the χ^2 distribution with 2 degrees of freedom, confirming that Wilk's theorem does indeed not hold for this type of model. The comparison to the likelihood obtained in the best fit yields a global significance of 1.5 standard deviations.

To perform an additional validation of the fit on data, the parameterization of the flavor-symmetric background component is varied. For both additional shapes introduced in Section 8.1.1, a scan of the log-likelihood is shown in Fig. 8.16. In both cases, the global minimum is found at a similar position as for the nominal shape. Fits with a floating edge position and a starting value close to the global minimum are performed for each additional parameterization and compared to the results with the nominal shape in Tab. 8.6. The obtained value for $-2\Delta\left(\log\left(L\right)\right)$ is used to calculate the local significance in each case, using Wilk's theorem. Very similar results are obtained for the three parameterizations. The fitted signal and background yields with the additional parameterizations differ by less than 5 events from the values in the fit with the nominal parameterization. The fitted edge positions agree within 0.2 GeV and the observed local significances are very similar.

	N_{Z/γ^*}	N_{FS}^{DF}	$R_{SF/DF}$	N_{FS}^{SF}	N_S	$m_{\ell\ell}^{edge}$[GeV]	Local sign.
Nominal	205 ± 20	767 ± 24	1.064 ± 0.031	816 ± 34	62 ± 26	158.7 ± 3.1	2.4 s. d.
2012 shape	204 ± 19	766 ± 24	1.063 ± 0.030	814 ± 33	65 ± 25	158.5 ± 2.4	2.5 s. d.
KDE	207 ± 19	767 ± 24	1.065 ± 0.030	817 ± 33	58 ± 25	158.6 ± 2.6	2.4 s. d.

Table 8.6: Comparison of the fit results in the edge fit signal region on data using different parameterizations of the flavor-symmetric background contribution.

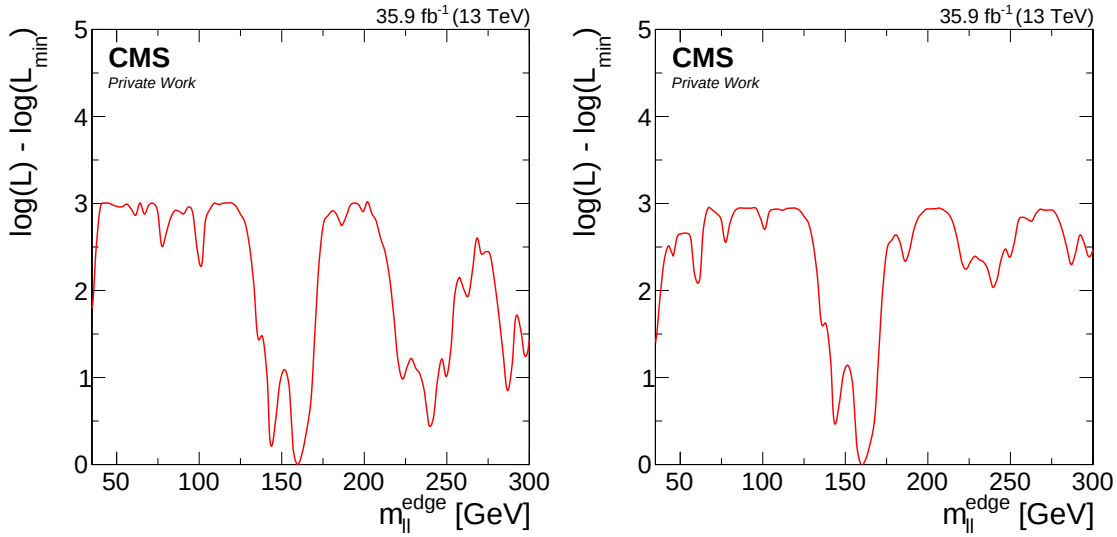

Figure 8.16: Scan of the observed log-likelihood as a function of $m_{\ell\ell}^{edge}$ in the edge fit region region for different parameterizations of the flavor-symmetric background component. Scans are shown for the shape used in the analysis on 2012 data (left) and a kernel density estimator (right). The minimal observed value is subtracted in each case.

9 Interpretation of the search results in the slepton model

A counting experiment analysis and a kinematic fit to search for an edge like feature have been performed to search for SUSY in opposite-charge, same-flavor dilepton events. While the observed number of events in the 8 TeV signal region agrees very well with the number of events expected from the background processes, some small deviations up to 2 standard deviations are observed in the counting experiment analysis for the newly defined signal regions. The number and magnitude of these deviations agree well with the expected statistical fluctuations for such a number of signal bins, given that the total uncertainty is dominated by the statistical uncertainty. The best fit to search for a kinematic edge has a local significance of 2.4 standard deviations. If the look-elsewhere-effect, introduced by the floating edge position, is taken into account a global significance of 1.5 standard deviations remains. This moderate significance and the fact that the fit compensates a large fraction of the fitted signal component by a reduced background contribution, indicate that the result is most likely a statistical fluctuation.

Since no significant excess could be observed, the results of the counting experiment approach can be used to constrain the allowed parameter space of supersymmetric models. To quantify this impact, the results of the counting experiment analysis are interpreted in the slepton model introduced in Section 2.3.4. This includes the discussion of the selection efficiencies of this analysis to the slepton model, the systematic uncertainties that need to be taken into account, and a statistical interpretation to obtain limits on the signal scenario.

9.1 Selection efficiencies and signal yields

A variety of factors affect the efficiency to select possible signal events. The signal scenario needs to have a branching fraction into the dileptonic final states, the leptons have to lie within the geometric and kinematic acceptance of the detector and to fulfill trigger and object selection requirements, and the event needs to satisfy the signal region requirements discussed in Section 6.2. The upper plots in Fig. 9.1 illustrate the combined effect of all these factors for mass points of the slepton model. The combined acceptance and efficiency is shown for the two bins of the $\mathrm{t\bar{t}}$ likelihood. No split into mass bins is applied, since the invariant dilepton mass distribution, and thereby the mass bin to which the signal point contributes, strongly depends on the mass difference between the neutralinos. As already noted for some example points of the slepton scenario in Section 6.2, most of the signal events are observed in the not-$\mathrm{t\bar{t}}$-like signal region, where for some signal points up to 25% of all generated events are selected. For most of the mass scenarios less than 1% of the generated events are observed in the $\mathrm{t\bar{t}}$-like selection with higher values up to 3% at low bottom squark masses. In general, the likelihood to select a generated event increases with the masses of the two SUSY particles. For higher $m_{\tilde{b}}$, the available energy in the event and thereby the momenta of all particles and $p_{\mathrm{T}}^{\mathrm{miss}}$ increase, making it more likely for the event to pass the selection thresholds. Increasing the mass of the $\tilde{\chi}_2^0$ for a given bottom squark mass increases the available energy for the decay products of the $\tilde{\chi}_2^0$, resulting in higher values for the lepton momenta, $p_{\mathrm{T}}^{\mathrm{miss}}$, and most importantly $\mathrm{M_{T2}}$, which depends on the magnitude of the former two quantities. A slightly lower efficiency is observed directly at the diagonal, where the mass difference between the

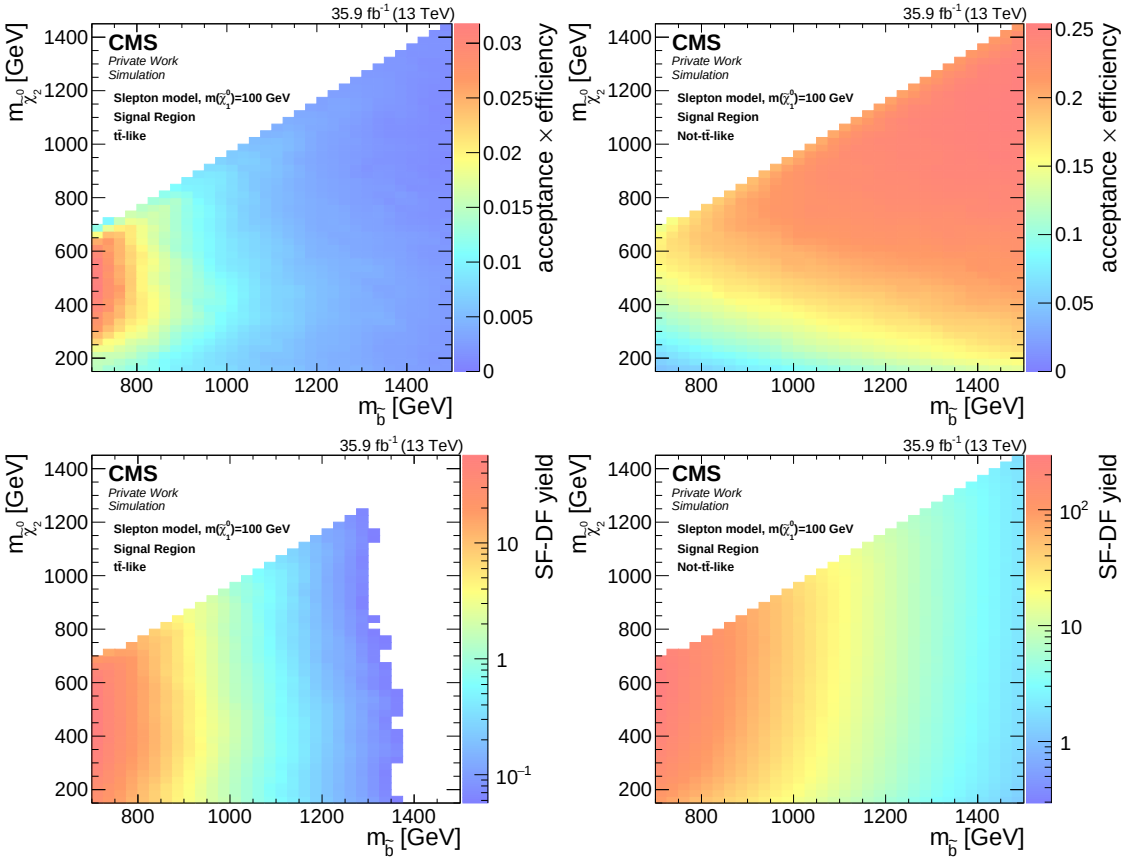

Figure 9.1: Signal acceptance×efficiency (top) and number of SF events after subtracting the DF event yield (bottom) in the $m_{\tilde{b}}$-$m_{\tilde{\chi}_2^0}$ plane for the slepton model. All mass regions in the $\mathrm{t\bar{t}}$-like (left) and not-$\mathrm{t\bar{t}}$-like signal bins (right) are combined.

bottom squark and the $\tilde{\chi}_2^0$ is small, reducing the energy of the generated b-quarks and thus the number of selected jets.

The lower plots in Fig. 9.1 show the signal yield for the two likelihood bins. The number of DF events is corrected by $R_{\mathrm{SF/DF}}$ and subtracted from the SF yield to account for a possible contribution of the signal processes to the DF sample and thereby the flavor-symmetric background prediction. The impact of this subtraction is small since the number of DF events amounts less than 10% of the number of SF events. The signal yields are dominated by the production cross section and therefore by the mass of the bottom squark. While about 200 events are expected at the lowest bottom squark masses, only a few events remain at $m_{\tilde{b}} = 1400\,\mathrm{GeV}$ and above. In case of the $\mathrm{t\bar{t}}$-like regions, less than one event is expected for bottom squark masses above 1.2–1.3 TeV, weakly depending on $m_{\tilde{\chi}_2^0}$.

Uncertainty source	Uncertainty in signal yield [%]
Luminosity	2.5
Lepton identification and isolation	4
Dilepton trigger efficiency	3
Fast simulation lepton identification and isolation	3
Fast simulation $p_{\mathrm{T}}^{\mathrm{miss}}$ modeling	0–5
b-tag modeling	0–5
Jet energy scale	0–4
Pileup modeling	1–2
Modeling of initial state radiation	0–2.5
Renormalization and factorization scales	0.5–2
Statistical uncertainty	1-16
Total uncertainty	8–17

Table 9.1: Summary of the systematic uncertainties in the signal yield.

9.2 Systematic uncertainties

Several systematic uncertainties need to be taken into account when using the simulation of the signal model for a statistical interpretation. The uncertainties considered in this analysis are summarized in Tab. 9.1. Only experimental uncertainties and those affecting the signal efficiency are stated here, while theoretical uncertainties in the cross section calculation are taken from [46].

The integrated luminosity, to which the simulation is normalized, was measured to a precision of 2.5% [132]. The uncertainties related to the lepton identification and isolation efficiencies are 3% per muon and 1-2% per electron. Assuming fully correlated uncertainties for leptons of the same flavor and no correlations between electrons and muons, this results in an uncertainty of about 4% on the signal efficiency. A similar treatment of the 3 (4)% uncertainty in the dilepton trigger efficiencies in the central (forward) lepton selection, obtained in Section 5.2.1, yields an uncertainty of 3% on the signal yield since most signal events are recorded in the central selection. An uncertainty of 2% per lepton is assumed for the corrections on the lepton modeling between fast and full detector simulation and results in an uncertainty of about 3% on the signal yield. Again fully correlated uncertainties for leptons of the same flavor and no correlations between the two flavors are assumed.

To account for inaccuracies of the $p_{\mathrm{T}}^{\mathrm{miss}}$ modeling in the fast simulation, the signal yields are obtained once with the generator level $p_{\mathrm{T}}^{\mathrm{miss}}$ and once with the reconstructed $p_{\mathrm{T}}^{\mathrm{miss}}$. The average of both signal yields is used as the resulting value and half of the difference between the simulated yields obtained with generated and reconstructed $p_{\mathrm{T}}^{\mathrm{miss}}$ is taken as an uncertainty in the modeling of $p_{\mathrm{T}}^{\mathrm{miss}}$. The impact of this uncertainty ranges from 0 to 5%, depending on the signal scenario, with larger values at low masses of the SUSY particles. The uncertainties in the b-tagging efficiency and the probability to mistag jets from light quarks varies between 0 and 5% as well, with higher values for large differences between the masses of the bottom squark and the $\tilde{\chi}_2^0$.

Varying the jet energy scales and reevaluating the jet momenta, and all derived observables

like $p_{\mathrm{T}}^{\mathrm{miss}}$, $\mathrm{M_{T2}}$, and $\Sigma m_{\ell b}$ has a negligible impact on the signal yield except for mass scenarios at the diagonal, where changes of the signal efficiency up to 4% can be observed.

The number of simulated simultaneous interactions used in the generation of the signal events deviates strongly from the number observed in data, since the pileup distribution for the signal simulation was determined at the beginning of the data taking period. To avoid events with very large weights, no pileup reweighting is applied. Instead the sample is split into two parts of similar size with a high and a low number of secondary vertices. The acceptance for both parts is evaluated separately and the difference taken as the uncertainty in the modeling of pileup. Small differences of 1–2% are observed.

The modeling of the number of jets from initial state radiation (ISR) in $\mathrm{t\bar{t}}$ events generated with MadGraph was found to differ from data. The effect can be removed by reweighting the MC events based on the number of ISR jets. The reweighting factors vary between 0.92 for one ISR jet and 0.51 for six ISR jets. Since the signal samples are produced with the same event generator, they are likely affected as well. The same weights are applied for signal simulation and the normalization of the samples takes these weights into account as well. The impact of the ISR uncertainty in the signal efficiency of 0–2.5% is obtained by simultaneously shifting the weights in the signal selection and the normalization by half of their deviation from unity.

The simulated samples are produced with weights according to different values of the renormalization and factorization scales. Again the weights in the normalization and the signal selection are varied simultaneously and the largest observed deviation, which ranges from 0.5 to 2%, is taken as the uncertainty from these scales.

The uncertainty due to the simulated sample statistics in the signal regions is about 1–2% in the not-$\mathrm{t\bar{t}}$-like selection, but can range up to 16% for high SUSY particle masses in the $\mathrm{t\bar{t}}$-like selection. For all of the stated uncertainties the mass bins in the two likelihood selections are combined to avoid statistical fluctuations in nearly empty signal bins. In general, the larger values for non-constant uncertainties are obtained for $\mathrm{t\bar{t}}$-like events.

9.3 Statistical interpretation

The results of the counting experiment analysis in the 14 signal regions of the counting experiment approach are translated into exclusion limits using methods described in Section 7. The obtained exclusion limits are shown in the left plot of Fig. 9.2. Masses of the bottom squark up to 980–1200 GeV are excluded, depending on the mass of the $\tilde{\chi}_2^0$. As discussed in Section 9.1, the not-$\mathrm{t\bar{t}}$-like signal regions are always the most sensitive ones. The split of the signal region into invariant dilepton mass bins is reflected by the limit contours and three contributing effects have been identified that can cause the expected limit to be weaker:

- A larger number of expected background events in the mass bins a signal point mainly contributes to.
- A signal yield that is spread more or less evenly between several signal bins instead of mainly contributing to one mass bin.

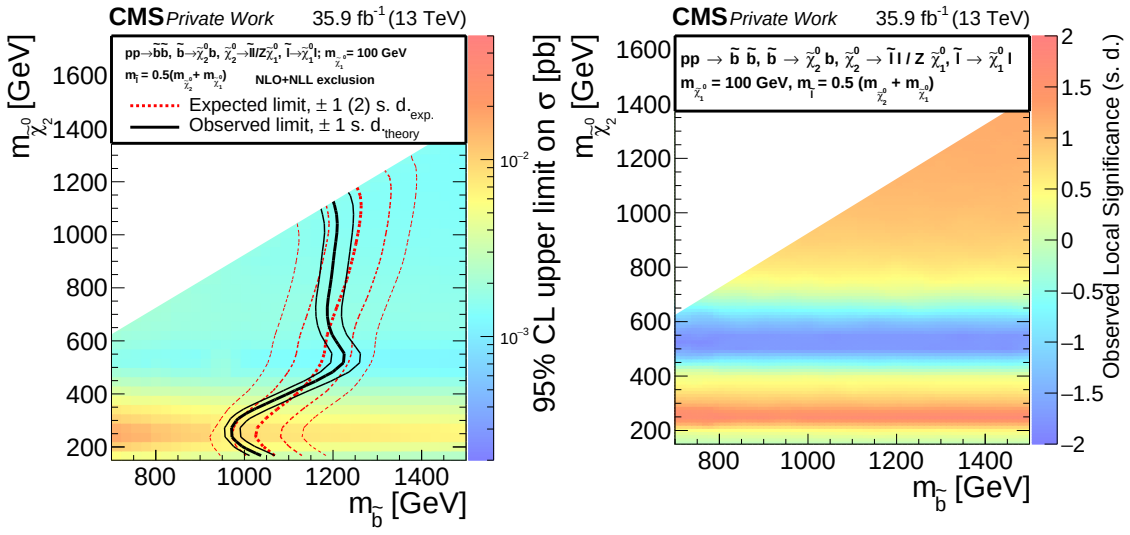

Figure 9.2: Cross section upper limit and exclusion contours at 95% CL (left) and observed significances (right) in the $m_{\tilde{b}}$-$m_{\tilde{\chi}_2^0}$ plane for the slepton model. In the left plot, the upper cross section limit is shown color coded. The mass points left of the solid black and dashed red lines are excluded by the observed and expected limit, respectively. The thin black and thin dashed red lines indicate the 1-s. d. theoretical and 1- and 2-s. d. experimental uncertainty intervals, respectively.

- A large fraction of signal events that would contribute to the excluded Z boson mass window and is therefore not considered.

Since the $\tilde{\chi}_1^0$ mass is set to 100 GeV, all the effects are present for $\tilde{\chi}_2^0$ masses between 200 and 350 GeV and have the maximal impact. These signal points mainly contribute to the mass bins around the Z boson mass, which contain the largest number of predicted background events. Additionally, the yield is split more or less evenly between two to four mass bins, which causes larger relative statistical fluctuations compared to the same number of events mainly observed in one bin. At high $m_{\tilde{\chi}_2^0}$ nearly all signal events contribute to the highest mass bin with only a small number of expected background events resulting in the best expected limits. For the lowest considered $\tilde{\chi}_2^0$ mass of 150 GeV, the expected limit reaches higher values than in the 200–350 GeV range, since the signal only contributes to the lowest mass bin with a moderate number of predicted not-$t\bar{t}$-like background events.

In case of the observed limit, this basic contour is similar but modified by the actual number of observed events. For the highest values of $m_{\tilde{\chi}_2^0}$, the highest $m_{\ell\ell}$ bin is the dominant one with 5 observed and 1.5 expected events, causing the observed limit to be lower than the expected one. The not-$t\bar{t}$-like bin from 300 to 400 GeV does not contain any observed events compared to an expectation of 3.5 events, resulting in a stronger observed limit for $\tilde{\chi}_2^0$ masses of 500 GeV. At $m_{\tilde{\chi}_2^0}$ values of 200 to 300 GeV, the upward deviation of 1.9 s. d. in the not-$t\bar{t}$-like mass bin from 96 to 150 GeV has the largest impact and results in a weaker observed limit.

An alternative visualization of the observed significances is shown in the right plot of Fig. 9.2.

No dependency on the bottom squark mass can be observed, since the $\tilde{\chi}_2^0$ mass determines to which mass regions a signal scenario contributes. The same dependencies on $m_{\tilde{\chi}_2^0}$ that were discussed above are present. In comparison to the observed significances for the individual signal bins, stated in Tab. 7.1, the combination of the signal regions reduces the magnitude of the observed significances, e.g., the upward deviation at $m_{\tilde{\chi}_2^0} \approx 250\,\text{GeV}$ has a significance of 1.5 s. d. compared to 1.9 s. d. in the not-$\mathrm{t\bar{t}}$-like mass bin from 96 to 150 GeV.

In comparison to the versions of the analysis on 8 TeV data [5, 6] and on $2.3\,\text{fb}^{-1}$ of 13 TeV data recorded in 2015 [7], the observed limit on the bottom squark mass is extended by 400–600 GeV, depending again on $m_{\tilde{\chi}_2^0}$, as can be seen in Fig. 9.3. This corresponds to a reduction of the production cross section (and therefore to an increase in the analysis' sensitivity) by a factor of 30–100. The increased luminosity accounts for about a factor of 4 when comparing to the results on 2015 data, under the assumption that the sensitivity increases with the square root of the sample size. This indicates that the improved methods increased the sensitivity by a factor of 7–25. An intermediate result on the first third of the data recorded in 2016, which was published in August 2016, is shown as well [133]. This version already used the $\mathrm{t\bar{t}}$ likelihood, but did not yet feature the requirement on the $\mathrm{M_{T2}}$ variable and used less invariant dilepton mass bins, providing expected limits on the bottom squark mass of 770–870 GeV. Taking the larger integrated luminosity into account, this corresponds to an increase in sensitivity by a factor of 2.5 to 7 for the full analysis. The observed limit in this intermediate version was weaker than the expected one due to an observation that exceeded the expectation by about 3 s. d. in one of the signal bins. Events in this bin were required to be not-$\mathrm{t\bar{t}}$-like and contain at least two jets, $p_\mathrm{T}^\mathrm{miss} > 150\,\text{GeV}$, and $m_{\ell\ell} > 101\,\text{GeV}$. The deviation was not consistent with the one observed at 8 TeV and disappeared completely when using the full data set, updated detector calibrations, and an improved treatment of the non-flavor-symmetric background contribution.

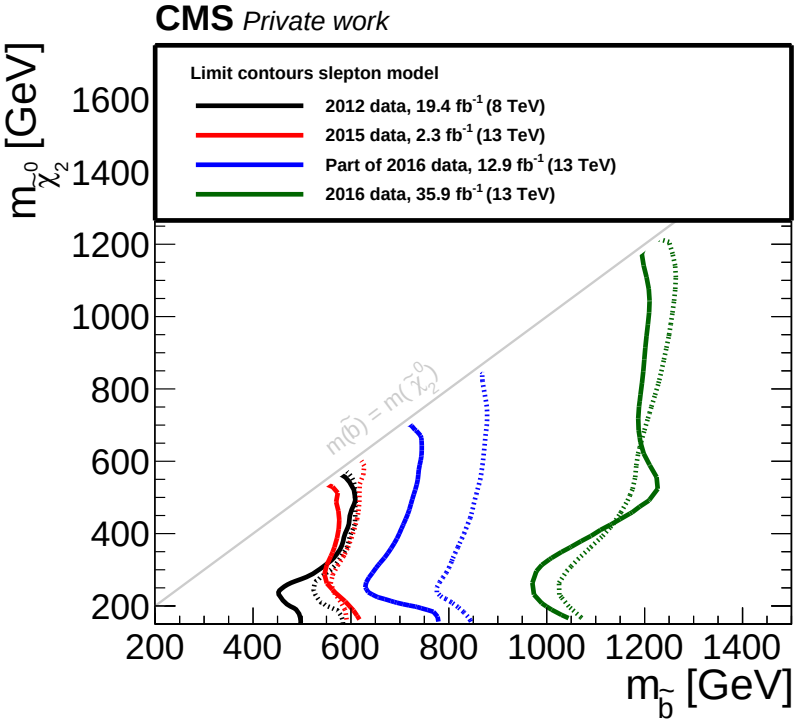

Figure 9.3: Comparison of the exclusion contours at 95% CL in the $m_{\tilde{b}}$-$m_{\tilde{\chi}_2^0}$ plane for the slepton model obtained in different version of the CMS search for SUSY in events OCSF lepton pairs. The limits obtained in this analysis, displayed in green, are compared to the results in 8 TeV data in black [5, 6], 13 TeV data taken in 2015 in red [7], and a result on the first third of the 13 TeV data taken in 2016 in blue [133]. The observed and expected limits are indicated by solid and dashed lines, respectively.

10 Summary

A search for supersymmetry in final states with two opposite-charge, same-flavor leptons has been presented, using the full data set of proton-proton collisions taken in 2016 by the CMS experiment at a center-of-mass energy of 13 TeV. The data set corresponds to an integrated luminosity of $35.9\,\mathrm{fb}^{-1}$. The analysis has focused on the correlated production of dielectron and dimuon pairs from the decay of the next-to-lightest neutralino into the lightest one, resulting in a characteristic edge structure in the invariant dilepton mass spectrum of the lepton pair.

A deviation observed in a previous version of the analysis on 8 TeV data was investigated. After discarding it as a statistical fluctuation, improvements have been made to increase the sensitivity of the analysis to the strong production of supersymmetric models assuming R-parity conservation. Both a counting experiment analysis and a kinematic fit were performed to search for an overall deviation and for an edge like structure in newly defined signal regions. In comparison to previous versions of the analysis, these signal regions use the $\mathrm{M_{T2}}$ variable and require more missing transverse momentum. For the counting experiment approach, a newly defined $\mathrm{t\bar{t}}$ likelihood and bins in the invariant dilepton mass have additionally been used.

The main contributions from standard model processes to these selections arise from flavor-symmetric processes and can therefore be estimated from different-flavor data. Corrections to account for differences in the lepton efficiencies were derived on data using two independent methods. Taking the transverse momenta and pseudorapidities of the leptons into account, these corrections have been obtained for each individual signal selection with a precision of 3–4%. Contributions from non-flavor-symmetric standard model processes to the counting experiment analysis were either extrapolated from photon data or obtained directly from the simulation of these processes. In the kinematic fit, the shape of the non-flavor-symmetric background contribution has been determined in a region enriched in events from Z boson decays in data. All methods have been validated using both simulated events and data.

In the counting experiment approach, the event yields in 14 regions of $\mathrm{t\bar{t}}$ likelihood and invariant dilepton mass are compared to the background prediction. The agreement is found to be consistent with the standard model expectation for such a number of regions, for which the sample statistics is the dominant uncertainty source.

An unbinned maximum likelihood fit was used to search for an edge in the invariant dilepton mass distribution. The fit was simultaneously applied to same-flavor and different-flavor data and consists of parameterizations for the flavor-symmetric and Z/γ^* backgrounds and a triangular signal model. The best fit yields a signal contribution of 62 ± 26 events with an endpoint at 158.7 ± 3.1 GeV. This corresponds to a local significance of 2.4 standard deviations, which is reduced to 1.5 standard deviations if the possibility to fit such a deviation anywhere in the mass spectrum is taken into account. Comparisons to the fit of the background-only hypothesis and to the results of the counting experiment analysis indicate that the fit uses the signal contribution to account for a downward fluctuation at low dilepton masses and an upward fluctuation in the range between the Z boson mass and the fitted endpoint. This endpoint does not match the edge position obtained in a previous version of the analysis on

8 TeV data.

No clear indication for supersymmetry has been observed and exclusion limits are set on a simplified model on the pair production of bottom squarks. The model contains the decay $\tilde{\chi}_2^0 \to \ell\ell\tilde{\chi}_1^0$ either via an intermediate slepton or a Z boson. Assuming the mass of the lightest neutralino to be 100 GeV, bottom squark masses up to 980–1200 GeV have been excluded, depending on the mass of the next-to-lightest neutralino. These results extend the exclusion limits from previous analyses at 8 TeV and on 13 TeV data recorded in 2015 by 400–600 GeV. At 13 TeV center-of-mass energy, this corresponds to a reduction of the production cross section, and thereby an increase of the analysis' sensitivity, by a factor of 30–100.

The increase of the center-of-mass energy, the large integrated luminosity recorded in 2016, and improvements in the signal selections made this increase in sensitivity compared to previous analyses possible. The prospect to achieve a similar improvement of the sensitivity to the studied signal scenario in the next years seems unlikely, at least before the end of the next long shutdown of the LHC, which will take place from the end of 2018 until the beginning of 2021. The current plan is to perform the search once more on the data taken in 2017 and 2018 and accompany it with a differential cross section measurement of this final state. This measurement will finalize about a decade of searching for supersymmetry in events with two opposite-charge, same-flavor leptons, jets, and missing transverse momentum by our analysis group and provide valuable information to theorists who want to cross check their new physics models.

A Data sets and triggers

The primary data sets used in this work are given in Tab. A.1 together with the main purpose and the corresponding database paths to the data sets from the eight run ranges in the CMS bookkeeping system (DBS). The "*" in the database path stands for "MINIAOD". The paths for the run ranges Run2016C to Run2016G are exactly the same except for the letter indicating the data period and are thus abbreviated as (C-G).

The triggers used to record these data sets are given in Tab. A.2. Dilepton triggers are split into isolated and non-isolated categories and the main purpose of each trigger is stated as well. The trigger paths indicate that these are part of the HLT menu, which objects were triggered and which trigger threshold was used (e.g. Ele17 stands for and electron with 17 GeV p_T). Further identification and isolation criteria in the corresponding detector components are also stated. As an example, CaloIdL in the double electron HLT path indicates that loose identification criteria were required in the ECAL.

Primary data set	Purpose	DBS data set path
DoubleEG	Signal	/DoubleEG/Run2016B-03Feb2017_ver2-v2/*
		/DoubleEG/Run2016(C-G)-03Feb2017-v1/*
		/DoubleEG/Run2016H-03Feb2017_ver2-v1/*
		/DoubleEG/Run2016H-03Feb2017_ver3-v1/*
DoubleMuon	Signal	/DoubleMuon/Run2016B-03Feb2017_ver2-v2/*
		/DoubleMuon/Run2016(C-G)-03Feb2017-v1/*
		/DoubleMuon/Run2016H-03Feb2017_ver2-v1/*
		/DoubleMuon/Run2016H-03Feb2017_ver3-v1/*
MuonEG	Background prediction	/MuonEG/Run2016B-03Feb2017_ver2-v2/*
		/MuonEG/Run2016(C-G)-03Feb2017-v1/*
		/MuonEG/Run2016H-03Feb2017_ver2-v1/*
		/MuonEG/Run2016H-03Feb2017_ver3-v1/*
JetHT	Trigger efficiencies	/JetHT/Run2016B-03Feb2017_ver2-v2/*
		/JetHT/Run2016(C-G)-03Feb2017-v1/*
		/JetHT/Run2016H-03Feb2017_ver2-v1/*
		/JetHT/Run2016H-03Feb2017_ver3-v1/*
SingleElectron	Fake rate determination	/SingleElectron/Run2016B-03Feb2017_ver2-v2/*
		/SingleElectron/Run2016(C-G)-03Feb2017-v1/*
		/SingleElectron/Run2016H-03Feb2017_ver2-v1/*
		/SingleElectron/Run2016H-03Feb2017_ver3-v1/*
SingleMuon	Fake rate determination	/SingleMuon/Run2016B-03Feb2017_ver2-v2/*
		/SingleMuon/Run2016(C-G)-03Feb2017-v1/*
		/SingleMuon/Run2016H-03Feb2017_ver2-v1/*
		/SingleMuon/Run2016H-03Feb2017_ver3-v1/*

Table A.1: List of primary data sets used in the analysis. Additionally, the main purpose of the data set and the data set paths is given. (C-G) is an abbreviation for the corresponding data sets of Run2016C to Run2016G for which the remaining DBS path is the identical.

Object	Purpose	HLT path
ee isolated	Signal	HLT_Ele17_Ele12_CaloIdL_TrackIdL_IsoVL_DZ HLT Ele23 Ele12 CaloIdL TrackIdL IsoVL DZ
ee non-isolated	Signal	HLT_DoubleEle33_CaloIdL_GsfTrkIdVL HLT_DoubleEle33_CaloIdL_GsfTrkIdVL_MW
$\mu\mu$ isolated	Signal	HLT_Mu17_TrkIsoVVL_Mu8_TrkIsoVVL HLT_Mu17_TrkIsoVVL_Mu8_TrkIsoVVL_DZ HLT_Mu17_TrkIsoVVL_TkMu8_TrkIsoVVL HLT_Mu17_TrkIsoVVL_TkMu8_TrkIsoVVL_DZ
$\mu\mu$ non-isolated	Signal	HLT_Mu27_TkMu8 HLT_Mu30_TkMu11
$e\mu$ isolated	Background prediction	HLT_Mu8_TrkIsoVVL_Ele17_CaloIdL_TrackIdL_IsoVL HLT_Mu8_TrkIsoVVL_Ele23_CaloIdL_TrackIdL_IsoVL HLT_Mu8_TrkIsoVVL_Ele23_CaloIdL_TrackIdL_IsoVL_DZ HLT_Mu17_TrkIsoVVL_Ele12_CaloIdL_TrackIdL_IsoVL HLT_Mu23_TrkIsoVVL_Ele8_CaloIdL_TrackIdL_IsoVL HLT_Mu23_TrkIsoVVL_Ele8_CaloIdL_TrackIdL_IsoVL_DZ HLT_Mu23_TrkIsoVVL_Ele12_CaloIdL_TrackIdL_IsoVL HLT_Mu23_TrkIsoVVL_Ele12_CaloIdL_TrackIdL_IsoVL_DZ
$e\mu$ non-isolated	Background prediction	HLT_Mu30_Ele30_CaloIdL_GsfTrkIdVL HLT_Mu33_Ele33_CaloIdL_GsfTrkIdVL
H_{T}	Trigger efficiencies	HLT_PFHT125, HLT_PFHT200, HLT_PFHT250 HLT_PFHT300, HLT_PFHT350, HLT_PFHT400 HLT_PFHT475, HLT_PFHT600, HLT_PFHT650 HLT_PFHT800, HLT_PFHT900
e	Fake rate determination	HLT_Ele8_CaloIdL_TrackIdL_IsoVL_PFJet30 HLT_Ele17_CaloIdL_TrackIdL_IsoVL_PFJet30
μ	Fake rate determination	HLT_Mu8_TrkIsoVVL HLT_Mu17_TrkIsoVVL

Table A.2: List of triggers used in the analysis.

B Simulated samples

The simulated samples of SM background processes and signal scenarios used in this work are given in Tab. B.1. The physics process is given together with information about the simulated decays or generator selection. The corresponding database paths are given as well. The "*" in the database path stands for "RunIISummer16MiniAODv2-PUMoriond17_80X_mcRun2_asymptotic_2016_TrancheIV_v6", "**" represents "MINIAODSIM", "TUNE" stands for "TuneCUETP8M", and "†" substitutes "TuneCUETP8M1_13TeV-madgraphMLM-pythia8/RunIISpring16MiniAODv2-pLHE_PUSpring16Fast_80X_mcRun2_asymptotic_2016_miniAODv2_v0".

A list of the QCD multijet samples used for the study of non-prompt leptons is given in Tab. B.2. Since the cross section drastically decreases with the jet momentum, the QCD multijet samples are generated for different ranges of the leading jet p_{T}. Furthermore, filters are applied to only select events that include a muon, electromagnetic object (electron or photon), or an electron from the decay of a heavy-flavor quark. The cross sections need to be corrected for the filter efficiency. The database paths are given by /QCD_Pt-‡_MuEnrichedPt5_TuneCUETP8M1_13TeV_pythia8/*-v1/**, /QCD_Pt-‡_EMEnrichedPt5_TuneCUETP8M1_13TeV_pythia8/*-v1/**, and /QCD_Pt-‡_bcToE_TuneCUETP8M1_13TeV_pythia8/*-v1/** for the samples enriched in muons, e/γ, and electrons from heavy-flavor decays, respectively. The "‡" stands for the generated p_{T} range of the leading jet, e.g. "15to20" for 15–20 GeV or "1000toInf" for > 1000 GeV.

category	process/mass range	DBS sample path
$t\bar{t}$	$t\bar{t} \to 2b2\ell2\nu$	/TTTo2L2Nu_TUNE2_ttHtranche3_13TeV-powheg-pythia8/*-v1/**
	$t\bar{t} \to 2b2q\ell\nu$	/TTToSemilepton_TUNE2_ttHtranche3_13TeV-powheg-pythia8/*-v1/**
DY+jets	$Z/\gamma* \to \ell\ell$, $m_{\ell\ell} \in [10, 50]$ GeV	/DYJetsToLL_M-10to50_TUNE1_13TeV-madgraphMLM-pythia8/*-v1/**
	$Z/\gamma* \to \ell\ell$, $m_{\ell\ell} > 50$ GeV	/DYJetsToLL_M-50_TUNE1_13TeV-madgraphMLM-pythia8/*_ext1-v2/**
	WZ$\to 2\ell$2q	/WZTo2L2Q_13TeV_amcatnloFXFX_madspin_pythia8/*-v1/**
	ZZ$\to 2\ell$2q	/ZZTo2L2Q_13TeV_amcatnloFXFX_madspin_pythia8/*-v1/**
	ZZ$\to 4\ell$	/ZZTo4L_13TeV_powheg_pythia8/*-v1/**
Z+ν	WZ$\to 3\ell\nu$	/WZTo3LNu_TUNE1_13TeV-powheg-pythia8/*-v1/**
	ZZ$\to 2\ell2\nu$	/ZZTo2L2Nu_13TeV_powheg_pythia8/*-v1/**
	WWZ	/WWZ_TUNE1_13TeV-amcatnlo-pythia8/*-v1/**
	WZZ	/WZZ_TUNE1_13TeV-amcatnlo-pythia8/*-v1/**
	ZZZ	/ZZZ_TUNE1_13TeV-amcatnlo-pythia8/*-v1/**
	$t\bar{t}$Z, Z$\to 2\ell/2\nu$	/TTZToLLNuNu_M-10_TUNE1_13TeV-amcatnlo-pythia8/*_ext1-v1/**
	tZ, Z$\to \ell\ell$	/tZq_ll_4f_13TeV-amcatnlo-pythia8/*_ext1-v1/**
	VH, H$\to$non b$\bar{b}$	/VHToNonbb_M125_13TeV_amcatnloFXFX_madspin_pythia8/*-v1/**
Single t	t/$\bar{t}$ s-channel, t$\to b\ell\nu$	/ST_s-channel_4f_leptonDecays_13TeV-amcatnlo-pythia8_TUNE1/*-v1/**
	t t-channel	/ST_t-channel_top_4f_inclusiveDecays_13TeV-powhegV2-madspin-pythia8_TUNE1/*-v1/**
	$\bar{t}$ t-channel	/ST_t-channel_antitop_4f_inclusiveDecays_13TeV-powhegV2-madspin-pythia8_TUNE1/*-v1/**
	t tW-channel, tW$\to$ b2$\ell2\nu$/b$\ell\nu$2q	/ST_tW_top_5f_NoFullyHadronicDecays_13TeV-powheg_TUNE1/*_ext1-v1/**
	$\bar{t}$ tW-channel, tW$\to$ b2$\ell2\nu$/b$\ell\nu$2q	/ST_tW_antitop_5f_NoFullyHadronicDecays_13TeV-powheg_TUNE1/*_ext1-v1/**
Other SM	W$\to \ell\nu$	/WJetsToLNu_TUNE1_13TeV-madgraphMLM-pythia8/*-v1/**
	WW$\to 2\ell2\nu$	/WWTo2L2Nu_13TeV-powheg/*-v1/**
	WW$\to \ell\nu$2q	/WWToLNuQQ_13TeV-powheg/*_ext1-v1/**
	WZ$\to \ell\nu$2q	/WZTo1L1Nu2Q_13TeV_amcatnloFXFX_madspin_pythia8/*-v3/**
	$t\bar{t}\gamma$	/TTGJets_TUNE1_13TeV-amcatnloFXFX-madspin-pythia8/*_ext1-v1/**
	$t\bar{t}$W, W$\to \ell\nu$	/TTWJetsToLNu_TUNE1_13TeV-amcatnloFXFX-madspin-pythia8/*_ext1-v3/**
	$t\bar{t}$W, W$\to$ 2q	/TTWJetsToQQ_TUNE1_13TeV-amcatnloFXFX-madspin-pythia8/*-v1/**
	$t\bar{t}$Z, Z$\to$ 2q	/TTZToQQ_TUNE1_13TeV-amcatnlo-pythia8/*-v1/**
	$t\bar{t}$H, H$\to$ b$\bar{b}$	/ttHTobb_M125_TUNE2_ttHtranche3_13TeV-powheg-pythia8/*-v1/**
	$t\bar{t}$H, H$\to$ non b$\bar{b}$	/ttHToNonbb_M125_TUNE2_ttHtranche3_13TeV-powheg-pythia8/*-v1/**
	$t\bar{t}t\bar{t}$	/TTTT_TUNE2T4_13TeV-amcatnlo-pythia8/*-v1/**
Signal	$m_{\tilde{b}}$: 600–775 GeV	/SMS-T6bbllslepton_mSbottom-600To775_mLSP-150To725_†-v1/**
	$m_{\tilde{b}}$: 800–950 GeV	/SMS-T6bbllslepton_mSbottom-800To950_mLSP-150To900_†-v1/**
	$m_{\tilde{b}}$: 1000–1500 GeV	/SMS-T6bbllslepton_mSbottom-1000To1500_mLSP-120To1450†-v1/**

Table B.1: List of simulated samples used in the analysis. The samples are grouped into background categories or signal samples. Information about the simulated decays or generator selection is given and the name of the sample in the database is stated.

category	jet p_{T} range	σ [pb]	filter efficiency	$N_{\mathrm{events}}^{\mathrm{gen}}$	weight
μ enriched	15–20 GeV	1 273 190 000	0.003	4 141 251	33 100
	20–30 GeV	558 528 000	0.005	31 253 042	3400
	30–50 GeV	139 803 000	0.012	29 954 820	1980
	50–80 GeV	19 222 500	0.023	19 806 916	793
	80–120 GeV	2 758 420	0.038	13 786 971	276
	120–170 GeV	469 797	0.054	8 042 721	112
	170–300 GeV	117 989	0.073	7 947 159	39.1
	300–470 GeV	7820	0.10	7 937 590	3.61
	470–600 GeV	646	0.12	3 851 524	0.74
	600–800 GeV	187	0.13	4 010 136	0.22
	800–1000 GeV	32.3	0.15	3 848 483	0.044
	>1000 GeV	10.4	0.16	3 990 117	0.015
e/γ enriched	20–30 GeV	557 600 000	0.0096	9 218 954	20 800
	30–50 GeV	136 000 000	0.073	4 730 195	75 300
	50–80 GeV	19 800 000	0.15	22 337 072	4650
	80–120 GeV	2 800 000	0.13	35 841 768	351
	120–170 GeV	477 000	0.13	35 817 296	63.1
	170–300 GeV	114 000	0.17	11 540 163	58.5
	>300 GeV	9000	0.15	7 373 633	6.57
$b/c \to e$ enriched	15–20 GeV	1 272 980 000	0.0002	2 685 602	3400
	20–30 GeV	557 627 000	0.00059	10 987 947	1070
	30–80 GeV	159 068 000	0.0026	15 328 096	950
	80–170 GeV	3 221 000	0.012	14 976 689	91.3
	170–250 GeV	105 771	0.025	9 720 760	9.73
	>250 GeV	21 094	0.034	9 773 617	2.62

Table B.2: Simulated QCD multijet data sets used for the study of non-prompt leptons. The samples are grouped by the process enriched in the sample. For each sample, information about the cross section, the filter efficiency for the desired process, the number of processed events, and the resulting weight used to scale the simulation to the recorded luminosity are given.

C Dependency studies of $R_{\mathrm{SF/DF}}$

Several dependency studies of $R_{\mathrm{SF/DF}}$ in the central lepton selection of the flavor-symmetric control region are shown in Section 5.2.1. The corresponding studies for events including forward leptons are presented in Fig. C.1. The data statistics in the forward lepton selection is smaller than in the central selection and results in larger statistical uncertainties and fluctuations of the data points. No significant dependencies of data or simulation are observed.

The likelihood discriminator defined in Section 6.2 uses $p_{\mathrm{T}}^{\mathrm{miss}}$, $\Delta\phi_{\ell\ell}$, the dilepton p_{T}, and $\sum m_{\ell b}$. as input variables. The dependency of $R_{\mathrm{SF/DF}}$ on $p_{\mathrm{T}}^{\mathrm{miss}}$ has been studied in Fig. C.1 and Section 5.2.1. Figure C.2 shows the dependency of $R_{\mathrm{SF/DF}}$ on the three remaining observables. No dependency of $R_{\mathrm{SF/DF}}$ on any of these observables can be observed.

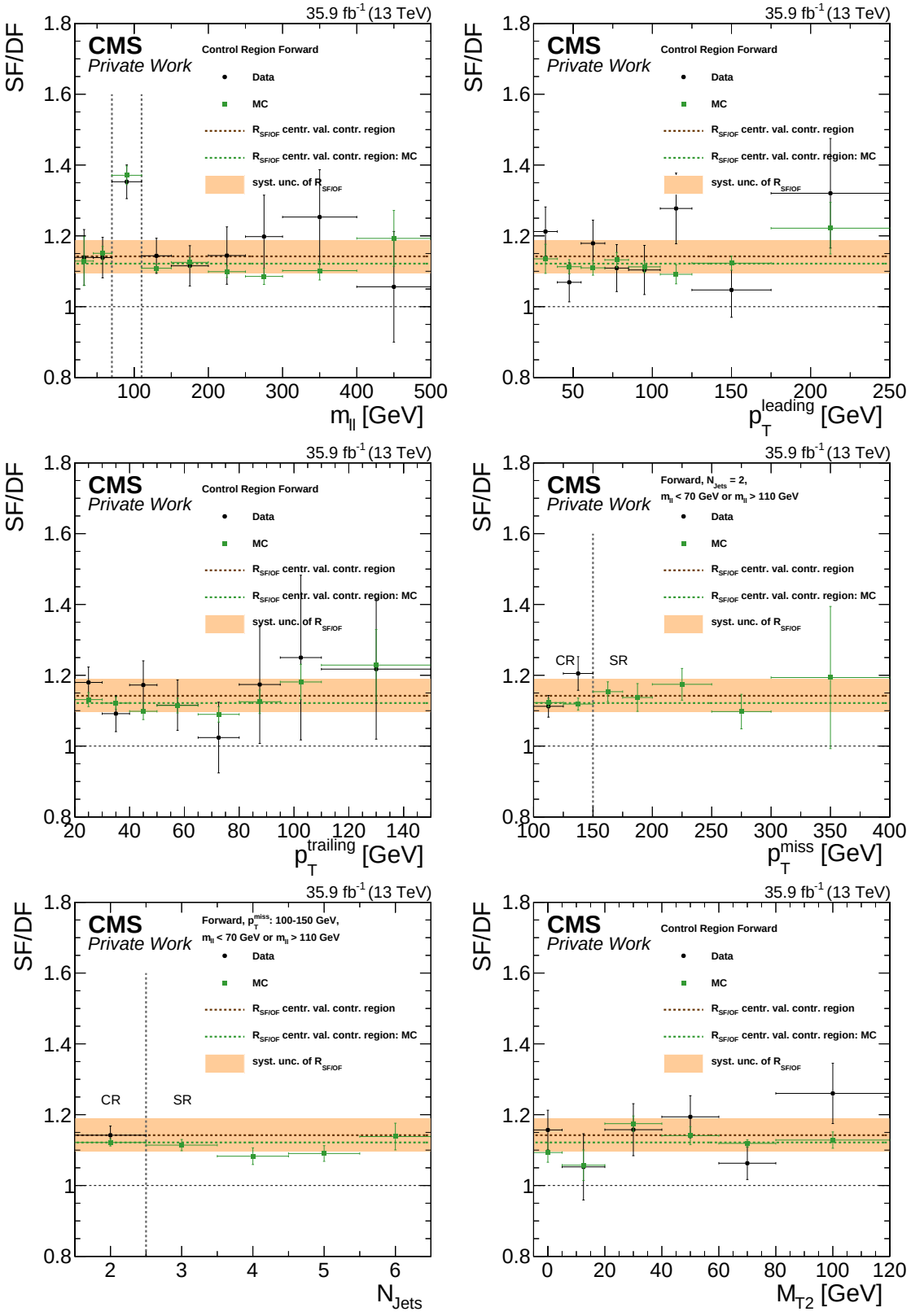

Figure C.1: $R_{\mathrm{SF/DF}}$ as a function of $m_{\ell\ell}$ (top left), leading lepton p_{T} (top right), subleading lepton p_{T} (center left), jet multiplicity (center right), $p_{\mathrm{T}}^{\mathrm{miss}}$ (bottom left), and $\mathrm{M_{T2}}$ (bottom right) in the flavor-symmetric control region in the forward lepton selection for data and simulation. Dashed gray lines indicate the boundaries of the flavor symmetric control region and the excluded mass window. The assigned systematic uncertainty of 4% is indicated as an orange band.

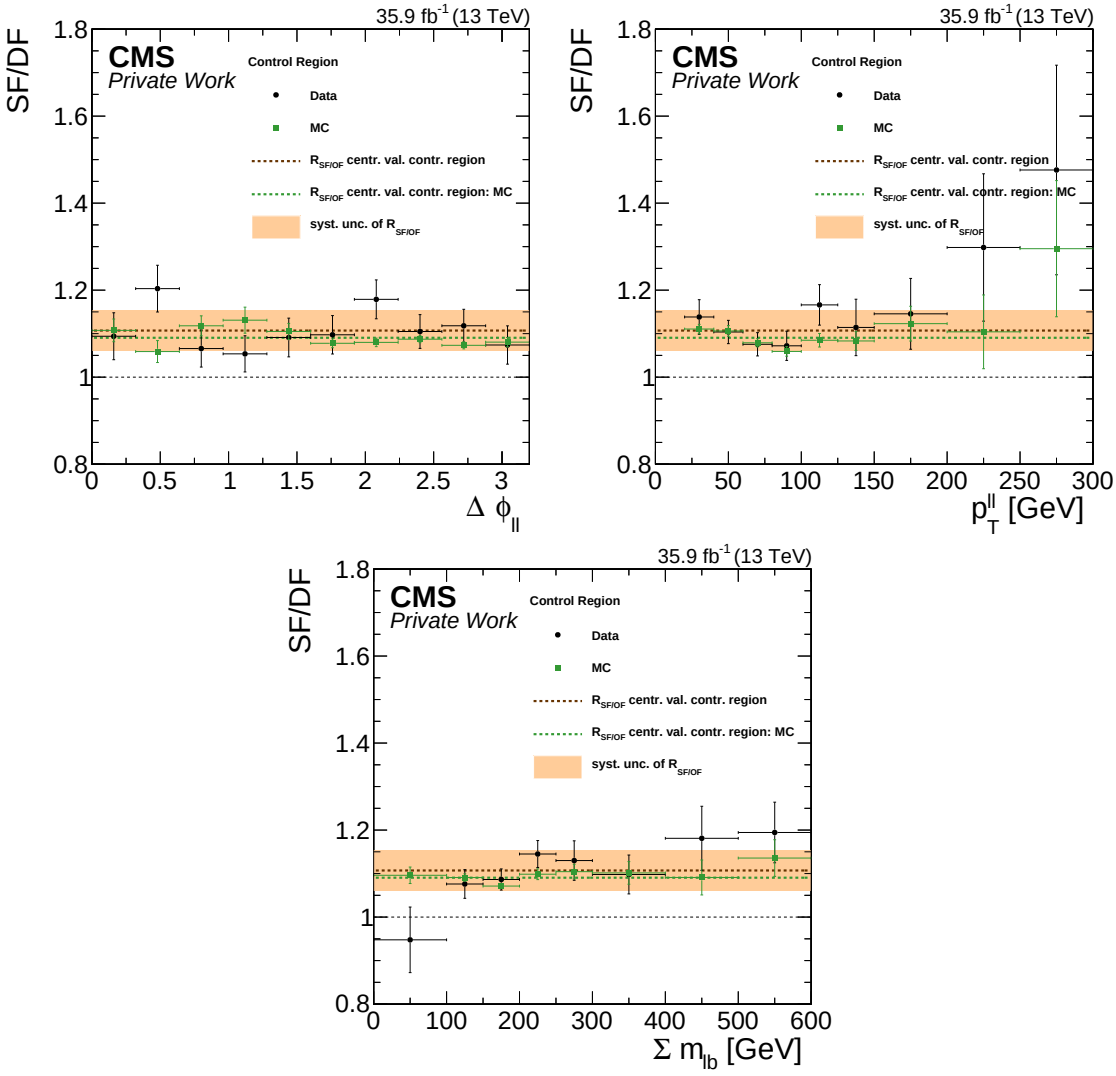

Figure C.2: $R_{\mathrm{SF/DF}}$ as a function of $\Delta\phi_{\ell\ell}$ (top left), the p_{T} of the dilepton system (top right), and $\Sigma m_{\ell b}$ (bottom) in the flavor-symmetric control region for data and simulation. The assigned systematic uncertainty of 4% is indicated as an orange band.

D Dependency studies of R_{T}

Several dependency studies of R_{T} in the central lepton selection are shown in Section 5.2.1. The corresponding studies for events including forward leptons are presented in Fig. D.1. The statistical precision in the forward lepton selection in data is smaller than in the central selection and results in larger statistical uncertainties and fluctuations of the data points. No significant dependencies of data or simulation are observed.

The likelihood discriminator defined in Section 6.2 uses $p_{\mathrm{T}}^{\mathrm{miss}}$, $\Delta\phi_{\ell\ell}$, $p_{\mathrm{T}}^{\ell\ell}$, and $\sum m_{\ell b}$. as input variables. The dependency of R_{T} on $p_{\mathrm{T}}^{\mathrm{miss}}$ has been studied in Fig. D.1 and Section 5.2.1. Figure D.2 shows the dependency of R_{T} on the three remaining observables. No dependency of R_{T} on any of these observables can be observed.

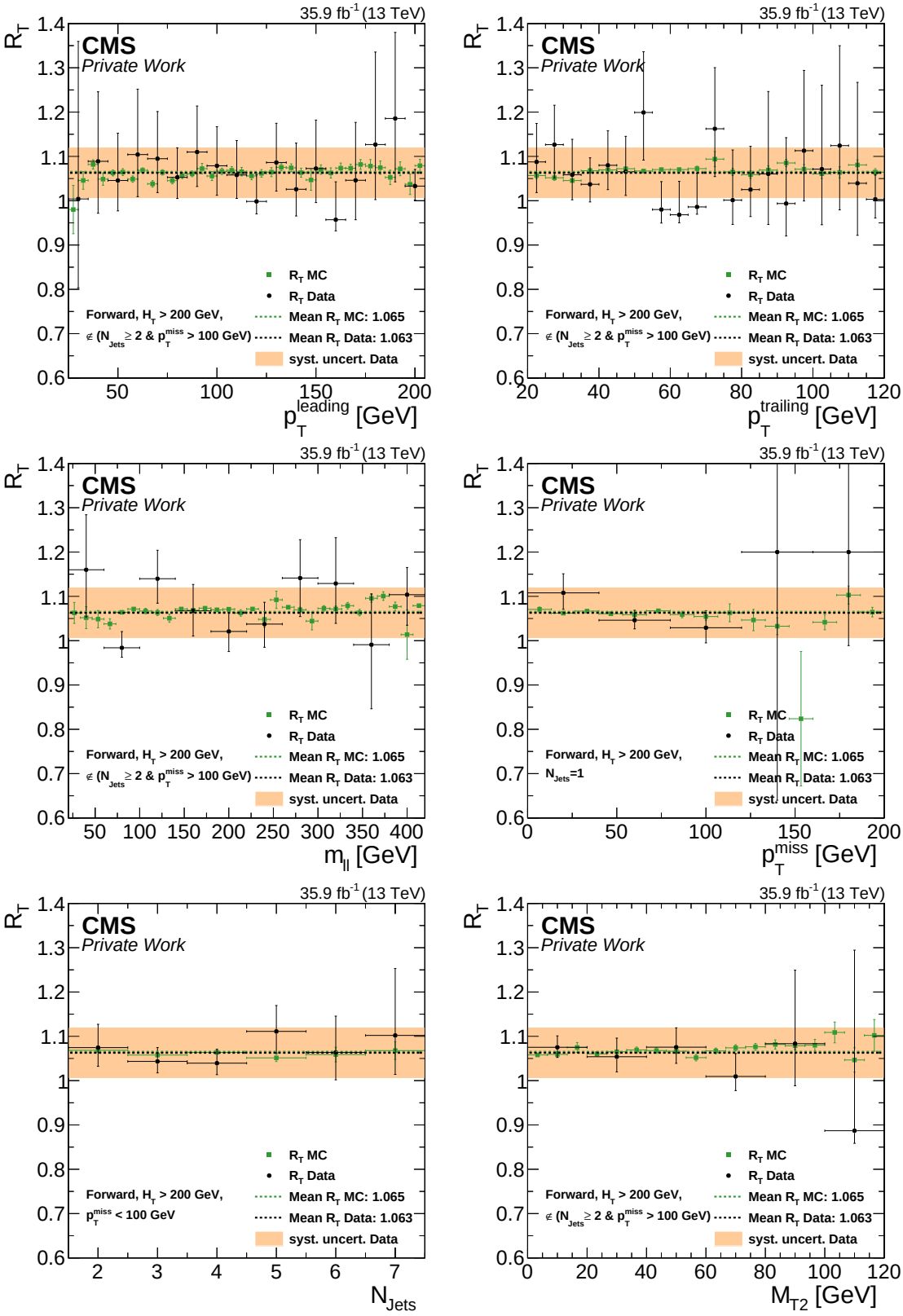

Figure D.1: R_{T} as a function of leading lepton p_{T} (top left), subleading lepton p_{T} (top right), $m_{\ell\ell}$ (center left), jet multiplicity (center right), $p_{\mathrm{T}}^{\mathrm{miss}}$ (bottom left), and $\mathrm{M_{T2}}$ (bottom right) for the forward lepton selection in data and simulation. The central value obtained in data(simulation) is shown as a black(green) dashed line, while the systematic uncertainty of about 4% is indicated as an orange band around the central value in data.

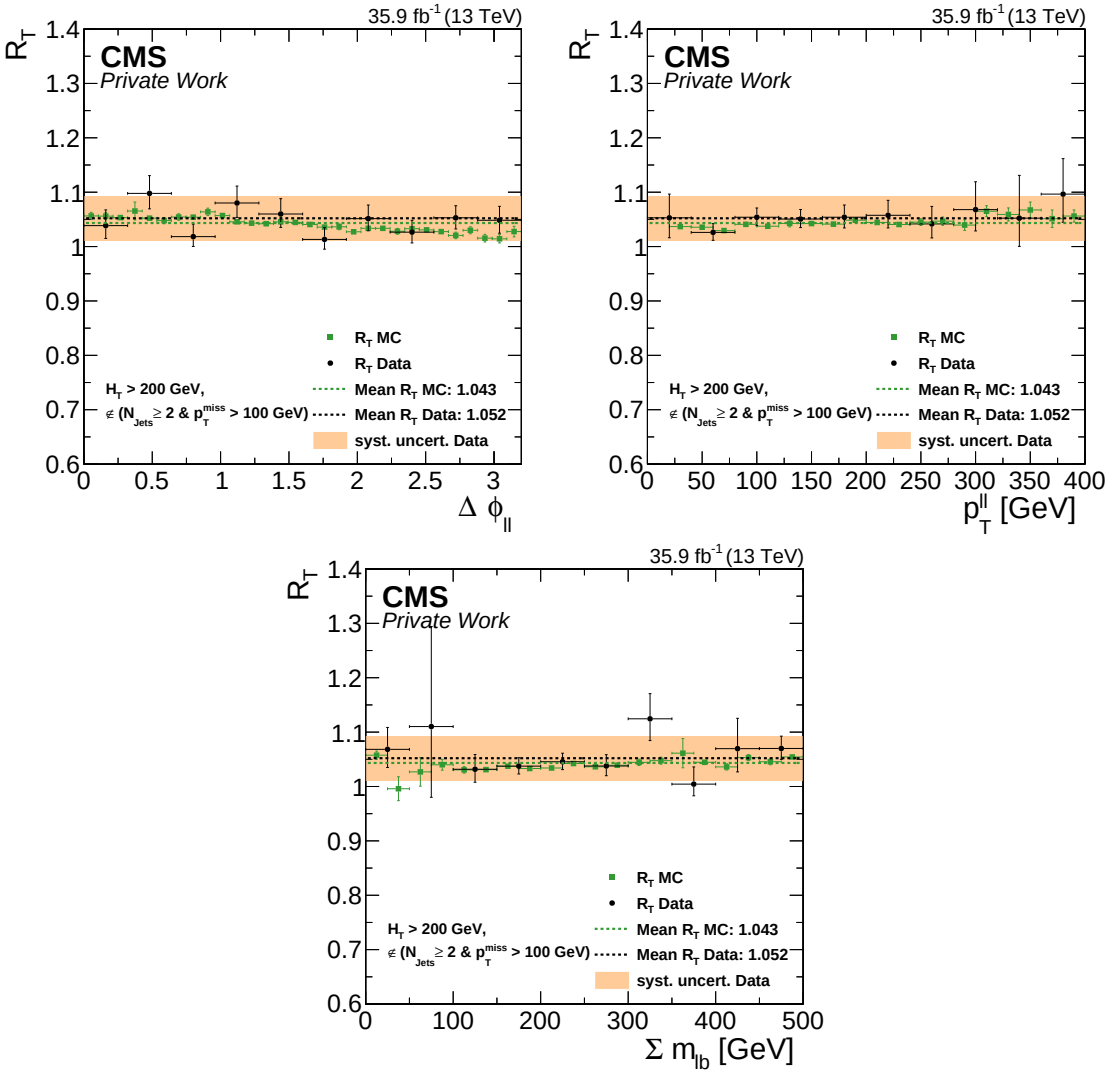

Figure D.2: R_{T} as a function of $\Delta\phi_{\ell\ell}$ (top left), the p_{T} of the dilepton system (top right), and $\Sigma m_{\ell b}$ (bottom) for data and simulation. The central value obtained in data(simulation) is shown as a black(green) dashed line, while the systematic uncertainty of about 4% is indicated as an orange band around the central value in data.

E Dependency studies of $r_{\mu/e}$

A dependency of $r_{\mu/e}$ on the lepton p_{T} is observed (see Section 5.2.1 and Fig. E.1). Three factors have been identified that contribute to this dependency and the impact of each on $r_{\mu/e}$ can be studied on simulation:

- Turn-on effects in the electron trigger efficiencies discussed in Section 5.2.1. Not requiring the HLT emulation removes this factor.
- Similar turn-on effects are known to affect the electron identification efficiency as is discussed in [96]. Note that a working point of the multivariate electron identification with lower overall efficiency is used in [96] but the general effect is the same. Events can be reweighted by the inverse of the p_{T} dependent efficiency to remove this influence.
- The asymmetric isolation requirements of $\mathrm{Iso}_{\mathrm{rel}} < 0.1$ for electrons and < 0.2 for muons defined in Section 4.3.2 has a small impact that can be avoided by using the same requirement of $\mathrm{Iso}_{\mathrm{rel}} < 0.1$ for both electrons and muons.

Figure E.2 shows $r_{\mu/e}$ as a function of the p_{T} of the leading and subleading lepton in simulation for the default selection (top) and with the three impact factors removed (bottom). The events are not split into a central and forward lepton selection. While the default selection shows a clear dependence on both lepton momenta, the distributions are flat if the impact of the three factors is removed. The same plots with only one of the influences removed are shown in Fig. E.3. Removing only one of the factors reduces the dependency but a removal of all three factors at the same time is required to eliminate it completely.

On data, the only way to avoid the turn-on effects is to increase the requirements on the lepton p_{T}. This is not desirable as it would reduce the available statistics significantly (see Section 5.2.1). Therefore, a parameterization is necessary. The impact of the isolation requirements could be removed by using symmetric thresholds for electrons and muons. This step is not taken to avoid an asymmetric fraction of non-prompt leptons and to use the same requirements as other CMS analyses do. Additionally, the asymmetric isolation requirements have the smallest effect of the three identified factors and a parameterization has to be used due to the dependencies introduced by the efficiency turn-on effects, anyway.

Figure E.4 shows $r_{\mu/e}^{\mathrm{corr.}}$ as a function of the p_{T} of the leading and trailing lepton, invariant mass and p_{T} of the dilepton system, jet multiplicity, and $p_{\mathrm{T}}^{\mathrm{miss}}$ in the forward region. $0.5\left(r_{\mu/e}^{\mathrm{corr.}} + 1/r_{\mu/e}^{\mathrm{corr.}}\right)$is displayed in Fig. E.5 as a function of the same variables . No dependency of $r_{\mu/e}^{\mathrm{corr.}}$ or $0.5\left(r_{\mu/e}^{\mathrm{corr.}} + 1/r_{\mu/e}^{\mathrm{corr.}}\right)$ on any of the observables can be observed.

The likelihood discriminator defined in Section 6.2 uses $p_{\mathrm{T}}^{\mathrm{miss}}$, $\Delta\phi_{\ell\ell}$, $p_{\mathrm{T}}^{\ell\ell}$, and $\sum m_{\ell b}$. as input variables. The dependencies of $r_{\mu/e}^{\mathrm{corr.}}$ or $0.5\left(r_{\mu/e}^{\mathrm{corr.}} + 1/r_{\mu/e}^{\mathrm{corr.}}\right)$ on $p_{\mathrm{T}}^{\mathrm{miss}}$ have been studied in Section 5.2.1 and in Fig. E.4 and E.5. Figure E.6 shows the dependency of $r_{\mu/e}^{\mathrm{corr.}}$ and $0.5\left(r_{\mu/e}^{\mathrm{corr.}} + 1/r_{\mu/e}^{\mathrm{corr.}}\right)$ on the two remaining observables. No dependency on these variables can be observed.

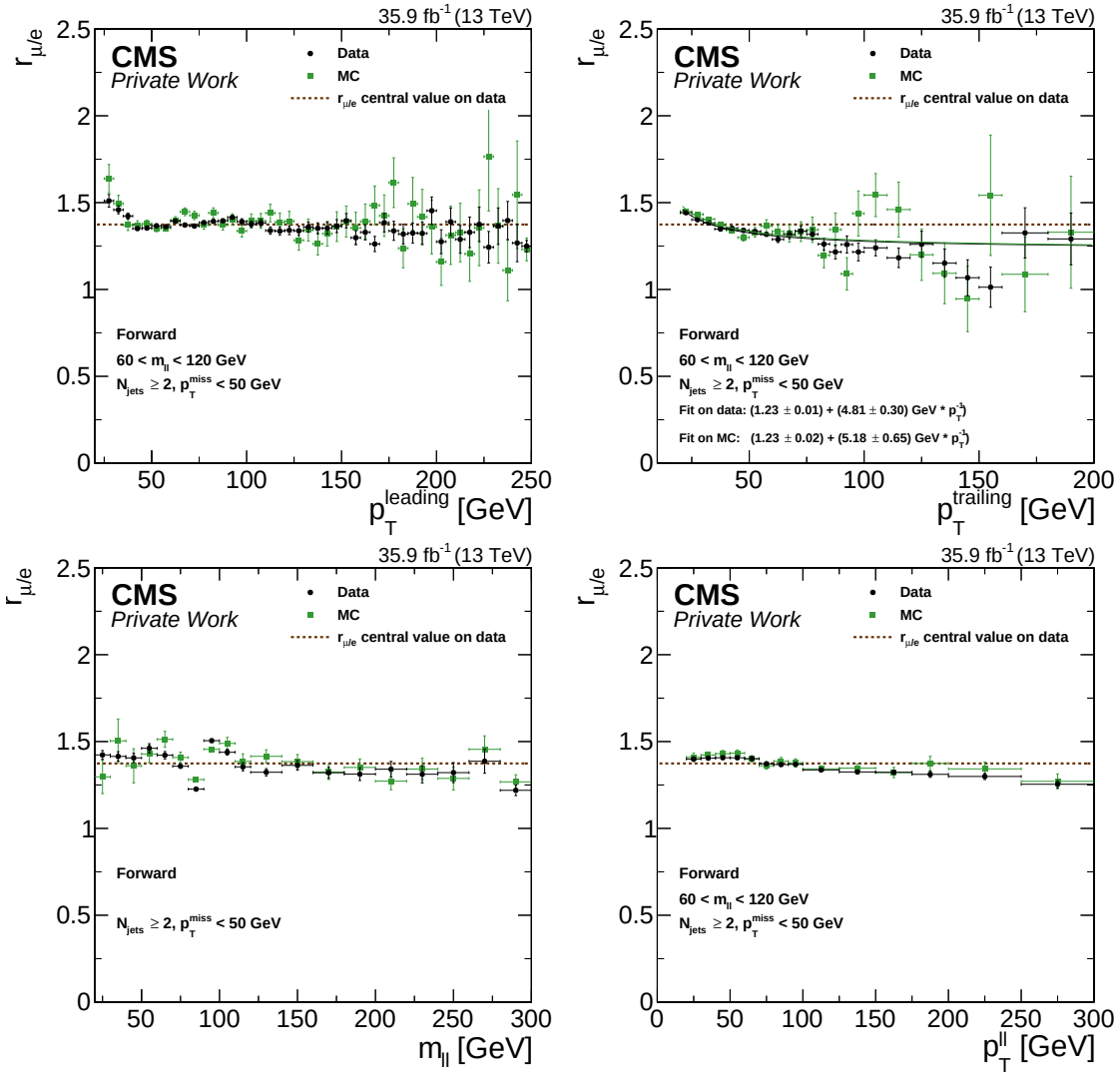

Figure E.1: $r_{\mu/e}$ as a function of the p_{T} of the leading (top left) and trailing lepton (top right) and the invariant mass (bottom left) and p_{T} of the dilepton system (bottom right) in the forward lepton selection for data and simulation. The central value indicates the $r_{\mu/e}$ value that would be used without the parameterization. The fit values of the parameterization are shown in the top right plot.

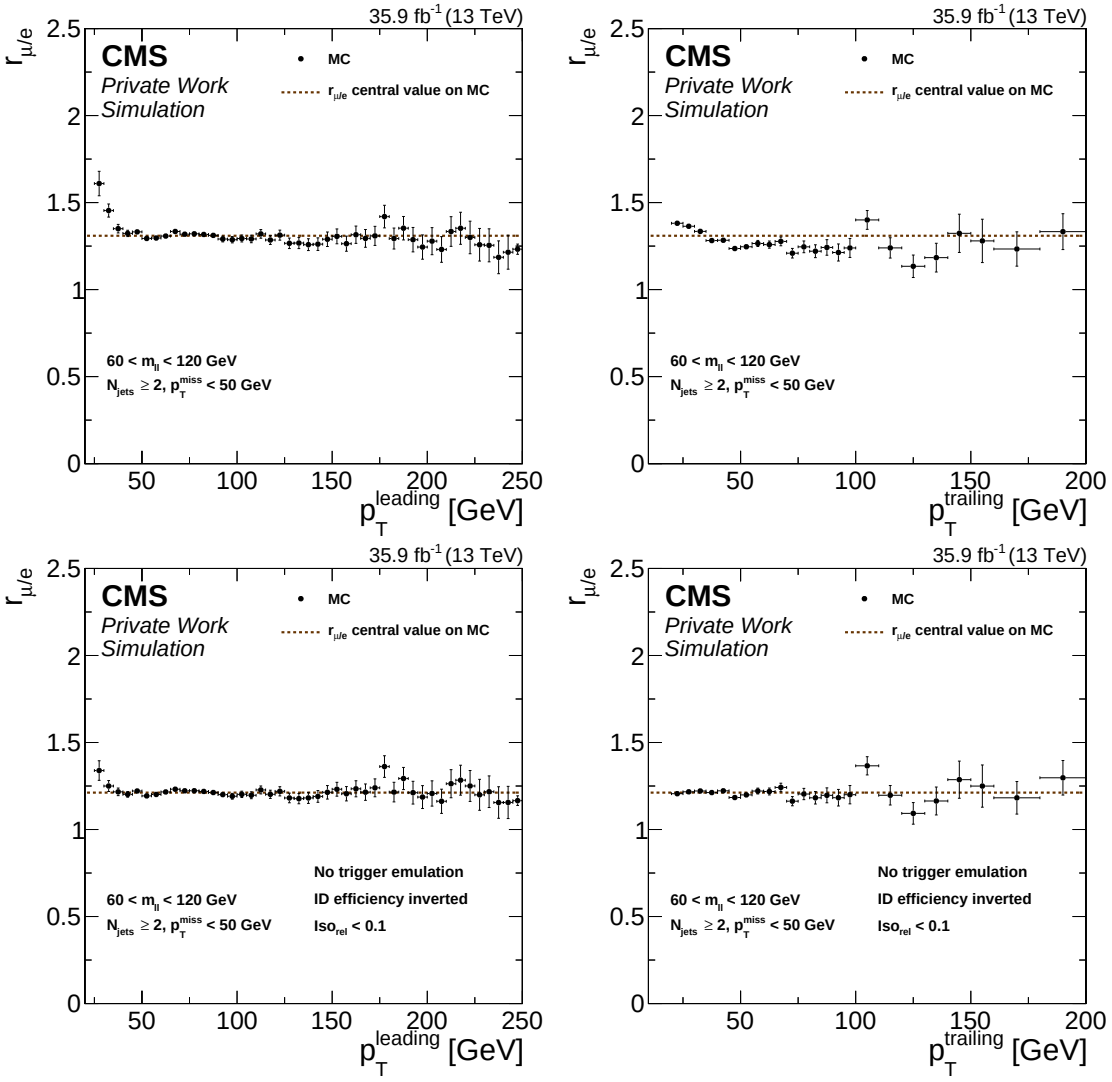

Figure E.2: $r_{\mu/e}$ in simulation as a function of leading lepton p_{T} (left) and subleading lepton p_{T} (right). The default selection is used in the plots at the top while in the bottom the trigger simulation is switched off, the electron identification efficiency is inverted, and an isolation cut of $\mathrm{Iso}_{\mathrm{rel}} < 0.1$ is used.

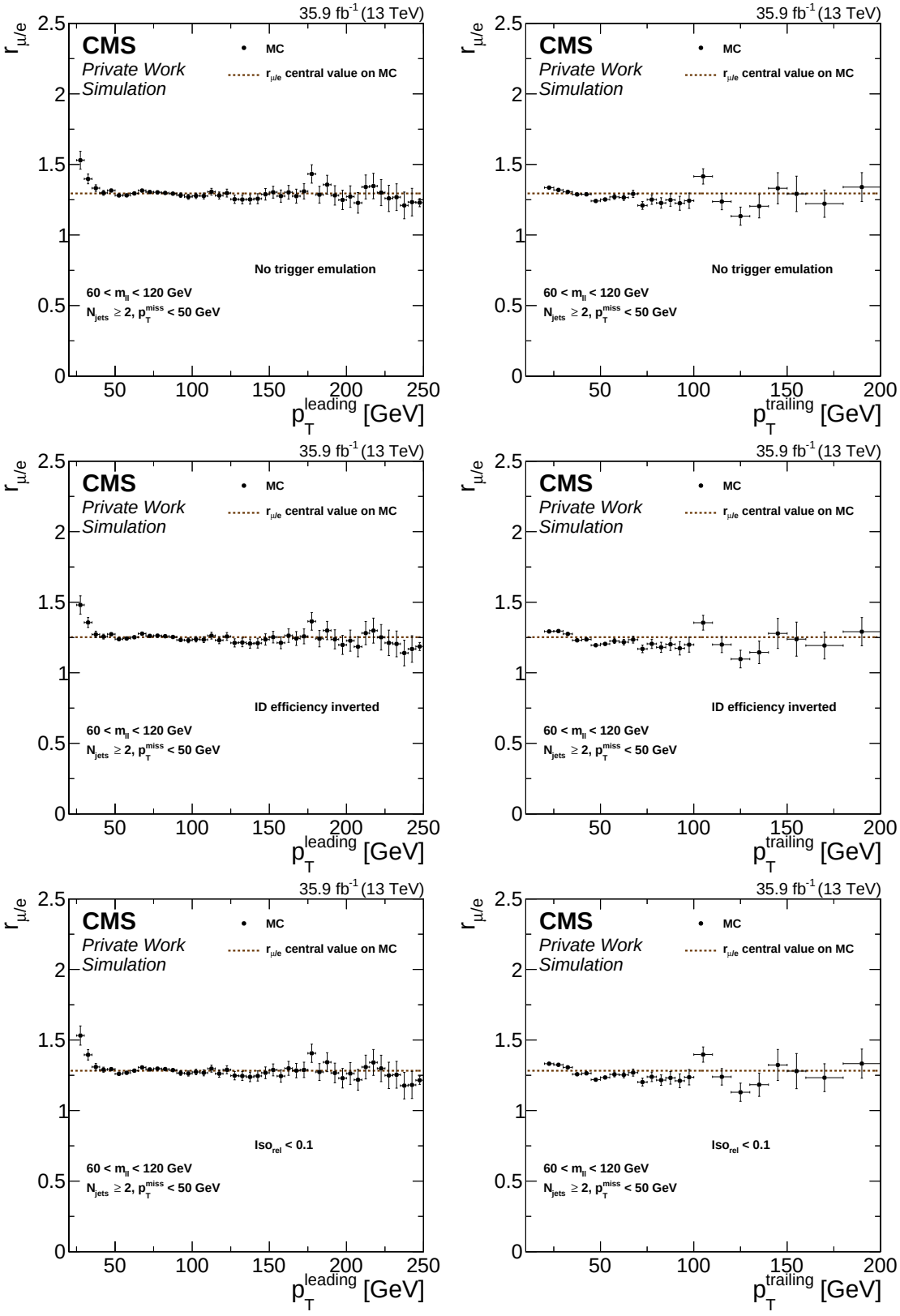

Figure E.3: $r_{\mu/e}$ in simulation as a function of leading lepton p_{T} (left) and subleading lepton p_{T} (right). In each of the rows either the trigger simulation is switched off (top), the electron identification efficiency is inverted (center), or an isolation cut of $\mathrm{Iso}_{\mathrm{rel}} < 0.1$ is used (bottom).

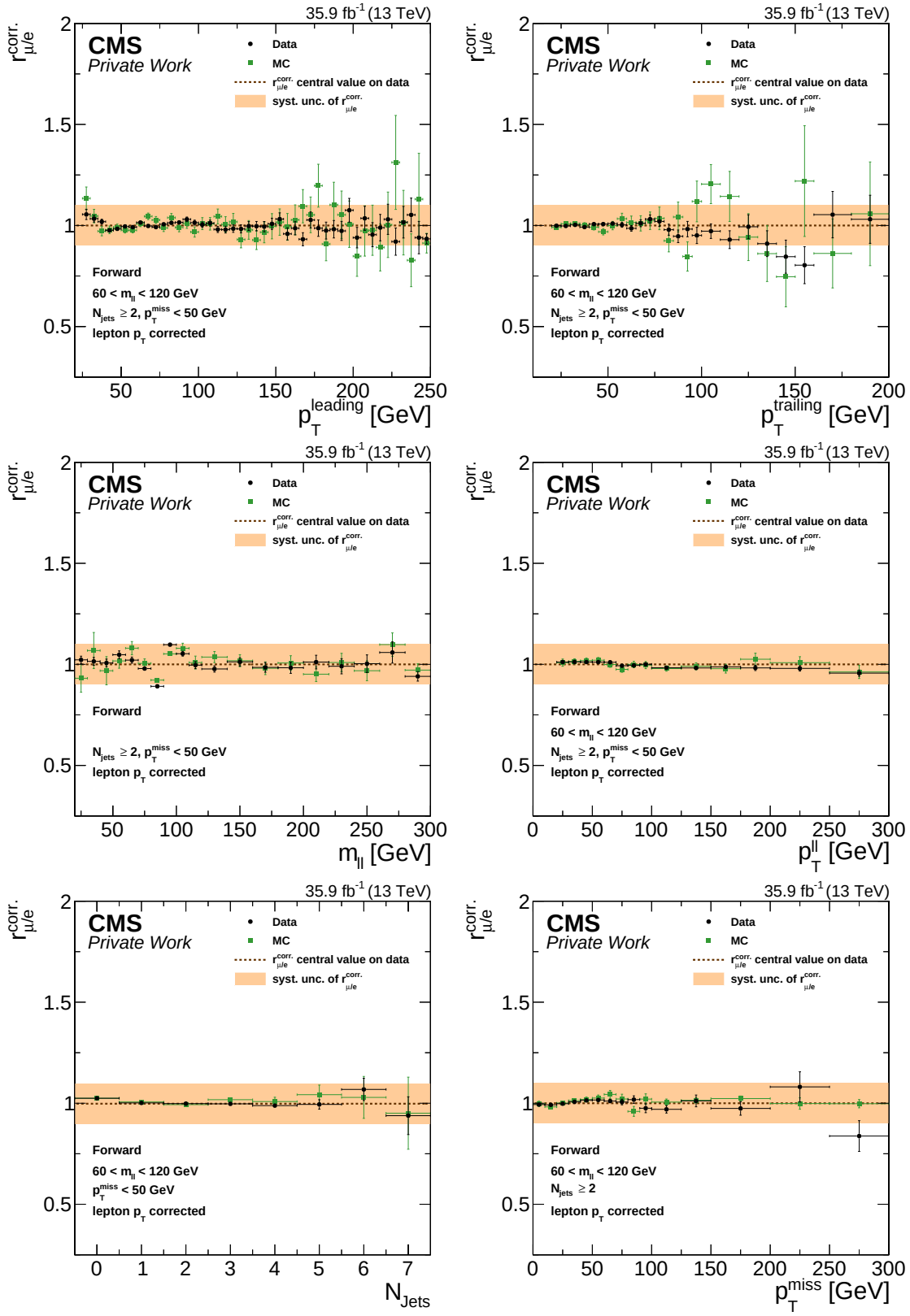

Figure E.4: $r_{\mu/e}^{\text{corr.}}$ as a function of the p_{T} of the leading (top left) and trailing lepton (top right),the invariant mass (center left) and p_{T} of the dilepton system (center right), the jet multiplicity (bottom left), and $p_{\text{T}}^{\text{miss}}$ (bottom right) in the forward lepton selection for data and simulation. The central value on data is indicated by a dashed line while the systematic uncertainty is shown by an orange band.

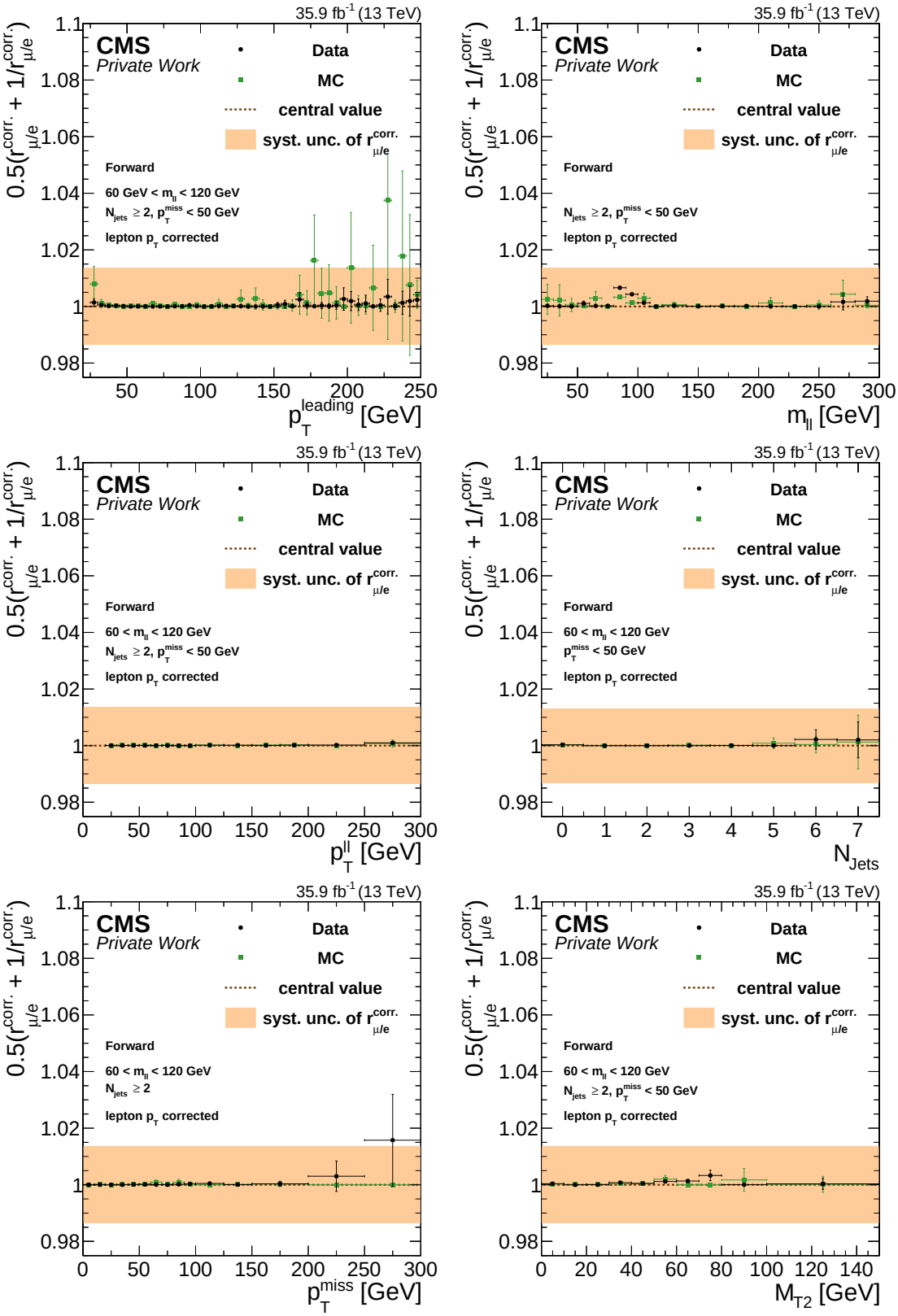

Figure E.5: $0.5\left(r^{\text{corr.}}_{\mu/e} + 1/r^{\text{corr.}}_{\mu/e}\right)$ as a function of the leading lepton p_{T} (top left),the invariant mass (top right) and p_{T} of the dilepton system (center left), the jet multiplicity (center right),$p_{\text{T}}^{\text{miss}}$ (bottom left), and M_{T2} (bottom right) in the forward lepton selection for data and simulation. The central value on data is indicated by a dashed line while the systematic uncertainty is shown by an orange band.

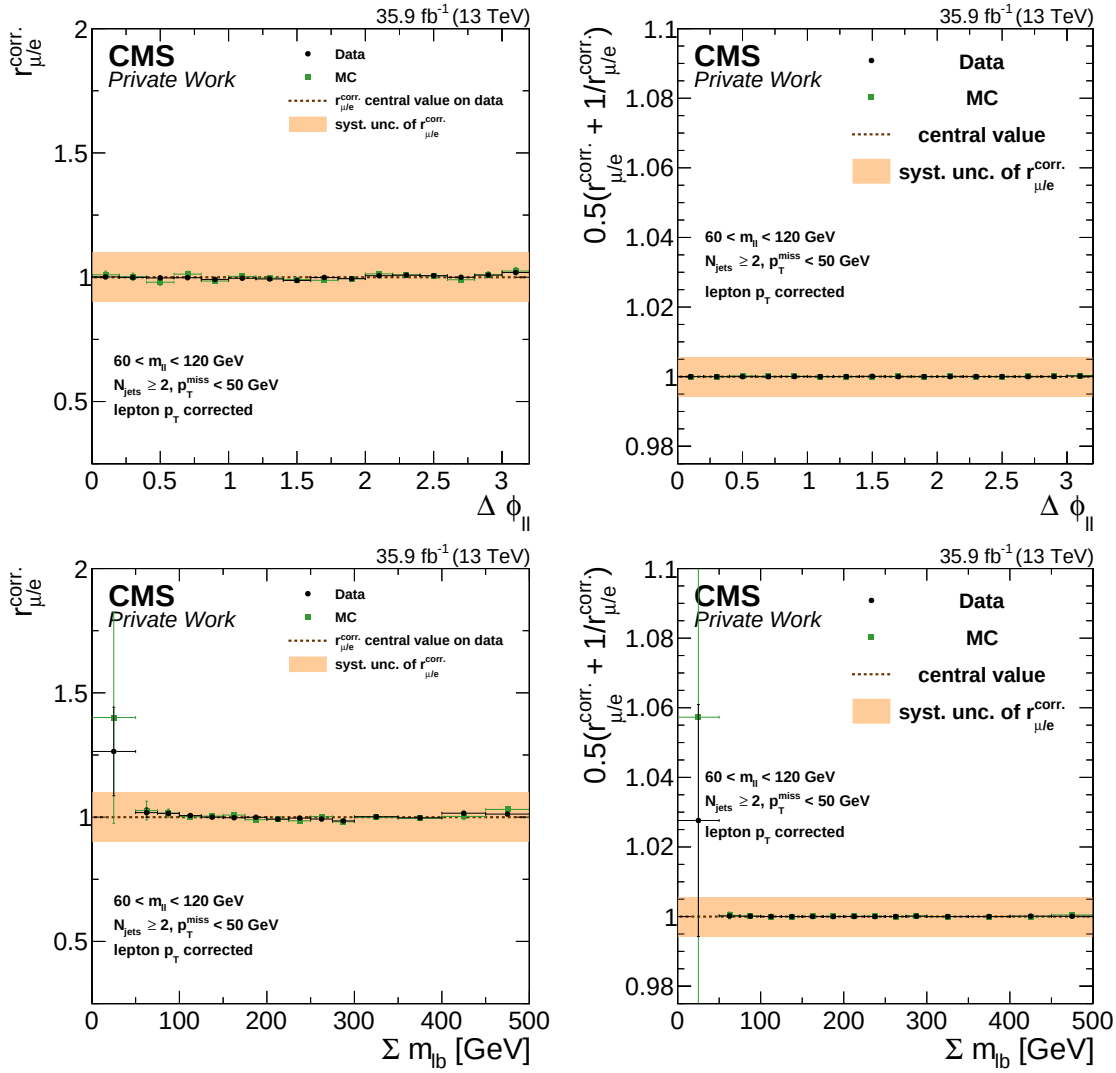

Figure E.6: $r^{\text{corr.}}_{\mu/e}$ (left) and $0.5\left(r^{\text{corr.}}_{\mu/e} + 1/r^{\text{corr.}}_{\mu/e}\right)$ (right) as a function of $\Delta\phi_{\ell\ell}$ (top) and $\Sigma m_{\ell b}$ (bottom) for data and simulation. The central value on data is indicated by a dashed line while the systematic uncertainty is shown by an orange band.

References

[1] CMS Collaboration, "Observation of a new boson at a mass of 125 GeV with the CMS experiment at the LHC", *Phys. Lett. B* **716** (2012) 30, DOI: 10.1016/j.physletb.2012.08.021. arXiv: 1207.7235.

[2] ATLAS Collaboration, "Observation of a new particle in the search for the Standard Model Higgs boson with the ATLAS detector at the LHC", *Phys. Lett. B* **716** (2012) 1, DOI: 10.1016/j.physletb.2012.08.020. arXiv: 1207.7214.

[3] ATLAS Collaboration, "Standard Model Results", "https://twiki.cern.ch/twiki/bin/view/AtlasPublic/StandardModelPublicResults last accessed 2017-12-15",

[4] CMS Collaboration, "CMS Standard Model Physics Results", "https://twiki.cern.ch/twiki/bin/view/CMSPublic/PhysicsResultsSMP last accessed 2017-12-15",

[5] CMS Collaboration, "Search for physics beyond the standard model in events with two leptons, jets, and missing transverse momentum in pp collisions at $\sqrt{s} = 8$TeV", *JHEP* **04** (2015) 124, DOI: 10.1007/jhep04(2015)124. arXiv: 1502.06031.

[6] J.-F. Schulte, "Search for supersymmetry in opposite sign same flavour dilepton events with the CMS detector", PhD thesis, RWTH Aachen University, 2015.

[7] CMS Collaboration, "Search for new physics in final states with two opposite-sign, same-flavor leptons, jets, and missing transverse momentum in pp collisions at $\sqrt{s} = 13\,\text{TeV}$", *JHEP* **12** (2016) 13, DOI: 10.1007/jhep12(2016)013. arXiv: 1607.00915.

[8] N. Mohr, "Search for Supersymmetry in Opposite-sign Dilepton Final States with the CMS Experiment", PhD thesis, RWTH Aachen University, 2011.

[9] D. Sprenger, "Search for Supersymmetry in Opposite-sign Dilepton Final States with the CMS Experiment", PhD thesis, RWTH Aachen University, 2012.

[10] CMS Collaboration, "Search for new phenomena in final states with two opposite-charge, same-flavor leptons, jets, and missing transverse momentum in pp collisions at $\sqrt{s} = 13\,\text{TeV}$", *Submitted to JHEP* (2017). arXiv: 1709.08908.

[11] C. Lester and D. Summers, "Measuring masses of semi-invisibly decaying particle pairs produced at hadron colliders", *Phys. Lett. B* **463** (1999) 99, DOI: 10.1016/s0370-2693(99)00945-4. arXiv: hep-ph/9906349.

[12] A. Barr, C. Lester, and P. Stephens, "A variable for measuring masses at hadron colliders when missing energy is expected; mT2: the truth behind the glamour", *J. Phys. G* **29** (2003) 2343, DOI: 10.1088/0954-3899/29/10/304. arXiv: hep-ph/0304226.

[13] S. L. Glashow, "Partial-symmetries of weak interactions", *Nuclear Physics* **22** (1961) 579, DOI: 10.1016/0029-5582(61)90469-2.

[14] A. Salam and J.C. Ward, "Electromagnetic and weak interactions", *Physics Letters* **13** (1964) 168, DOI: 10.1016/0031-9163(64)90711-5.

[15] S. Weinberg, "A Model of Leptons", *Phys. Rev. Lett.* **19** (1967) 1264, DOI: 10.1103/physrevlett.19.1264.

[16] S. Weinberg, "Effects of a Neutral Intermediate Boson in Semileptonic Processes", *Phys. Rev. D* **5** (1972) 1412, DOI: 10.1103/physrevd.5.1412.

[17] F. Halzen and A. Martin, "Quarks and Leptons: An Introductory Course in Modern Particle Physics", Wiley, 1984.

[18] S. F. Novaes, "Standard Model: An Introduction", arXiv: hep-ph/0001283.

[19] A. Pich, "The Standard Model of Electroweak Interactions", arXiv: hep-ph/0705.4264.

[20] C. Patrignani et al. (Particle Data Group), "2016 Review of Particle Physics", *Chin. Phys. C* **40** (2016) 100001, DOI: 10.1088/1674-1137/40/10/100001.

[21] P. Higgs, "Broken Symmetries and the Masses of Gauge Bosons", *Phys. Rev. Lett.* **13** (1964) 508, DOI: 10.1103/physrevlett.13.508.

[22] F. Englert and R. Brout, "Broken Symmetry and the Mass of Gauge Vector Mesons", *Phys. Rev. Lett.* **13** (1964) 321, DOI: 10.1103/physrevlett.13.321.

[23] G. Guralnik, C. Hagen, and T. Kibble, "Global Conservation Laws and Massless Particles", *Phys. Rev. Lett.* **13** (1964) 585, DOI: 10.1103/physrevlett.13.585.

[24] ATLAS and CMS Collaborations, "Combined Measurement of the Higgs Boson Mass in pp Collisions at $\sqrt(s) = 7$ and 8 TeV with the ATLAS and CMS Experiments", *Phys. Rev. Lett.* **114** (2015) 191803, DOI: 10.1103/PhysRevLett.114.191803. arXiv: 1503.07589.

[25] CMS Collaboration, "Precise determination of the mass of the Higgs boson and tests of compatibility of its couplings with the standard model predictions using proton collisions at 7 and 8 TeV", *Eur. Phys. J. C* **75** (2015). DOI: 10.1140/epjc/s10052-015-3351-7. arXiv: 1412.8662.

[26] UA1 Collaboration, "Experimental observation of isolated large transverse energy electrons with associated missing energy at $\sqrt{s} = 540$ GeV", *Phys. Lett. B* **122** (1983) 103, DOI: 10.1016/0370-2693(83)91177-2.

[27] UA2 Collaboration, "Observation of single isolated electrons of high transverse momentum in events with missing transverse energy at the CERN $p\bar{p}$ collider", *Phys. Lett. B* **122** (1983) 476, DOI: 10.1016/0370-2693(83)91605-2.

[28] CDF Collaboration, "Observation of Top Quark Production in $p\bar{p}$ Collisions with the Collider Detector at Fermilab", *Phys. Rev. Lett.* **74** (1995) 2626, DOI: 10.1103/physrevlett.74.2626. arXiv: hep-ex/9503002.

[29] D0 Collaboration, "Search for High Mass Top Quark Production in $p\bar{p}$ Collisions at s= 1.8 TeV", *Phys. Rev. Lett.* **74** (1995) 2422, DOI: 10.1103/physrevlett.74.2422.

[30] S. P. Martin, "A supersymmetry primer", *Adv. Ser. Direct. High Energy Phys* **21** (2010) 1, DOI: 10.1142/9789814307505_0001. arXiv: hep-ph/9709356.

[31] S. M. Bilenky, "The History of Neutrino Oscillations", *Phys. Scr.* **T121** (2005) 17, DOI: 10.1088/0031-8949/2005/t121/001. arXiv: hep-ph/0410090.

[32] J. W. F. Valle, "Neutrino physics overview", *J. Phys. Conf. Ser.* **53** (2006) 473, DOI: 10.1088/1742-6596/53/1/031. arXiv: hep-ph/0608101.

[33] E. Komatsu et al., "Seven-Year Wilkinson Microwave Anisotropy Probe (WMAP) Observations: Cosmological Interpretation", *Astrophys. J. Suppl. Ser.* **192** (2011) 18, DOI: 10.1088/0067-0049/192/2/18. arXiv: 1001.4538.

[34] Planck Collaboration, "Planck 2015 results. I. Overview of products and scientific results", *A&A* **594** (2016) A1, DOI: 10.1051/0004-6361/201527101. arXiv: 1502.01582.

[35] V. C. Rubin, N. Thonnard, and Jr. Ford W. K., "Rotational properties of 21 SC galaxies with a large range of luminosities and radii, from NGC 4605 R = 4kpc to UGC 2885 R = 122 kpc", *Astrophys. J.* **238** (1980) 471, DOI: 10.1086/158003.

[36] D. Clowe et al., "A Direct Empirical Proof of the Existence of Dark Matter", *Astrophys. J.* **648** (2006) 109, DOI: 10.1086/508162. arXiv: astro-ph/0608407.

[37] G. Bertone, D. Hooper, and J. Silk, "Particle dark matter: evidence, candidates and constraints", *Phys. Rep.* **405** (2005) 279, DOI: 10.1016/j.physrep.2004.08.031. arXiv: hep-ph/0404175.

[38] K. Freese, "Can scalar neutrinos or massive Dirac neutrinos be the missing mass?", *Phys. Lett. B* **167** (1986) 295, DOI: 10.1016/0370-2693(86)90349-7.

[39] M. Drees, R. Godbole, and P. Roy, "Theory and Phenomenology of Sparticles", World Scientific Publishing Co. Pte. Ltd, 2004.

[40] I. Hinchliffe et al., "Precision SUSY measurements at CERN LHC", *Phys. Rev. D* **55** (1997) 5520, DOI: 10.1103/physrevd.55.5520. arXiv: hep-ph/9610544.

[41] M. Nojiri and Y. Yamada, "Neutralino decays at the CERN LHC", *Phys. Rev. D* **60** (1999). DOI: 10.1103/physrevd.60.015006. arXiv: hep-ph/9902201.

[42] C. Han et al., "Status of CMSSM in light of current LHC Run-2 and LUX data", *Phys. Lett. B* **769** (2017) 470, DOI: 10.1016/j.physletb.2017.04.026. arXiv: 1612.02296.

[43] A. Djouadi et al., "The Minimal Supersymmetric Standard Model: Group Summary Report", arXiv: hep-ph/9901246.

[44] D. Alves et al., "Simplified models for LHC new physics searches", *J. Phys. G* **39** (2012) 105005, DOI: 10.1088/0954-3899/39/10/105005. arXiv: 1105.2838.

[45] C. Schomakers, "Studies of simplified models and projection to $\sqrt{s} = 13\,\text{TeV}$ for the CMS SUSY dilepton edge search", Master thesis, RWTH Aachen University, 2014.

[46] C. Borschensky et al., "Squark and gluino production cross sections in pp collisions at $\sqrt{s} = 13, 14, 33$ and $100\,\text{TeV}$", *Eur. Phys. J. C* **74** (2014) 3174, DOI: 10.1140/epjc/s10052-014-3174-y. arXiv: 1407.5066.

[47] L. Evans and P. Bryant, "LHC Machine", *JINST* **3** (2008) S08001, DOI: 10.1088/1748-0221/3/08/s08001.

[48] ATLAS Collaboration, "The ATLAS Experiment at the CERN Large Hadron Collider", *JINST* **3** (2008) S08003, DOI: 10.1088/1748-0221/3/08/s08003.

[49] CMS Collaboration, "The CMS experiment at the CERN LHC", *JINST* **3** (2008). DOI: 10.1088/1748-0221/3/08/s08004.

[50] ALICE Collaboration, "The ALICE experiment at the CERN LHC", *JINST* **3** (2008) S08002, DOI: 10.1088/1748-0221/3/08/s08002.

[51] LHCb Collaboration, "The LHCb Detector at the LHC", *JINST* **3** (2008) S08005, DOI: 10.1088/1748-0221/3/08/s08005.

[52] F. Marcastel, "CERN's Accelerator Complex. . La chaîne des accélérateurs du CERN." "https://cds.cern.ch/record/1621583", OPEN-PHO-CHART-2013-001. 2013.

[53] CMS Collaboration, "CMS Luminosity - Public Results", "https://twiki.cern.ch/twiki/bin/view/CMSPublic/LumiPublicResults last accessed 2017-12-15",

[54] CMS Collaboration, "Description and performance of track and primary-vertex reconstruction with the CMS tracker", *JINST* **9** (2014) 10009, DOI: 10.1088/1748-0221/9/10/p10009. arXiv: 1405.6569.

[55] CMS Collaboration, "Energy calibration and resolution of the CMS electromagnetic calorimeter in pp collisions at $\sqrt{s} = 7$ TeV", *JINST* **8** (2013) P09009, DOI: 10.1088/1748-0221/8/09/p09009. arXiv: 1306.2016.

[56] CMS Collaboration, "Performance of CMS muon reconstruction in pp collision events at $\sqrt{s} = 7$ TeV", *JINST* **7** (2012) P10002, DOI: 10.1088/1748-0221/7/10/p10002. arXiv: 1206.4071.

[57] CMS Collaboration, "The CMS trigger system", *JINST* **12** (2017) P01020, DOI: 10.1088/1748-0221/12/01/p01020. arXiv: 1609.02366.

[58] T. Virdee, A. Petrilli, and A. Ball, *CMS High Level Trigger*. Tech. rep. revised version submitted on 2007-10-19 16:57:09. Geneva: CERN, 2007.

[59] D. Spiga et al., "The CMS Remote Analysis Builder (CRAB)", *Lecture Notes in Computer Science* **4873** (2007) 580, DOI: 10.1007/978-3-540-77220-0_52.

[60] CMS Collaboration, "CMS Physics: Technical Design Report Volume 1: Detector Performance and Software", Technical Design Report CMS, Geneva: CERN, 2006.

[61] G Petrucciani, A Rizzi, and C Vuosalo, "Mini-AOD: A New Analysis Data Format for CMS", *J. Phys. Conf. Ser.* **664** (2015) 072052, DOI: 10.1088/1742-6596/664/7/072052. arXiv: 1702.04685.

[62] "Worldwide LHC Computing Grid", "http://wlcg.web.cern.ch/ last accessed: 2017-12-10",

[63] I. Bird, "Computing for the Large Hadron Collider", *Annu. Rev. Nucl. Part. Sci.* **61** (2011) 99, DOI: 10.1146/annurev-nucl-102010-130059.

[64] R. Brun and F. Rademakers, "ROOT - An object oriented data analysis framework", *Nucl. Instrum. Meth. A* **389** (1997) 81, DOI: 10.1016/s0168-9002(97)00048-x.

[65] R. D. Ball et al., "Parton distributions for the LHC run II", *JHEP* **04** (2015) 040, DOI: 10.1007/jhep04(2015)040. arXiv: 1410.8849.

[66] F. D. Aaron et al., "Combined measurement and QCD analysis of the inclusive ep scattering cross sections at HERA", *JHEP* **01** (2010) 109, DOI: 10.1007/jhep01(2010)109. arXiv: 0911.0884.

[67] V. N. Gribov and L. N. Lipatov, "Deep inelastic electron scattering in perturbation theory", *Phys. Lett. B* **37** (1971) 78, DOI: 10.1016/0370-2693(71)90576-4.

[68] Y. L. Dokshitzer, "Calculation of the Structure Functions for Deep Inelastic Scattering and e+ e- Annihilation by Perturbation Theory in Quantum Chromodynamics." *Sov. Phys. JETP* **46** (1977) 641,

[69] G. Altarelli and G. Parisi, "Asymptotic freedom in parton language", *Nucl. Phys. B* **126** (1977) 298, DOI: 10.1016/0550-3213(77)90384-4.

[70] P. Nason, "A New Method for Combining NLO QCD with Shower Monte Carlo Algorithms", *JHEP* **2004** (2004) 040, DOI: 10.1088/1126-6708/2004/11/040. arXiv: hep-ph/0409146.

[71] S. Frixione, P. Nason, and C. Oleari, "Matching NLO QCD computations with parton shower simulations: the POWHEG method", *JHEP* **2007** (2007) 070, DOI: 10.1088/1126-6708/2007/11/070. arXiv: 0709.2092.

[72] S. Alioli et al., "A general framework for implementing NLO calculations in shower Monte Carlo programs: the POWHEG BOX", *JHEP* **06** (2010) 043, DOI: 10.1007/jhep06(2010)043. arXiv: 1002.2581.

[73] S. Alioli, S.-O. Moch, and P. Uwer, "Hadronic top-quark pair-production with one jet and parton showering", *JHEP* **01** (2012) 137, DOI: 10.1007/jhep01(2012)137. arXiv: 1110.5251.

[74] S. Alioli et al., "NLO single-top production matched with shower in POWHEG: s- and t-channel contributions", *JHEP* **09** (2009) 111, DOI: 10.1088/1126-6708/2009/09/111. arXiv: 0907.4076.

[75] E. Re, "Single-top Wt-channel production matched with parton showers using the POWHEG method", *Eur. Phys. J. C* **71** (2011) 1, DOI: 10.1140/epjc/s10052-011-1547-z. arXiv: 1009.2450.

[76] T. Melia et al., "W^+W^-, WZ and ZZ production in the POWHEG BOX", *JHEP* **11** (2011) 078, DOI: 10.1007/jhep11(2011)078. arXiv: 1107.5051.

[77] H. B. Hartanto et al., "Higgs boson production in association with top quarks in the POWHEG BOX", *Phys. Rev. D* **91** (2015) 094003, DOI: 10.1103/physrevd.91.094003. arXiv: 1501.04498.

[78] J. Alwall et al., "The automated computation of tree-level and next-to-leading order differential cross sections, and their matching to parton shower simulations", *JHEP* **07** (2014) 079, DOI: 10.1007/jhep07(2014)079. arXiv: 1405.0301.

[79] T. Sjöstrand, S. Mrenna, and P. Skands, "A brief introduction to PYTHIA 8.1", *Comput. Phys. Commun.* **178** (2008) 852, DOI: 10.1016/j.cpc.2008.01.036. arXiv: 0710.3820.

[80] CMS Collaboration, "Event generator tunes obtained from underlying event and multiparton scattering measurements", *Eur. Phys. J. C* **76** (2016) 155, DOI: 10.1140/epjc/s10052-016-3988-x. arXiv: 1512.00815.

[81] J. Alwall et al., "Comparative study of various algorithms for the merging of parton showers and matrix elements in hadronic collisions", *Eur. Phys. J. C* **53** (2007) 473, DOI: 10.1140/epjc/s10052-007-0490-5. arXiv: 0706.2569.

[82] R. Frederix and S. Frixione, "Merging meets matching in MC@NLO", *JHEP* **12** (2012) 061, DOI: 10.1007/jhep12(2012)061. arXiv: 1209.6215.

[83] S. Agostinelli et al., "Geant4: A simulation toolkit", *Nucl.Instrum.Meth.* **A506** (2003) 250, DOI: 10.1016/s0168-9002(03)01368-8.

[84] CMS Collaboration, "The Fast Simulation of the CMS Detector at LHC", *J. Phys. Conf. Ser.* **331** (2011) 032049, DOI: 10.1088/1742-6596/331/3/032049.

[85] M. Czakon and A. Mitov, "Top++: A program for the calculation of the top-pair cross-section at hadron colliders", *Comput. Phys. Commun.* **185** (2014) 2930, DOI: 10.1016/j.cpc.2014.06.021. arXiv: 1112.5675.

[86] Y. Li and F. Petriello, "Combining QCD and electroweak corrections to dilepton production in the framework of the FEWZ simulation code", *Phys. Rev. D* **86** (2012) 094034, DOI: 10.1103/physrevd.86.094034. arXiv: 1208.5967.

[87] R. Gavin et al., "FEWZ 2.0: A code for hadronic Z production at next-to-next-to-leading order", *Comput. Phys. Commun.* **182** (2011) 2388, DOI: 10.1016/j.cpc.2011.06.008. arXiv: 1011.3540.

[88] S. Quackenbush et al., "W physics at the LHC with FEWZ 2.1", *Comput. Phys. Commun.* **184** (2013) 209, DOI: 10.1016/j.cpc.2012.09.005. arXiv: 1201.5896.

[89] J. M. Campbell, R. K. Ellis, and C. Williams, "Vector boson pair production at the LHC", *JHEP* **07** (2011) 018, DOI: 10.1007/jhep07(2011)018. arXiv: 1105.0020.

[90] N. Kidonakis, "Two-loop soft anomalous dimensions for single top quark associated production with a W- or H-", *Phys. Rev. D* **82** (2010) 054018, DOI: 10.1103/physrevd.82.054018. arXiv: 1005.4451.

[91] M. Aliev et al., "HATHOR: HAdronic Top and Heavy quarks crOss section calculatoR", *Comput. Phys. Commun.* **182** (2011) 1034, DOI: 10.1016/j.cpc.2010.12.040. arXiv: 1007.1327.

[92] P. Kant et al., "Hathor for single top-quark production: Updated predictions and uncertainty estimates for single top-quark production in hadronic collisions", *Comput. Phys. Commun.* **191** (2015) 74, DOI: 10.1016/j.cpc.2015.02.001. arXiv: 1406.4403.

[93] S. Frixione and B. R. Webber, "Matching NLO QCD computations and parton shower simulations", *JHEP* **06** (2002) 029, DOI: 10.1088/1126-6708/2002/06/029. arXiv: hep-ph/0204244.

[94] P. Nason and G. Ridolfi, "A positive-weight next-to-leading-order Monte Carlo for Z pair hadroproduction", *JHEP* **08** (2006) 077, DOI: 10.1088/1126-6708/2006/08/077. arXiv: hep-ph/0606275.

[95] S. Höche et al., "A critical appraisal of NLO+PS matching methods", *JHEP* **09** (2012) 049, DOI: 10.1007/jhep09(2012)049. arXiv: 1111.1220.

[96] CMS Collaboration, "Electron and photon performance in CMS with the full 2016 data sample", "https://cds.cern.ch/record/2255497", CMS-DP-2017-004. 2017.

[97] CMS Collaboration, "Muon Identification and Isolation efficiency on full 2016 dataset", "http://cds.cern.ch/record/2257968", CMS-DP-2017-007. 2017.

[98] CMS Collaboration, "Heavy flavor identification at CMS with deep neural networks", "https://cds.cern.ch/record/2255736", CMS-DP-2017-005. 2017.

[99] CMS Collaboration, "Measurement of differential cross sections for top quark pair production using the lepton+jets final state in proton-proton collisions at 13 TeV", *Phys. Rev. D* **95** (2017) 092001, DOI: 10.1103/physrevd.95.092001. arXiv: 1610.04191.

[100] CMS Collaboration, "Measurement of the differential cross section for $t\bar{t}$ production in the dilepton final state at $\sqrt{s} = 13$ TeV", "Technical Report CMS-PAS-TOP-16-011", 2016.

[101] CMS Collaboration, "Particle-flow reconstruction and global event description with the CMS detector", *JINST* **12** (2017) P10003, DOI: 10.1088/1748-0221/12/10/P10003. arXiv: 1706.04965.

[102] R. Frühwirth, "Application of Kalman filtering to track and vertex fitting", *Nucl. Instrum. Methods Phys. Res., A* **262** (1987) 444, DOI: 10.1016/0168-9002(87)90887-4.

[103] CMS Collaboration, "Performance of CMS muon reconstruction in cosmic-ray events", *JINST* **5** (2010) T03022, DOI: 10.1088/1748-0221/5/03/t03022. arXiv: 0911.4994.

[104] CMS Collaboration, "Particle-flow commissioning with muons and electrons from J/Psi and W events at 7 TeV", "Technical Report CMS-PAS-PFT-10-003", 2010.

[105] CMS Collaboration, "Performance of electron reconstruction and selection with the CMS detector in proton-proton collisions at $\sqrt(s) = 8$ TeV", *JINST* **10** (2015) P06005, DOI: 10.1088/1748-0221/10/06/p06005. arXiv: 1502.02701.

[106] W. Adam et al., "Reconstruction of electrons with the Gaussian-sum filter in the CMS tracker at LHC", *J. Phys. G* **31** (2005) N9, DOI: 10.1088/0954-3899/31/9/N01. arXiv: physics/0306087.

[107] K. Rose, "Deterministic annealing for clustering, compression, classification, regression, and related optimization problems", *Proceedings of the IEEE* **86** (1998) 2210, DOI: 10.1109/5.726788.

[108] W. Waltenberger, R. Frühwirth, and P. Vanlaer, "Adaptive vertex fitting", *J. Phys. G* **34** (2007) N343, DOI: 10.1088/0954-3899/34/12/n01.

[109] M. Cacciari, G. P. Salam, and G. Soyez, "The anti-k_t jet clustering algorithm", *JHEP* **04** (2008) 063, DOI: 10.1088/1126-6708/2008/04/063. arXiv: 0802.1189.

[110] M. Cacciari, G. P. Salam, and G. Soyez, "FastJet user manual", *Eur. Phys. J. C* **72** (2012) 1896, DOI: 10.1140/epjc/s10052-012-1896-2. arXiv: 1111.6097.

[111] S. D. Ellis, "Successive combination jet algorithm for hadron collisions", *Phys. Rev. D* **48** (1993) 3160, DOI: 10.1103/physrevd.48.3160. arXiv: hep-ph/9305266.

[112] CMS Collaboration, "Determination of jet energy calibration and transverse momentum resolution in CMS", *JINST* **6** (2011) P11002, DOI: 10.1088/1748-0221/6/11/P11002. arXiv: 1107.4277.

[113] CMS Collaboration, "Identification of b quark jets at the CMS Experiment in the LHC Run 2", "Technical Report CMS-PAS-BTV-15-001", 2016.

[114] CMS Collaboration, "Performance of missing energy reconstruction in 13 TeV pp collision data using the CMS detector", "Technical Report CMS-PAS-JME-16-004", 2016.

[115] L. Tuura et al., "CMS data quality monitoring: Systems and experiences", *J. Phys. Conf. Ser.* **219** (2010) 072020, DOI: 10.1088/1742-6596/219/7/072020.

[116] CMS Collaboration, "Search for physics beyond the standard model in events with two leptons of same sign, missing transverse momentum, and jets in proton-proton collisions at $\sqrt{s} = 13$ TeV", *Eur. Phys. J. C* **77** (2017) 578, DOI: 10.1140/epjc/s10052-017-5079-z. arXiv: 1704.07323.

[117] CMS Collaboration, "Search for new physics with multileptons and jets in 35.9 fb^{-1} of pp collision data at $\sqrt{s} = 13$ TeV", "Technical Report CMS-PAS-SUS-16-041", 2017.

[118] CMS Collaboration, "Search for physics beyond the standard model in events with a Z boson, jets, and missing transverse energy in pp collisions at $\sqrt{s} = 7\,\text{TeV}$", *Phys. Lett. B* **716** (2012) 260, DOI: 10.1016/j.physletb.2012.08.026. arXiv: 1204.3774.

[119] ATLAS Collaboration, "Search for supersymmetry in events containing a same-flavour opposite-sign dilepton pair, jets, and large missing transverse momentum in $\sqrt{s} = 8$TeV pp collisions with the ATLAS detector", *The European Physical Journal C* **75hi** (2015). DOI: 10.1140/epjc/s10052-015-3518-2.

[120] ATLAS Collaboration, "Search for new phenomena in events containing a same-flavour opposite-sign dilepton pair, jets, and large missing transverse momentum in $\sqrt{s} = 13\,\text{TeV}$ pp collisions with the ATLAS detector", *Eur. Phys. J. C* **77** (2017) 144, DOI: 10.1140/epjc/s10052-017-4700-5.

[121] M. J. Oreglia, "A Study of the Reactions $\psi' \to \gamma\gamma\psi''$", SLAC Report SLAC-R-236, see appendix D, PhD thesis, Stanford University, 1980.

[122] T. Junk, "Confidence level computation for combining searches with small statistics", *Nucl. Instrum. Meth. A* **434** (1999) 435, DOI: 10.1016/s0168-9002(99)00498-2. arXiv: hep-ex/9902006.

[123] A. L. Read, "Presentation of search results: the CLs technique", *J. Phys. G* **28** (2002) 2693, DOI: 10.1088/0954-3899/28/10/313.

[124] ATLAS and CMS Collaborations, "Procedure for the LHC Higgs boson search combination in Summer 2011", "Technical Report ATL-PHYS-PUB-2011-11, CMS-NOTE-2011-005, 2011, Available on the CERN document server: http://cds.cern.ch/record/1379837",

[125] G. Cowan et al., "Asymptotic formulae for likelihood-based tests of new physics", *Eur. Phys. J. C* **71** (2011) 1554, Erratum: Eur. Phys. J. C 73 (2013) 2501, DOI: 10.1140/epjc/s10052-011-1554-0. arXiv: 1007.1727.

[126] L. Moneta et al., "The RooStats Project", 2010. arXiv: 1009.1003.

[127] W. Verkerke and D. P. Kirkby, "The RooFit toolkit for data modeling", *13th International Conference on Computing in High-Enery and Nuclear Physics (CHEP 2003)* **C0303241** (2003) 183, arXiv: physics/0306116.

[128] K. Cranmer, "Kernel estimation in high-energy physics", *Comput. Phys. Commun.* **136** (2001) 198, DOI: 10.1016/s0010-4655(00)00243-5. arXiv: hep-ex/0011057.

[129] V. Blobel and E. Lohrmann, "Statistische und numerische Methoden der Datenanalyse", Teubner Verlag, 1998.

[130] E. Gross and O. Vitells, "Trial factors for the look elsewhere effect in high energy physics", *The European Physical Journal C* **70** (2010) 525, DOI: 10.1140/epjc/s10052-010-1470-8.

[131] S. S. Wilks, "The Large-Sample Distribution of the Likelihood Ratio for Testing Composite Hypotheses", *The Annals of Mathematical Statistics* **9** (1938) 60, DOI: 10.1214/aoms/1177732360.

[132] CMS Collaboration, "CMS Luminosity Measurements for the 2016 Data Taking Period", "Technical Report CMS-PAS-LUM-17-001", 2017.

[133] CMS Collaboration, "Search for new physics in final states with two opposite-sign, same-flavor leptons, jets, and missing transverse momentum in pp collisions at $\sqrt{s} = 13\,\text{TeV}$", "Technical Report CMS-PAS-SUS-16-021", 2016.

Acknowledgments

Writing up this thesis finalizes my work in the dilepton edge group. It started about four and a half years ago, when I joined at the height of the excitement on the deviation observed at 8 TeV to write my master thesis and provide a signal scenario that might explain the excess. After handing in the master thesis, I stayed on, hoping that we might be able to confirm the deviation and thereby discover new physics. Unfortunately, this was not the case, but it was a very interesting time, nevertheless. All of this would not have been possible without the help and collaboration of many people, to all of whom I am thankful.

First of all, I would like to thank Prof. Lutz Feld for providing the opportunity to work on this interesting topic in these exciting times and for supervising my thesis. I profited a lot from his advice and support during these years.

I would also like to thank Prof. Thomas Hebbeker for agreeing to be the second referee of this work.

Special thanks to Jan Schulte for the introduction to the framework and the analysis, for the guidance in the first years, for the fruitful cooperation, and for still being available to answer questions on details of the framework even after leaving our group and Aachen.

Marius Teroerde will succeed me as the main dilepton edge analyst in Aachen. Many thanks to him for the support in the last time and for not being too critical regarding my too infrequent commits and the general state of the code.

All of my current and former colleagues in the analysis group, Prof. Lutz Feld, Christian Autermann, Jan Schulte, Knut Kiesel, Johannes Schulz, and Marius Teroerde, gave valuable input and contributed to a productive yet pleasant working environment. Beside the aforementioned, I also thank Katja Klein, Marius Preuten, Martin Lipinski, and Max Rauch for providing a enjoyable atmosphere in the working group.

A lot of people within the CMS collaboration have contributed to the success of this analysis. I would especially like to thank Pablo Martinez, Dominick Olivito, Vince Welke, Marc Dünser, Bobak Hashemi, Sergio Sanchez, Leonora Vesterbacka, and Konstantinos Theofilatos for their collaboration when performing this analysis in the recent years. Thanks to the CMS SUSY group and its conveners and leptonic subgroup conveners Claudio Campagneri, Wolfgang Adam, Filip Moortgat, Lesya Shchutska, Christina Botta, and Dominick Olivito who provided a lot of support during the constant review of this analysis.

Many thanks to the whole CMS collaboration for constructing and maintaining this great experiment and to the LHC team. Both provided me with the data necessary for my thesis.

Of course, such an analysis would not be possible without the computing infrastructure, namely the LHC grid as well as the T2 grid cluster and desktop PC cluster in Aachen. Helping to maintain the T2 cluster in Aachen gave me some insight in this context. Therefore, I am especially grateful to Thomas Kress and Andreas Nowack for their tireless efforts.

Lastly, I would like to thank my family. I am very grateful to my parents for their support in general and especially for making my studies possible. Most of all, I want to thank my wife Eva, for all the love and care in the last years, especially when our common time was cut short by long working hours, time consuming football practice and matches, trips to CERN and conferences, and other commitments.